Experimental Investigation of Friction Drag Reduction in Turbulent Boundary Layer by Super-Hydrophobic Surfaces

by

Hangjian Ling

A dissertation submitted to Johns Hopkins University in conformity with

the requirements for the degree of Doctor of Philosophy

Baltimore, Maryland

July, 2017

Abstract

The micro/nano-textured Super-Hydrophobic Surface (SHS), which traps air bubbles between the textures, has shown great potential to reduce the skin-friction drag of turbulent flows. Fabricating SHS for successful drag reduction requires an innate understanding of the interaction between the SHS and the turbulent flow. Here, a novel optical technique, dual-view digital holographic microscopy (DHM), is developed to solve the long-standing virtual image problem inherent to the inline holography. This technique is used for characterizing the velocity and turbulence in the inner part of turbulent boundary layers over SHSs with various values of rms roughness height, k_{rms}. For flow over SHSs with $k_{rms}^{+}=k_{rms}/\delta_{\nu}<1$ (δ_{ν} is the viscous length scale), drag reduction up to 30% and an upward shift of the mean velocity profile occur, along with a mild increase in turbulence in the inner part of the boundary layer. As k_{rms}^{+} increases above 1, the flow over the SHSs transitions from drag reduction, where the viscous stress dominates the total stress, to drag increase where the Reynolds shear stress becomes the primary contributor. For the present maximum value of $k_{rms}^{+}=3.28$, the inner region exhibits the characteristics of a rough-wall boundary layer, including elevated wall friction and turbulence, as well as a downward shift in the mean velocity profile. Increasing the pressure in the test facility to a level that compresses the air layer on the SHSs and exposes the protruding roughness elements reduces the extent of drag reduction. Aligning the roughness elements in the streamwise direction enhances the drag reduction. For SHSs where the roughness effect is not dominant ($k_{rms}^{+}<1$), the present measurements confirm previous theoretical predictions of the relationships between drag reduction and slip velocity allowing for both spanwise and streamwise slips.

The stability and lifetime of an air bubble (plastron) on SHSs are characterized based on total internal reflection, direct imaging, and digital holography. Increasing hydrostatic pressure causes the air-water interface to de-pin from the tip of the roughness. SHSs with larger roughness height could sustain a higher hydrostatic pressure. The mass diffusion rate of gas, either from the SHS to under-saturate liquid or from super-saturated liquid into SHS, has been measured by tracking the time-evaluation of interface height and plastron volume. As expected, the diffusion rate increases with the level of under- or super-saturation, as well as with the Reynolds number. For the turbulent flow regime, a power-law relation, $Sh_{\Theta 0}=0.47Re_{\Theta 0}^{0.77}$, is obtained using the smooth wall momentum thickness for calculating the Sherwood ($Sh_{\Theta 0}$) and Reynolds ($Re_{\Theta 0}$) numbers. This relation agrees with published diffusion rates for smooth-wall turbulent boundary layers. For a transitional boundary layer, the magnitude of $Sh_{\Theta 0}$ is lower than the turbulent power law relation. However, when $Sh_{\Theta 0}$ is plotted against the friction Reynolds number ($Re_{\tau 0}$), both the transitional and turbulent boundary layer results collapse onto a single power law, $Sh_{\Theta 0}=0.34Re_{\tau 0}^{0.913}$. This trend suggests that turbulent diffusion and wall friction are correlated. Finally, when the plastron is maintained on the SHS in a turbulent boundary layer, downstream convection of interface deformations with speed similar to those of the log layer turbulent structures have been observed.

Advisor: Dr. Joseph Katz

Reader: Dr. Tamer Zaki, Dr. Michael Schultz

Acknowledgements

This thesis would not have been possible without the inspiration and support of a number of wonderful individuals — my thanks and appreciation to all of them for being part of this journey and making this thesis possible. I owe my deepest gratitude to my advisor, Prof. Joseph Katz, for providing me such an excellent opportunity to work on this exciting project, for giving me the freedom to explore different aspects of the subject, for the timely and insightful guidance through the experiments, and for the support and encouragements at different stages of my study. Besides helping me to become a better researcher, my advisor also help me to grow and to become a better person. It is my great privilege to work with my advisor.

I would also like to thank Prof. Tamer Zaki and Prof. Michael Schultz for reading my thesis and providing detailed suggestions which greatly improve the quality of the thesis. I would like to thank other faculty members and staff for their help in past few years. Among many of them, Prof. Andrea Prosperetti, Prof. Charles Meneveau, Prof. Rajat Mittal, and Prof. Markus Hilpert provided excellent courses on various topics which prepared me well for my research. I also would like to thank Prof. John Goutsias, Prof. Andrea Prosperetti, Prof. Anand Gnanadesikan, and Prof. Darryn Waugh for serving as my GBO committee. Special thanks are due to Dr. Yury Ronzhes for his very close involvement and valuable suggestions during the facility design and assembly. My thanks also go to Stephen King who designed the electronic devices for the control and data acquisition. I would also like to thank Mike Bernard, Barbara Adamson, and other for taking care of all the administrative matters.

I especially like to express my sincere thanks to the ONR MURI research group, Prof. Gareth McKinley, Prof. Anish Tuteja, Profs. Marc Perlin, Prof. Alexander Smiths, Prof. Marcus Hultmark, Prof. Wonjae Choi, Prof. Ali Mani, Prof. Krishnan Mahesh, Dr. Siddarth Sriniviasan, Dhananjai Saranadhi, Dr. Kevin Golovin, Dr. James Gose, Matthew Fu, Abhijeet, Venkata Pillutla, Dr. Jongmin Seo for the fruitful discussion, as well as for manufacturing and characterization of SHS samples. I would like to thanks Prof. Steven Ceccio for his leading of this ONR MURI research project. I also would like to thank the financial supports from sponsors of ONR and the program manager Dr. Ki-Han Kim.

I would like to express my sincere thanks to my colleagues in the lab for their generous help both in the studies and in daily life. The name list is a long one: Prof. Jian Sheng, Prof. Huixuan Wu, Prof. Jiarong Hong, Prof. Xiaofeng Liu, Prof. David Murphy, Dr. Pranav Joshi, Dr. Siddharth Talapatra, Dr. Kunlun Bai, Dr. Cao Zhang, Dr. Rinaldo Miorini, Dr. Jacopo Biasetti, Dr. Jian Gao, Yuan Lu, Dr. Aditya Nayak, Dr. David Tan, Dr. Cheng Li, Kaushik Sampath, Yuanchao Li, Jin Wang, Courtney Engle, Huang Chen, Xinzhi Xue, Jibu Jose, Karuna Agarwal, Subhra Shankha Koley, Wonseok Heo, and others. It is my great pleasure to know all of you.

Last but not the least, I would like to thank my family: my parents and my brothers, for their continuous and unparalleled love, help and support. Without their love, I would not have continued down this very lonely road.

Table of Contents

List of Figures

List of Tables

Chapter 1. Introduction

1.1 Drag reduction by super-hydrophobic surfaces

The Super-Hydrophobic Surface (SHS), characterized by high contact angle (>150°) and low contact angle hysteresis (<5°), has existed in the nature for a long time, e.g. lotus leaf (Figure 1.1a) (Bhushan & Jung 2011, Guo et al. 2011, Yan et al. 2011). However, only recently with the development of micro/nano fabrication techniques, the manufacture of SHS has become possible (Subhash Latthe 2012). The SHS is typically constructed based on a combination of micro- or/and nano-scale surface roughness (Figure 1.1b) and a hydrophobic chemistry (Liu et al. 2013). When contacting with water, the surface promotes the retention of micro/nano air pockets between the asperities of the roughness, creating the so-called Cassie-Baxter state (Figure 1.1c) (Xue et al. 2016). Due to the existence of this air-water interface, the SHS has potential to reduce friction drag in both laminar and turbulent flows (Min & Kim 2004, Rothstein 2010).

It has been demonstrated and widely accepted that SHS reduces drag in laminar flows, starting from the early demonstrations by Cottin-Bizonne et al. (2003), Ou et al. (2004) and others. Based on Navier's model (Rothstein 2010), the slip boundary condition is characterized by the so-called slip velocity u_s and the slip length b satisfying $u_s=bdu/dy$, where y is the wall-normal direction, and u is the streamwise velocity (Figure 1.2). Experiments performed in various microfluidic devices have reported that the values of b on SHS extend to 100 μm, and the drag reduction to 40% (Lee et al. 2008, Ou & Rothstein 2005, Song et al. 2014, Srinivasan et al. 2013). Key geometric parameters of SHSs associated with drag reduction are the solid fraction Φ_s and pattern wavelength β. Ybert et al. (2007) show and Lee et al. (2008) confirm that $b \sim \beta/\Phi_s^{0.5}$. Theoretical work by Lauga & Stone (2003) reveals a functional relation $DR=f(\Phi_s, \beta/L_c)$, where DR is the drag reduction, and L_c is the characteristic length scale of the laminar flow. This relation is presumably independent of the Reynolds number Re.

Numerical simulations have predicted appreciable turbulent drag reduction by SHSs, and have provided valuable physical insight into the processes involved. Most of these simulations have assumed ideal conditions, e.g., a flat air-water interface and no air loss. Simple surface textures have been simulated, such as posts (Martell et al. 2010), ridges (Jelly et al. 2014), and sinusoidal grooves (Hasegawa et al. 2011). The solid-liquid and air-liquid interfaces have been modeled either separately as no-slip and shear-free boundaries (Martell et al. 2009), or combined as an effective slip boundary (Min & Kim 2004; You & Moin 2007), i.e., by assuming that:

$$u\big|_{y=0} = u_s = b_x \left.\frac{\partial u}{\partial y}\right|_{y=0}, \qquad v\big|_{y=0} = 0, \qquad w\big|_{y=0} = w_s = b_z \left.\frac{\partial w}{\partial y}\right|_{y=0} \tag{1.1}$$

where u, v, and w are the streamwise (x), wall-normal (y), and spanwise (z) velocity components, respectively, u_s and w_s are the slip velocity components at the wall, and b_x and b_z are components of the so-called slip lengths in directions indicated by the subscripts.

The existence of a non-zero streamwise slip length has several effects: (i) Significant drag reduction occurs when b_x is on the order of δ_υ or larger, and this effect increases with $b_x^+ = b_x/\delta_\upsilon$ (Park et al. 2013a). Here, δ_υ denotes the viscous length scale, $\delta_\upsilon=\upsilon/u_\tau$, where υ is the kinematic viscosity and u_τ is the friction velocity. A superscript + denotes a quantity normalized by δ_υ or u_τ. For example, reduction of drag by more than 50% has been predicted in the DNS studies by Martell *et al.* (2010). (ii) The mean velocity profile is shifted upward by u_s^+ (Jeffs et al. 2010) compared to that of the smooth wall. (iii) The peak magnitudes of all Reynolds stress components are significantly reduced but there is non-zero turbulence at the interface (Jelly *et al.* 2014). (iv) The streamwise vortical structures are suppressed (Park et al. 2013a) and near wall streaks are weakened (Busse & Sandham 2012; Min & Kim 2004). However, the existence of a finite spanwise slip length has opposite effects, such as an increase in drag and Reynolds stresses, as well as a downward shift in the mean velocity profile (Fukagata et al. 2006). When both b_x and b_z are non-zero, drag reduction is expected to be achieved when $b_x \geq b_z$ or when $b_x^+ > 3.5$ for all values of b_z (Busse & Sandham 2012). The effects of Φ_s, β, and roughness type (post or ridge) on b and drag reduction have be evaluated (Hasegawa et al. 2011, Lee et al. 2015). Using streamwise grooves, Park et al. (2013a) investigate a wide range of Φ_s, from 0.06 to 0.5, and β, from 0.01δ to 3δ, where δ denotes the boundary layer thickness or half channel height. They show that the drag reduction increases with increasing *Re* or β or decreasing Φ_s. Moreover, they find a correlation between drag reduction and b^+ for different values of *Re*, Φ_s and β. High values of b_x and b_z can be obtained by increasing the air fraction of the SHSs, e.g., by increasing the spacing between micro-features for a fixed feature size (Jeffs *et al.* 2010).

In parallel, numerous experimental studies have investigated the performance of SHSs in turbulent boundary layers (Henoch *et al.* 2006), channel flows (Daniello et al. 2009), and Taylor-Couette flows (Greidanus *et al.* 2011; Srinivasan *et al.* 2015). These tests have evaluated regularly patterned SHSs, such as ridges (Park et al. 2013b) and posts (Henoch et al. 2006), as well as random roughness (Aljallis *et al.* 2013). The roughness heights have ranged from nano-scale (Zhao et al. 2007) to tens of microns (Bidkar *et al.* 2014). The skin friction exerted on the textured surfaces have been quantified using floating surfaces connected to strain gages (Bidkar *et al.* 2014), as well as measuring the torque on the inner rotor in a Taylor-Couette facility (Greidanus *et al.* 2011; Srinivasan *et al.* 2015), or the pressure drop in a channel flow (Jung & Bhushan 2010). Studies involving application of Particle Image Velocimetry (PIV) have typically resolved only the buffer and outer parts of the boundary layer ($y>5\delta_\nu$) (Daniello et al. 2009; Peguero & Breuer 2009; Tian et al. 2015; Hokmabad & Ghaemi 2016; Woolford et al. 2009). The velocity distributions have been used for examining the effects of SHSs on the flow structures and on the wall friction, the latter by fitting the mean velocity profiles in the log region (Tian *et al.* 2015), or by linearly extending the total stress profiles to the wall (Woolford *et al.* 2009).

Many experimental studies have successfully detected drag reduction with values that are consistent with the numerical results. In particular, they show that: (i) The drag reduction increases with increasing gas fraction ($1-\Phi_s$), β and *Re*. Using SHSs with streamwise grooves with β=60 and 120 μm, Daniello et al. (2009) show that the SHS with the larger wavelength has a higher drag reduction. In addition, they show an increase of *DR* by up to 50% as the *Re* increases from 2000 to 8000 (based on channel height and mean flow speed). For SHSs with streamwise grooves of various Φ_s, Park et al. (2014) show that *DR* increases by up to 75% as Φ_s decreases to 5%. Using a randomly distributed rough SHS (spray-coated), Srinivasan et al. (2015) show that the drag reduction increases by up to 22% as *Re* increases to 80,000. (ii) By using spanwise-aligned ridges, Woolford *et al.* (2009) argue that spanwise slip increases drag. (iii) The mean velocity profile is shifted upward and the peak Reynolds shear stress decreases for $b_x>0$ (Tian *et al.* 2015). Conversely, for $b_z>0$, the mean velocity is shifted downward, and the Reynolds stress increases. (iv) SHSs suppress the sweep and ejection events and attenuate the spanwise vortical structures in the buffer layer (Hokmabad & Ghaemi 2016).

In contrast, several other experimental studies involving randomly textured SHSs show that *DR* decreases with increasing *Re* (Aljallis et al. 2013, Bidkar et al. 2014, Henoch et al. 2006, Ling et al. 2016, Watanabe et al. 1999, Zhao et al. 2007). In a 6 mm pipe flow, Watanabe et al. (1999) show that a SHS with roughness height of less than 10 μm reduces the drag by 14% for laminar flow, but does not reduce the drag in the turbulent flow regime. In a towing tank, Aljallis et al. (2013) show that a nanoscale textured SHS reduces the drag by about 30% in the transition regime, but causes an increase of drag in the fully turbulent regime. They attribute this trend to entrapment of an air layer at high *Re*. Bidkar *et al.* (2014) report that drag reduction seen at low *Re* diminishes with increasing *Re* when the surface roughness height k becomes comparable to δ_v, i.e., $k^+=k/\delta_v>0.5$. In other experiments, there has been no observable drag reduction, which the authors and later researchers have postulated to be a result of air layer depletion (Aljallis *et al.* 2013), air layer vibrations (Peguero & Breuer 2009; Zhao *et al.* 2007), dominance of wall roughness effects (Bidkar *et al.* 2014), as well as measurement uncertainties and errors (Greidanus *et al.* 2011).

Several notable theoretical studies have also attempted to predict and model the turbulent drag reduction induced by SHSs. Fukagata *et al.* (2006) have introduced a functional relationship between drag reduction and slip length by matching the bulk mean velocity of the no-slip flow to that of the slip flow as:

$$u_{\tau 0}\left(\frac{1}{\kappa}\log\left(\mathrm{Re}_\tau\, u_{\tau 0}/u_\tau\right)+F\left(b_z^+=0\right)\right)=u_\tau\left(b_x^+ +\frac{1}{\kappa}\log\left(\mathrm{Re}_\tau\right)+F\left(b_z^+\right)\right) \tag{1.2}$$

Here $u_{\tau 0}$ is the friction velocity of the no-slip flow, $\kappa=0.41$ is the von Karman constant, $Re_\tau=u_\tau\delta/\nu$ is the friction Reynolds number (δ is the boundary layer thickness), and $F(b_z^+)$ is a function of b_z^+. For the no-slip flow, $F(b_z^+=0)=3.2$ (Dean 1978). For the slip flow, $F(b_z^+)$ is obtained from empirical fitting to DNS results for flow with only spanwise slip. This model assumes that the effects of spanwise slip and streamwise slip are independent of each other, that κ does not change, and that drag reduction is caused solely by modification to the mean velocity profile. Substituting the b_x^+, b_z^+ and Re_τ in Equation 1.2, the calculated ratio of $u_\tau/u_{\tau 0}$ agrees with their DNS results. Subsequently, Busse & Sandham (2012) have proposed a modified $F(b_z^+)$, which requires few parameters for fitting the numerical simulation data. For SHSs in Taylor-Couette flows, Srinivasan *et al.* (2015) have proposed a modified Prandtl–von Karman–type law to relate the skin friction coefficient to the slip length that is consistent within their range of Reynolds number ($10{,}000<Re<80{,}000$). For SHSs comprised of periodic post arrays, Seo & Mani (2016) have introduced a model for slip length as a function of the cube root of the pattern wavelength, which agrees with their DNS results.

In summary, both numerical simulations and a number of prior experiments have shown great promise for applying SHSs for turbulent drag reduction. However, due to the limited resolution of previous experimental studies, direct measurements of several key features are still unavailable. For example, the impact of SHSs on the profiles of mean velocity and turbulent parameters in the inner parts of boundary layers ($y<5\delta_\upsilon$) remains unclear. Importantly, the relative contributions between viscous and Reynolds stress components have not been resolved considering that slip can occur over a substantial fraction of the wall. Furthermore, the slip velocity and the slip length have not been measured directly in turbulent flows. Thus, the functional relations between b_x^+, b_z^+ and drag reduction proposed in the theoretical (Busse & Sandham 2012; Fukagata *et al.* 2006) and numerical (Park et al. 2013a) studies have not been verified. Thus, the present study focuses on measuring the flow structure and Reynolds stresses very close to the wall ($y<5\delta_\upsilon$) for several different SHSs, including direct measurements of the local wall friction and slip velocity.

1.2 Challenges in near-wall velocity measurement over SHSs

Fully resolving the flow in the inner part of the turbulent boundary layer requires a resolution on the order of δ_υ, e.g., 5 to 20 μm, which decreases with increasing Reynolds number. The typical PIV has a resolution on the order of $5\delta_\upsilon$, which is not high enough. The inline Digital Holographic Microscopy (DHM), which takes advantages of digital holography and microscopy (Katz & Sheng 2010, Kim 2010, Sheng et al. 2006), could achieve high resolution as well as three-dimensional (3D) velocity measurements. For example, DHM has been used to measure the wall stress distribution in turbulent boundary layer over a smooth wall (Sheng et al. 2009). Therefore, we opt to use DHM for current purpose.

In inline DHM, a collimated beam illuminates the sample volume, as shown in Figure 1.3(a). The light scattered by objects in the sample volume is the object beam ($Oe^{i\varphi}$) and the undisturbed light serves as the reference beam ($Re^{i\phi}$), where O and R denote the wave amplitudes, and φ and ϕ denote wave phases. The interference pattern (hologram) between object and reference beams at the focal plane of a lens system is magnified and transmitted by an imaging lens to the digital sensor. The intensity distribution on the hologram plane I_ϕ is given by:

$$I_\phi = \left|Oe^{i\varphi} + Re^{i\phi}\right|^2 = \left(O^2 + R^2\right) + ROe^{i(\varphi-\phi)} + ROe^{-i(\varphi-\phi)} . \tag{1.3}$$

To reduce the noise level, prior to reconstruction, R^2 estimated by averaging a large number of holograms, are subtracted from each image. Since O^2 is very weak, numerical reconstruction produces the three-dimensional complex amplitude $\tilde{A}$ as well as intensity distribution A:

$$\tilde{A} = (I_\phi - R^2) \otimes h = ROe^{i(\varphi-\phi)} \otimes h + ROe^{-i(\varphi-\phi)} \otimes h \tag{1.4}$$

$$A(x, y, z) = \bigl|\,\tilde{} \qquad (1.5)$$

Here, ⊗ represents a two dimensional (2D) convolution, and *h* is a kernel function, either in the Rayleigh-Sommerfeld or the Kirchhoff-Fresnel formulas (Katz & Sheng 2010). The first term on the right hand side of Equation 1.4 generates a virtual image, and the second term creates a real image. Figure 1.3(b) shows a sample 3D intensity distribution reconstructed from a hologram of a 2 μm opaque particle located 40 μm away from the hologram plane. Clearly, two particle images, one is real and the other is virtual, locate symmetrically on two sides of the hologram plane. To avoid the virtual image, previous studies have utilized a setup (Figure 1.4a) where the sample volume is very close to a wall, and the hologram plane is located just outside of the sample volume (Sheng et al. 2008, Sheng et al. 2009, Talapatra & Katz 2012, 2013). Therefore, only the real or virtual image is reconstructed. Such an optical setup is only applicable for a transparent wall where the laser beam could pass through it. For the SHS with random surface roughness and air bubbles, however, the laser beam could not pass through. Thus, one has to use a setup (Figure 1.4b) where the sample volume is illuminated from a direction parallel to the SHS, and the hologram plane is intentionally positioned inside the sample volume, e.g. to maximize the spatial resolution. During the conventional reconstruction process, the real and virtual images are "mixed". To measure the 3D velocity distribution for this case, one has to develop a method for distinguishing between real and virtual images or eliminating one of them.

Several approaches have been developed to resolve this long-standing challenge of discriminating between real and virtual images. For example, Wilson & Zhang (2012) and Lee & Grier (2007) develop a technique suitable for weak scattering objects, namely for particles with size smaller than the recording/reconstruction wavelength and refractive index close to that of the surrounding medium. They show that the intensity at the center of the reconstructed image of the particle transits either from dark to bright or from bright to dark along the depth direction, depending on which side of the hologram plane the particle is located. For inline holography without a separate reference beam, Wilson & Zhang (2012) use this approach to separate real and virtual images of 0.5 μm diameter polystyrene particles submerged in oil. Such an approach would be very efficient in microbiological applications, for which the particles being reconstructed could be classified as weak phase objects. Unfortunately, this intensity transition does not exist in objects that cannot be classified as weak scatterers, e.g. particles with size of a few μm and/or amplitude (opaque) objects.

Phase shift digital holography (PSDH), which is based on reconstructing the complex amplitude of the object beam, and consequently, only the real image, is another widely adopted technique. Using a separate reference beam, PSDH is based on sequentially recording several holograms of the same object for varying phases of the reference beam. For example, the optical path lengths of the reference beam of four holograms are phase-shifted by quarter wavelength (Lai et al. 2000, Yamaguchi & Zhang 1997), denoted as I_0, $I_{\pi/2}$, I_π and $I_{3\pi/2}$. These holograms are then combined to give the original object wave field multiplied by a constant:

$$I_0 - I_\pi + i\left(I_{3\pi/2} - I_{\pi/2}\right) = 4ROe^{i\varphi} \tag{1.6}$$

Another approach that achieves the same goal involves recording of two quarter-wavelength phase-shifted holograms, along with either separate images of the reference and object beams (Guo & Devaney 2004) or only an image of the reference beam (Meng et al. 2006):

$$I_0 - iI_{\pi/2} - \left(R^2 + O^2 - i\left(R^2 + O^2\right)\right) = 2ROe^{i\varphi} \tag{1.7}$$

Liu & Poon (2009) suggest that two quarter wavelength phase-shifted holograms are sufficient. They correlate two reconstructed images, the first involving one of the original holograms, and the second incorporating guess values for the reference beam intensity. They deduce the correct reference beam intensity from the correlation peak.

The above applications involve a Mach-Zehnder interferometry setup, and the phase-shifted holograms are recorded at different times, e.g. by inserting quarter/half wave plates. As a result, these approaches are not suitable for dynamic systems. Several dynamic adaptations, so-called parallel/single-shot phase-shifting techniques (Araiza-Esquivel et al. 2011, Awatsuji et al. 2008, Das et al. 2012, Lin et al. 2012, Murata et al. 2009, Nomura et al. 2006, Shaked et al. 2010, Suzuki et al. 2010, Toge et al. 2008), consist of instantaneous or nearly instantaneous acquisition of two to four phase-shifted holograms. One straight-forward method is based on inserting a pixelated phase-shifting device in the path of the separated reference beam to create periodic phase difference across the digital sensor. Included in this category are the spatial light modulator (SLM) (Lin et al. 2012), a glass plate with periodic thickness (Awatsuji et al. 2008), pixelated retarder array combined with a polarizer (Suzuki et al. 2010), a binary amplitude grating (Araiza-Esquivel et al. 2011), and tilting the reference beam with a proper angle to establish quarter wavelength (Toge et al. 2008) or half wavelength (Murata et al. 2009) phase variations between neighboring pixel lines. These approaches are simple to implement, but inherently involve a decrease in spatial resolution. Another approach consists of inserting a quarter-wave plate in the path of the reference beam to establish a quarter wavelength phase shifting between perpendicularly polarized components of this beam. They are then spatially separated by a polarized beam splitter (Das et al. 2012, Shaked et al. 2010) or pixelated micro polarizers in front of the digital sensor (Nomura et al. 2006, Tahara et al. 2010). This attractive approach has been demonstrated e.g. in interferometric measurements of the morphology of biological cells (Shaked et al. 2010) and in the observation of density variations in high speed gas flows (Kakue et al. 2011). Unlike the abovementioned methods, which require a separate reference beam to install phase-shifting devices, Micó et al. (2009) introduce a method to obtain phase-shifted holograms in a classical Gabor configuration. They insert a condenser lens before the object, and an SLM in the path of the combined object and reference beams, at the focus of the condenser lens. Consequently, the SLM only modulates the phase of the reference beam. The phase-shifted holograms are recorded at different times using different SLM settings, making this approach useful for static systems. The primary advantage of the phase-shifting methods is elimination of the virtual image, resulting in improved image quality.

Methods to eliminate the twin image involving phase retrieval based on two (or multi) axially displaced inline holograms have also been introduced (Denis et al. 2005). The deconvolution procedure is based on reconstructing an image using one hologram at the plane corresponding to the other, and then subtracting this image from the second hologram. Multiple subtractions displace the twin image to a plane located far from the hologram plane (Das & Yelleswarapu 2010, Situ et al. 2008, Zhang et al. 2004). A second approach consists of iterative propagation of light back and forth between hologram planes to determine the phase distribution in these planes (Lu Rong et al. 2012, Zhang et al. 2003). Once the phase is known (estimated), only the real image is reconstructed. Both methods do not require a separated reference beam, simplifying the optical setup. Additionally, the real image quality is improved by removing the out of focus signature of the virtual image.

Here, we will introduce a simple approach to discriminate between real and virtual images in DHM. The optical setup also involves two cameras to record two holograms separated by a short distance from each other. During reconstruction, the real images overlap, whereas the virtual images are separated by twice the distance between hologram planes. This setup and followed data analysis procedures will be developed and implemented to measure the velocity in the inner part of turbulent boundary layers over SHSs.

1.3 Stability and longevity of plastron on super-hydrophobic surfaces

The Cassie-Baxter (CB) state may transition to the Wenzel state (Figure 1.5) leading to a loss of super-hydrophobicity, promoted by an increase of hydrostatic pressure in water, mass diffusion of gas, gas entrainment by turbulent flow, and others (Bormashenko 2014, Dorrer & Rühe 2009, Ling et al. 2016, Quéré 2008, Seo et al. 2015, Tian et al. 2016). Thus, understanding the effects of pressure and flow on the state of the surface is essential for the design of SHSs.

During the last decade, several criteria have been proposed to predict the stability of CB state. One of them is based on thermodynamic free energy analysis (Bico et al. 2002, Giacomello et al. 2012, Kusumaatmaja et al. 2008, Nosonovsky 2007, Patankar 2003, 2004; Sarkar & Kietzig 2015, Tsai et al. 2010, Whyman & Bormashenko 2011, Xue et al. 2012). Here, we use $\Delta E=E^{W}-E^{CB}$ to denote the difference in free energies per unit area between the Wenzel state E^{W} and the CB state E^{CB}. The CB state is thermodynamically stable when $\Delta E>0$ and wetting transition occurs when ΔE is overcome by external work (Bico et al. 2002, Nosonovsky 2007, Patankar 2003, 2004). To calculate ΔE, an early study (Bico et al. 2002) assumes a flat gas-liquid interface and no change of bulk energy, and derives $\Delta E=\gamma[(\phi_s-\varepsilon)\cos\theta_0+\phi_s-1]$, where γ is surface tension, ε the ratio of total surface area to projected surface area, and θ_0 the equilibrium contact angle on a flat surface of the same material. The stability criterion derived from $\Delta E>0$ is thus $\cos\theta_0<(\phi_s-1)/(\varepsilon-\phi_s)$ (Bico et al. 2002, Nosonovsky 2007, Patankar 2003, 2004). One way to increase ΔE and thus the stability of the CB state is to increase ε, e.g., adding nano-scale roughness on the micro-textures (Kwon et al. 2009, Whyman & Bormashenko 2011). Later calculations (Giacomello et al. 2012, Xue et al. 2012) account for the bulk energy of liquid and gas and show that increasing hydrostatic pressure causes a reduction of ΔE and thus wetting transitions.

Another criterion is derived from the balance between surface tension γ and the pressure difference across the plastron-liquid interface, $\Delta p=p_w-p_p$, where p_w and p_p are the liquid and plastron pressures, respectively. To maintain a CB state on a groove with width w, the maximum pressure difference is $\Delta p_{max}=-2\gamma\cos\theta_{adv}/w$, where θ_{adv} is the local advancing contact angle (Rothstein 2010). For an SHS with a single-level topography, θ_{adv} typically falls within $110°\leq\theta_{adv}\leq120°$ (Checco et al. 2014, Extrand 2011, Kwon et al. 2011, Papadopoulos et al. 2013, Zheng et al. 2005). Hierarchical textures involving nano-plastron on the side walls of the mirco-textures have been proposed as a means to achieve $\theta_{adv}>120°$ (Verho et al. 2012, Xue et al. 2012). The magnitude of Δp_{max} ranges from $O(10^{-2})$ atm for mirco-textures (Papadopoulos et al. 2013) to $O(10^{1})$ atm for nano-textures (Checco et al. 2014). Increases of p_w have been reported for circumstances including droplet impact (Bartolo et al. 2006), droplet evaporation (Papadopoulos et al. 2013), droplet deposition (Kwon et al. 2011), and turbulent flow (Seo et al. 2015). Due to the compressibility of gas, a submersed plastron is shown to sustain higher p_w compared to one opened to atmosphere (Amrei & Tafreshi 2015, Extrand 2011).

Even when the above criteria are satisfied, since the solubility of dissolved gas increases with pressure, gas diffusion out of the plastron might also cause a wetting transition.

Change of the SHS state due to gas diffusion has been determined by illuminating surfaces at the total internal reflection angle and observing changes to the intensity of reflection from the surface (Bobji et al. 2009; Dilip et al. 2014, 2015; Hokmabad & Ghaemi 2017, Poetes et al. 2010, Samaha et al. 2012a,b). This approach has been used in stationary liquid (Bobji et al. 2009, Poetes et al. 2010, Samaha et al. 2012b), laminar micro-channel flows (Dilip et al. 2014, 2015), laminar boundary layers (Hokmabad & Ghaemi 2017), and for jets injected parallel to a surface (Samaha et al. 2012a). Confocal microscopy (Lv et al. 2014, Poetes et al. 2010, Xiang et al. 2016, Xue et al. 2015) and direct imaging (Xu et al. 2014) have also been used to measure the height of the interface within the textures to calculate the diffusion rate in stationary liquid (Lv et al. 2014, Poetes et al. 2010, Xu et al. 2014) and laminar micro-channel flows (Xiang et al. 2016). Numerical simulations (Emami et al. 2013, Piao & Park 2015) and theoretical predictions (Lv et al. 2014, Xu et al. 2014) of the interface shape and lifetime of the CB state in stationary liquid have been performed by specifying the mass transfer coefficient of gas. Simulations for a laminar boundary layer assuming a flat, shear-free interface have also been implemented (Barth et al. 2013a). Diffusion rate estimates for a turbulent boundary layer has been based on a theoretical integral analysis involving assumed velocity profiles as well as eddy viscosity and mass diffusivity (Barth et al. 2013b). To the best of our knowledge, the mass diffusion rate has never been measured for a turbulent boundary layer.

The mass flux from plastron to liquid per unit area, J, can be approximated using Fick's law (Cussler 1997) as: $J=D(c_i-c_\infty)/\delta_c$, where D is the diffusion coefficient, c_i and c_∞ are the gas concentrations in the liquid at the interface and in the bulk, respectively, and δ_c is the gas diffusion length scale. According to Henry's law, $c_i=p_g/k_H$, where p_g is partial pressure of gas in the plastron, and k_H is the Henry's law constant. For convenience, we also define $p_\infty=k_H c_\infty$ to represent the saturation pressure corresponding to c_∞. Considering the plastron contains both gas and water vapor, $p_p=p_g+p_v$, where p_v is the water vapor pressure. For a 2D plastron within a groove, $p_p=p_w+2\gamma cos\theta_{CL}/w$, where θ_{CL} is the local contact angle. Therefore,

$$J=D(p_w+2\gamma cos\theta_{CL}/w-p_v-p_\infty)/(k_H\delta_c). \tag{1.8}$$

The CB state could be maintained when $J\leq 0$ (Dilip et al. 2014, 2015; Hokmabad & Ghaemi 2017, Xu et al. 2014), but wetting transition is expected to occur as p_w increases to a level that $J>0$. For flow with a characteristic length scale of δ, e.g. boundary layer or channel height, J is typically non-dimensionalized into the Sherwood number, $Sh_\delta=\delta/\delta_c$ (Baehr & Stephan 2006). There are several reported relationships between Sh_δ and the Reynolds number, $Re_\delta=U\delta/\nu,$ where U and ν are the characteristic velocity and liquid kinematic viscosity. For stationary liquid, Sh_δ depends only on p_w (Lv et al. 2014). In a fully-developed laminar channel flow at $0<Re_\delta<20$, Xiang *et. al.* (2016) show that $Sh_\delta\propto Re_\delta^{1/3}$. For a laminar boundary layer, simulations by Barth *et. al.* (2013a) show that Sh_δ is independent of Re_δ. The classical relation for mass transfer for a turbulent boundary layer over a solid flat plate (Baehr & Stephan 2006, Sharma & Rahman 2002) is $Sh_\delta\propto Re_\delta^{0.75}$, assuming that $\delta/x\propto(Ux/\nu)^{-0.2}$, where x is the streamwise distance. Barth *et. al* (2013b) proposes that the same relation applies to a slip boundary layer. However, this relation has yet to be proved either numerically or experimentally.

1.4 Outline of thesis

The objective of this experimental study is to understand the interaction between the turbulent boundary layer and the super-hydrophobic surface, and to guide the design of SHS for achieving drag reduction in high-Reynolds number turbulent flows. In Chapter 2, a novel optical technique, dual-view digital holographic microscopy (DHM), is developed to resolve the flow in the inner part of the turbulent boundary layer over the SHS. The purpose of using two views is to solve the long-standing virtual image problem inherent to the inline holography. The principle, optical setup and data analysis procedures will be described. Using this novel optical technique, Chapter 3 will discuss the effect of SHSs on the turbulent boundary layer including wall friction, profiles of mean velocity, viscous and Reynolds shear stresses, as well as turbulence level. The effects of surface roughness height, roughness alignment, hydrostatic pressure in the facility, as well as streamwise distance on the stress profiles will also be discussed. Since maintaining a stable air-water interface is essential for drag reduction, Chapter 4 will experimentally examine the stability and longevity of the plastron on SHSs. The effects of saturation level and Reynolds number on the rate of gas diffusion out of or into SHS will be discussed. The flow-induced vibration of interface under turbulent flow will be examined. The entrainment rate of air bubbles by turbulent flow will be measured. We will also introduce methods to restore the air-water interface after the SHS is wetted. Chapter 5 concludes the present study and discusses some possible extensions and unsolved issues.

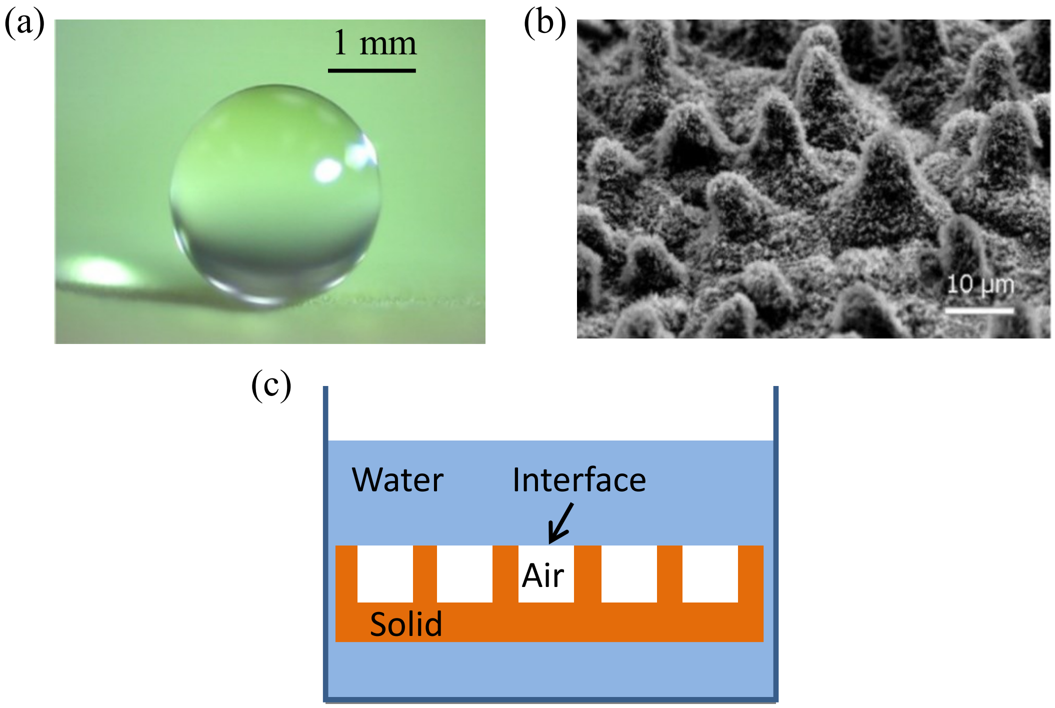

Figure 1.1. (a) A water droplet seating on the lotus leaf (Bhushan & Jung 2011); (b) Micro/nano-scale surface roughness of the lotus leaf (Bhushan & Jung 2011); (c) A schematic of the Cassie-Baxter state where air bubbles are trapped between the surface roughness.

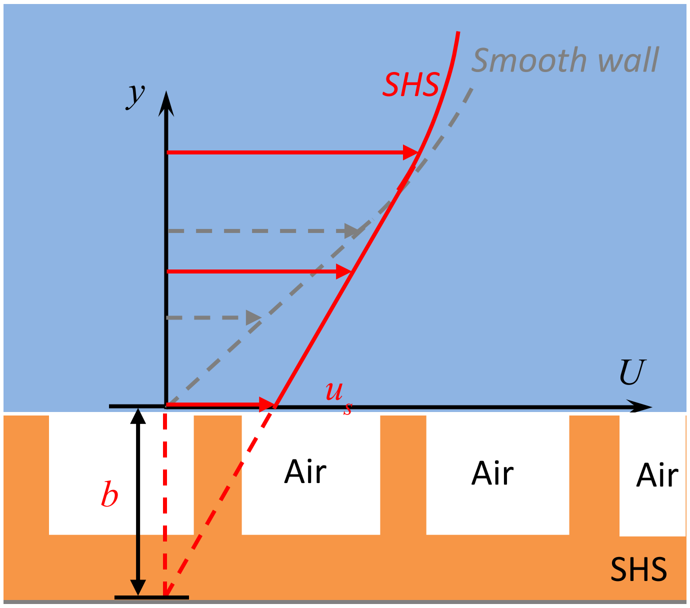

Figure 1.2. Illustration of the slip boundary condition for a liquid flow over a super-hydrophobic surface.

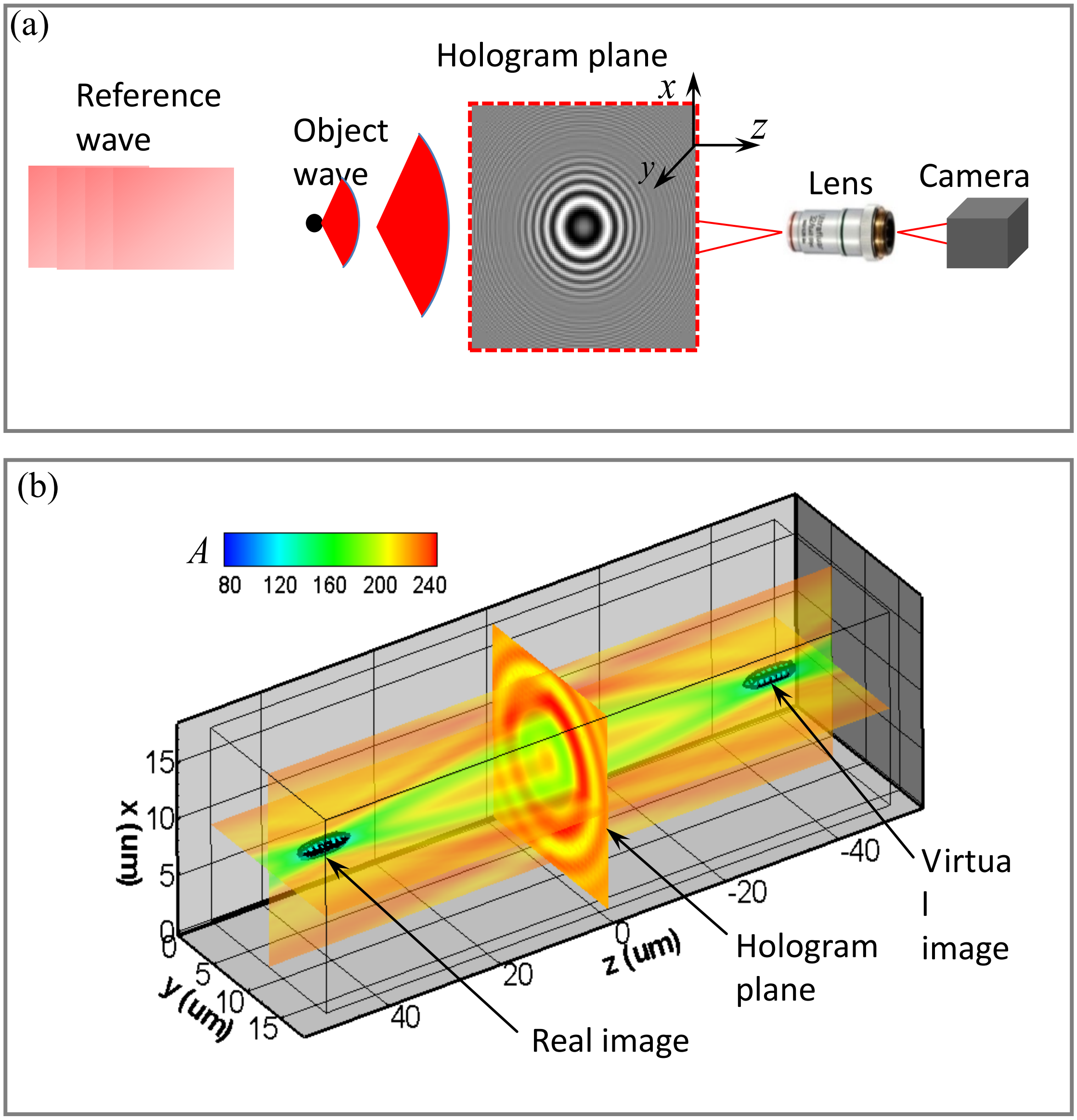

Figure 1.3. Illustration of the inline digital holography: (a) digital recording of the interference (hologram) between the reference and object beams; (b) a sample three-dimensional intensity distribution reconstructed from a hologram of a 2 μm particle.

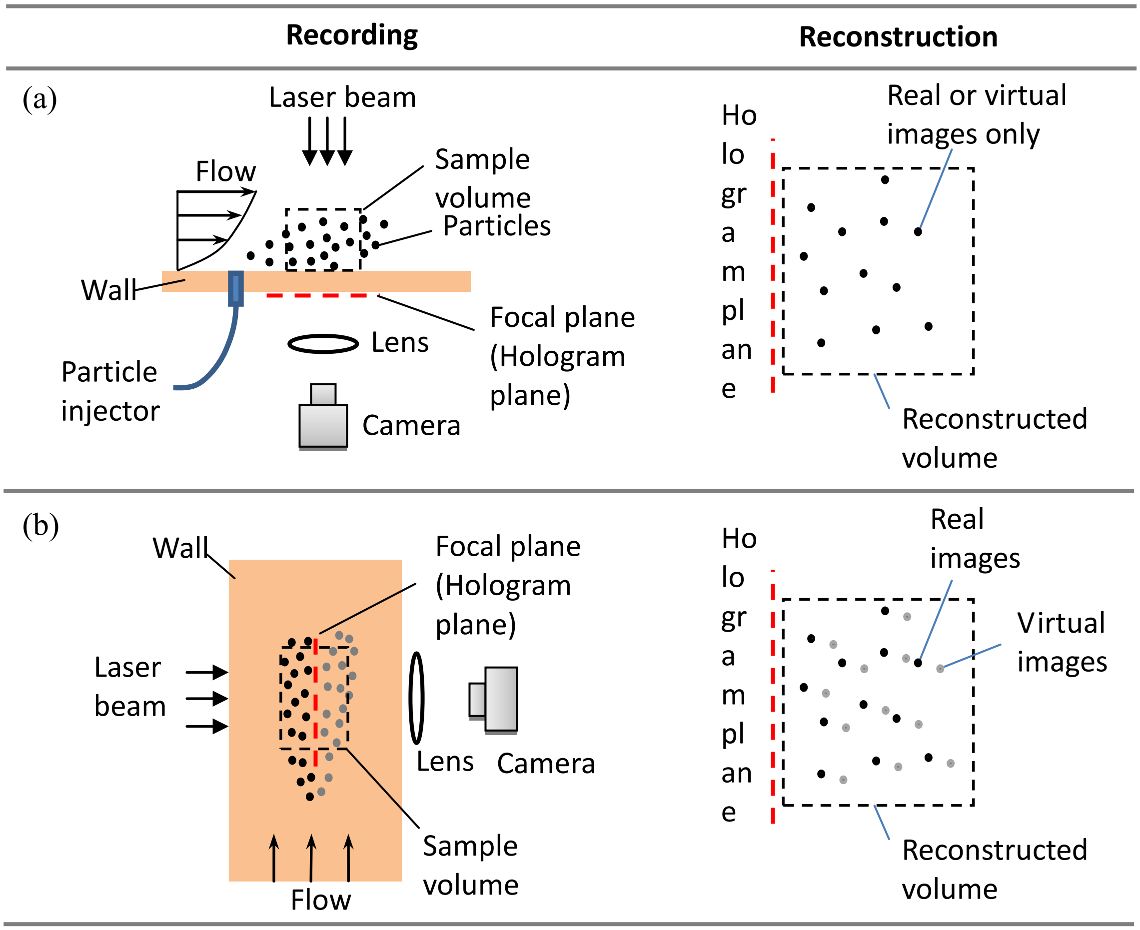

Figure 1.4. Implementation of inline digital holography for near wall velocity measurements: (a) transparent wall where focal plane is located outside of the sample volume and only real or virtual image is reconstructed; (b) non-transparent wall where focal plane has to be located inside the sample volume and both real (black circles) and virtual images (gray circles) are reconstructed.

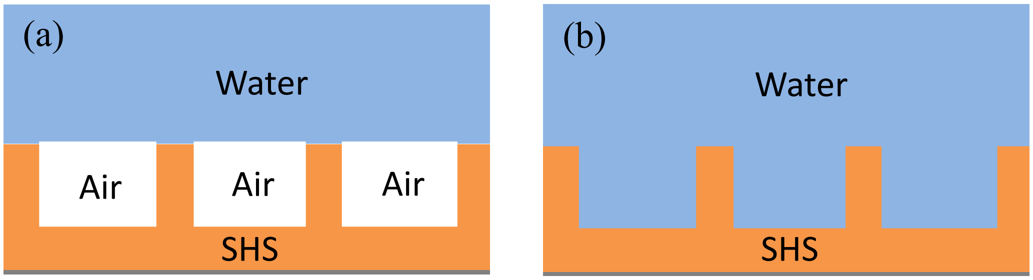

Figure 1.5. Schematics of (a) Cassie-Baxter and (b) Wenzel states.

Chapter 2. Dual-view inline digital holographic microscopy

In this chapter, the optical technique for near-wall velocity measurement in turbulent boundary layers over the non-transparent SHSs will be developed. In section 2.1, the principle of using two views to distinguish between real and virtual images in the inline digital holography is provided, followed by a discussion of the data analysis procedures in section 2.2. Since the typical reconstructed particle image is elongated in the optical path direction, i.e., the so-called depth-of-focus problem, section 2.3 introduces a novel method to detect the particle center more precisely.

2.1 Principle of dual-view digital holographic microscopy

To solve the virtual image problem, the proposed method consists of recording two holograms separated by a short distance *D*, as illustrated in Figure 2.1. The light is split by a beam splitter, and the two holograms are recorded by two digital cameras. Following Equation 1.3, the intensity distributions of these two holograms, denoted by subscripts 1 and 2, can be expressed as:

$$I_1 = \left|O_1 e^{i\varphi_1} + Re^{i\phi_1}\right|^2 = \left(O_1^2 + R^2\right) + RO_1 e^{i(\varphi_1 - \phi_1)} + RO_1 e^{-i(\varphi_1 - \phi_1)} \tag{2.1}$$

$$I_2 = \left|O_2 e^{i\varphi_2} + Re^{i\phi_2}\right|^2 = \left(O_2^2 + R^2\right) + RO_2 e^{i(\varphi_2 - \phi_2)} + RO_2 e^{-i(\varphi_2 - \phi_2)} \tag{2.2}$$

Here $O_1e^{i\varphi 1}$ and $O_2e^{i\varphi 2}$ represent object beams originating from the same sample volume encountered at plane 1 and plane 2, respectively, $Re^{i\phi 1}$ and $Re^{i\phi 2}$ are reference beams.

Following Equation 1.4, the reconstruction of the two holograms generates two 3D complex amplitude fields:

$$\tilde{A}_1 = (I_1 - R^2) \otimes h\left(x, y, z\right) = RO_1 e^{i\left(\varphi_1 - \phi_1\right)} \otimes h + RO_1 e^{-i\left(\varphi_1 - \phi_1\right)} \otimes h \tag{2.3}$$

$$\tilde{A}_2 = (I_2 - R^2) \otimes h\left(x, y, z - D\right) = \left[RO_2 e^{i\left(\varphi_2 - \phi_2\right)} + RO_2 e^{-i\left(\varphi_2 - \phi_2\right)} \right] \otimes h\left(x, y, z - D\right) \tag{2.4}$$

Therefore the two 3D intensity distributions are $A_1 = \tilde{A}_1$ and $A_2 = \tilde{A}_2$. The first terms on the right hand side of Equations 2.3 and 2.4 generate real images, and the second terms create virtual images. As illustrated in Figure 2.2, real images of a same object coincide, even if the magnifications are slightly different, whereas the virtual images, which are located symmetrically on the other side of the hologram planes, are separated by 2*D*, enabling us to distinguish between them.

To demonstrate the principle, Figures 2.3(a) are numerically generated holograms of a 2 μm spherical particle using the near-field Mie theory (Cheong et al. 2010, Slimani et al. 1984, Wu et al. 2012). This particle is located at $x_p = y_p = 0$, and $z_p = -100$ μm, and the hologram planes are separated by 20 μm. Using the Rayleigh-Sommerfeld kernel to reconstruct the intensity distribution every $\Delta z = 2$ μm, Figure 2.3(b) compares the results in the $x = 0$ planes. The overlapping of real images and separated virtual images are evident. One can thus distinguish between real and virtual images based on the displacement of particles images between two volumes $dz = z_t^2 - z_t^1$, i.e., real images have $dz = 0$ and virtual images have $dz = 2D$. Here, z_t^2 and z_t^1 are the depth coordinates of particle traces in reconstruction volume of hologram 1 and 2, respectively.

Two considerations affect the optimal distance between two hologram planes. On one hand, the difference in magnification increases with *D*, which complicates the matching process. On the other hand, due to the depth of focus (DOF) problem, *D* must be sufficiently large so that the overlap between elongated traces does not prevent us to calculate the *dz*. For dilute suspensions recorded at high magnification, and well resolved interference patterns, scattering theory based fitting methods (Kapfenberger et al. 2013) could be used for achieving a 40-60 nm uncertainty in calculation *dz*. For these cases, *D*~1 μm would be sufficient. However, for a densely seeded sample volume and small particle signatures, the uncertainty is substantially larger, and the particle center must be determined from the 3D distribution of reconstructed intensity. Thus, we have conservatively opted to maintain *D* to be larger than the elongation of the trace. To quantify particle elongation, we record holograms of particles with diameters *d* ranging from 2 to 7 μm and measure the distribution of $E(z)$:

$$E(z) = \bar{A}_{x,y\in S}(z) - \bar{A}_{x,y\in P}(z) \tag{2.5}$$

Here, the overbar denotes spatially averaged of intensity distribution over an (*x,y*) area of interest defined by *P*, a square 2D region with width that covers the particle image at its narrowest point, and *S*, a 2D region with width twice as large as that of *P*. The maximum value of $E(z)$ is defined as E_m. Then, the particle elongation is determined based on a selected threshold fraction of E_m. Results for a threshold level of 0.75, based on analysis of 500 particle traces, are plotted in Figure 2.4 along with a parabolic least-square fit for them. Accordingly, we have used $D = 27.0$ μm for 2 μm particles.

2.2 Data analysis procedures

Two methods have been developed to process the two holograms in order to distinguish between real and virtual images. The first method is based on the displacement of particle images between two reconstructed fields. Thus correlations are used to detect the displacement of real and virtual images. The second method is based on reconstruction of the complex amplitude of the wave field, which generates only real image. The phase distributions on hologram planes are estimated by propagating the wave field back and forth between two planes. Both methods will be described in details in the following two sub-sections.

2.2.1 Correlation between two reconstructed fields

For real experiments, the distance between hologram planes may not be known accurately, and might even vary across the image, when the two planes are tilted slightly relative to each other. However, when many particles are involved, data analysis enables us to determine $D(x,y)$ accurately. A convenient procedure involves the following steps: First, both holograms are reconstructed independently using Equation 1.4, i.e. without shifting the kernel coordinates. Consequently, the entire reconstructed field generated from hologram 2, including the real and virtual images, is shifted to the left by D. Therefore, relative to the reconstructed field of hologram 1, real images are displaced by $-D$ and virtual images are displaced by $+D$, irrespective of whether the original particle depth location is positive or negative. Hence, real and virtual particles can be simply distinguished by the sign of dz.

Furthermore, using the measured displacement of all the particles within the cloud, one could map the spatial distribution of $D(x,y)$. Note that there is no reason to reconstruct the 3D field on both sides of the hologram plane since the particles found on one side already include mirror images of all of those that are located on the other side as virtual images. After being separated based on the sign of D, the virtual images could be repositioned in their proper location. While adapting this approach, one should be careful in dealing with particles located in the narrow gap (specific recommendations follow) between hologram planes. These particles would appear as virtual images in one reconstruction and real images in the other. Consequently, the distance between these images is different from D, and could be positive or negative depending on their locations relative to the hologram planes. Accordingly, we start the analysis of hologram 1 from $z<-D$ (approximately initially). And then, when D is measured, a simple procedure is used to complete the analysis for the gap between holograms, as discussed later.

The following discussion is based on analysis of a $1\text{K}\times 1\text{K}$ pixels part of both holograms. Both are reconstructed using the Kirchhoff-Fresnel kernel from $z=-0.7$ μm to −665 μm at axial intervals of 0.7 μm. Then, following the procedures described in (Sheng et al. 2006), 3D segmentation of the intensity distribution in hologram 1 (only) identifies 1550 3D traces, which include real and virtual images of particles along with noise. Sample 3D traces are provided in Figure 2.5 (black objects). There is no need to perform 3D segmentation for hologram 2, although Figure 2.5 shows both. Ideally, two traces of a same particle would be located in the same (x,y) coordinates. However, due to distortion and slight relative inclination of the two cameras, in reality the two traces are slightly displaced relative to each other (e.g. Figure 2.5). To estimate the differences in the (x,y) coordinates of the two views, we collapse the reconstructed 3D field into a 2D (x,y) plane, where each pixel assumes the minimum intensity over the entire depth. Figure 2.6(a) shows a sample collapsed image of particles from hologram 1 and 2. Then, 2D spatial correlations, similar to typical particle image velocimetry (PIV) provide the distribution of relative displacements, dx and dy, for the entire field, as illustrated in Figure 2.6(b). This procedure ignores situations where more than one particle is aligned along the same (*x,y*) region. Using *dx* and *dy* to align the (*x,y*) coordinates of each segmented trace detected in hologram 1, the one dimensional correlation, defined as

$$C(\delta z) = \frac{\sum\limits_{x,y,z\in V} A_1(x,y,z)\,A_2(x+dx,y+dy,z+\delta z)}{\sqrt{\sum\limits_{x,y,z\in V} A_1^2(x,y,z)\sum\limits_{x,y,z\in V} A_2^2(x+dx,y+dy,z+\delta z)}}, \tag{2.6}$$

is sufficient for determining the *dz*. The correlations are calculated over a domain, *V*, covering the particle center, defined based on a threshold fraction of E_m (0.9 used). Typical profiles of $C(\delta z)$ for real and virtual particle traces are shown in Figure 2.7. For an actual particle, as opposed to noise, the peak correlation, C_m, should be high (close to 1), and located close to either $-D$ or $+D$. Note that the 3D displacement (*dx*, *dy*, *dz*) could also be calculated directly by performing 3D correlations between two intensity fields, without the step of collapsing the particle traces, but at a higher computational cost.

Figure 2.8 shows the probability density function (PDF) of *dz* and C_m for 1514 traces (real and virtual) whose centers are located at $z_t^1<-27$ μm (nominal *D*). As expected, the mean value of $|dz|$ is 27 μm. Using $C_m\geq0.5$ as a minimum threshold for particle detection, the 811 traces satisfying $-1.4<dz/D<-0.6$ are assumed to represent real images, and the 535 traces giving $1.4<dz/D<0.6$ are considered as virtual images. Traces not satisfying these criteria are treated as noise. The 36 traces located at -27 μm$\leq z_t^1<0$ includes real images from particles located at -27 μm$\leq z_p<0$ satisfying $dz=-D$, and virtual images from particles located at $0\leq z_p<27$ μm, for which $dz=-D+2z_p$. For $|z_p|>0.3D$, the difference between *dz* is sufficient for separating between real and virtual images. However, because of the uncertainty in the magnitude of dz, it is difficult to separate real and virtual images when $|z_p|<0.3D$. A simple approach to solve this problem is to calculate z_t^2 for these traces directly based on the distribution $E(z)$ of hologram 2, where the (real images) traces have some separation from the hologram plane. Then z_p can be calculated as $z_p=z_t^2+D$. Following this approach, and using $C_{max}\geq 0.5$ again as a detection threshold, we identify 15 real images with $z_p<0$ and 11 virtual images with $z_p>0$. Figure 2.9 shows the three dimension spatial distribution of particles on two sides of the hologram plane (z=0).

Using the results for $z_t^1<-27$ μm to calculate the depth-averaged $|dz|(x,y)$, one can determine the distribution of $D(x,y)$, which varies due to slight misalignment between the two views. The results shown in Figure 2.10 indicate that the relative position between two hologram planes varies from 26.2 μm to 27.5 μm across the image plane. Such a variation could be caused by a misalignment of 0.2 degrees.

2.2.2 Phase retrieval method

As discussed in the introduction, the phase retrieval method (Denis et al. 2005) is another procedure for separating between real and virtual images. This approach is based on reconstruction of the complex amplitude of the wave field on the hologram plane, where only real image are reconstructed. The phases on two hologram planes are obtained by iteratively propagating the wave field back and forth between two planes, which is known as the Gerchberg-Saxton iterative algorithm. As illustrated in Figure 2.11, this iterative process consists of the following four steps: (1) propagate the estimate of complex amplitude in the first hologram plane to the second hologram plane; (2) replace the amplitude of the resulting complex amplitude with the square root of the second hologram; (3) back-propagate this new estimate to the first hologram plane; and (4) replace the amplitude of the computed complex amplitude with the square root of the first hologram. When expressed in equations, these four steps in the *n-th* iteration are:

$$\tilde{A}_2^n = \left|A_2^n\right| \exp\left(i\varphi_2\right) = \tilde{A}_1^n \otimes h\left(x, y, z = D\right) \tag{2.7}$$

$$\tilde{A}_2^{n'} = \left|\sqrt{I_2}\right| \exp\left(i\varphi_2\right) \tag{2.8}$$

$$\tilde{A}_1^n = \left|A_1^n\right| \exp\left(i\varphi_1\right) = \tilde{A}_2^{n'} \otimes h\left(x, y, z = -D\right) \tag{2.9}$$

$$\tilde{A}_1^{n+1} = \left|\sqrt{I_1}\right| \exp\left(i\varphi_1\right) \tag{2.10}$$

This procedure is tested by both numerical and experimental data. Figures 2.12(a)-(g) show a numerical test. Figures 2.12(a)-(b) are two numerically generated holograms, I_1 and I_2, of a 2 μm opaque particle located at z_p=40 μm. The hologram I_1 is located at z=0, and I_2 at z=−20 μm. Figure 2.12(c) is the phase distribution φ_1 corresponding to hologram I_1, obtained through the phase retrieval method. Figures 2.12(d) and (f) are the reconstructed particle images at z=40 μm obtained by using I_1 and I_1exp(iφ_1), respectively. The formal one includes both the in-focal real image and out-focal virtual image noise. While the latter one only consists of the real image. Figures 2.12(e) and (g) are the 3D intensity distributions obtained by using I_1 and I_1exp(iφ_1), respectively. For the former, real and virtual images are reconstructed on two sides of the hologram plane. While in the latter, only real image is reconstructed.

Figures 2.13(a)-(d) are show an experimental test of the phase retrieval method. The two holograms involved are the same holograms discussed in section 2.2.1. Before applying the phase retrieval method, the two holograms are re-aligned, based on the PIV results showing in Figure 2.6, such that there is no in plane motion. Figures 2.13(a) and (c) compare the 2D intensity distributions in y-z plane of a single particle reconstructed by using I_1 and $I_1\exp(i\varphi_1)$, respectively. The low intensity regions (blue) correspond to the trace of particles. As is evident, for the former, real and virtual images are located on two sides of the hologram plane. While in the latter, only the real image is reconstructed. Figures 2.13(b) and (d) are the reconstructed images in the x-y plane at a same z location obtained by using I_1 and $I_1\exp(i\varphi_1)$, respectively. Compared to the former, in the latter image, traces of both in-focus (solid square) and out-of-focus (dashed square) virtual images are suppressed, and the contrast of real in-focus images (circles) is greatly improved.

However, trace signatures of the virtual images with varying intensity levels may persist because of misalignment between two holograms. To quantify these signatures, for each test, we provide the ratio between the spatially averaged intensities of the virtual and real images, i.e. $\xi=E(-z_p)/E(z_p)$. Our tests evaluate effects of: (i) Distance between hologram planes: The value of ξ decreases with increasing D. It is larger than 20% when $D < 2.5d$, but decreases to less than 10% for $D > 25d$. (ii) Particle size d: Consistent with the previous item, ξ increases with increasing particle size. For $d > 0.4D$, ξ is larger than 50%. (iii) Difference in magnifications of holograms: As discussed before, when we use a single objective, the holograms have slightly different magnifications. Without corrections for this difference, small ξ of less than 10% is obtained when the difference between magnifications is smaller than 1% of the mean value. However, ξ increases to more than 50% when the magnification difference is larger than 3%. (iv) Relative lateral shift between planes: A one pixel cross-plane misalignment results in a ξ of about 25%. A shift exceeding two pixels generates substantial noise over the entire field. (v) Error/uncertainty in the distance between hologram planes: When the error in D is lower than 30%, ξ is about 10%. However, it increases rapidly, e.g. to 47%, when the error is larger than 50%. (vi) Angular misalignment between hologram planes: When the tilt angle between planes is less than 5º, ξ is smaller than 16%, and when the angle is larger than 10º, $\xi \sim 25\%$.

As a consequence of these effects, for a system containing a cloud of particles with different sizes, varying distance from the hologram planes, slightly different magnifications, and small misalignment, the phase retrieval method leaves signatures of weakened virtual images among the real ones. Since the intensity of real particles images varies due to differences in size and location of particles, non-uniformity of the reference beam, interference among particle traces, and background noise, it is difficult sometimes to distinguish between real signatures of e.g. small particles, and the weakened virtual images. Conversely, the correlation based method introduced in this paper is still effective for varying particle properties and under realistic misalignment conditions. However, when the two views are numerically re-aligned, the phase retrieval method is used to improve the quality of real traces by suppressing the signature of virtual images.

2.3 Particle center localization

As is shown in Figure 2.5, the reconstructed particle image is elongated in optical path direction. To pinpoint the particle center inside the elongated trace, criteria based on intensity (Sheng et al. 2007), image sharpness (Langehanenberg et al. 2011, Lee et al. 2011, Talapatra & Katz 2013), intensity axial-gradient (Lee & Grier 2007, Wilson & Zhang 2012) and correlation between two axial-separated planes (Choo & Kang 2006, Yang & Kang 2008) have been developed. Methods involving multiple views, such as recording two orthogonal off-axis holograms (Tao et al. 2002), single-beam two-views (Sheng et al. 2003), and tomographic reconstruction of the particle field from two orthogonal inline holograms

(Buchmann et al. 2013) have also been introduced. Since current study involves correlations among reconstructed image, we explore and expand the approach introduced in (Choo & Kang 2006, Yang & Kang 2008). The spatial correlation $\psi(z)$ is defined as:

$$\psi(z)=\frac{\sum_{i=1}^{N}\sum_{x,y\in P}A_1(x,y,z-i\Delta z)A_1(x,y,z+i\Delta z)}{\sum_{i=1}^{N}\sqrt{\sum_{x,y\in P}A_1^2(x,y,z-i\Delta z)\sum_{x,y\in P}A_1^2(x,y,z+i\Delta z)}} \tag{2.11}$$

Here Δz denotes the reconstruction interval, and $2N$ represents is the total number of planes within the elongated reconstructed particle trace. For the present purpose, the elongated particle length ($2N\Delta z$) is determined from the planes where the spatially averaged intensity exceeds 60% of E_m. If we assume that the axial distribution of the elongated trace is symmetric, and that the plane of symmetry is located at the particle center, $\psi(z)$ is expected peak in the center of the particle since intensities on both side of this center are multiplied by each other. Conversely, in other z, the intensity in some of the planes located within the particle trace is multiplied by background noise. This assumption is true for an ideal spherical particle, but may not be true for particles with random shapes.

The correlation method has been tested using both numerically and experimentally obtained 3D traces, and appears to identify the particle center more sharply than the plane of E_m. Figure 2.14 compares the profiles of $E(z)$ and $\psi(z)$ for the numerical hologram of Figure 2.3(a) where z_p=−100μm. Gaussian fitting near the peaks of $E(z)$ and $\psi(z)$ gives z_t=−99.44 μm and −99.37 μm, respectively, i.e. both have an error of less than half the particle diameter. However, the axial gradients of $\psi(z)$ are much higher than those of $E(z)$, i.e. the center can be detected with less ambiguity. To test this method experimentally, we calculate z_t^1 and z_t^2 for many particles, and use $|dz|$ to estimate the uncertainty in the measurements. Presumably, the closer $|dz|$ is to $D(x,y)$, the more accurate z_t^1 and z_t^2 are. Figure 2.15 shows sample profiles of

$E^1(z)$, $\psi^1(z)$, $E^2(z)$ and $\psi^2(z)$ for traces of the same particle, where, as before, the superscripts 1 and 2 denote the corresponding hologram. For this case, the distance between (Gaussian fitted) peaks of $E^1(z)$ and $E^2(z)$ is $|dz|_E = 25.4$ μm, and that between $\psi^1(z)$ and $\psi^2(z)$ is $|dz|_\psi = 27.2$ μm. The latter is very close to the expected value of $D(x,y)$=27.1 μm in the region where the particle is located. Figure 2.16 shows histograms of $|dz|_E - D(x,y)$ and $|dz|_\psi - D(x,y)$ based on analysis of 903 traces. The standard deviations are 5.6 μm and 2.6 μm for $|dz|_E - D(x,y)$ and $|dz|_\psi - D(x,y)$, respectively (2.8 and 1.3 particle diameters), clearly indicating that the correlation based results have a substantially lower uncertainty. Considering that both images contribute to this uncertainty, it appears that the correlation method can detect the axial location of the particle center to within about one diameter.

Several points need to be made about the correlation method. First, in reference (Choo & Kang 2006, Yang & Kang 2008), the correlation value for each z is based on the intensity in two planes separated by a fixed distance, i.e. a fixed $i\Delta z$. In the present analysis, each correlation value is based on the entire 3D intensity distribution (averaged over all i). Both involve Gaussian curve fitting. When results are compared, the uncertainty of the present approach, as evaluated based on the standard deviation of $|dz| - D(x,y)$ for the 903 traces, is about three times smaller (8.2 μm vs. 2.6 μm). Indeed in (Choo & Kang 2006, Yang & Kang 2008), the authors state that their method is only suitable for large particles. However, the present approach is inherently more computationally intensive.

Second, when the elongated trace is not parallel to the z axis, owing to, for example, noise or interference from neighboring traces, large errors might occur while using the correlation method. There are two possible solutions to this problem. One approach consists of replacing the 1D correlation with a 3D correlation, and finding the location of the 3D peak.

Another approach is to align the particle trace with the z axis. Such alignment could be performed by, e.g. finding the location of minimum gray value for each plane by weighted averaging (or Gaussian curve fitting), and shifting the center of each plane. Bi-cubic interpolation is used to assign intensity values for sub-pixel shifts. As an example, Figure 2.17 (a) compares a pair of particle traces obtained from holograms 1 (solid) and 2 (mesh) before alignment, shifted by $dz=D$ and the corresponding dx and dy to highlight differences in their shapes. Figure 2.17 (b) shows the same pair after alignment. The corresponding profiles of $\psi(z)$ are plotted in Figures 2.17 (c) and (d). Clearly, prior to alignment, the correlation method causes an error of 2.8 μm (more than one particle diameter) in predicting the location of the particle center. For this case, using the plane of E_m gives much better result (1.2μm). After alignment, the uncertainty decreases drastically to 0.01 μm after Gaussian curve fitting.

Third, when traces of several particles overlap, the correlation procedure will not detect the particle center. Moreover, the alignment procedure combines multiple traces. To prevent this problem, we compare the differences in (x,y) coordinates of the minimum gray values in adjacent planes, and stop the alignment if the difference between centers exceeds a certain threshold, set here as half the particle diameter.

Finally, when the distance between a particle and the hologram plane is smaller than its elongation, the correlation method gives the wrong result. For such a case, the real and virtual images overlap, and the correlation peak is expected to be located on the hologram plane. In such a case, the particle center could be determined by performing the correlation using the other hologram.

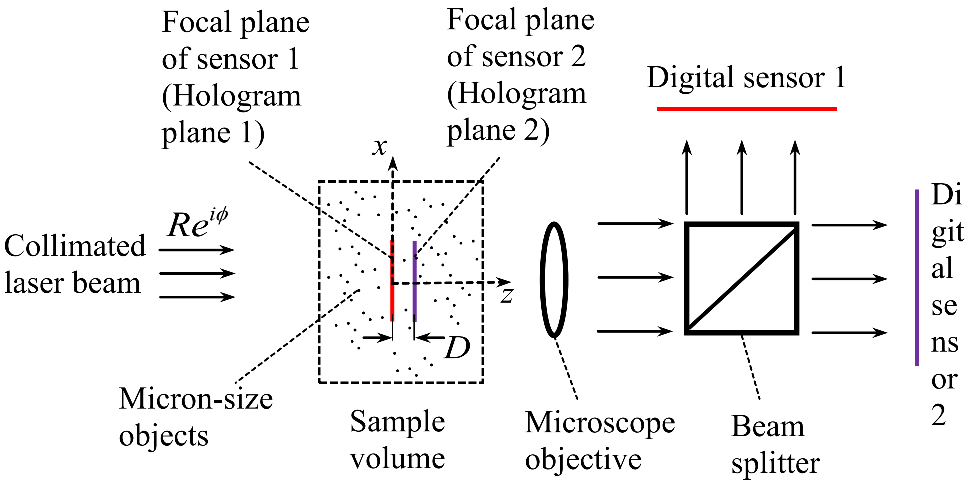

Figure 2.1. Setup for recording two inline holograms in planes separated by a short distance.

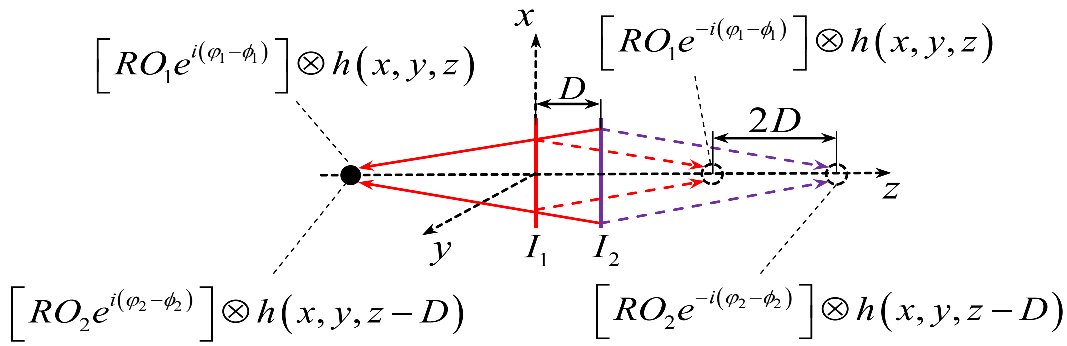

Figure 2.2. Locations of reconstructed images of a particle based on the two holograms.

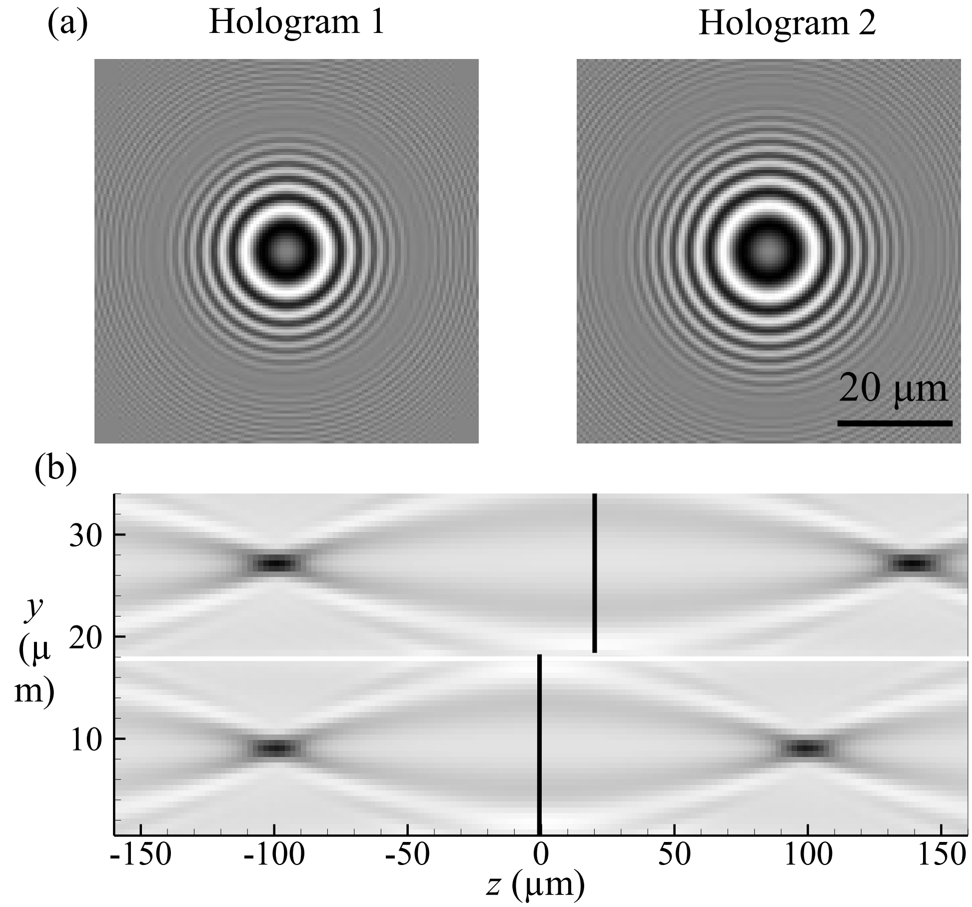

Figure 2.3. (a) Numerically generated holograms of a 2 μm particle with refractive index of 1.33+2000*i*, based on Mie scattering, in planes 1 and 2. Other relevant parameters are: light wavelength 523 nm, resolution 0.55 μm/pixel, and the medium refractive index 1.33 (water); and (b) reconstructed intensity distributions in the *x*=0 plane of hologram 1 (bottom) and hologram 2 (top).

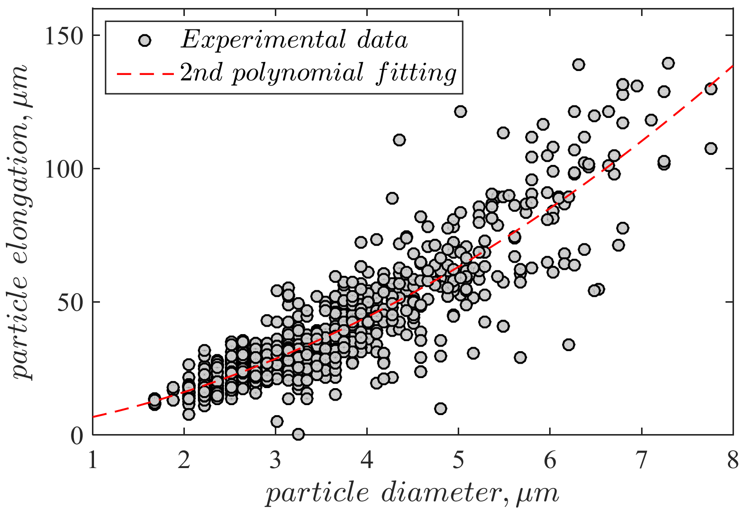

Figure 2.4. Particle elongation for mean intensity threshold at 0.75 and parabolic least square fit for them.

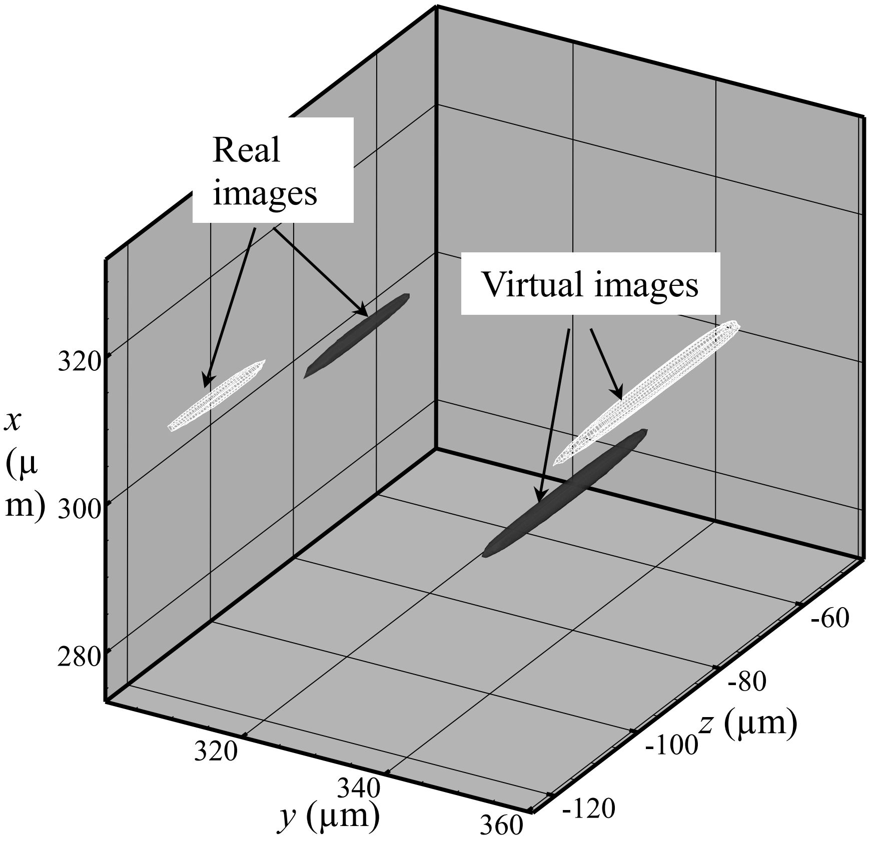

Figure 2.5. Sample reconstructed 3D real and virtual particle traces of holograms 1 (black) and 2 (white). Both holograms are reconstructed independently without shifting the kernel coordinates.

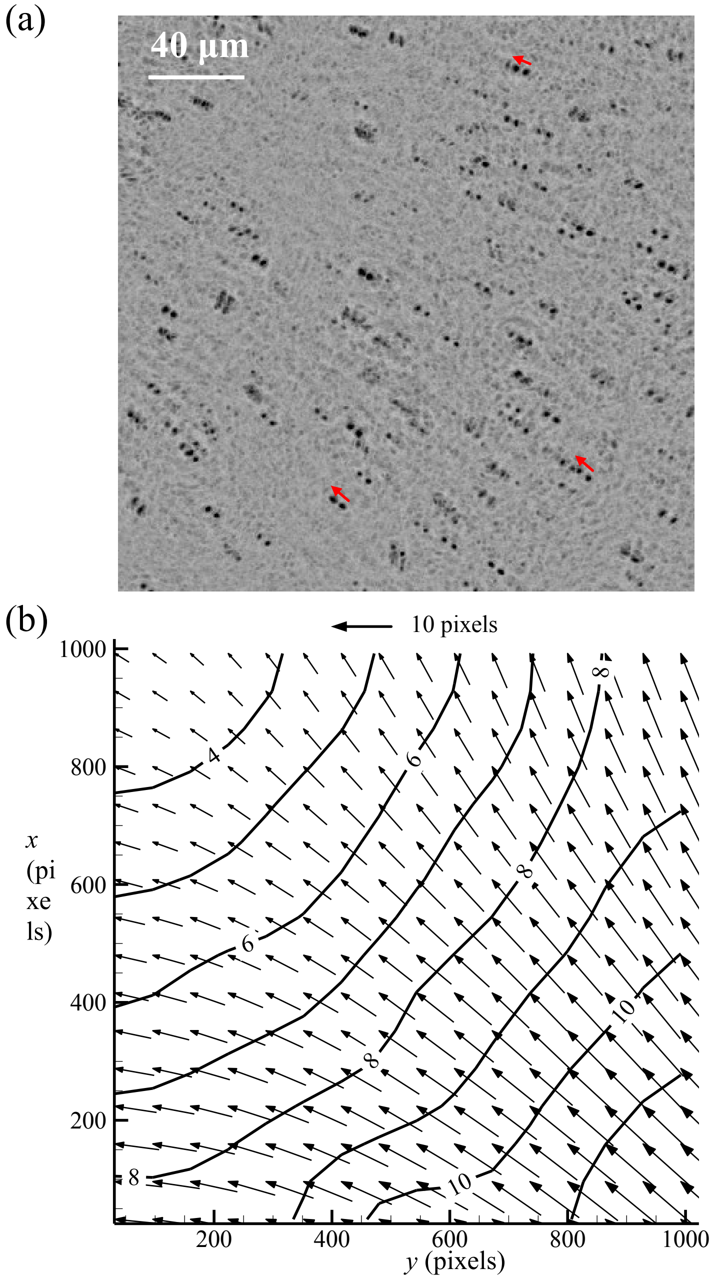

Figure 2.6. (a) Collapsed image of all particle reconstructed from hologram 1 and 2, showing the mismatch between two views in *x*-*y* direction; (b) Distribution of relative displacement of the particle traces in the cross plane (*x*,*y*). Contours denote the magnitude of the displacement in pixels.

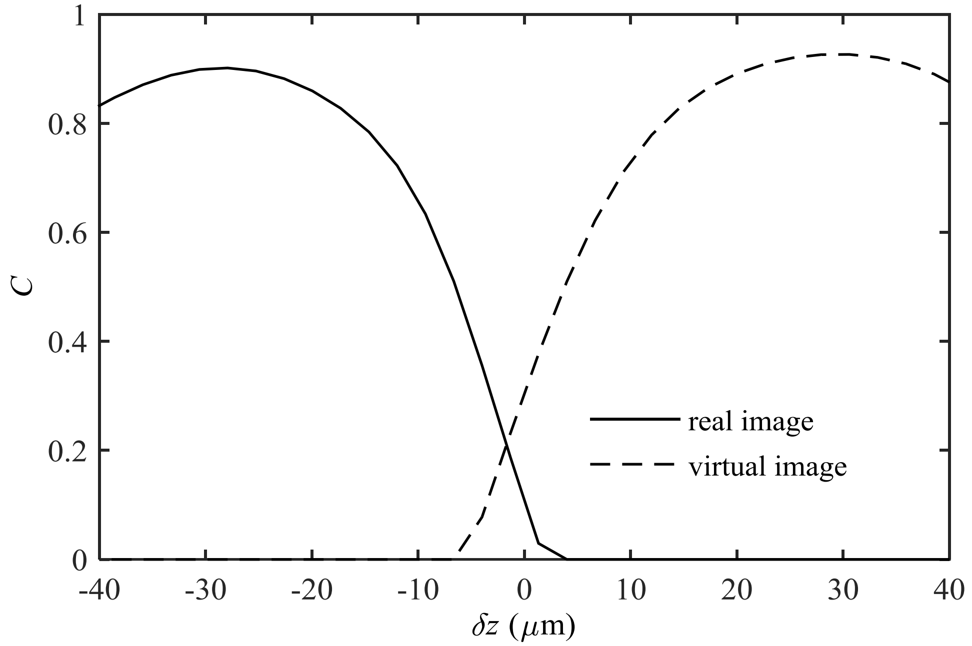

Figure 2.7. Distributions of $C(\delta z)$ for the sample real and virtual particle traces shown in Figure 2.5.

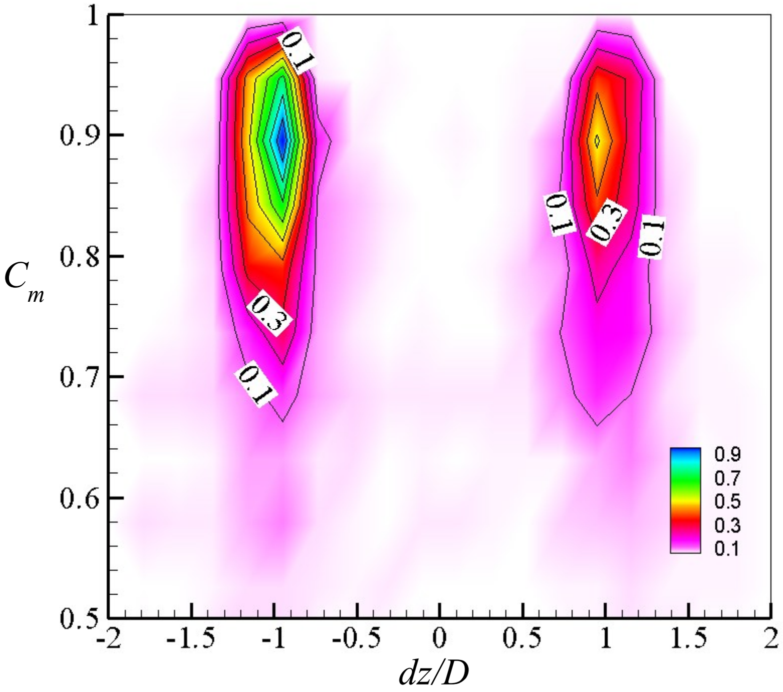

Figure 2.8. PDF of axial displacements between the reconstructed particle fields, and the corresponding correlation values for particles located at $z_t^1 < -27$ μm. Increment between contour lines is 0.1.

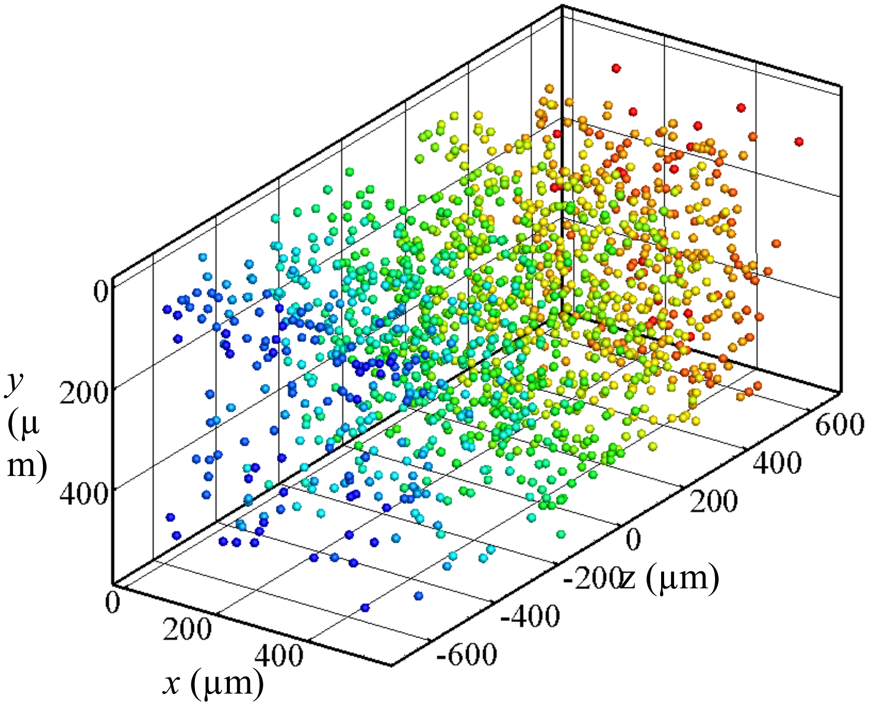

Figure 2.9. Three-dimensional distribution of particles on two sides of the hologram plane. The hologram plane is located at z=0. The color of particle indicates the magnitude of z.

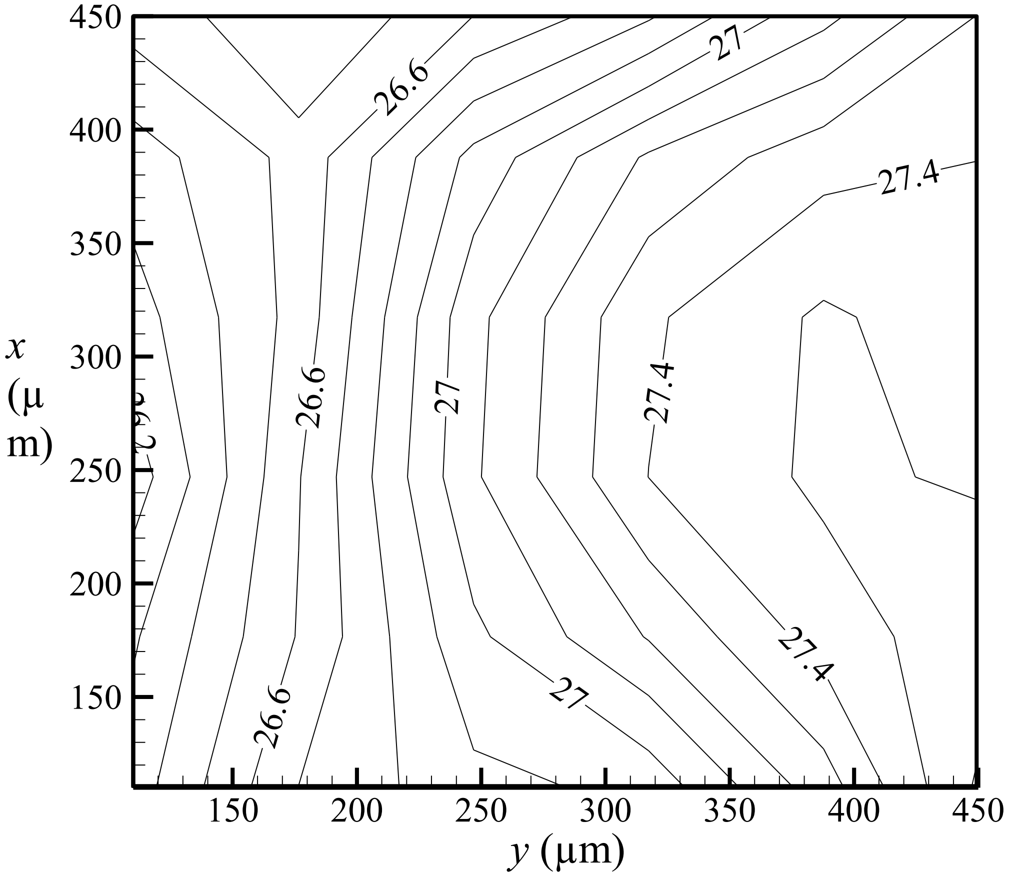

Figure 2.10. Spatial distribution of the depth-averaged magnitude of the difference between particle trace locations in the two holograms for particles located at $|z_p|$>27 μm.

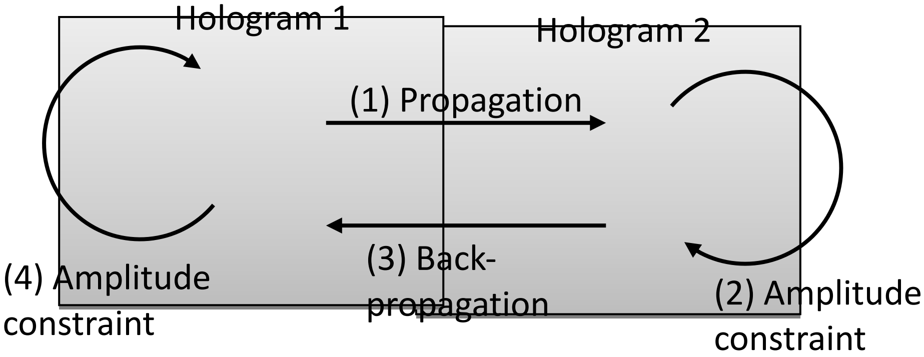

Figure 2.11. Schematic for the Gerchberg-Saxton iterative phase retrieval method (Denis et al. 2005).

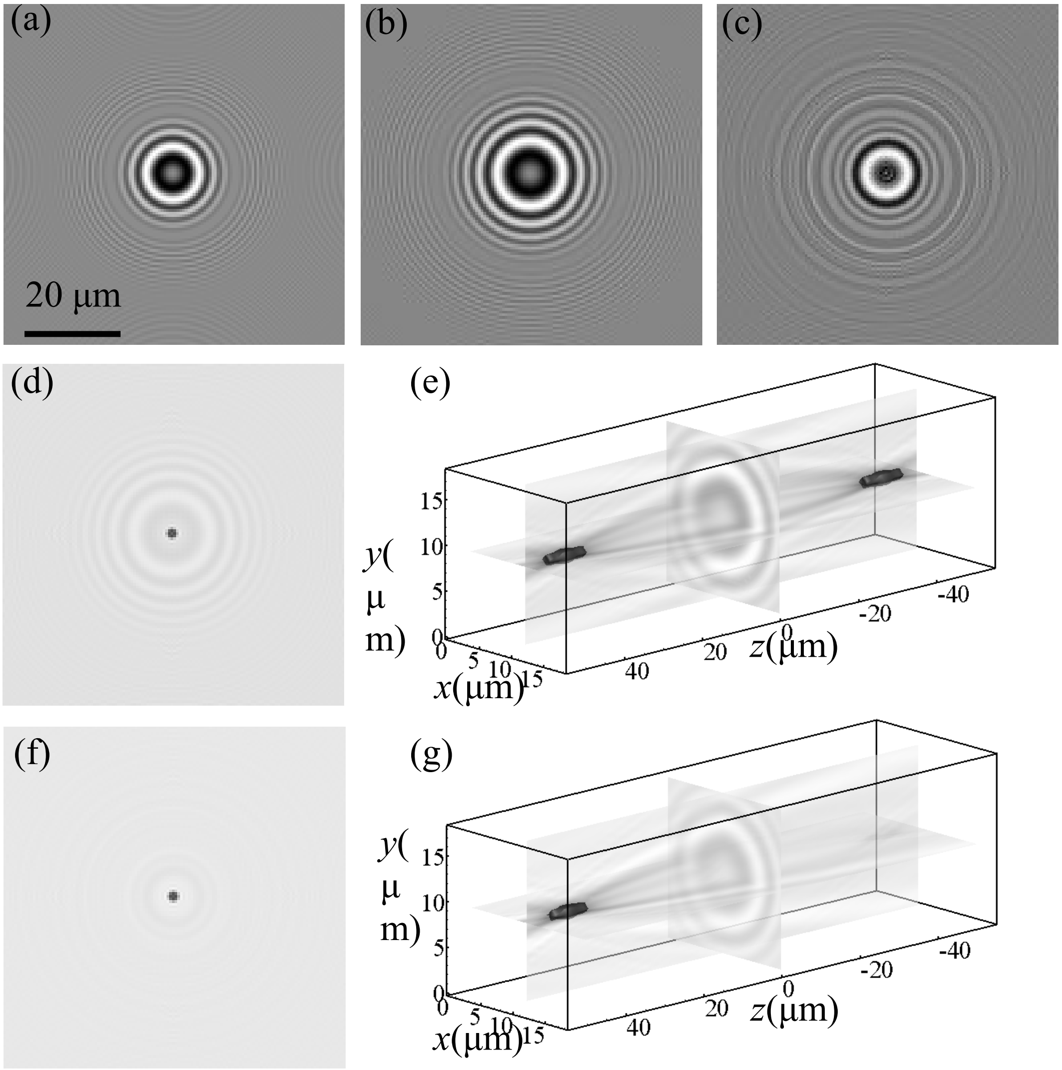

Figure 2.12. Numerical demonstration of phase retrieval method: (a) hologram 1; (b) hologram 2; (c) phase distribution on hologram 1 estimated by phase retrieval method; (d) reconstructed particle image based on hologram 1; (e) 3D intensity distribution reconstructed based on hologram 1; (f) reconstructed particle image based on phase retrieval method; (g) 3D intensity distribution reconstructed based on phase retrieval method.

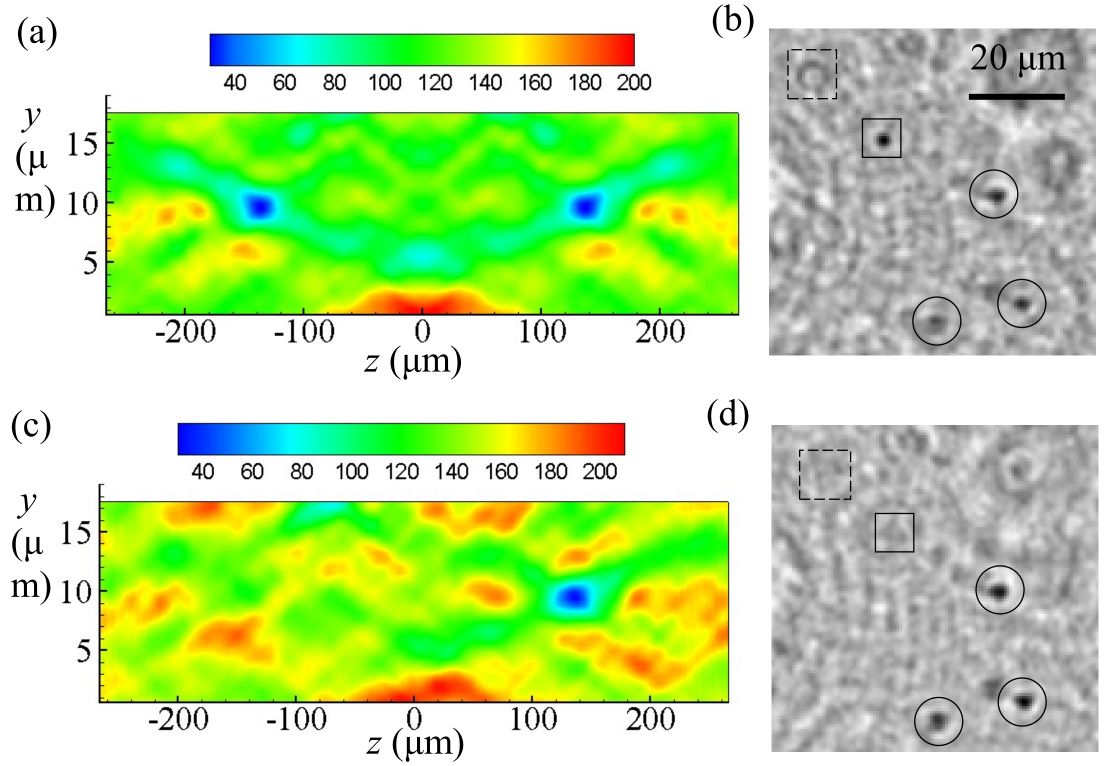

Figure 2.13. Experimental demonstration of phase retrieval method: (a) 2D intensity distribution in *y*-*z* plane reconstructed based on hologram 1 only (hologram plane is located at *z*=0); (b) reconstructed image of particles based on hologram 1 only; (c) 2D intensity distribution reconstructed in *y*-*z* plane based on phase retrieval method; (d) reconstructed image of particles at the same *z* location as image (b) based on phase retrieval method.

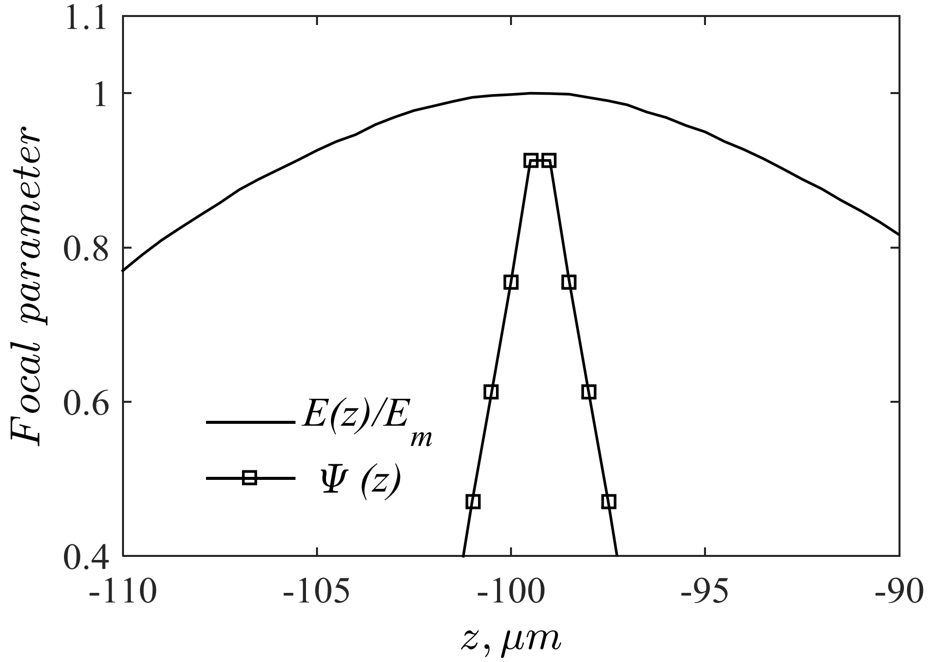

Figure 2.14. Profiles of $E(z)$ (normalized by E_m) and $\psi(z)$ of a numerically generated particle trace.

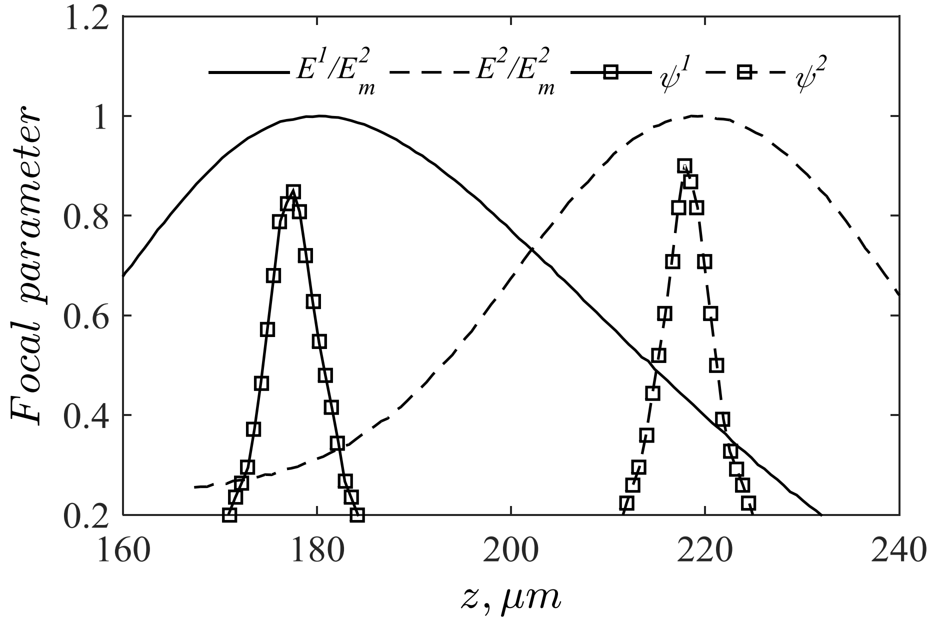

Figure 2.15. Profiles of $E^1(z)$, $\psi^1(z)$, $E^2(z)$ and $\psi^2(z)$ of traces of a same particle from hologram 1 and 2.

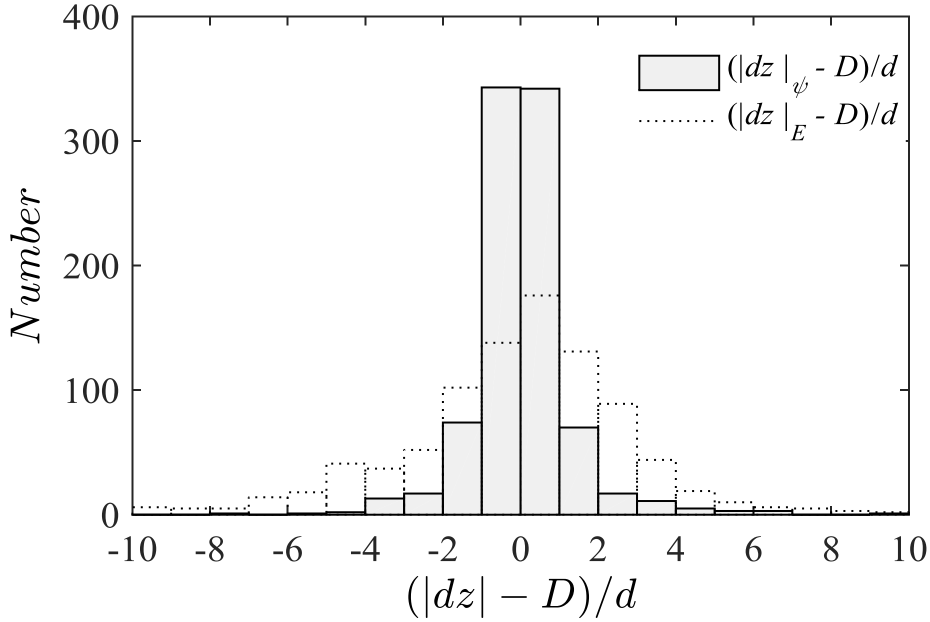

Figure 2.16. Histograms of $|dz|-D(x,y)$ (normalized by particle diameter d) determined based on $E(z)$ (dashed line) and $\psi(z)$ (solid line).

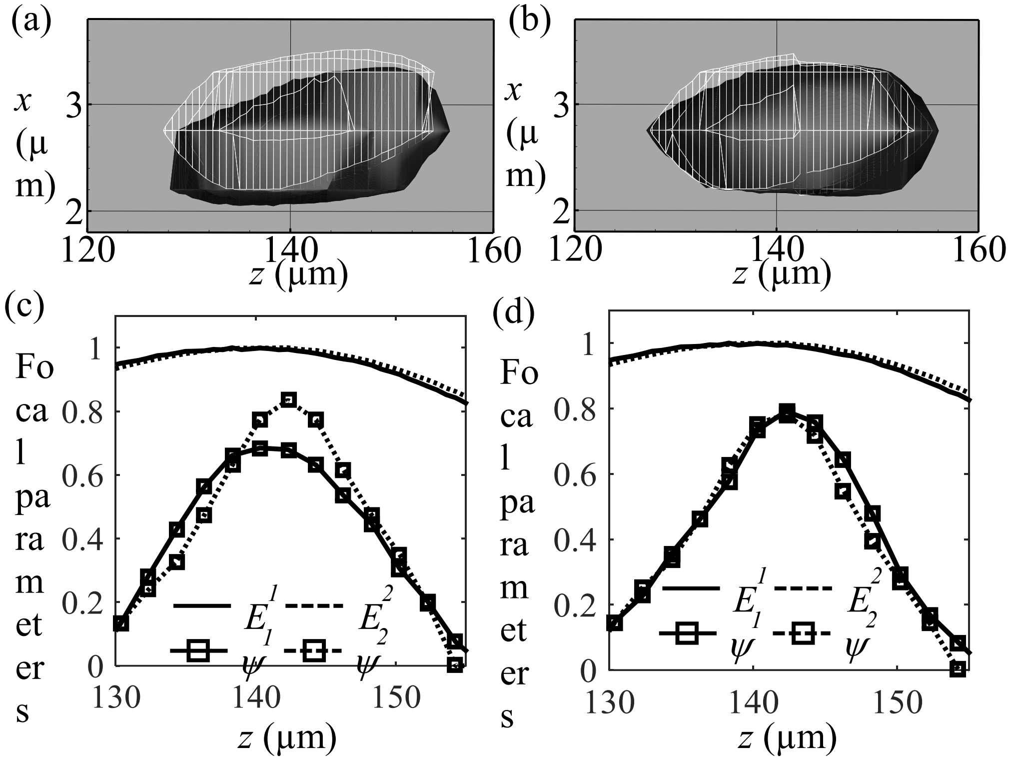

Figure 2.17. (a) A pair of particle traces obtained from hologram 1(solid) and 2(mesh); (b) The same particle traces after alignment; (c) Profiles of $E(z)$ and $\psi(z)$ for traces in (a); (d) Profiles of $E(z)$ for traces in (a) and $\psi(z)$ for traces showing in (b) .

Chapter 3. High-resolution velocity measurement in inner part of turbulent boundary layers over super-hydrophobic surfaces

Using the dual-view digital holographic microscopy developed in Chapter 2 and published in (Ling & Katz 2014), we will report high resolution velocity measurement in the inner part of turbulent boundary layers over super-hydrophobic surfaces. The experimental techniques, including the water tunnel, manufacture and characterization of SHSs, and velocity measurement methods will be described in Section 1. Results on smooth wall baselines including mean velocity profiles, viscous and Reynolds shear stresses, as well as turbulence level will be presented in Section 2. Section 3 discusses the effects of SHSs on the wall friction and mean flow quantities. Sections 4 to 6 discuss the effects of roughness height, hydrostatic pressure, and streamwise distance on the performance of SHSs, respectively. Section 7 summarizes the results by presenting the relationship between drag reduction and slip length. Finally, the effects of SHSs on the spatial energy spectra are discussed in section 8.

3.1 Experimental techniques

3.1.1 High-speed water tunnel

The experiments were performed in a small, high-speed water tunnel described by Gopalan & Katz (2000) and Liu & Katz (2006), as shown in Figure 3.1. The flow is driven by two 15 HP (maximum) centrifugal pumps located 5 m below the test section, and passes through a settling tank, an electromagnetic flow meter, a settling chamber containing honeycombs and screen, as well as a 9:1 contraction before entering the test section. The test section is transparent, and has a dimension of 406 mm × 61 mm × 50 mm. The mean tunnel speeds (flow rate divided by the tunnel cross section), U_m, are between 2 to 20 m/s. At the entrance to the test section, the bottom window contains a series of machined spanwise tripping grooves, which are located 165 mm upstream of the SHSs. The purpose of these grooves is to force early boundary layer transition to turbulence, as shown in prior studies (Liu & Katz 2013). The 152 mm long and 50 mm wide SHS is flush mounted on the same wall. The coordinate system is also shown, with x, y, and z denoting the streamwise, wall-normal, and spanwise direction, respectively, and with x=0 coinciding with the leading edge of the SHS, all consistent with the coordinates used in the Introduction. The pressure in the test section, p_w, is controled by connecting a compressor and vacumm pump to an air-water interface located in a chamber well above the test section. The magnitude of pressure is monitored by a pressure transducer.

3.1.2 Manufacture and characterization of super-hydrophobic surfaces

One smooth wall (baseline) and four types of SHSs are manufactured for the present study. The smooth surface is created on a PVC base and serves as the baseline. The SHSs have been created either on porous stainless steel bases or non-porous aluminum bases. The installation of the former is shown in Figure 3.2(a). The reason for using a porous substrate as a base is to provide a means for continuously replenishing the micro-air pockets that are gouged away and entrained by the flow. A sample scanning electron micrograph (SEM) of the porous bases prior to spraying is shown in Figure 3.2(b). They have a permeability of 0.27~0.98 μm^2 (1/700~1/200 acfm·cp·inch/psid/ft^2) and porosity of 17~26%, as specified by the manufacturers. The size of particles forming the bases as seen in the SEM images (since the manufacturer does not provide them) varies from 20 to 40 μm. The porous bases are tightly glued to six 6.4×6.4 mm^2 support legs and 5.2 mm wide edges, leaving ~70% of their underside exposed to an air chamber. This chamber is connected through valves to a compressor and a vacuum pump, allowing us to set it at desired pressures p_{por}.

The methods of creating the roughness and making them hydrophobic are listed in Table 3.1. For samples denoted as SP_{Por} and SP_{Al}, the roughness are created by spray-coating (Srinivasan et al. 2011) on porous bases and solid aluminum base, respectively. The sprayed material for SP_{Por} is a mixture of poly methyl methacrylate (PMMA) binder and fluorinated polyhedral oligomeric silsesquioxane (F-POSS). By controlling the spraying speed, surfaces with different roughness heights are generated, as will be discussed later. The sprayed material for SP_{Al} is a mixture of F-POSS and ethyl cyanoacrylate (superglue). For the sample denoted as ETH, the roughness is created by firstly polishing an aluminum base manually using sandpaper of grit 1200, and then etching it in 2.5 molar HCl for 20 minutes (Yang et al. 2011). Two different subtypes of ETH are involved in this study. For the first, surface polishing is performed in random directions, denoted as ETH_r. For the second, denoted as ETH_x, the polishing is intentionally aligned in the *x* direction forming preferentially streamwise grooves that have spatially non-uniform spacing and depth. The average spacing, as determined by laser interferometry, is 110 μm. For the sample denoted as SB, the aluminum base is sandblasted first using sandpaper of grit 150 to create micro-pores and then etched in 12 molar HCl for 25 seconds to generate nanoscale structures (Pillutla et al. 2016). Both ETH and SB are further coated with low surface energy materials, as specified in Table 3.1, using chemical vapor deposition or sputtering.

Scanning electron micrograph (SEM) images of the four types of SHSs are provided in Figures 3.3(a)-(d). The static contact angles are measured by recording images of 4 mm (270 μL) water droplets situated on the SHSs. Results are listed in Table 3.1. Moreover, the

SHS topography is also characterized by imaging the roughness elements using high resolution holography at a resolutions of 0.68 μm/pixel in the *x* and *y* direction and ~100 μm in *z* direction. The holograms are recorded while the facility is filled with water, accounting for the presence of the air layer. Figure 3.4(a) shows a sample hologram of the surface topography of SP_{Por}. By selecting a threshold of intensity to include roughness elements, which are nearly in focus, the projection local roughness height $k(x)$ is tracked. The probability densities of $k(x)$ corresponding to Figure 3.4(a) together with that of ETH_r are shown in Figure 3.4(b). Since the histograms are nearly Gaussian, we characterize the roughness height using the root-mean-square (rms) value of $k(x)$, and denote it as $k_{rms}=(\int k^2dx)^{1/2}/L$, where L is the sample length. The values of k_{rms} calculated from this method are listed in Table 3.1. The magnitudes of k_{rms} of current SHSs are in the range of 3 to 20 μm. The uncertainty, evaluated by selecting different intensity thresholds to estimate k_{rms}, is less than 1 μm. Figure 3.4(c) shows cumulative distribution of $k(x)$ for five different SHSs with krms ranging from 4 to 20 μm. When the roughness height is evaluated in air using a laser interferometer with 0.1 μm resolution, the values of k_{rms} are 10~20% lower than those obtained using DHM. Hence, the results are consistent.

The location of y=0 is selected as the mean roughness height, consistent with previous rough walls studies (Brzek *et al.* 2008; Chan *et al.* 2015). It is indicated by solid lines in Figure 3.4(a). To minimize the potential effects of form drag, the wall friction and slip velocity are calculated at the top of the roughness, which is selected as the elevation where the cumulative distribution of $k(x)$ reaches 95%, namely $y=2k_{rms}$. The location of this elevation is indicated by the dashed lines in the inserts of Figure 3.4(a). While one could also define the top of the roughness as the point where the cumulative distribution of *k(x)* reaches e.g., 90% or 99%, the impact of this choice on the uncertainties in slip velocity and wall friction is discussed and accounted for later. The present choice for y=0 facilitates displaying the velocity and stress profiles at the top of the roughness, namely at y=2k_{rms}. Altering this reference height within the roughness domain has not led to collapse of data. It has negligible effect on the mean profile in the log region and does not change the overall trends.

The present surface geometries and composition prevent us from providing a reliable scale for the roughness spacing, especially if one wants to compare between the surfaces. Spraying inherently involves a multiscale surface pattern. Thus, evaluating the surface only based on the observed peaks is questionable, since much smaller crevices might affect the trapping of air as well. We estimate the mean spacing between roughness elements by counting the total number of maxima that exceed two local standard deviations of the local mean height. Assuming they are distributed randomly within the hologram depth of focus ~200 μm (without reconstruction), the characteristic roughness wavelength α for the SHS_{Por} and SHS_{AIr} falls in $90<\alpha<100$ μm. This value does not differ significantly among different samples, even through the magnitude of k_{rms} does change. The magnitude and distribution of α should also be accounted for while characterizing the efficacy of the SHS or roughness effects. However, due to the higher confidence in its magnitude, we opt to characterize the surfaces based on k_{rms}. The randomly distributed roughness also prevents us from quantifying the gas fraction for the different surfaces and flow conditions.

3.1.3 Velocity measurements and data analysis procedures

The optical setup for performing high resolution velocity measurements in the inner part of the boundary layer is illustrated in Figure 3.5. As has been discussed in the Chapter 1 and 2, we have opted to use in-line digital holographic microscopy to achieve high-resolution. We have also developed a technique of recording a pair of holograms to distinguish particles on two sides of the hologram plane. The light source is an Nd-YAG laser (532 nm). Since very little energy is required for inline DHM, only light reflected from an uncoated flat glass surface is used. The beam is spatially filtered, expanded and collimated to 5 mm diameter before illuminating the sample volume. The flow is seeded locally with 2 μm silver-coated glass particles. To minimize the effect of injection on the flow, the particles are injected at a low speed of less than $0.08U_m$ from twenty-five evenly-distributed 100 μm holes located ≥100 mm (1000 injector diameters) upstream of the sample volume. The light scattered by these particles interferes with the remainder of the collimated beam to form the inline hologram. An 8× infinity-corrected, long working distance microscope objective magnifies the images, while focusing on the selected hologram planes. A cube beam splitter directs the images to two interline transfer digital cameras (Imperx ICL-B6640, 4400×6600 pixels, 5.5 μm/pixel) generating a pair of holograms. Their focal planes are located about 2 mm away from the center of the test section, separated by 50 μm, and at x=70 mm. They have calibrated spatial resolutions of 0.677 and 0.685 μm/pixel. The total sample area cross section is 4.4×2.4 mm^2 (x×y) and the total depth of the interrogated volume extends to 3.2 mm in the z direction for most cases. However, as discussed below, this domain is divided into multiple sample volumes, which are interrogated separately.

To calculate the velocity field from the holograms, the following data analysis procedures are employed. First, to reconstruct only the real particle images, we use the phase retrieval method as described in Section 2.2.2. The reconstruction is performed every 13 μm in depth to generate a series of closely spaced planes containing real images only. Then, following Sheng *et al.* (2008) and Talapatra & Katz (2013), the 3D fields are segmented to generate the spatial distribution of particles, followed by particle tracking to match particle traces in the hologram pairs. Between 6000 to 10,000 particles pairs are typically matched in each of the 4.4×2.4×3.2 mm^3 ($x\times y\times z$) sample volumes. Matching involves seven criteria, including similarity of particle size, shape and intensity, as well as smoothness of the velocity field and agreement with guess 2D vectors generated using standard PIV cross-correlations of images created by compressing the entire volume into a plane. Symbols u, v, and w are used to denote the instantaneous velocity components in x, y, and z directions respectively. The magnitudes of u and v are calculated from the in-plane centroids of the particles and w is calculated based on locations of minimum intensity within the elongated traces of the particle in the spanwise direction. The accuracy of w is lower compared to u and v but could be improved by locating the center of the particles using edge detection (Talapatra & Katz 2013) or correlations among the elongated traces. However, as the focus of this study is on the distributions of u and v, additional effort is not invested in improving the accuracy of w. The sample volume is divided into multiple small windows with a size of $10\delta_\upsilon\times1\delta_\upsilon\times10\delta_\upsilon$ ($x\times y\times z$) for U_m=2 m/s, and $20\delta_\upsilon\times1\delta_\upsilon\times20\delta_\upsilon$ ($x\times y\times z$) for U_m=6 m/s. Only the windows containing particles are included in the statistical analysis for each volume.

Each flow measurement is started after running the facility continuously at a particular condition for at least one hour to make sure the air-layer is indeed maintained on the SHSs. Each data acquisition lasts about two hours. More than 1000 instantaneous velocity fields are obtained and ensemble-averaged locally for each window to obtain the mean (denoted as U and V) and the corresponding Reynolds normal and shear stress components, $<u'u'>$, $<v'v'>$ and $<u'v'>$. Results are then spatially averaged in the x and z directions to obtain data that are not dependent on the local roughness patterns. Spatially averaged values are denoted with an over bar, e.g., $\overline{U}$, $\overline{<u'v'>}$, etc.

For most of the cases, the measurement domain starts from y=0, and the first data point included here is located at $y=\delta_\upsilon$. The values of the mean spatially averaged viscous stress, τ^μ, are calculated using $\tau^\mu = \mu\,\partial\overline{U}/\partial y$, where $\mu=1\times10^{-3}$ *kg/m/s*. Since the mean velocity profiles for the smooth walls and the SHSs with $k_{rms}\leq\delta_\upsilon$ are nearly linear at $y\leq5\delta_\upsilon$, the values for $y<3\delta_\upsilon$ are calculated by linearly fitting the mean velocity profiles based on the $y\leq5\delta_\upsilon$ data. However, for the SHSs with $k_{rms}>\delta_\upsilon$, the mean profiles are not linear at $y\leq5\delta_\upsilon$. Thus, τ^μ at $y=\delta_\upsilon$ (first point) is not available, 2nd order finite differencing is used for $y=2\delta_\upsilon$, and 5 points are used for higher elevations. The total stress $\tau_t=\tau^\mu+\tau^R$ is determined by adding τ^μ and the spatially averaged Reynolds shear stress, $\tau^R=-\rho\overline{<u'v'>}$, where $\rho=1\times10^3$ *kg/m³*. The wall viscous stress $\tau_w{}^\mu$, wall Reynolds shear stress $\tau_w{}^R$ and total wall friction τ_w are determined from the corresponding stresses at y=0 for smooth walls and $y=2k_{rms}$ for SHSs. The friction velocity is then calculated as $u_\tau=(\tau_w/\rho)^{1/2}$. In the rest of this thesis, a superscript $^+$ is used for quantities that are normalized by u_τ and δ_υ, a subscript $_0$ for quantities measured above the smooth wall (the baseline), and the combination of the superscript $^+$ and subscript $_0$ for quantities normalized by $u_{\tau0}$ and $\delta_{\upsilon0}$.

To estimate the slip velocity, we calculate the mean and spatially averaged velocity at $y=2k_{rms}$, the same location where the wall stress is measured, and denote it as $\overline{U}_s$. The slip length is calculated using $b=\mu\overline{U}_s/\tau_w^\mu$, where $\tau_w{}^\mu$ is the viscous stress at the same elevation. In addition to τ_w, logarithmic fitting to the mean velocity profile in the regions where values of $y\,\partial\overline{U}/\partial y$ are nearly constant, which fall in the range of $50\delta_\upsilon<y<180\delta_\upsilon$ for U_m=2 m/s, and $50\delta_\upsilon<y<350\delta_\upsilon$ for U_m=6 m/s, provides another estimate for the wall friction, and denoted as $\tau_w{}^{Log}$. There are mismatches between $\tau_w{}^{Log}$ and τ_w, due to non-equilibrium boundary layer. Implications of these findings are discussed later in this chapter.

The uncertainty in velocity measurements is based on prior studies where many of the present tools for applying digital holography to perform near wall velocity measurements are introduced (Sheng *et al.* 2008; Talapatra & Katz 2013). In both studies, the uncertainty is evaluated by testing how well the measurements satisfy the continuity equation. Using their results, and considering the resolution of the current setup (0.68 μm/pixel), the uncertainty in x-y motions is about 0.5 pixel, corresponding to an uncertainty in the instantaneously interpolated u and v of $0.01U_m$. The corresponding uncertainty in velocity gradient used for calculating the viscous stress is an order of magnitude higher, but decreases back to about 1% when ensemble averaged. However, a bigger contributor to wall stress uncertainty involves the selection of elevation for evaluating the wall stress for the "rough" SHSs. It is estimated by calculating the differences between the stresses at $y=2k_{rms}$ and those at $y=2.5k_{rms}$ and $1.5k_{rms}$, namely on both sides of the roughness peak, and selecting the larger of the two differences as an uncertainty.

Because the high resolution measurements only cover the inner part of the turbulent boundary layer, two-dimensional (2D) PIV has also been used to obtain the entire boundary profile, including the missing wake region. It has been performed at a lower magnification (5.4 μm/pixel), using a larger sample area (36×24 mm^2, $x\times y$). The centers of the sample areas (x=70 mm) coincide with those of high resolution measurements. These 2D PIV measurements have also been performed after running at a particular experimental condition continuously for one hour. Data acquisitions typically last for 30 minutes, during which more than 500 pairs of images are captured. Standard PIV cross-correlations using in-house software (Roth & Katz 2001) with window size of $64\delta_\upsilon\times16\delta_\upsilon$ ($x\times y$) for U_m=2 m/s, $128\delta_\upsilon\times32\delta_\upsilon$ ($x\times y$) for U_m=6 m/s and 50% overlap are used to calculate the velocity, resulting in a characteristic grid spacing of $32\delta_\upsilon\times8\delta_\upsilon$ ($x\times y$) for U_m=2 m/s and $64\delta_\upsilon\times16\delta_\upsilon$ ($x\times y$) for U_m=6 m/s.

The boundary layer thicknesses, δ_{99}, are obtained based on the elevation where 99% of the maximum velocity (U_0) is reached. Note that U_0 is slightly higher (typically by 8~12%) than U_m owing to the boundary layer induced blockage. The momentum thicknesses, Θ, are calculated by integrating the mean velocity profile. The magnitudes of the drag reduction are defined as

$$DR = (\tau_{w0} - \tau_w)/\tau_{w0}, \tag{3.1}$$

where τ_{w0} is the value obtained for the smooth wall at the same U_m and very similar δ_{99}.

3.1.4 Comparison with fully developed turbulent boundary layers

Two facts need to be considered when comparing the presently measured wall friction to that of much larger surfaces. First, there is a relative short distance ($4\text{-}9\delta_{99}$) from the beginning of the SHSs to the sample area. Prior studies have reported an overshot of the wall friction after transitioning from a smooth to a rough wall and an undershot after transitioning from a rough to a smooth wall (Antonia & Luxton 1971). Further downstream, the wall friction adjusts to the new boundary condition after a distance that increases with decreasing δ_{99}/k. For example, a relatively short distance of $2\sim3\delta_{99}$ is required for $\delta_{99}/k>1000$ (Saito & Pullin 2014), and a much longer distance of about $30\delta_{99}$ is needed for $\delta_{99}/k<25$ (Lee & Sung 2007). If the roughness effects are dominant (as will be shown to occur in some cases), one would expect a rather quick transition considering $\delta_{99}/k_{rms}>100$ for current samples. There is limited information about the transition from a smooth wall to an SHS. However, recent numerical study by Park (2015) reports undershoots of the wall friction and adjustment distances to constant wall friction of $5\delta_{99}$ to $20\delta_{99}$ for SHSs with streamwise grooves of different wavelengths at $Re_\tau\sim200$. Most of the present measurements are performed at substantially higher Reynolds numbers and with random roughness.

Moreover, due to this short distance, the outer region does not reach equilibrium condition, namely, the velocity profile in the log layer does not fully adjust to the local stress in the inner part of the boundary layer. For transition from a smooth to a rough wall, the required distance for mean velocity to be self-preserved varies from $10\delta_{99}$ to $40\delta_{99}$ (Saito & Pullin 2014). Overshoots of Reynolds stresses in this transition region have also been reported (Lee & Sung, 2007; Saito & Pullin, 2014). Hence, in discussing the results, our main focus is on the inner region while highlighting discrepancies between the inner and outer regions. Furthermore, data are presented to demonstrate the streamwise evolution of the wall friction and Reynolds stresses in the outer part of the boundary layer.

Second, without the plastron, the current SHSs fall in the transitionally-rough to rough regimes (Schultz & Flack 2007), and form drag might affect the total stress at the spatially averaged top of the roughness elements. However, based on computational results found in Chan *et al.* (2015), for a transitionally rough surface with k^+=10, the total stress normalized by the wall friction near the roughness tip increases from about 0.87 to 0.97 as δ_{99}/k increases from 9 to 25. The viscous stress contributes about 60% in both cases. In the current study, considering that $\delta_{99}/k_{rms}>100$ and $k_{rms}^+<5$, it is reasonable to expect that the total stress near the roughness tip represents the wall friction.

3.2 Mean flow quantities on smooth walls (baselines)

Firstly, measurements have been performed on smooth walls which provide baselines for comparison with results on the SHSs. Results at four different flow conditions are summarized in Table 3.2, which includes values of U_m, U_0, δ_{99}, Θ, τ_w^{μ}, τ_w^{R}, τ_w, τ_w^{Log}, $Re_{\delta}=U_0\delta_{99}/\upsilon$ and $Re_{\Theta}=U_0\Theta/\upsilon$. The corresponding values of δ_{υ}, u_{τ}, and $Re_{\tau}=\delta_{99}/\delta_{\upsilon}$ deduced from τ_w are also listed. Due to differences in the inlet boundary conditions at the entrance to the test section imposed in the settling chamber, we achieve two different boundary layer characteristics. The first one is thinner, with δ_{99}=9.1 mm and 7.4 mm for U_m=2.0 m/s and 5.5 m/s, respectively. The second one is thicker, with δ_{99}=16.6 mm and 18.8 mm for U_m=2.0 m/s and 5.9 m/s, respectively. The corresponding values of Re_τ vary from 863 to 4287. In all cases, the differences between the measured wall stress and the predictions based on fits to the log layer profiles are less than 2%, further emphasizing the validity of the procedures used for calculating the stresses in this study.

Figure 3.6 shows all the normalized mean velocity profiles, including both high resolution DHM and low resolution PIV data. For comparison, results for similar values of Re_τ obtained in high-resolution Laser-Doppler Anemometer measurements by DeGraaff & Eaton (2000) and a DNS study by Spalart (1988) are also included. The DHM results collapse onto the classical law of the wall for the viscous sublayer ($y^+\leq 5$) and the familiar log-law for the log layers. The PIV data coincide with the DHM results in the log region, but extend to the wake and free stream flow. The results of Spalart (1988) and DeGraaff and Eaton (2000) also collapse to the same profiles. In the rest of the paper, only DHM results will be shown.

Figure 3.7 shows the streamwise and wall-normal velocity fluctuations. The present $\overline{<u'u'>}^+$ profiles mostly coincide with the previously published boundary layer profiles at the corresponding Re_τ. The present peaks fall between the Spalart (1988) and DeGraaff and Eaton (2000) values, i.e., slightly above the low Re_τ values of the former, and slightly below the higher Re_τ results of the latter. As expected, $\overline{<u'u'>}^+$ peaks in the y^+=12 to 20 range. The peak value increases with Re_τ, e.g., increases from 7 to 8 as increasing Re_τ from 500 to 2000. In the log layer, $\overline{<u'u'>}^+$ increases with Re_τ, in agreement with Smits *et al.* (2011).

The values of $\overline{<v'v'>}^{+}$ reach a maximum of 1.6 to 1.9 at y^{+}=50 to 100, again consistent with expectations although the peak values are slightly higher than literature (Smiths *et al.* 2011).

Figure 3.8 presents profiles of the viscous and Reynolds shear stresses along with the total stress. These results are also consistent with expectations, with the viscous stress decreasing monotonically and Reynolds shear stress increasing with elevation for $y^{+}<70$, and then decreasing. For $y^{+}>70$, the Reynolds shear stresses increases with increasing Re_τ. The total stress remains nearly constant up to about y^{+}=20, and then starts decreasing at a rate that decreases with increasing Re_τ.

3.3 Mean flow quantities on super-hydrophobic surface with $k_{rms}^{+}<1$

The measurements results on the five different SHSs, i.e., SP_{Por}, SP_{Al}, ETH_r, ETH_x, and SB, all at same flow condition U_m=2.1 m/s and δ_{99}=9.1 mm, are listed in Table 3.3. In all cases, the pressure in the test section is small, p_w<1.06 atm (absoluate value), such that the air layers are not suppressed. The SHSs appear to be very shiny when viewed from the side due to the total internal reflection from the air-water interfaces. While it does not guarantee that the entire surface is covered by the air layer, the uniformity of the reflection suggests that most of it does. Most SHSs show a slightly reduction of the contact angle, but remain super-hydrophobic after the experiments. The corresponding smooth wall result at same U_m and δ_{99} is also listed for comparison. Quantities listed in the Table 3.3 include k_{rms}, τ_w^{μ}, τ_w^{R}, τ_w, τ_w^{Log}, δ_υ, $\overline{U}_s$, b, DR, and their uncertainties due to the selection of wall location. Note that for all cases, $k_{rms}^{+}<1$. Results show 10% to 36% reduction in wall friction compared to the smooth wall. The corresponding slip velocities are 15% to 34% of U_m, and the slip lengths vary from 30 to 150 μm ($3<b^{+}<15$). The values of slip length agree with the reported results obtained in microfluidic devices (e.g., Lee et al. 2008). There are mismatches between τ_w^{Log} and τ_w for all SHSs, and the reason will be explained in the following text.

Figures 3.9(a)-(c) show the profiles of viscous, Reynolds shear and total shear stresses, respectively, for the five SHSs together with those of the smooth wall. The specific experimental conditions corresponding to each of the symbols can be found in Table 3.3. All profiles are normalized based on smooth wall values to highlight the actual differences. The location of $y=2k_{rms}$ for each profile is marked by a short vertical line. As expected for all the SHSs, the viscous stresses decrease with distance from the wall. At $y^+<30$, all the SHSs have lower viscous stresses compared to those of the smooth wall. At $y^+>30$, the profiles for both SHSs and the smooth wall collapse. The Reynolds shear stress on the top of the roughness ($y=2k_{rms}$) is nearly zero for $k_{rms}^+<0.5$ (SP_{Por} and SB), but increases slightly to $\sim0.2\tau_w$ for $0.5<k_{rms}^+<1$ (ETH_r, ETH_x and SP_{Al}). At $5<y^+<10$, the Reynolds shear stresses of all the SHSs are slightly larger than those on the smooth wall. The possible reason may due to vibration of air-water interface, non-uniformity of air layer distribution, or non-equilibrium boundary layer. Conversely, the peak values of the Reynolds shear stresses decrease.

The total stresses on SHSs are located below the smooth wall profile for all y. The corresponding values at $y=2k_{rms}$ show 10-36% reduction of wall friction compared to the smooth wall. For all SHSs except SB, the total stresses increase slightly with distance from the wall for $y^+\leq 2k_{rms}^++5$, peaking with values of about τ_{w0}, and then decrease. It suggests that boundary layers over SHSs are under non-equilibrium conditions, i.e., the outer layers have not ‘relaxed’ yet from the smooth wall conditions. The non-equilibrium conditions appear to be more severe for the ETH_r, ETH_x and SP_{Al} for which the drag reduction are significantly higher. As a result, there are shape gradients of wall stress profiles at $y^+\leq 2k_{rms}^++5$. The mismatches between τ_w^{Log} and τ_w, as indicated in Table 3.3, are another way to show non-equilibrium conditions on SHSs. As listed in Table 3.3, the values of $\tau_w{}^{Log}$ are larger than the corresponding τ_w, and are very close to those of τ_{w0} for the same Reynolds number. This trend implies that the log region has not adjusted yet to the lower skin friction. The non-equilibrium effect is not so serve for SB. The possible reason may due to that the SB has the smallest roughness height.

Note the $\mathrm{ETH_r}$ and $\mathrm{ETH_x}$ are generated by the same method, except the polishing direction: one is polished in streamwise direction ($\mathrm{ETH_x}$), and the second randomly ($\mathrm{ETH_r}$). The streamwise polished sample shows more drag reduction (36%) than the randomly polished sample (27%). At $y^+<5$, both the viscous and Reynolds stresses above the $\mathrm{ETH_x}$ are lower than those of $\mathrm{ETH_r}$, indicating that the axially aligned grooves are more effective in reducing drag. Accordingly, the slip velocity on the $\mathrm{ETH_x}$ is also higher than that of $\mathrm{ETH_r}$ as shown in Table 3.3. As both k_{rms} and contact angles are very similar, this difference might be associated with geometric differences, namely the ~110 μm (~$8.5\delta_\upsilon$) spaced streamwise grooves (Figure 3.3c). Considering that the deeper ($5\sim15\delta_\upsilon$) streamwise riblets have already been shown to reduce drag in turbulent boundary layers over rigid walls, e.g., by 10% when the space of grooves is $15\delta_\upsilon$ (García-Mayoral & Jiménez 2011), the groove alignment seems to play a role in the SHSs as well.

Using the same symbols, Figure 3.10 shows the mean velocity profiles for the same six surfaces, scaled by their own u_τ and δ_υ. As expected, all the drag reduction SHS profiles are shifted upward from that the smooth wall, consistent with the numerical results by Min & Kim (2004) and experimental measurements by Woolford *et al.* (2009). For all SHSs except SB, the upward shifts in the log region are smaller than near wall region. There are two possible reasons for the non-constant shifting. First, it might be influenced by the previously discussed non-equilibrium condition, i.e., that the log layer mean momentum has only partially adjusted to the lower wall friction. However, these differences have also been observed in DNS results obtained for equilibrium conditions, which Min & Kim (2004) attribute to spanwise slip, which increases the skin friction by enhance the strength of streamwise vortices. In simulations prescribing only streamwise slip, i.e., $b_x \neq 0$ and $b_z=0$, the upward shift in the velocity profile is uniform. Indeed, the current roughness geometries are randomly rough. Both streamwise and spanwise slips are expected, while their ratio may vary between surfaces. For SB, however, the upward shift is nearly uniform across the entire inner boundary layer. The reason might due to the smallest roughness height of SB.

Figures 3.11(a) and (b) show the streamwise and wall-normal velocity fluctuations, respectively, for the six surfaces. Both are normalized by inner wall units of each's own surface. Near the wall ($y^+<10$), all the SHSs have higher velocity fluctuations than those of the smooth wall. These trends are consistent with reported numerical results for SHSs (Busse & Sandham 2012). The $\overline{<u'u'>}^+$ increases with distance from the wall in the inner layer, peaks at $6<y^+\leq 10$, and then decreases at higher elevations. The peak values are larger than those of the smooth wall, and are located closer to the wall. While the shift in location is consistent with the numerical results, the higher magnitude is not (Min & Kim 2004). There are several likely reasons for the discrepancy, such as roughness effects, motion of the air-water interface, spatial non-uniformity of air-coverage, and even the non-equilibrium conditions. The profiles of $\overline{<v'v'>}^+$ on SHSs have maximums in the $10<y^+<50$ range, also closer to the wall than the smooth wall peaks. The entire SHSs profiles, including the peak values, are higher than the corresponding smooth wall. The differences are bigger for the SHSs which have the larger drag reduction.

Figures 3.12(a) and (b) show the streamwise and wall-normal velocity fluctuations normalized by inner wall units of smooth wall, allowing us to compare the actual magnitudes. As obvious from the figures, the actual magnitudes of the $\overline{<u'u'>}^{+}$ and $\overline{<v'v'>}^{+}$ peaks for all the drag reduction cases are slightly lower than those of the corresponding smooth walls. For the highest drag reduction cases (ETH$_{r}$, ETH$_{x}$ and SP$_{Al}$), the magnitudes of $\overline{<u'u'>}^{+}$ at y^{+}>10 are smaller than the smooth wall case. The differences between the profiles of SHSs and smooth wall decrease as increasing y, and finally diminish in the outer layers. Those results again confirm that the outer regions of SHSs are still affected by the previous smooth wall boundary layer.

3.4 Effects of roughness height (k_{rms}^{+})

In this section, the effects of k_{rms}^{+} on the profiles of mean velocity, stresses, turbulence, shear production, as well as mixing length are studied. The value of k_{rms} ranges from 4.8 to 20.4 μm. The magnitude of Re_{τ} increases from 863 to 4496, corresponding to a decrease of δ_{v} from ~11 to ~4 μm. Therefore, the magnitude of k_{rms}^{+} increases from 0.4 to 3.3 for the five SHSs as listed in Table 3.4. The five cases include: three SP$_{Por}$ with three different magnitudes of k_{rms}, and one SP$_{Al}$ at two different Reynolds numbers. The corresponding four smooth wall results at same mean flow velocity and similar boundary layer thickness, i.e., similar Re_{Θ}, are also listed for comparison. Note, the smooth wall cases are the same as those listed in Table 3.2, indicated by same symbols. The two SHSs with k_{rms}^{+}<1 are the same as those listed in Table 3.3, also denoted by same symbols.

Figures 3.13 to 3.15 show the viscous, Reynolds shear and total shear stresses profiles for the nine cases listed in Table 3.4. Each profile is presented using two scales. In Figures 3.13(a), 3.14(a), and 3.15(a), the results are scaled by the total wall stresses of the smooth walls for the same U_m and very similar δ_{99} in order to highlight the differences from the smooth wall behavior. In Figures 3.13(b), 3.14(b), and 3.15(b), each profile is scaled by its own wall stress. Several trends are immediately evident. As increasing k_{rms}^+ from 0 to 3.3, the contribution of the viscous stress to the wall friction decreases from 100% to less than 20%, while that of the Reynolds shear stress increases. The locations and values of peak Reynolds shear stress also depend on k_{rms}^+. For $k_{rms}^+<1$, the peaks normalized by τ_{w0} have values and locations that are very close to those of the smooth walls, as discussed before. For $k_{rms}^+>1$, the magnitudes are distinctly higher. When the Reynolds stresses are normalized by their own τ_w, all the SHSs peaks are larger than those of the smooth walls.

The total stresses on the SHSs also depend strongly on k_{rms}^+. For all the $k_{rms}^+<1$ cases, $\tau_w/\tau_{w0}<1$ at $y=2k_{rms}$, indicating a reduction of drag by these surfaces. For the $k_{rms}^+\sim1.7$ cases, τ_w/τ_{w0} are very close to 1, but for $k_{rms}^+=3.28$, τ_w/τ_{w0} is already significantly larger than 1. Considering that for the latter case, τ_w^R is the primary contributor to the total stress, it is clear that the surface roughness dominates the total drag. With increasing rms values of roughness height, the SHSs switch from facilitating drag reduction when $k_{rms}^+<1$ to increasing the drag for larger k_{rms}^+. Similar trends are reported by Bidkar *et al.* (2014) based on force measurements of floating SHSs in a water tunnel. Their SHSs are generated by spray coating, covering a range of k_{rms}^+ ranging from 0.1 to 6, and show a maximum drag reduction of 30% for $k_{rms}^+<0.5$, and an increase in drag for $k_{rms}^+>1$. DNS results for textured surface by Busse & Sandham (2013) also show similar trends. Except for the highest drag reduction case, the values of τ_t^+ collapse at $10<y^+<30$, irrespective of roughness height as shown in Figure 3.15(b). For cases with $k_{rms}^+>1$, the total stresses remain nearly constant up to $y^+=300$. The higher total stress in the log region is consistent with the higher τ_w^{Log} than τ_w. The trend suggests that the roughness effect speeds up turbulent mixing and momentum exchange between the inner and outer regions.

Using the same symbols, Figure 3.16 shows the mean velocity profiles for the nine cases scaled by their own inner units. The inset highlights the near wall velocity profiles using a linear scale (with the axes switched), which allows direct comparison to linear least square fits. It confirms that for $k_{rms}^+<1$, the inner profiles are nearly linear when $y^+\leq 5$, but are slightly curved for $k_{rms}^+>1$. For all the $k_{rms}^+<1$, or drag reduction SHS cases, the mean velocity is higher than that of the smooth wall at all elevations. Conversely, for the drag increase case ($k_{rms}^+=3.28$), the log layer mean momentum is lower than that of the smooth wall. The entire profile resembles that measured over rough wall, which is characterized by lower mean velocity gradients in the inner part of the boundary layer (Chan *et al.* 2015). For $k_{rms}^+\sim 1.7$, the profile appears to be a transition from drag reduction to drag increase, with the inner region resembling a rough wall and a mild slope, and the outer region in the process of crossing from the momentum increase to momentum decrease regimes.

Figures 3.17(a) and (b) present distributions of $\overline{<u'u'>}^+$ and $\overline{<v'v'>}^+$, respectively. For all non-smooth wall cases, regardless of the magnitude of k_{rms}^+, both $\overline{<u'u'>}^+$ and $\overline{<v'v'>}^+$ are significant in the vicinity of the roughness tips, and remain higher than the smooth wall values at $y^+<10$. For the drag reduction cases ($k_{rms}^+<1$), $\overline{<u'u'>}^+$ increases with distance from the wall in the inner layer, peaks at $6<y^+\leq 10$, and collapses to the corresponding smooth wall data at $y^+>20$. Trends are quite different for the drag increase case ($k_{rms}^+=3.28$), for which $\overline{<u'u'>}^+$ flattens at $y^+<5$. After having a broad maximum centered around $y^+\sim 9$, $\overline{<u'u'>}^+$ decreases but remains higher than that of the corresponding smooth walls. While previously published trends for transitionally rough walls show that in the inner region $\overline{<u'u'>}^+$ can be higher or smaller than that of the smooth wall (Chan *et al.* 2015), the present trends for the log layer are inconsistent with the expected collapse to the smooth wall data (Hong *et al.* 2011; Jimenez 2004). The non-equilibrium condition appears to be a primary cause for this difference. Indeed, rescaling the $\overline{<u'u'>}^+$ profile based on τ_w^{Log} substantially reduces the difference from the smooth wall results, as shown in Figure 3.18(a). Furthermore, simulations of the transition from a smooth to a fully rough surface show overshoots of $\overline{<u'u'>}^+$ by ~10% in the log region (Saito & Pullin 2014). For the k_{rms}^+=1.71 case, at y^+<5, $\overline{<u'u'>}^+$ appears to have values and trends falling between those of the skin friction reduction and increase, but the broad peak appears at a lower elevation and has a lower magnitude than both. In the outer region, trends are similar to that of the $\mathrm{SHS}_{\mathrm{Por}}$ for the same Reynolds number.

For all the SHSs, the profiles of $\overline{<v'v'>}^+$ have maximums in the 10<y^+<50 range, closer to the wall than the smooth wall peaks. At y^+>50, for the cases with mild drag reduction (k_{rms}^+<1) and k_{rms}^+=1.71, the values of $\overline{<v'v'>}^+$ remain only slightly higher than those of the corresponding smooth wall. Conversely, for the drag increase case (k_{rms}^+=3.28), the values of $\overline{<v'v'>}^+$ in the inner part of the boundary layer are substantially higher than those of the smooth wall. This difference diminishes but does not vanish in the log layer. Such an overshot of the peak value of $\overline{<v'v'>}^+$ has been reported before for a boundary layer transitioning from a smooth to a rough wall, based on numerical simulations performed by Lee & Sung (2007) and by Saito & Pullin (2014). Both indicate that the elevated values decay slowly, e.g., for more than 500 momentum thicknesses in the former study. When the $\overline{<v'v'>}^+$ profiles are re-normalized based τ_w^{Log}, as shown in Figure 3.18(b), the SHS profiles collapse to the smooth wall values at y^+>20 for k_{rms}^+<2 and at y^+>100 for the drag increase case (k_{rms}^{+}=3.28). But the differences in the inner part of the boundary layer persist, especially for the drag increase case. Even under non-equilibrium conditions, trends of the outer parts of the evolving boundary layer in the rough wall case differ from those of the drag decrease cases. Both the rate at which the log layers response to the changing boundary conditions, and the involved turbulence levels are different.

The effect of SHSs, including both drag reduction and increase cases, on the turbulent kinetic energy (TKE) shear production P_s is discussed here. The values of P_s are calculated as $P_s = -\overline{<u'v'>} d\overline{U}/dy$. Figure 3.19(a) shows the distributions of P_s for two drag reduction cases (k_{rms}^{+}<1), three cases without drag reduction (k_{rms}^{+}>1), and four smooth wall cases (k_{rms}^{+}=0), which corresponding to the cases listed in Table 3.4. Following Marusic et al. (2010), the profile of yP_s is also calculated and plotted in Figure 3.19(b). Here, the area under each profile in the semi-log plot is equals to the integral of P_s. The DNS result of Spalart (1988) are also included for comparison. All magnitudes are normalized based on the smooth wall inner units. The four smooth walls profiles, which represent different Re_τ, share nearly the same peak value and location, and all agree with the DNS results.

For the SHSs, at the top of roughness, the magnitude of P_s increases with k_{rms}^{+}. It is nearly zero for k_{rms}^{+}<0.5, and high for k_{rms}^{+}>1.0. However, regardless of drag reduction or increase, at y^{+}<5, all the SHSs have higher production rates than those of the smooth walls. High production rates near roughness peaks have been reported before both experimentally (Hong et al. 2011) and computationally (Ikeda & Durbin 2007). Figure 3.19(b) shows that for all the drag reduction cases, the production rates in the log region are lower than that of the smooth walls. In contrast, the surfaces with k_{rms}^{+}≥1, the production rates are much higher than those of the smooth walls, and increase with elevation. Keeping in mind that the majority of the TKE in boundary layer is produced in the log region (Marusic et al. 2010), Figure 3.19(b) indicates that in spite of the higher Reynolds stresses very near the wall, the overall shear productions in drag-reducing SHSs are lower than that of the smooth wall.

Based on turbulent-viscosity hypothesis (Pope 2000):

$$-\overline{<u'v'>} = \upsilon_T\left(\frac{\partial\overline{U}}{\partial y}+\frac{\partial\overline{V}}{\partial x}\right), \tag{3.2}$$

where υ_T is the so-called eddy viscosity. The second term on the right side of this equation is usually neglected in turbulent boundary layers, giving:

$$\upsilon_T \approx -\frac{\overline{<u'v'>}}{\partial\overline{U}/\partial y}. \tag{3.3}$$

We also perform the analysis using the total stress to calculate the total viscosity υ_T^t:

$$\upsilon_T^t = \frac{\tau_t/\rho}{\partial\overline{U}/\partial y} = \upsilon_T + \upsilon \tag{3.4}$$

Accordingly, one can also calculate two values for the Prandtl’s mixing length, l_m and l_m^t:

$$l_m = \left(\frac{\upsilon_T}{\partial\overline{U}/\partial y}\right)^{1/2}, \qquad l_m^t = \left(\frac{\upsilon_T^t}{\partial\overline{U}/\partial y}\right)^{1/2} \tag{3.5}$$

Figures 3.20(a) and 3.21(a) show the distributions of υ_T and l_m, respectively, along with Spalart's (1988) DNS results. The model by Van Driest (1956):

$$l_m^+ = \kappa y^+\left(1-e^{-y^+/26}\right) \tag{3.6}$$

is also included in Figure 3.21(a). All values are normalized based on their own inner units. For the current measurement domains ($0<y<0.3\delta_{99}$), both υ_T and l_m increase with y. However, at higher elevations, the values of υ_T are expected to decrease with y, while the mixing length is expected to plateau. All the current smooth wall results nearly collapse onto the DNS data and Van Driest model at $y^+<100$. At $y^+<10$ where viscous stress dominates, the values of υ_T/υ and l_m^+ are smaller than 1. At the beginning of log region $y^+>30$, υ_T/υ and l_m^+ are larger than 5. The smooth wall results do not collapse at $y^+>100$, presumably due to Reynolds number dependent changes to turbulence in the outer layer (Smits et al. 2011).

For the SHSs, both υ_T and l_m increase with elevation. Near the wall ($y^+<10$), they are higher than those of smooth walls, increasing from values of less than 1 for drag reduction cases, to values larger than 1 for the drag increase surfaces. These trends correspond to the increase of Reynolds shear stress and reduction in viscous stress with increasing k_{rms}^+. The differences between all the SHSs and the smooth walls results diminish with increasing y, and they appear to coincide in the log layer. The profiles of l_m^+ collapse better than those of υ_T/υ.

Figures 3.20(b) and 3.21(b) show the distributions of υ_T^t and l_m^t, respectively. Since the values of υ_T^t/υ and υ_T/υ only differ by 1, the trends are inherently similar. However, being presented in a log-log plots, near the wall ($y^+<10$), the profiles of υ_T^t/υ and l_m^{t+} for the drag reduction cases appear to be much closer to those of the smooth wall. Conversely, results for the cases where roughness begins to dominate, values of υ_T^t/υ and l_m^t are much higher than those of smooth walls.

3.5 Effects of hydrostatic pressure

All the previous measurements are performed at relative low pressure in the facility such that the air layer on SHSs is not suppressed. In this subsection, the effects of air layer suppression by hydrostatic pressure are studied. Two surfaces (SP_{Por} and ETH_x) are involved and both are tested at two different pressure levels. Here, p_w is used to denote the pressure in the test section. For the porous surfaces (SP_{Por}) at the first pressure level, p_w=0.97 atm, the air on SHS is slow replenished from the air chamber located below the porous base (p_{por}=1.0 atm). At the second one, p_w=1.20 atm and p_{por}=1.0 atm, the air layer is suppressed. For the ETH_x, the two pressure levels include one where the air layer is maintained (p_w=1.04 atm), and the second where the air layer is suppressed (p_w=1.20 atm). The measurement results for these four cases together with the smooth wall baseline are listed in Table 3.5. It should be noted that the smooth wall and two SHS cases when the air layer is not suppressed correspond to cases listed in Table 3.2, indicated by same symbols. The magnitudes of p_w are normalized by the surface tension to obtain the non-dimensionalized pressure, $p_w^*=(p_w-p_0)k_{rms}/\gamma$, where γ is the surface tension and p_0 denotes the atmosphere pressure (p_0=1.0 atm).

Figures 3.22(a) and (b) compare the viscous, Reynolds shear and total stresses for SHSs at different p_w^*. Figure 3.22(a) presents results for SP_{Por} at $p_w^*=-0.02$ and 1.33. Figure 3.22(b) shows the results for ETH_x at p_w^*=0.49 and 2.47. As expected, increasing p_w^* causes a mild decrease on the viscous stresses and significant increases in Reynolds shear stress and total stress. Both SP_{Por} and ETH_x have less drag reduction at higher p_w^*. Those trends are very similar to those caused by increasing k_{rms}^+. Indeed, at the higher p_w^* when the plastron is suppressed, more roughness elements are exposed to the flow resulting in an increase of "effective" roughness height. Thus, the effects of increasing p_w^* are similar to those caused by increasing k_{rms}^+. Yet, the skin friction is still significantly lower than that of the smooth wall. It appears that the capillary forces are sufficient to maintain the air layer under such high pressure.

Figures 3.23(a) and (b) show the mean velocity profiles for the same cases. Consistent to the decrease in drag reduction, the mean velocity profiles for both SP_{Por} and ETH_x at higher p_w* are less upward shifted than those at lower p_w*. Moreover, the mean profile at higher p_w* decreases slightly in the near wall region, but significantly in the log region, compared to that at low p_w*. This again indicates the increase of roughness effect. The increasing role of the roughness with increasing p_w* can also be observed from the distributions of the Reynolds normal stresses shown in Figures 3.24(a) and (b). Both the magnitudes of $\overline{<u'u'>}_0^+$ and $\overline{<v'v'>}_0^+$ increase with p_w* over the entire inner part of the boundary layer.

3.6 Effects of streamwise distance

Due to the streamwise short length of current sample, the boundary layer is not fully developed. It is worthwhile to study the transition of boundary layer. Therefore, the effects of streamwise distance from the transition between smooth to SHS have been evaluated by performing measurements over the same SHS at two different streamwise distances, namely, $x=3.9\delta_{99}$ and $7.7\delta_{99}$. The latter being the location of most of the present tests. The results are listed in Table 3.6. The first two cases have been presented in Table 3.2 using same symbols. Here, they are listed again for a comparison to the last case.

The stress profiles are plotted in Figures 3.25(a)-(c). Several trends can be observed. Except for the first point, where results are essentially identical, the total stress at $x=3.9\delta_{99}$ is slightly higher, by 10-15%, than that further downstream for all the elevations. This difference could be used as an estimate for non-equilibrium effects on the total stress. Trends of the two contributors to the total stress differ. At $y^+<8$, the viscous stress at $x=3.9\delta_{99}$ is lower than that further downstream, but the profiles completely collapse at higher elevations. Conversely, the Reynolds shear stress at $x=3.9\delta_{99}$ is higher, and the difference between them slowly diminishes with increasing elevation, becoming very small at $y^+>40$. For both contributors to the total stress, the profiles at $x=3.9\delta_{99}$ do not have intermediate values falling between the smooth wall and the more developed SHS further downstream. Such phenomena should be expected, as an overshoot in drag at the transition from smooth to rough walls (Saito & Pullin 2014), and an undershoot at the transition from rough to smooth walls (Antonia & Luxton 1971) and from smooth wall to SHS (Park 2015) have been seen before. At the wall, the present results show an undershoot of viscous stress by 18% and an overshoot of (very low) Reynolds shear stress by 88%, both of which might be associated with the transitional effects.

3.7 Relationship between slip length and drag reduction

Here, the relationship between slip velocity, based on values measured at the top of the roughness, and the drag reduction is discussed. Figure 3.26 is a plot of DR as a function of $\overline{U}_s^+$, where each case is represented by the symbols listed in Table 3.2 to 3.6 and used throughout this chapter. It also shows the theoretical predictions by Busse & Sandham (2012), based on Equation 1.2 and their empirical function $F(b_z^+)=16/(4+b_z^+)-1$. The model results are provided for two relevant values of Re_τ, both for $b_z=0$ and $b_z=b_x$. However, for the experimental data, b_x^+ is replaced by $\overline{U}_s^+$ at the top of the roughness. That means that we assume that the present measurements are equivalent to a hypothetical case for which the air layer surface is aligned with the top of the roughness, and the viscous stress there is equal to the total stress. As discussed before, $\overline{U}_s^+ \le b_x^+$, and the equal sign is only valid when $\tau_w{}^R=0$.

As discussed in Busse & Sandham (2012), the introduction of spanwise slip and an increase in Re_τ reduces the extent of drag reduction. The λ_z=0 case predictions agree with the DNS results of Park *et al.* (2013a) for an SHS consisting of long and broadly spaced streamwise grooves, which presumably involve limited spanwise slip.

However, the present cases that involve drag reduction (>10%) fall close to the predicted values assuming $b_z^+=b_x^+$ (SP_{Al}, SP_{Por}, ETH_r, ETH_x) or $b_z^+=0$ (SB). It is not surprising for the randomly distributed roughness on samples SP_{Al}, SP_{Por} and ETH_r that results fall on $b_z^+=b_x^+$. The reason why the SB results fall on $b_z^+=0$ is still unclear. The uniformly upward shift of the mean velocity profile on SB (Figure 3.10) is consistent with the results that $b_z^+=0$. It also raises questions for the ETH_x results, where the non-uniformly distributed grooves are preferentially aligned in the streamwise direction. It is difficult to assess why ETH_x results fall on the $b_z^+=b_x^+$ curve. If the streamwise slip is preferentially higher, one would expect that the drag reduction would also fall above the $b_z^+=b_x^+$ curve. There are several possible reasons for this trend, such as effects of the non-uniform spacing, which may allow some spanwise slip, and/or roughness effects, as evidenced by the elevated Reynolds stress at the top of the grooves (Figure 3.9). We have not performed measurements using other groove spacing or depth, so the significance of this observation remains unclear.

Four cases deviate significantly from the predicted values, all of which involve an increasing role of roughness. Three of them are the $k_{rms}^+>1$ cases, and the fourth is the ETH_x with $p_w^*=2.47$, namely when the plastron is partially suppressed by increasing the pressure in the test facility. Hence, for situations where the roughness effect is not dominant, i.e., the Reynolds stress at the top of the roughness is much lower than the viscous stress, the present measurements confirm the theoretical relationship between drag reduction and slip length for a turbulent boundary layer over an SHS. To the best of our knowledge, the present study provides the first simultaneous direct measurement of both slip velocity and drag reduction, allowing such a comparison.

3.8 Effects of SHSs on spatial energy spectra

Fast Fourier transform (FFT) of the instantaneous 2D-PIV data is used for calculating the spatial energy spectra, $E_{11}(k_x)$ and $E_{22}(k_x)$, of the streamwise and wall-normal velocity fluctuations, respectively, with k_x being the spatial wavenumber. Each realization contains ~100 vectors spaced by $32\delta_v$ in the x direction. Details of the procedures are provided in Hong et al. (2011). The resolved wavenumber falls in the range of $3\times10^{-4}<k_x\delta_v<0.02$. Results have been obtained for two drag reduction SHSs (SP_{Por} and SP_{Al}) and the corresponding smooth wall.

Figure 3.27(a) and (b) show the spectra at $y_0^+ = 30$ and $y_0^+ = 100$, respectively. In order to compare the actual differences, the spectral values are normalized by same $u_{\tau 0}^2\delta_{v0}$, and the wavenumber is normalized by δ_{v0}. Several trends are evident, as some expected for turbulent boundary layers. For example, the difference between E_{11} and E_{22} decreases with elevation, and with increasing k_x. This trend has been attributed to the suppression of large scale wall-normal turbulence near the wall. Second, the slopes increase with wavenumber, as E_{11} transitions from the turbulence production range to the inertial subrange (slope −5/3), and then to the dissipation range.

At $y_0^+ = 30$, the values of E_{11} for the SHSs are similar to those of the smooth wall at low wavenumbers ($k_x\delta_{v0}<0.001$), but are clearly smaller at higher wavenumbers. Conversely, the magnitudes of E_{22} of both SHSs are larger than those of the smooth wall at low wavenumbers $k_x\delta_{v0}<0.001$, but are similar at high wavenumbers. These trends suggest that the

SHSs alter the structure of the near wall turbulence. While the rough and/or vibrating SHSs are expected to increase the wall normal fluctuations, what scale of the fluctuations is affected by them need to be further studied. The reasons for the slight suppression of small-scale streamwise energy are not clear. In contract, in a recent paper, Vajdi Hokmabad & Ghaemi (2016) report that the ejection and sweeping events are suppressed, and the width of low speed streaks increases above the SHS, which would presumably cause a decrease of large-scale streamwise fluctuations. The differences in E_{22} spectra between the smooth wall and the SHSs diminish at $y_0^+ = 100$. The differences in small scale streamwise fluctuations persist.

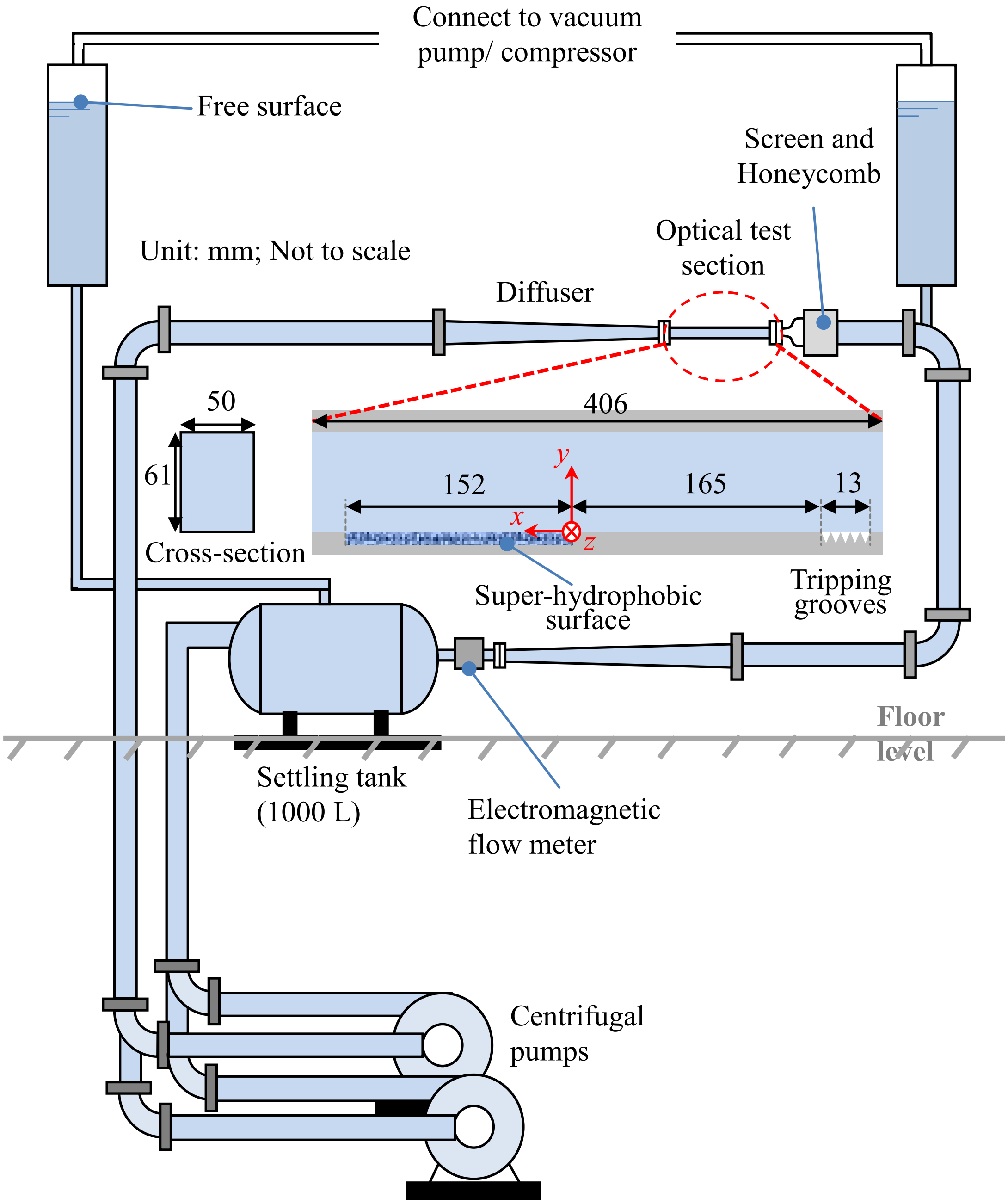

Figure 3.1. Sketch of high speed water tunnel facility and the optical test section.

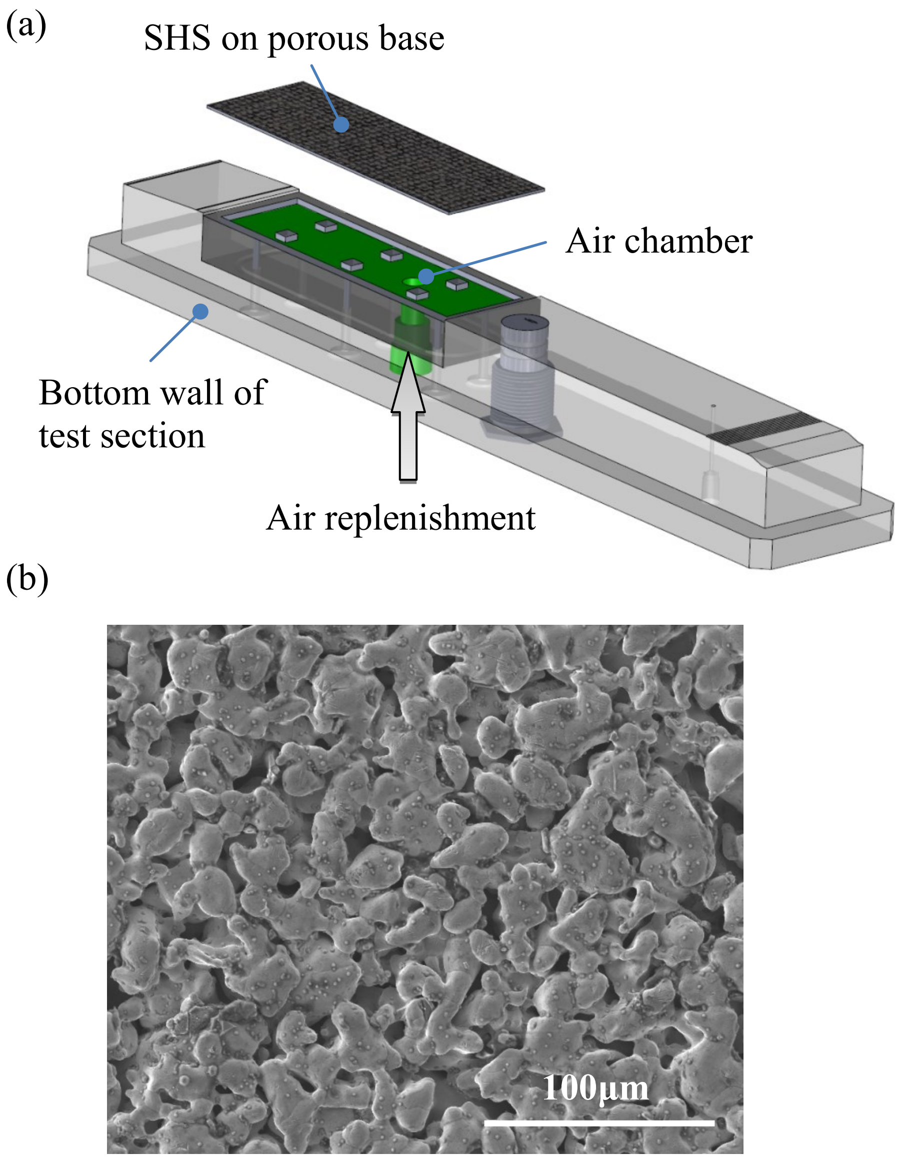

Figure 3.2. (a) Installation of the super-hydrophobic surface with porous base into the water tunnel; and (b) scanning electron micrograph of the porous base.

#	**Base**	**Roughness type**	**Chemistry**	**Contact**	**k_{rms}, µm**

				angle	
Smooth	Solid	-	-	<90°	<<1
SP_{Por}	Porous	Sprayed	F-POSS	156±2°	4.8~20
SP_{Al}	Solid	Sprayed	F-POSS	162±2°	7.4
ETH_r, ETH_x	Solid	Etched	F-silane	153±2°	10.9
SB	Solid	Sandblasted & etched	PTFE	160±2°	<3

Table 3.1. Specifications of four types of SHSs involved in this study, including base type, roughness manufacture method, surface chemistry, contact angle, and rms roughness height. F-POSS denotes fluorinated polyhedral oligomeric silsesquioxane, F-silane as (heptadecafluoro-1,1,2,2-tetrahydrodecyl) trichlorosilane, and PTFE as polytetrafluoroethylene.

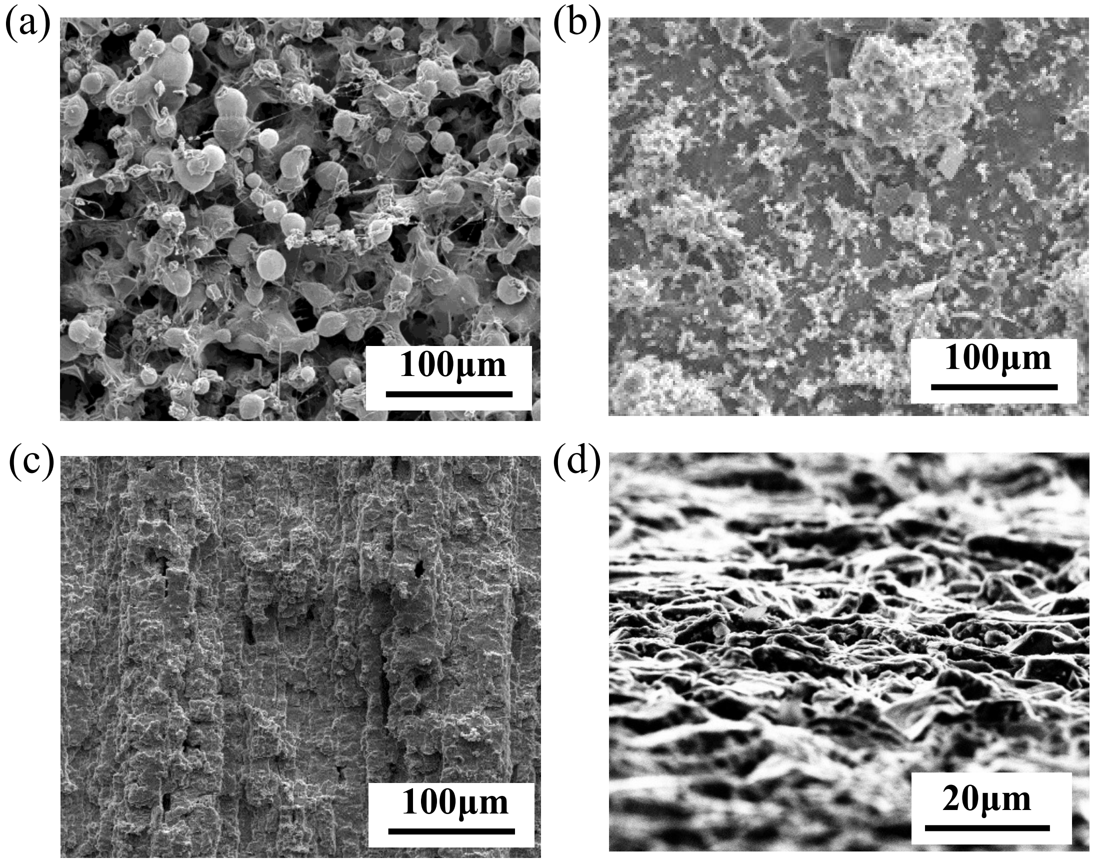

Figure 3.3. SEM images of four types of SHSs as listed in Table 3.1: (a) SP_{Por}; (b) SP_{Al}; (c) ETH_x; (d) SB.

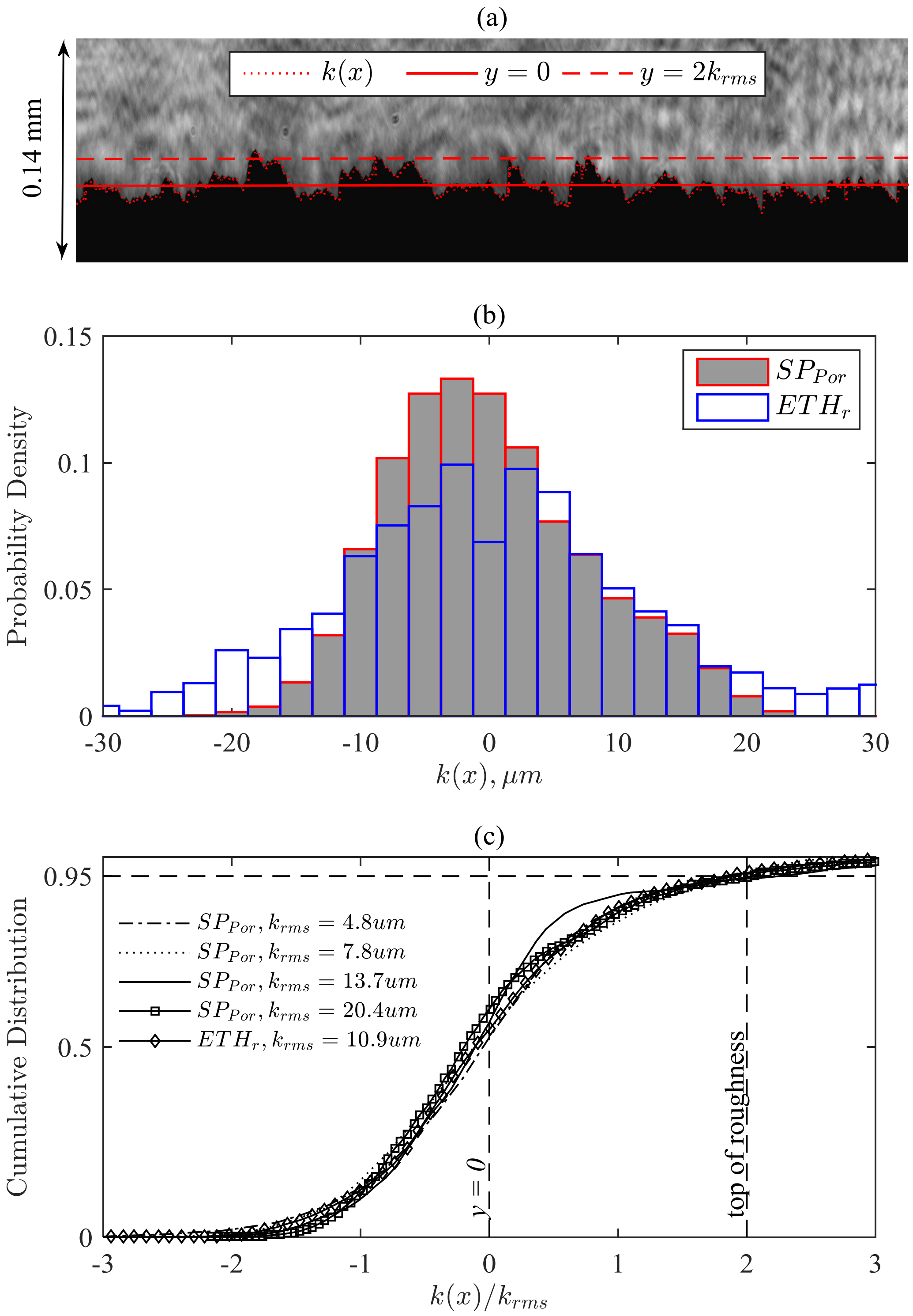

Figure 3.4. (a) The sample hologram of SHS topography; (b) sample probability density functions of the roughness height *k(x)* for one of the SP_{Por} (k_{rms}=7.8 µm) and the ETH_r; and (c) cumulative distributions of *k(x)* for five SHSs with different k_{rms}.

]

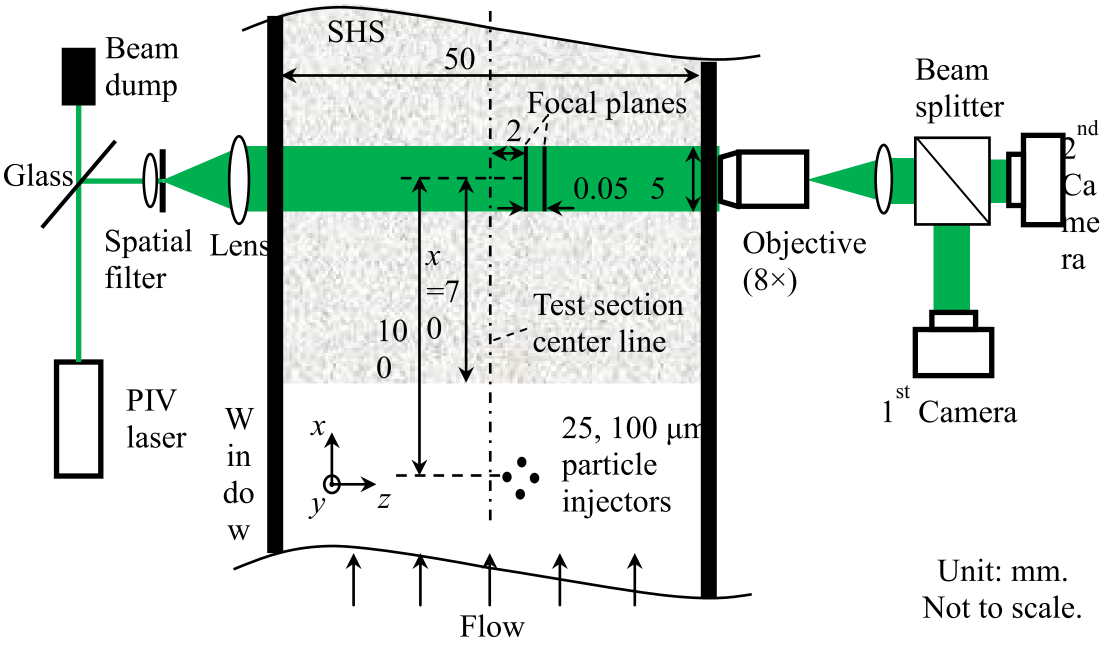

Figure 3.5. Optical setup for high-resolution velocity measurement in turbulent boundary layers over SHSs (setup based on dual-view digital holographic microscopy).

	U_m, m/s	U_0, m/s	δ_{99}, mm	Θ, mm	Re_δ	Re_Θ	τ_w^μ, Pa	τ_w^R, Pa	τ_w, Pa	τ_w^{Log}, Pa	δ_υ, µm	u_τ, m/s	Re_τ
△	2.1	2.2	9.1	1.0	20,020	2200	9.0	0	9.0	9.0	10.5	0.095	863
□	2.1	2.2	16.6	1.6	36,520	3520	7.2	0	7.2	7.3	12	0.085	1408
☆	5.5	6.0	7.4	0.9	44,400	5400	51	0	51	51	4.42	0.226	1671
✡	5.9	6.4	18.8	1.7	120,320	10,880	52	0	52	51	4.39	0.228	4287

Table 3.2. Measurement results for smooth walls at four different Reynolds numbers. The indicated symbols are used for all the figures in this chapter.

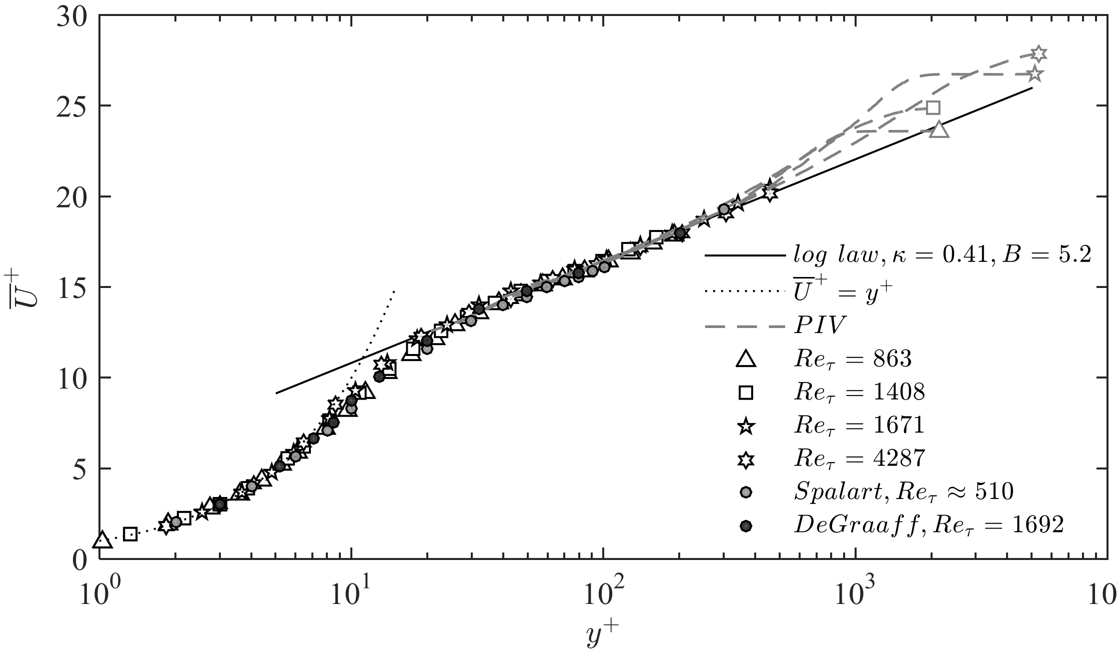

Figure 3.6. Mean velocity profiles for the baseline (smooth wall) cases. Gray dashed lines and symbols are obtained from 2D PIV, and black symbols show DHM data.

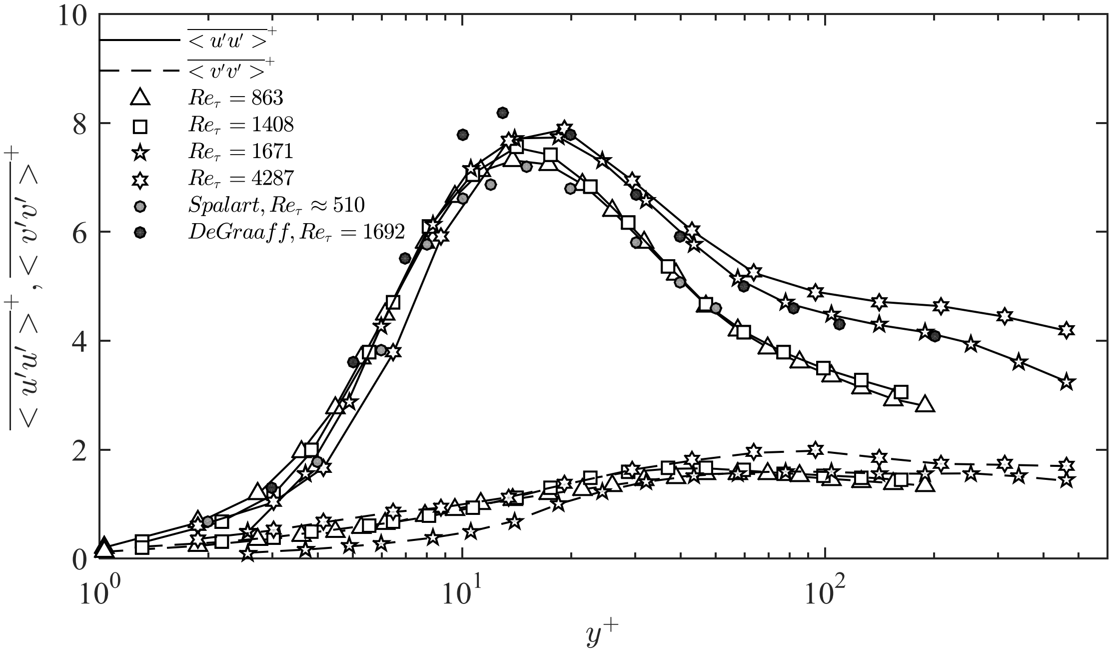

Figure 3.7. Baseline statistics of streamwise and wall-normal velocity fluctuations.

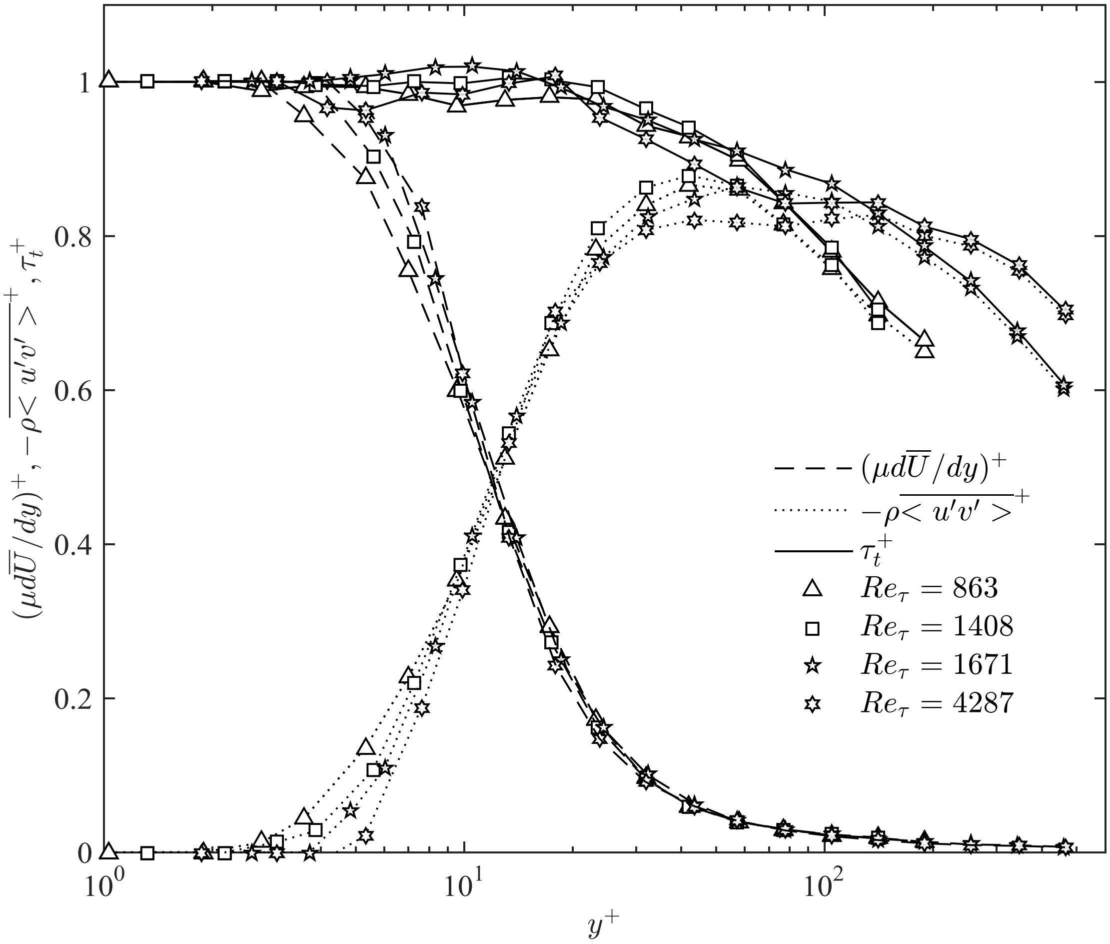

Figure 3.8. Profiles of baseline viscous shear stress (dashed lines), Reynolds shear stresses (dotted lines), and total shear stress (solid lines).

Sample	***k_{rms}*, µm**	**τ_w^{μ}, Pa**	**τ_w^{R}, Pa**	**τ_w, Pa**	**τ_w^{Log}, Pa**	***δ_υ*, µm**	**Re_τ**	**k_{rms}^{+}**	**$\bar{U}_s$, m/s**	**b, µm**	**DR, %**
△ Smooth	0	9.0	0	9.0	9.0	10.5	863	0	0	0	0
▲ SP_{Por}	4.8	7.9 ±0.0	0 ±0.1	7.9 ±0.1	9.2	11.3	809	0.43	0.30 ±0.02	38	12
■ SP_{Al}	7.3	5.3 ±0.0	1.1 ±0.4	6.6 ±0.4	8.5	12.3	739	0.59	0.52 ±0.02	96	27
● ETH_r	10.9	5.3 ±0.0	1.2 ±0.4	6.6 ±0.4	8.5	12.3	739	0.89	0.58 ±0.03	109	27
★ ETH_x	8.9	4.9 ±0.0	0.9 ±0.5	5.8 ±0.5	8.1	13.1	693	0.68	0.71 ±0.02	145	36
◆ SB	<3	7.2 ±0.0	0 ±0.2	7.2 ±0.3	7.7	11.8	772	<0.3	0.17 ±0.02	24	20

Table 3.3. Measurement results for five SHSs all at same flow condition U_m=2.1 m/s and δ_{99}=9.1 mm, and all with k_{rms}^{+}<1. The indicated symbols are used for all the figures in this chapter.

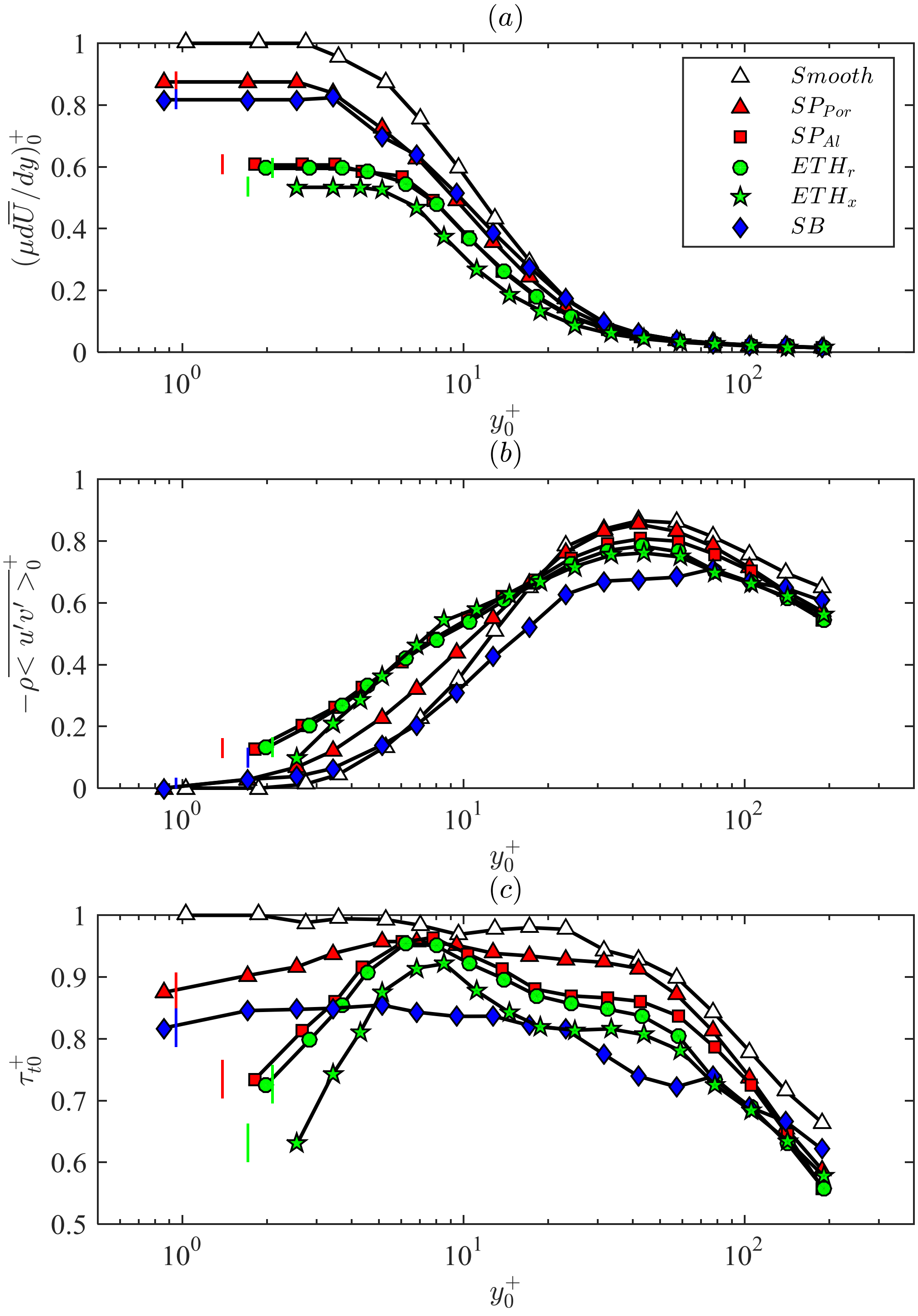

Figure 3.9. Profiles of (a) viscous, (b) Reynolds, and (c) total shear stress of five SHSs with k_{rms}^{+}<1 and the corresponding smooth wall. Results are scaled by the smooth wall inner units.

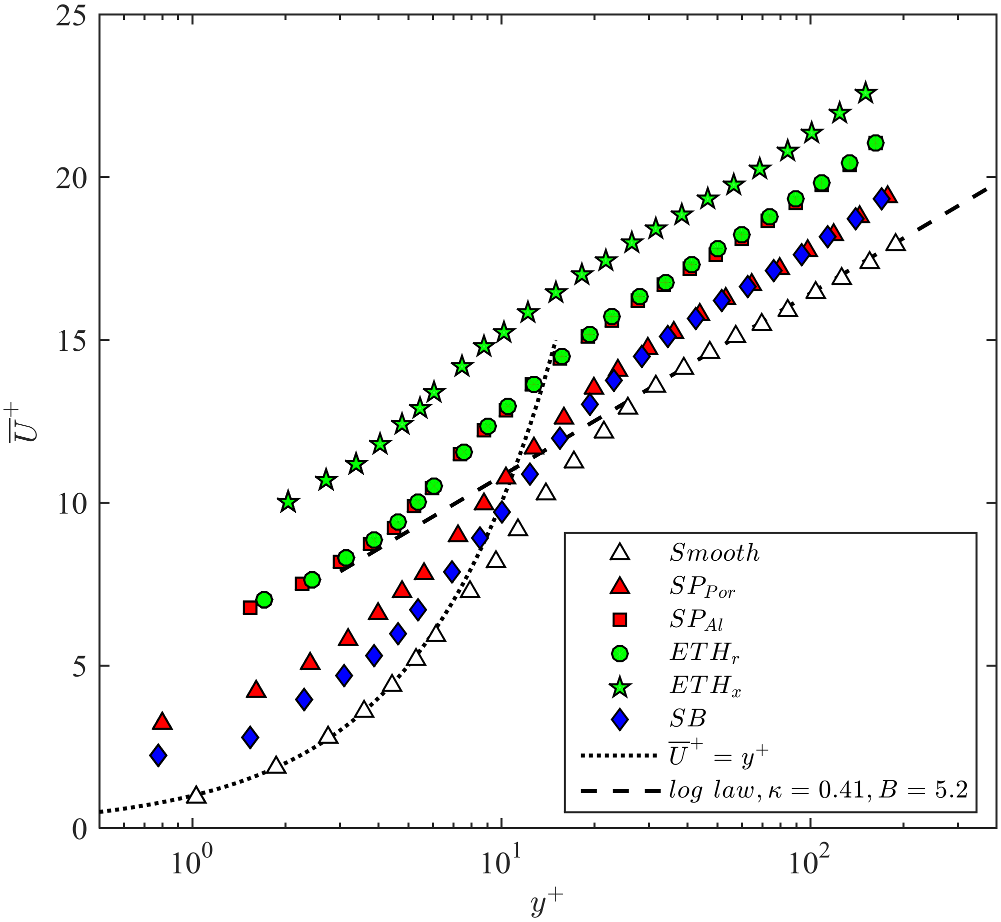

Figure 3.10. Mean velocity profiles of five drag reduction SHSs with $k_{rms}^+<1$ and the corresponding smooth wall. Results are scaled by inner units of each own surface.

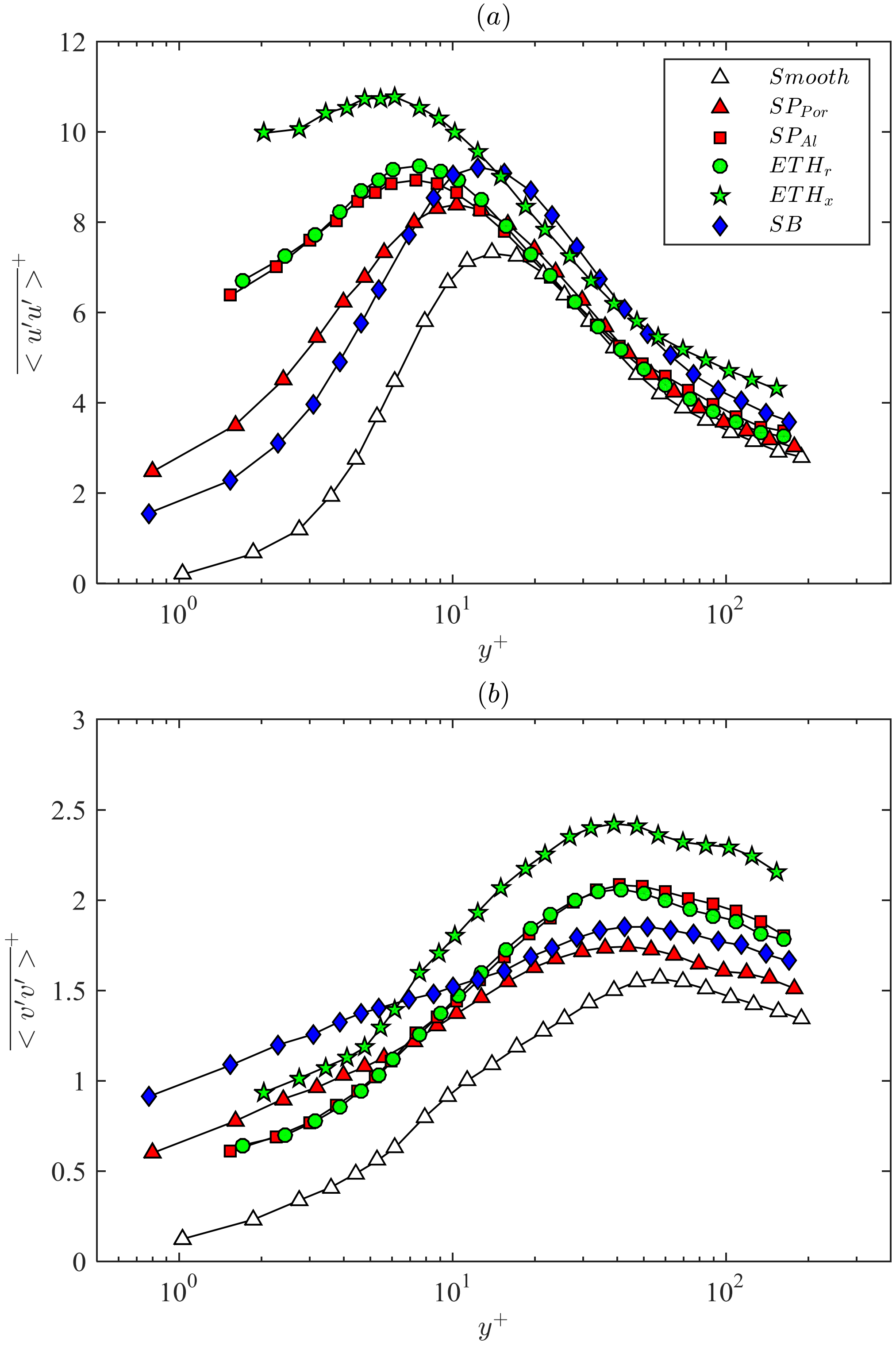

Figure 3.11. (a) Streamwise and (b) wall-normal velocity fluctuations of five SHSs with k_{rms}^+<1 and the corresponding smooth wall. Results are scaled by inner wall units of each own surface.

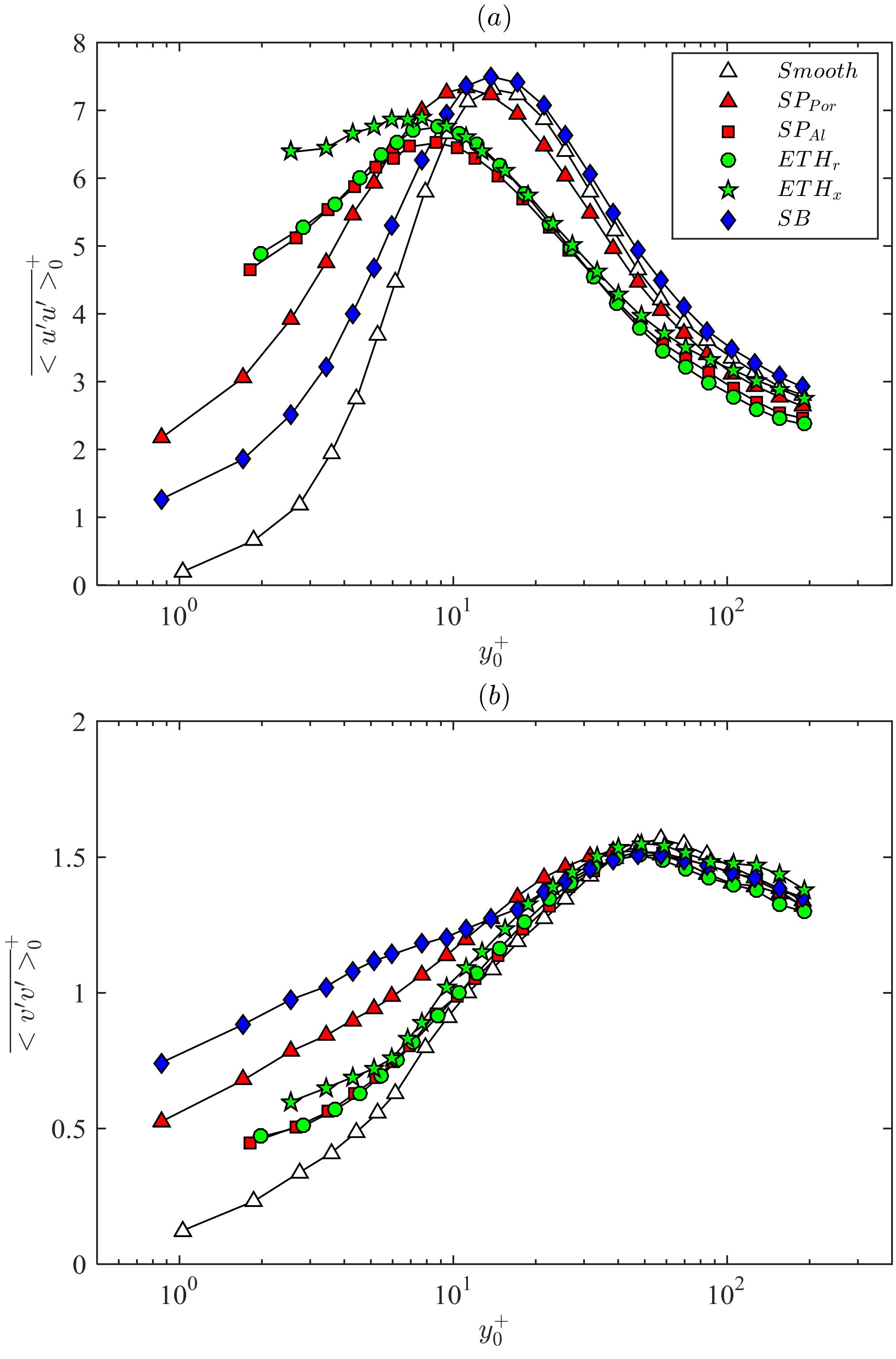

Figure 3.12. (a) Streamwise and (b) wall-normal velocity fluctuations of five SHSs with k_{rms}^+<1 and the corresponding smooth wall. Results are scaled by inner wall units of smooth wall.

Sample	$Re_{\Theta 0}$	k_{rms}, ***μm***	τ_w^{μ}, **Pa**	τ_w^{R}, **Pa**	τ_w, **Pa**	τ_w^{Log}, **Pa**	δ_υ, ***μm***	Re_τ	k_{rms}^+	$\bar{U}_s$, ***m/s***	***DR, %***
△ Smooth	2200	-	9.0	0	9.0	9.0	10.5	863	-	-	-
▲ SP_{Por}		4.8	7.9 ±0.0	0 ±0.1	7.9 ±0.1	9.2	11.3	809	0.43	0.30 ±0.02	12
■ SP_{Al}		7.3	5.3 ±0.0	1.1 ±0.4	6.6 ±0.4	8.5	12.3	739	0.59	0.52 ±0.02	27
□ Smooth	3520	-	7.2	0	7.2	7.3	11.8	1408	-	-	-
■ SP_{Por}		20.4	4.1 ±0.0	3.0 ±0.5	7.0 ±0.3	7.7	12.0	1389	1.71	0.67 ±0.04	3
☆ Smooth	5400	-	51	0	51	52	4.42	1671	-	-	-
★ SP_{Al}		7.3	13.8 ±0.5	35.0 ±1.6	50 ±1.6	53	4.49	1642	1.65	2.13 ±0.05	2
✡ Smooth	10,880	-	52	0	52	51	4.39	4287	-	-	-
✶ SP_{Por}		13.7	14.6 ±1.3	42.6 ±4.1	57.2 ±2.8	64	4.18	4496	3.28	2.08 ±0.08	−10

Table 3.4. Measurement results for SHSs with k_{rms}^+ increases from 0.4 to 3.3, and the smooth wall at similar Reynolds number. The indicated symbols apply for all the figures in this chapter.

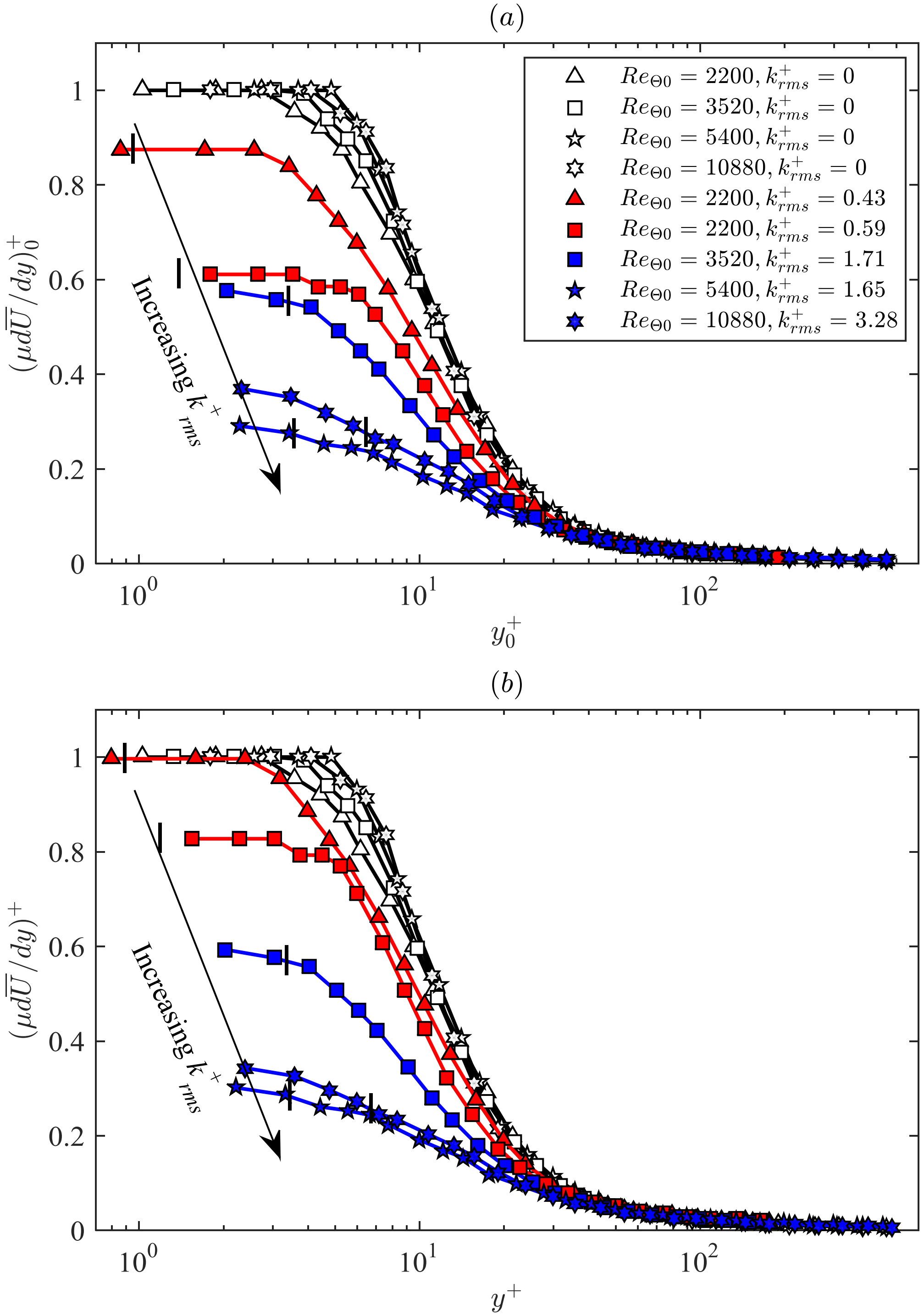

Figure 3.13. Effect of $k_{rms}{}^+$ on profiles of viscous shear stress. Open symbols for smooth wall. Red symbols for $k_{rms}{}^+<1$. Blue symbols for $k_{rms}{}^+>1$. Results are scaled by: (a) the smooth wall inner units, and (b) their own inner units. The location of $y=2k_{rms}$ for each profile is marked by a short vertical line.

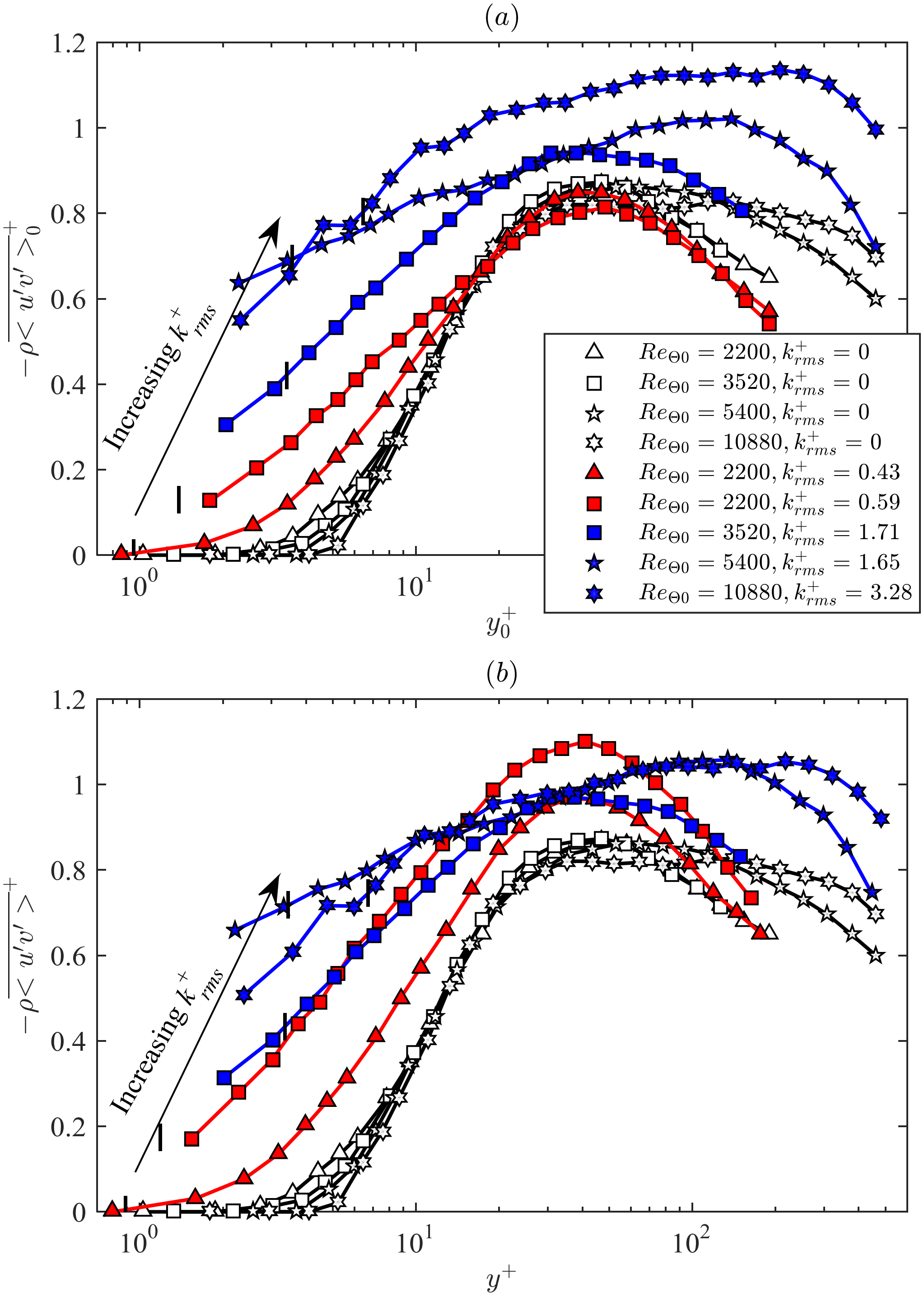

Figure 3.14. Effect of $k_{rms}{}^+$ on profiles of Reynolds shear stress. Open symbols for smooth wall. Red symbols for $k_{rms}{}^+<1$. Blue symbols for $k_{rms}{}^+>1$. Results are scaled by: (a) the smooth wall inner units, and (b) their own inner units.

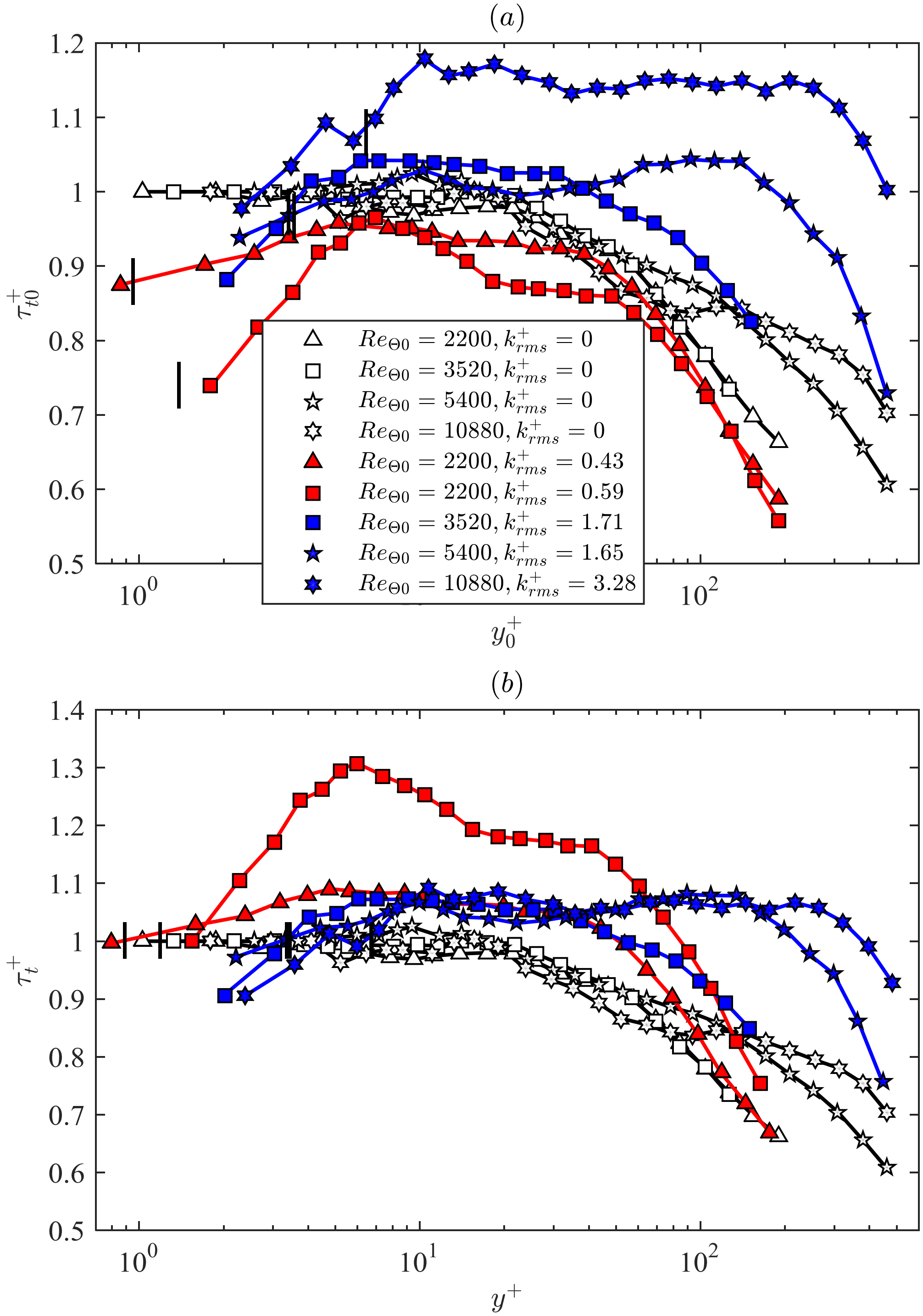

Figure 3.15. Effect of k_{rms}^+ on profiles of total shear stress. Open symbols for smooth wall. Red symbols for $k_{rms}^+<1$. Blue symbols for $k_{rms}^+>1$. Results are scaled by: (a) the smooth wall inner units, and (b) their own inner units.

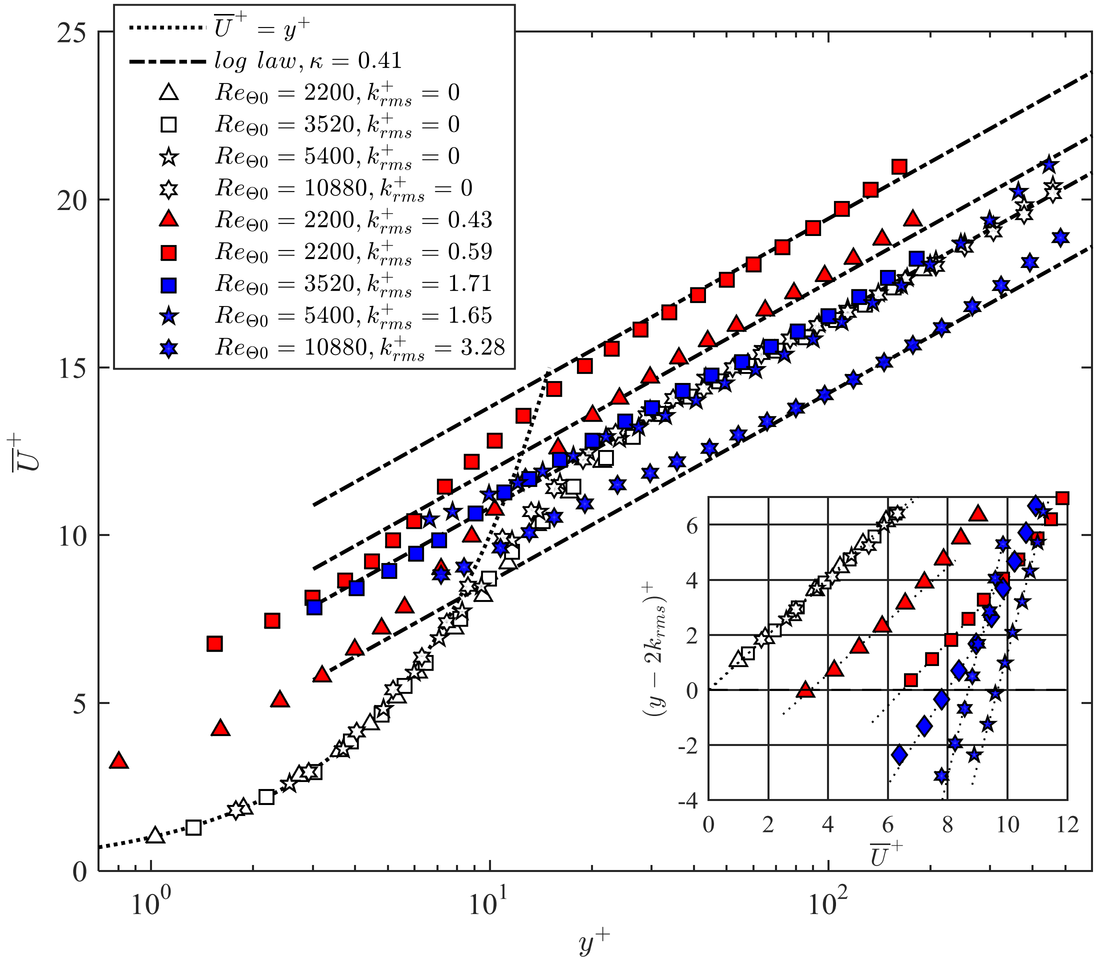

Figure 3.16. Effect of $k_{rms}{}^+$ on mean velocity profiles. All profiles are scaled by their own inner units. The inset shows the near wall profiles in linear scales, with dotted lines indicating linear least square fits.

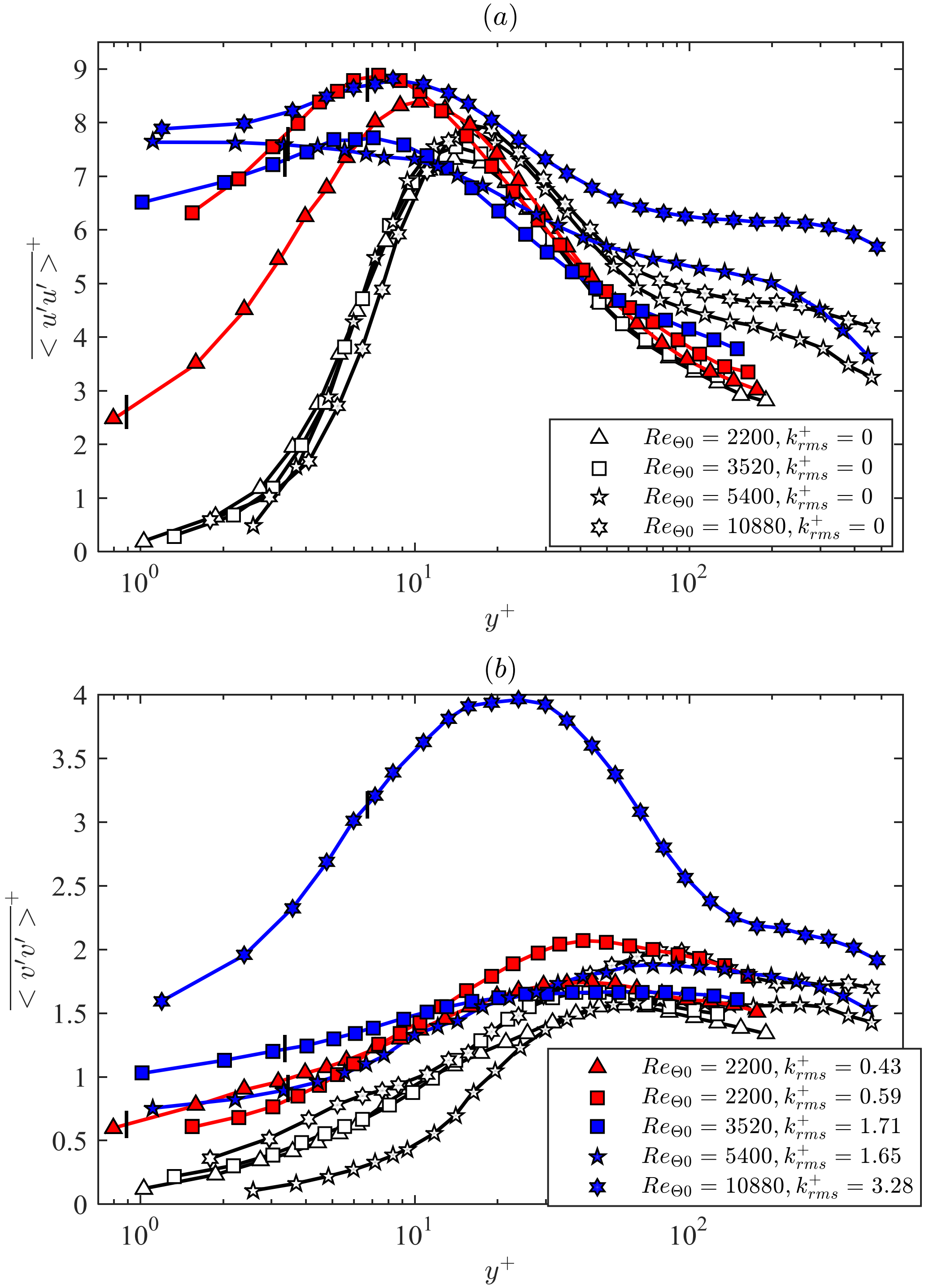

Figure 3.17. Effect of $k_{rms}{}^{+}$ on (a) streamwise and (b) wall-normal velocity fluctuations. All profiles are scaled by their own inner units.

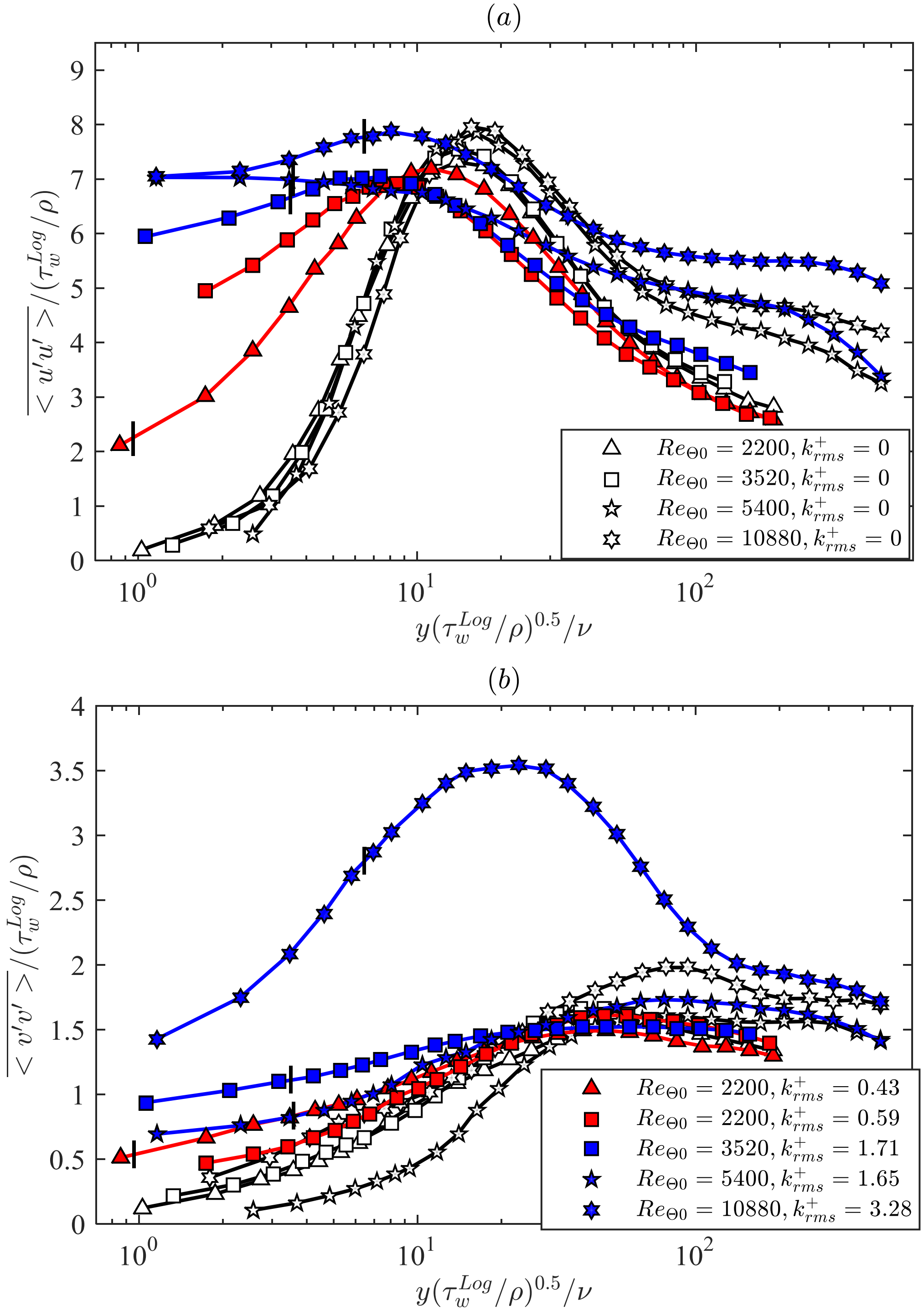

Figure 3.18. Effect of $k_{rms}{}^+$ on (a) streamwise and (b) wall-normal velocity fluctuations. All profiles are normalized by the shear stress estimated from a fit to the mean velocity profile in the log region.

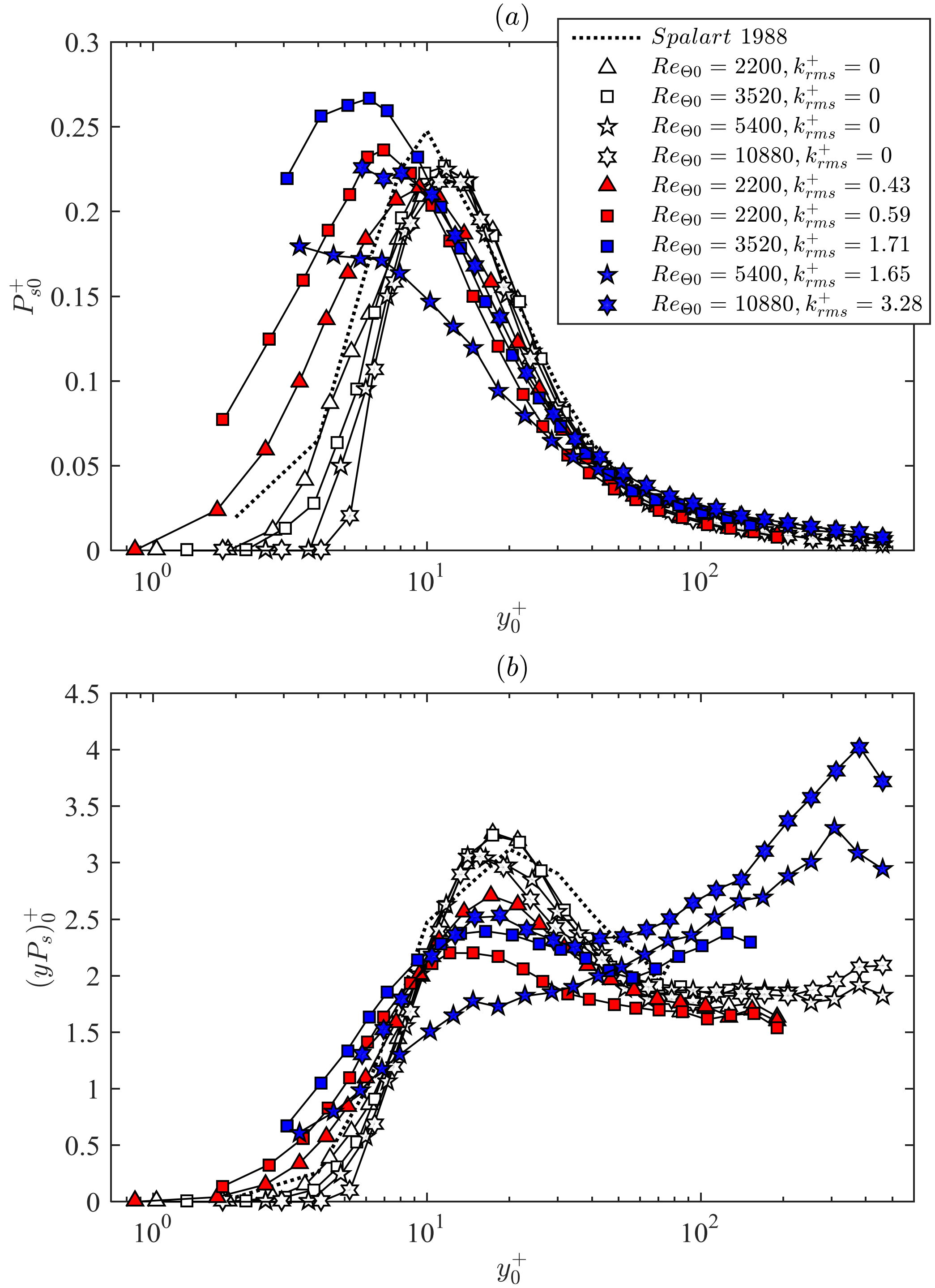

Figure 3.19. Effect of $k_{rms}{}^+$ on turbulence kinetic energy shear production: (a) in a semi-logarithmic plot, and (b) per-multiplied by y. All profiles are scaled by smooth wall inner units.

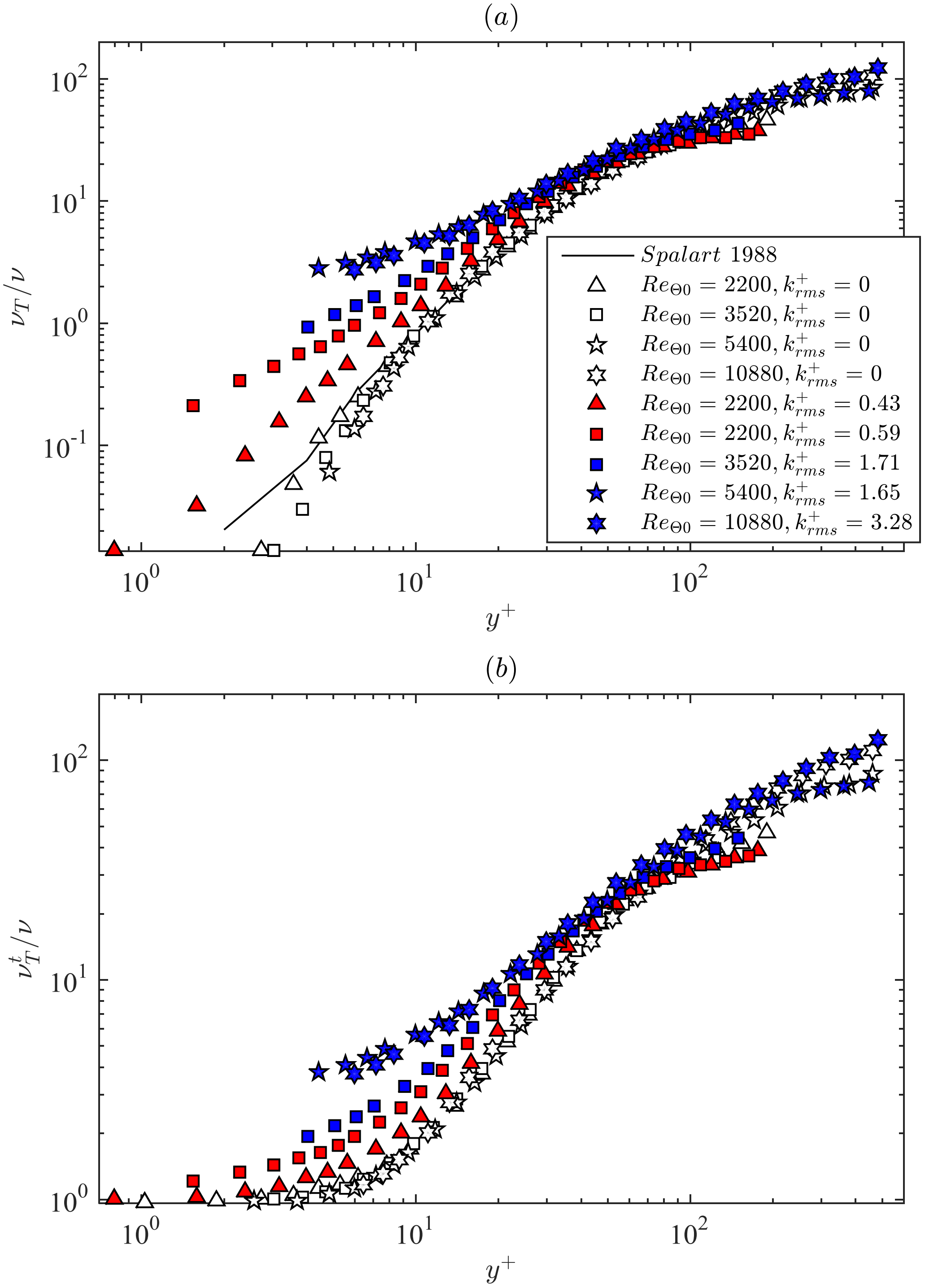

Figure 3.20. Effect of $k_{rms}{}^+$ on eddy viscosity: (a) values based on Reynolds shear stress, and (b) values based on total stress. All profiles are scaled by inner units of each own surface.

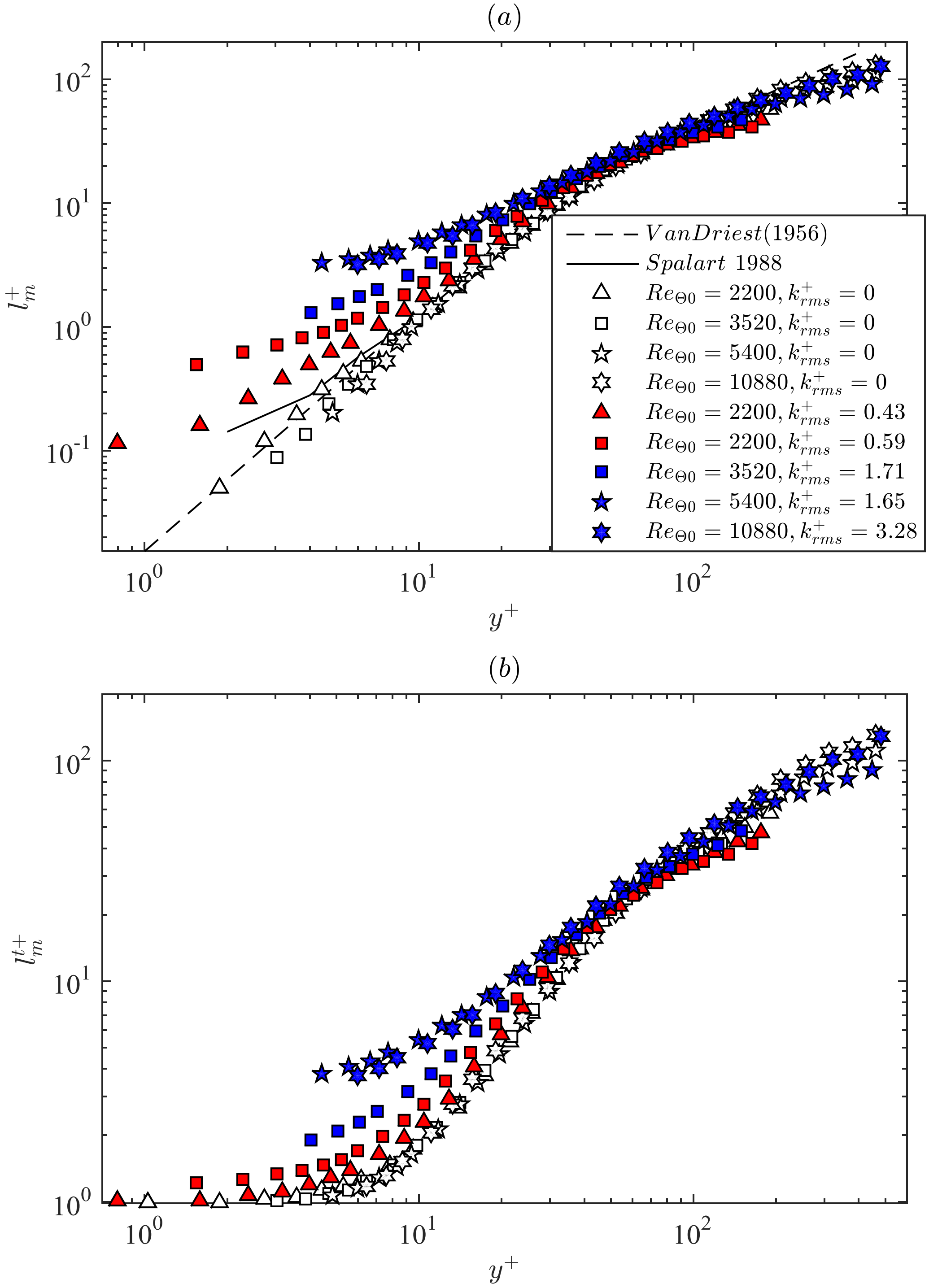

Figure 3.21. Effect of ${k_{rms}}^+$ on mixing length scale: (a) values based on Reynolds shear stress, and (b) values based on total stress. All profiles are scaled by inner units of each own surface.

Sample	p_w, ***atm***	p_w*	$\tau_w{}^{\mu}$, **Pa**	$\tau_w{}^{R}$, **Pa**	τ_w, **Pa**	$\tau_w{}^{Log}$, **Pa**	δ_υ, ***µm***	Re_τ	$\bar{U}_s$, ***m/s***	***DR, %***
△ Smooth	-	-	9.0	0	9.0	9.0	10.5	863	-	-
▲ $\mathrm{SP_{Por}}$	0.97	−0.02	7.9 ±0.0	0 ±0.1	7.9 ±0.1	9.2	11.3	809	0.30 ±0.02	12
● $\mathrm{SP_{Por}}$	1.20	1.33	7.8 ±0.0	0.4 ±0.1	8.2 ±0.1	9.4	11.0	824	0.29 ±0.02	9
★ $\mathrm{ETH_x}$	1.04	0.49	4.9 ±0.0	0.9 ±0.5	5.8 ±0.5	8.1	13.1	693	0.71 ±0.02	36
✶ $\mathrm{ETH_x}$	1.20	2.47	4.1 ±0.0	3.0 ±0.4	7.1 ±0.4	8.6	11.9	767	0.75 ±0.03	21

Table 3.5. Measurement results for SHSs at different pressure levels in the test section, and the corresponding smooth wall at similar Reynolds number. The indicated symbols apply for all the figures in this chapter.

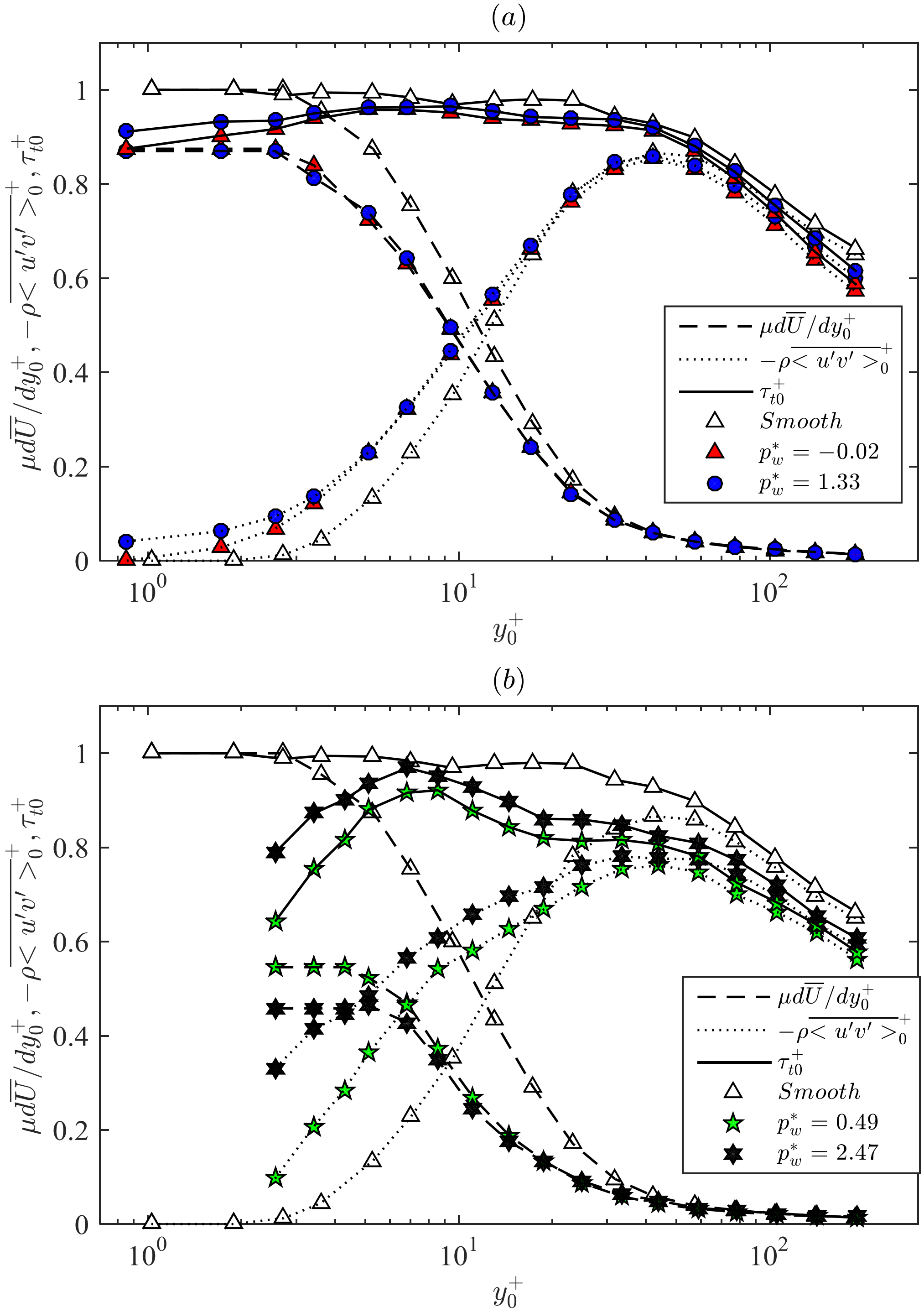

Figure 3.22. Effects of air layer suppression on viscous, Reynolds shear and total stresses profiles for: (a) SP_{Por} and (b) ETH_x. All profiles are normalized by the smooth wall inner scales.

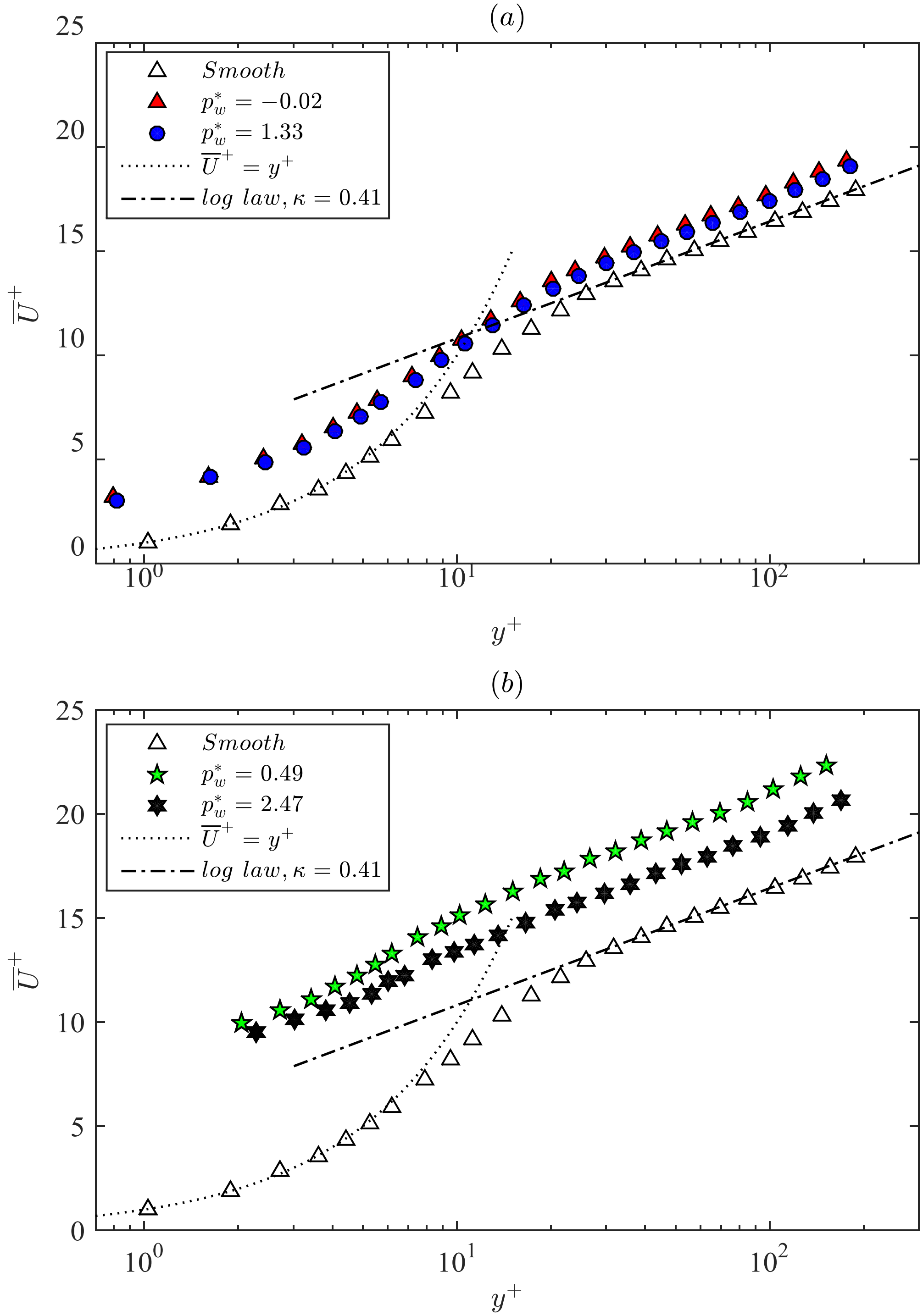

Figure 3.23. Effects of air layer suppression on mean velocity profiles for (a) SP_{Por} and (b) ETH_x. All profiles are normalized by their own inner scales.

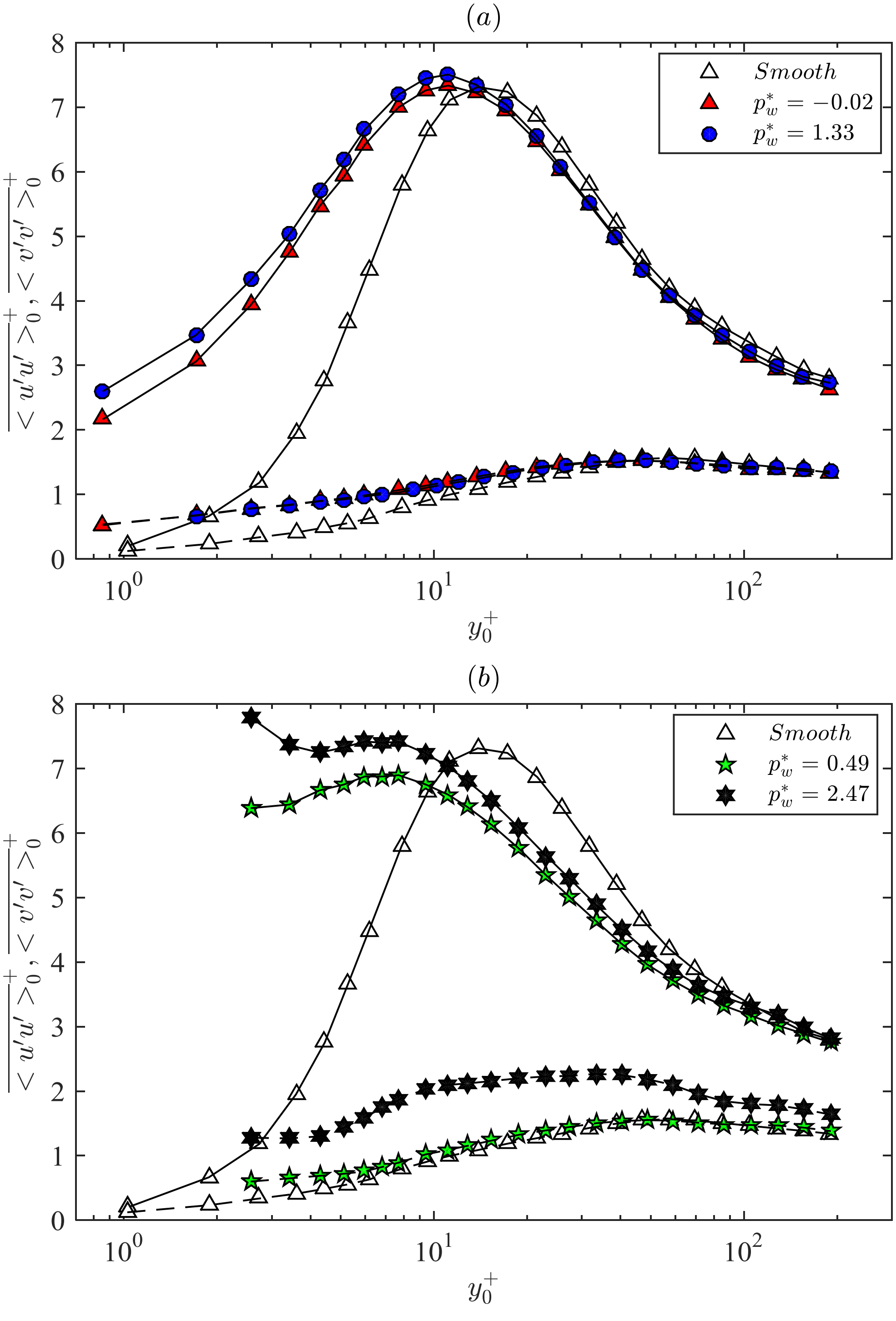

Figure 3.24. Effects of air layer suppression on streamwise and wall-normal velocity fluctuations for (a) SP$_{\text{Por}}$ and (b) ETH$_{\text{x}}$. All profiles are normalized by the smooth wall inner scales.

Sample	***x, mm***	***x/δ_{99}***	***τ_w^{μ}*, Pa**	***τ_w^{R}*, Pa**	***τ_w*, Pa**	***τ_w^{Log}*, Pa**	***δ_υ*, *μm***	***Re_τ***	***$\bar{U}_s$*, *m/s***	***DR, %***
△ Smooth	70	7.7	9.0	0	9.0	9.0	10.5	863	-	-
★ ETH$_x$	70	7.7	4.9 ±0.0	0.9 ±0.5	5.8 ±0.5	8.1	13.1	693	0.71 ±0.02	36
▼ ETH$_x$	35	3.8	4.0 ±0.0	1.7 ±0.8	5.8 ±0.8	9.0	13.1	693	0.73 ±0.02	36

Table 3.6. Measurement results for a same SHS at two different streamwise locations, and the corresponding smooth wall. All cases are measured at U_m=2.1 m/s and δ_{99}=9.1mm.

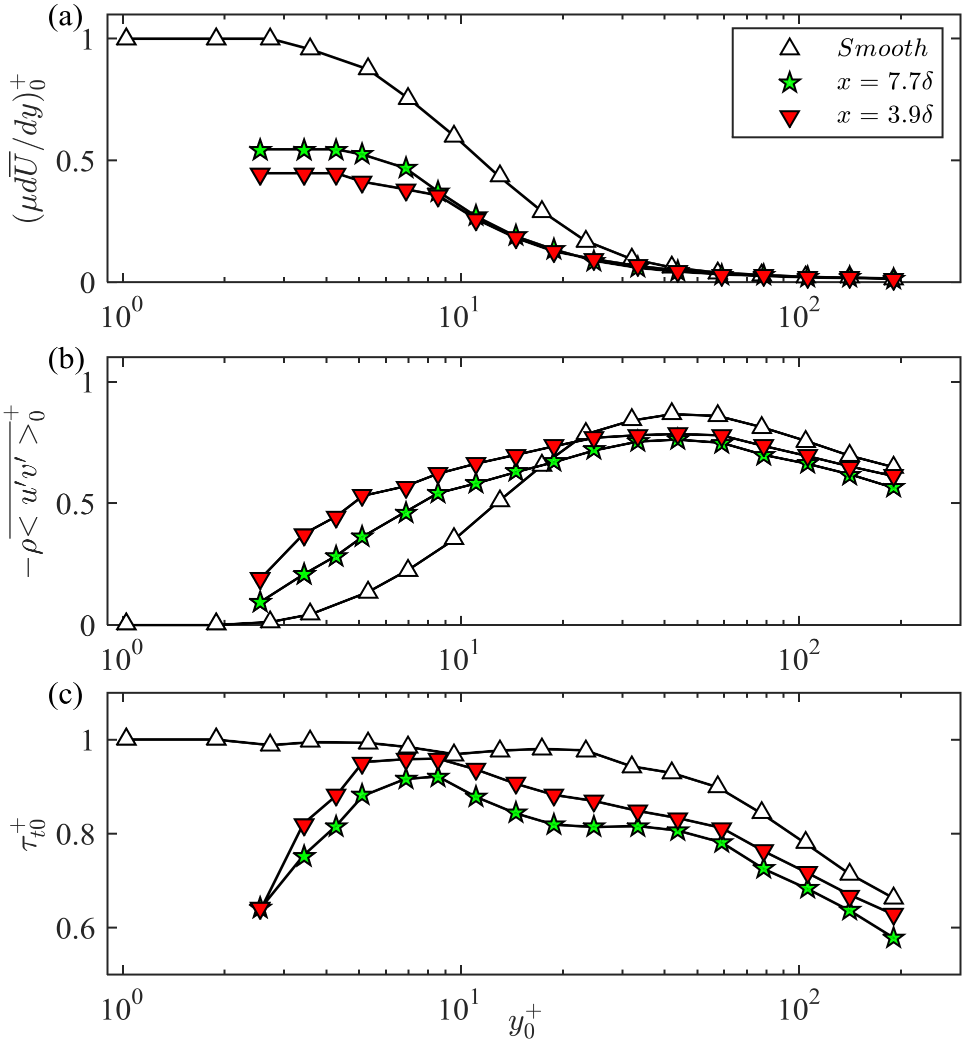

Figure 3.25. Effect of streamwise distance on stress profiles: (a) viscous stress, (b) Reynolds shear stress, and (c) total stress. All profiles are normalized by the smooth wall inner scales.

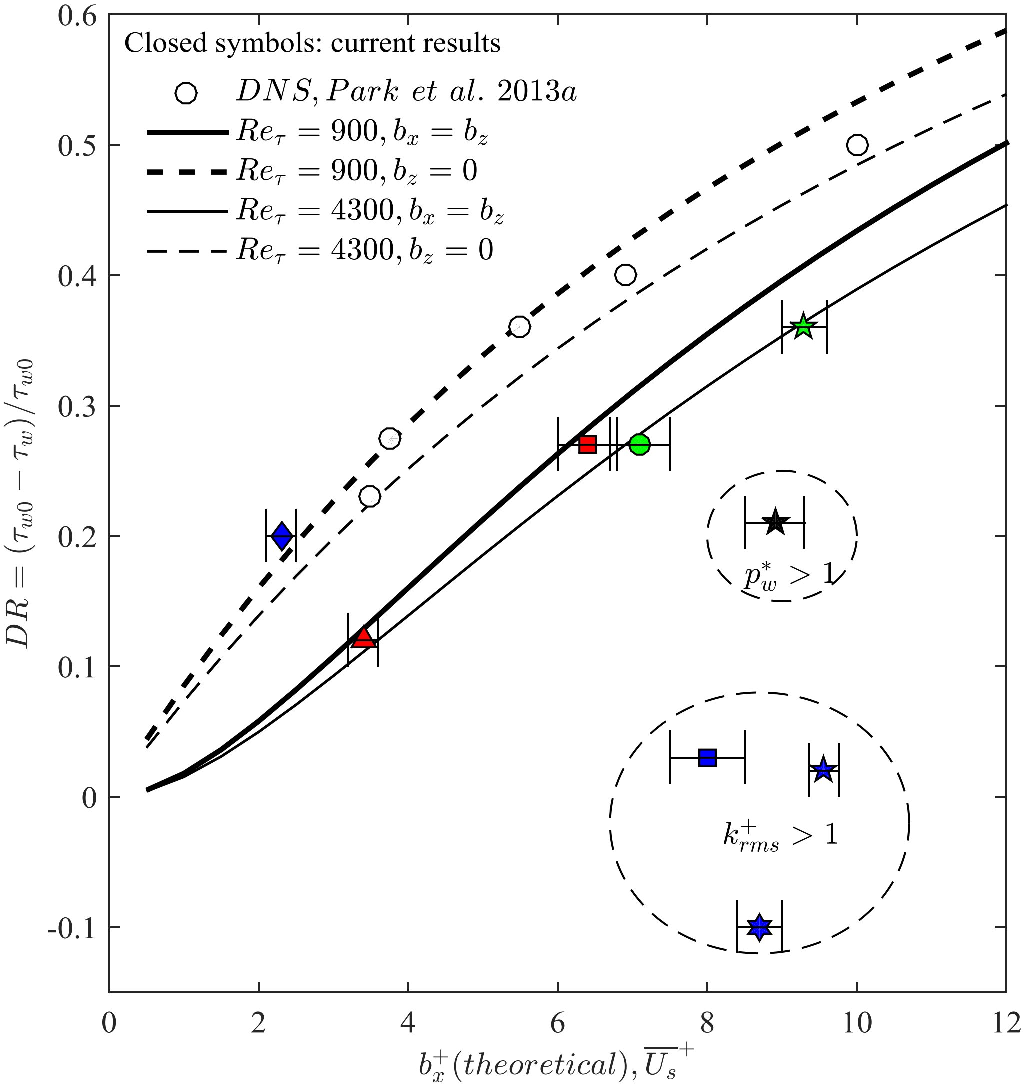

Figure 3.26.Relationship between drag reduction and slip length: closed and color symbols show the current measurements, lines are theoretical prediction by Busse & Sandham (2012), and open circles show DNS results by Park *et al.* (2013a) for broadly spaced streamwise grooves.

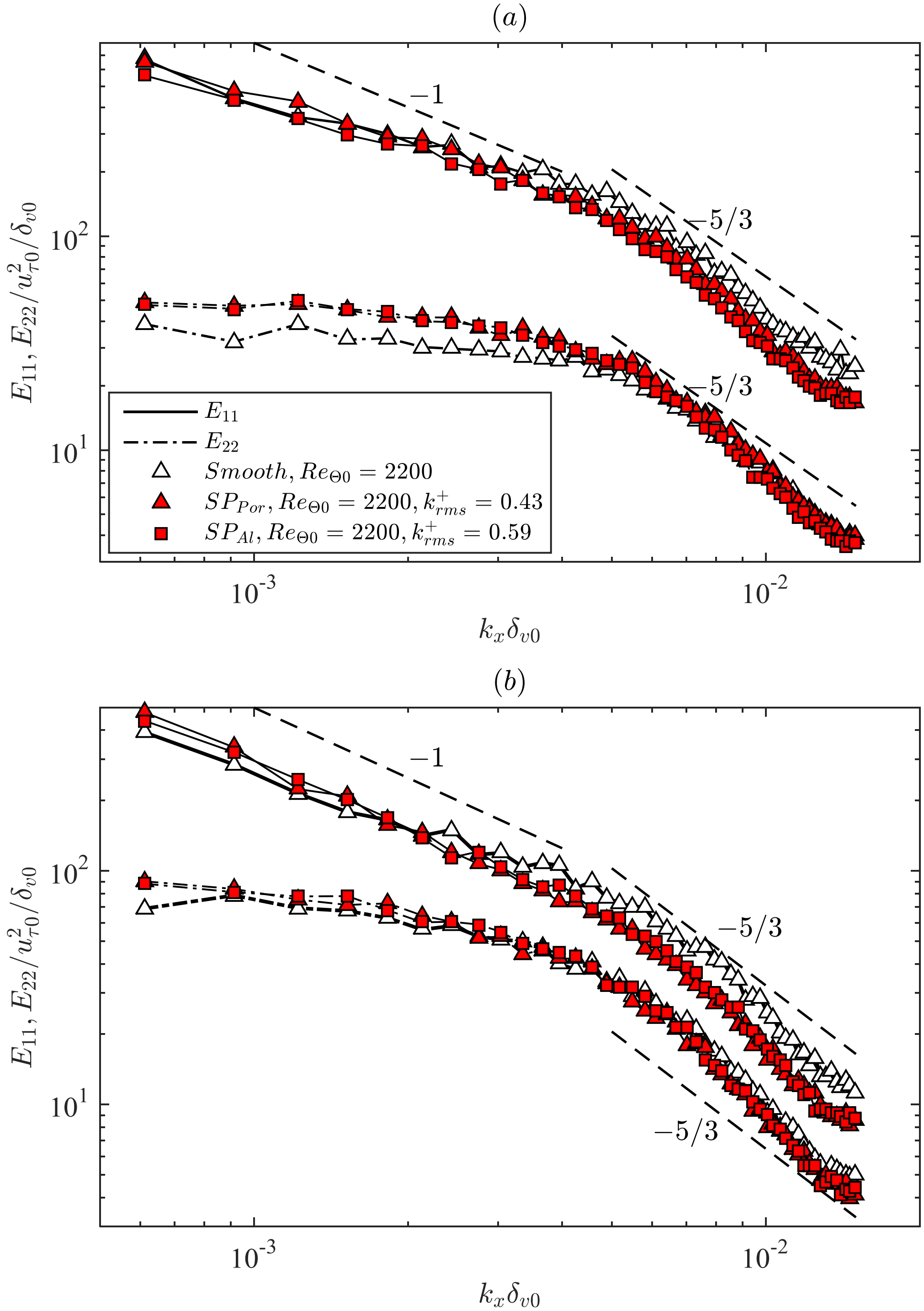

Figure 3.27. Spatial energy spectra, $E_{11}(k_x)$ and $E_{22}(k_x)$, for two drag reduction SHSs and the corresponding smooth wall at (a) $y_0^+ = 30$ and (b) $y_0^+ = 100$.

Chapter 4. Stability and longevity of plastron on super-hydrophobic surfaces

Maintaining a stable air-layer is essential for achieving drag reduction by super-hydrophobic surfaces (SHSs). However, the plastron may be unstable due to effects of hydrostatic pressure, gas diffusion, turbulent flow, and others. In this chapter, the behavior of plastron subjected to these effects will be studied. In section 1, the experimental techniques will be described. In section 2, the behavior of air layer due to an increase and then decrease of hydrostatic pressure will be discussed. In section 3, the effects of saturation level and Reynolds number on gas diffusion out of and into SHSs will be studied. In section 4, the flow-induced vibration of air-water interface in a turbulent boundary layer will be presented. In section 5, the entrainment of an air bubble due to turbulent flow will be described. Finally, one air-layer restoration method by moving an air bubble on the wetted SHS is introduced in section 6.

4.1 Experimental techniques

4.1.1 Flow facility

The experiments are performed in the same high-speed water tunnel used for velocity measurements in the inner part of turbulent boundary layer over SHSs, as described in Chapter 3 and Figure 3.1. Therefore, it is not described again here. The pressure in the test section, p_w, is controlled by connecting a compressor and a vacuum pump to an air-water interface located in a chamber well above the test section (Gopalan & Katz 2000). The value of p_w is monitored by a pressure transducer connected to a tap located at the bottom wall of the test section, 140 mm upstream of the SHS. In the current study, the absolute value of p_w

varies from 0.9 to 1.9 atm. The temperature of bulk liquid is maintained at 23±1 °C, corresponding to p_v=0.03 atm. The concentration of dissolved air in water is inferred from measurement of dissolved oxygen using an optical sensor (FirestingO_2, Pyro Science). The concentrations of O_2 and N_2 in water at atmospheric pressure and temperature of 23 °C, are 8.6 and 14.1 mg/l, respectively, and the ratio between these values is maintained as long as the nearby air composition does not change (Weiss 1970). The sensor is calibrated and the concentration measurements are performed prior to each experiment. The associated uncertainty is ±0.1 mg/l, as specified by the manufacturer. To establish elevated dissolved gas content, air bubbles are injected into the water through a series of 100 μm holes located at the bottom wall of the test section while running the tunnel at U_m=5 m/s and p_w~0.9 atm for about 4 hours prior to each experiment. It should be noted that p_w is the lowest pressure in the facility, and the corresponding pressure in the 1000 l storage tank upstream of the test section is well above the atmospheric pressure (~1.2 atm). Consequently, all the present tests are performed at a concentration of 9.5 mg/l of O_2, corresponding to p_∞=1.10 atm using the Henry constant for oxygen (11.6 atm m^3/g). The total dissolved air concentration is c_∞=25.1 mg/l. Accounting for the vapor pressure, Equation 1.8 indicates that one should expect J>0 when p_w>1.13 atm, and J<0 when p_w<1.13 atm.

4.1.2 Manufacture of super-hydrophobic surfaces

Several types of super-hydrophobic surfaces are involves in this study, as summarized in Table 4.1. It includes the methods of creating the roughness and the material of the hydrophobic coating. The first one a hierarchical SHS consists of nano-textured, ~100 μm wide spanwise grooves, denoted as GROOVE. Figure 4.1(a) shows sample profiles of the grooves of the SHS obtained using confocal laser scanning microscopy. The periodicity of spanwise groove is 200 μm, its height is H=210±35 μm, varying in the spanwise and axial directions, and its width, *w,* decreases from 130 μm at the top to 100 μm at the bottom. The SHS is fabricated on a 2024 aluminum substrate using the following procedures: First, the spanwise grooves are fabricated by a slitting saw. Second, following the procedures described in Kim et al. (2013), nano-textures are generated by boiling the sample in deionized water for approximately 15 minutes. Third, the hydrophobic functionalization is performed by immersing the sample overnight in an ethanol based solution containing 1% (by weight) of Masurf FS100 (Pilot Chemical Co.), a phosphate ester with mixed length of fluorinated alkyl chains (Kim et al. 2013).

The second and third ones are generated by spray coating hydrophobic material onto aluminum and PVC bases, respectively. The hydrophobic material is a mixture of fluorinated silica nanoparticles and fluorinated urethane polyol (PTFE vinyl ether copolymer). The two surfaces are denoted as SP_{Al} and SP_{PVC}. The SEM image of the surface roughness of SP_{Al} is shown in Figure 4.1(b). The fourth and fifth types of SHSs, denoted as SB and SP_{Por}, are generated using the same methods as described in Chapter 3. The same abbreviations are used here. The details of the surface roughness and surface chemistry for these two samples could be found in Table 3.1 and Figure 3.3.

Lastly, a transparent SHS is generated using polydimethylsiloxane, denoted as POST. Since the material by itself is hydrophobic, no additional hydrophobic coating is applied. The roughness geometry is regular posts with a width of 12 μm, a height of 24 μm, and a wavelength 36 μm. The textures are generated by photolithography and shown in Figure 4.1(c). By calculating and comparing the free surface energy between Wenzel and Cassie-Baxter states, one could find that the CB state is not thermodynamically stable for the POST. Indeed, a wetting transition is very easily triggered, e.g., by simply placing a water droplet on top. Thus, the POST will be used only for studying de-wetting transitions in section 6.

4.1.3 Optical setups

Three optical setups with various purposes have been used to study the behavior of the air layer. The first setup is based on total internal reflection, as shown in Figure 4.2. The surface is illuminated at an angle larger than the total reflection angle of light reflected at the air-water interface, i.e., 49°. In the Cassie-Baxter state, the light will be totally reflected and received by the sensor (Figure 4.2a). However, in the Wenzel state, the light will be scattered by the roughness and only a very small fraction will be received by the sensor (Figure 4.2b). Therefore, based on the reflected light intensity, one could distinguish between the Cassie-Baxter and Wenzel states, and qualitatively determine the fraction of surface that is covered by air. Based on this principle, Figure 4.2(c) shows the optical setup. A collimated LED light is used. Images are recorded by a high-speed camera (PCO.Dimax HD). An 8×, infinity corrected, long working distance microscope objective is inserted before the camera to magnify the image and achieve a resolution of 1.3 μm/pixel. The center of the in-focus plane is located at x=70 mm and z=2 mm. This setup will be used for imaging the air layer on SHSs with randomly distributed roughness and under various magnitudes of p_w. Results will be shown in section 4.2. The highest image acquisition rate is up to 40,000 frames per second (fps) for an image size of 1.2×0.3 mm. Therefore, this setup is also used for examining the flow-induced interface vibrations on GROOVE. The corresponding results will be presented in section 4.4.

Taking advantage of the large feature size of the GROOVE, a second optical setup is used to measure the shape of the interface and plastron, as shown in Figure 4.3. All optical components are same as these used in Figure 4.2, except the illumination angle. Here, the surface is illuminated along the spanwise direction, parallel to the air-water interface. Thus the plastron shapes including interface heights and contact angles are able to be measured. By monitoring the time-evolution of interface height and plastron shape, the mass diffusion rate of air is able to be measured. For characterizing the relatively slow diffusion process, the images are recorded at 10 fps. Therefore, this setup is used to study the change of plastron shape due to variation of pressure, as well as mass diffusion. Results will be presented in sections 4.2 and 4.3.

High-speed digital holography has been used to monitor the air layer interface and measure the entrainment rate of air, as sketched in Figure 4.4. Here, the light source is a Q-switched Nd:YLF laser (523 nm) whose output is expanded and collimated to a 10 mm diameter beam. The holograms are recorded by the same high-speed camera at 20,000 frames per second and at a resolution of 11 μm/pixel. The sample volume is centered at x=70 mm, and has a streamwise length of 9.5 mm, a wall-normal height of 2.5 mm, and a depth of 50 mm, the latter covering the entire depth of the water tunnel. To measure the size distribution of bubbles and their cumulative volume, the holograms are reconstructed every 100 μm. The 3D intensity field is subsequently collapsed into a single plane, where each pixel has the minimum intensity (darkest) over the entire depth. The collapsed image is thresholded and segmented to identify each bubble and obtain its size. The flux of bubbles is calculated by dividing the cumulative volume of all the bubbles in the sample volume, averaged over eight realizations, by the time that is required for them to pass through the sample volume. This time is estimated by dividing the length of the sample area by the height-dependent mean streamwise velocity of the fluid. This flux is used for estimating the rate of bubbles entrained from the upstream 70 mm of the porous surface (3,500 mm^2). This estimate is smaller than the actual entrainment rate since some of the bubbles might be lifted to elevations located above the sample volume. However, by tracking the vertical bubble flux at different elevations and determining that it is negligible at the top of the sample volume, and by insuring that the buoyancy alone is insufficient to lift the bubbles away from the field of view, the overwhelming majority (>99%) of the bubbles entrained from the wall remain inside the sample volume. It should also be noted that without the air layer, there are no freestream bubbles with resolvable sizes near the bottom wall. The entrainment rate of the bubbles is then divided by the surface area and U_m to obtain the dimensionless, spatially and time averaged air velocity $U^*_{a\mathrm{ir}}$. Results will be presented in section 4.5.

4.1.4 Boundary layer characterizations

Although the detailed velocity distributions are not of primary interest in a study focusing on plastron behavior, we have measured the characteristic length scales of the boundary layer for the purpose of developing empirical relations between the Sherwood number (*Sh*) and Reynolds number (*Re*). In the current study, the mean tunnel speed (flow rate divided by the tunnel cross section), U_m, varies between 0.65 to 2.2 m/s, as measured using an electromagnetic flow meter. The velocity profile in the boundary layer in the abovementioned imaging region is characterized by 2D particle image velocimetry (PIV) at a resolution that covers the entire boundary layer, and dual-view digital holographic microscopy (DHM) at a magnification that fully resolves the flow structure in the inner part of the boundary layer (Ling et al. 2016). In the PIV measurements, the instantaneous velocity in the x-y plane is calculated using an in-house developed code (Roth & Katz 2001) to calculate the spatial cross-correlations using a rectangular interrogation window of size 346μm×86μm (x×y). With 50% overlap between windows, the vector spacing is 173 μm×43 μm. The field of view is 36×24 mm^2 (x×y). For DHM measurements, the instantaneous velocity is calculated using particle tracking velocimetry, followed by first-order Taylor series expansion and singular value decomposition (Ling et al. 2016, Sheng et al. 2008, Talapatra & Katz 2013) to interpolate the data onto 3D regular grids with spacing of

120μm×10μm×240μm (x×y×z). The field of view is 4.4×2.4×3.2 mm^3 (x×y×z). For both PIV and DHM, the mean flow quantities are obtained by local ensemble-averaging over more than 500 realizations, followed by spatial averaging in the x direction for the PIV data over 205 lines, and in the x, and z directions for the DHM data over 468 profiles.

Baseline PIV measurements for a smooth wall have been performed at the same location by replacing the SHS with a solid surface. The data are used for estimating the wall friction by a fit to the log layer in the turbulent Reynolds number range and by a fit to the mean velocity profile near the wall for the transitional case, taking advantage of the relatively larger length scales. The baseline mean flow quantities for four different U_m are listed in Table 4.2, including U_0 - the free stream velocity at the top of the boundary layer, δ_{99} - the boundary layer thickness based on 99% of U_0, Θ - the momentum thickness obtained by integrating the velocity profile, τ_w - the wall shear stress, $\delta_v=\nu(\rho_w/\tau_w)^{1/2}$ - the viscous length scale, where ρ_w is the liquid density, as well as $Re_\Theta=U_0\Theta/\nu$, and $Re_\tau=\delta/\delta_v$. The range of Re_Θ, 518-2088 covers both the transitional and turbulent regimes, as confirmed later in this paper.

The DHM measurement has been used for determining the τ_w of the GROOVE in the CB state at U_m=2.13 m/s. Following the procedures described in Chapter 3, τ_w is calculated by summing the Reynolds shear stress at the top of the grooves and the viscous stress ($\rho_w\nu dU/dy$), where the velocity gradient is determined by a linear fit to the mean velocity profile at y<60 μm. Results are denoted as GROOVE$_{\mathrm{CB}}$, and summarized in Table 4.2. It shows a 4% reduction of wall friction. PIV has been utilized for measuring the mean velocity profiles over the GROOVE in the Wenzel state, after wetting the SHS at high pressure. The results are denoted as GROOVE$_{\mathrm{W}}$ in Table 4.2. In these cases, τ_w are estimated from a logarithmic fit to mean velocity profile at $30<y/\delta_v<120$, similar to the procedures used for the baseline cases. This estimate may differ from the true wall friction due to the short distance

(x=8δ) from the front of the grooved surface (Lee 2015, Ling et al. 2016). For an SHS where the roughness effect is dominant, Ling *et. al.* (2016) show that at x=4δ, τ_w estimated from a log law fit is 12% higher than the directly measured value. For spanwise grooves with H/δ_v~40, i.e., similar to the present highest Re_Θ case, direct numerical simulations (DNS) by Lee (2015) shows that the equilibrium log layer is established at x>7δ. Therefore, the log fit based estimate of the τ_w is reasonable for the purpose of evaluating the associated Reynolds numbers. As is evident, for case U_m=2.11 m/s, τ_w at the Wenzel state is 70% higher than that of the CB state for the same surface, speed and location. The 2D PIV measurements have also been performed for the CB state at U_m=2.13 m/s for calculating the boundary layer length scales and the corresponding Reynolds numbers. In this case, the smooth wall and CB results do not differ significantly, and as shown in Table 4.2.

Figure 4.5 presents baseline wall friction coefficient, $f_0=2\tau_{w0}/(\rho_w U_0^2)$, as a function of $Re_{\Theta 0}$ based on the quantities listed in Table 4.2. Here and in the following sections, a subscript 0 denotes quantities measured for the baseline flow at the same U_m. The measured magnitudes and trends agree well with the DNS data of Wu and Moin (Wu & Moin 2010), which is also plotted. For $Re_{\Theta 0}\geq 900$, the values of f_0 fall on the classical power law $f_0 \sim Re_{\Theta 0}^{-0.25}$ (Smits et al. 1983) confirming that the boundary layer is turbulent. For the lowest Reynolds number, $Re_{\Theta 0}$=518, the magnitude of f_0 is significantly lower than the turbulent power law prediction and higher than trends of a laminar boundary layer, indicating, consistent with the DNS results, that the boundary layer is transitional.

Figure 4.6 shows four sample mean velocity profiles scaled with inner variables, $U^+(y^+)$, where $y^+=y/\delta_v$, $U^+=U/u_\tau$, and $u_\tau=(\tau_w/\rho_w)^{1/2}$. Here, and in the following discussions, the subscripts CB and W denote quantities measured for SHS in Cassie Baxter and Wenzel states, respectively. Included are baselines cases at $Re_{\Theta 0}$=518 and 2088, GROOVE$_\mathrm{W}$ at $Re_{\Theta \mathrm{W}}$=1968, as well as two GROOVE$_{CB}$ results measured at U_m=2.13 m/s. The first is obtained using DHM and focuses on the inner part of the boundary layer, and the second is based on the 2D PIV data, for which $Re_{\Theta CB}$=2080. Since the profiles collapse into each other in overlapping elevations, we refer to both using the same Reynolds numbers. As expected, the baseline profile at $Re_{\Theta 0}$=2088, for which the PIV data do not resolve the inner part of the boundary layer, collapses onto the classical log law for $30<y^+<120$. Conversely, at $Re_{\Theta 0}$=518, the near wall profile ($y^+<10$) agrees with that of a laminar boundary layer, which is also shown, but falls between the laminar and log law profiles at higher elevations. The GROOVE$_{CB}$ profile is shifted upward slightly in the log region and significantly in the viscous sublayer compared to baseline case, consistent with the 4% reduction in wall friction. Such an upward shift has been observed for simulated or measured drag reduction cases (Ling et al. 2016, Min & Kim 2004). In contrast, the GROOVE$_W$ profile is shifted downward significantly, consistent with trends of rough wall boundary layers (Jimenez 2004). The difference between the GROOVE$_{CB}$ and GROOVE$_W$ results demonstrate the effect of the plastron since the surface and freestream velocity are identical.

4.2 Hydrostatic pressure effects

In this section, the effect of pressure on the SHS state is examined initially *without flow*. The experiment consists of gradually increasing p_w from 1.0 to 1.9 atm and then decreasing p_w back to 1.0 atm. At certain pressure level, the status of the interface is measured after keeping the pressure at this level for more than 10 s. The interface is recorded by either total internal reflection (Figure 4.2) for randomly roughed SHSs or direct imaging (Figure 4.3) for GROOVE. The entire cycles usually last for 30 to 60 mins. Since the molecular diffusion coefficient is very small (~10^{-9} m^2/s) in stationary liquid, one should expect little mass diffusion in and out of the plastron during this experiment.

4.2.1 Hydrostatic pressure effect on GROOVE

Firstly, the effects of hydrostatic pressure on GROOVE are studied by direct imaging (Figure 4.3). Figure 4.7(a) provides a series sample characteristic images of the plastron. During this process, the time evolution of θ_{CL} (averaged value of two sides) and the averaged interface height at the contact line, h_{CL}, are measured as shown in Figures 4.7(b) and (c). Both are illustrated in one of the images in Figure 4.7(a). The low mass diffusion in stationary liquid has been confirmed by using the plastron shape (Figure. 4.7a) for calculating and comparing the volume of gas in the plastron at the beginning and at the end of the experiment (after 51 minutes), keeping in mind that the liquid is undersaturated most of the time. The volumes differ by less than 5%, which is barely above the uncertainty level. Hence, we neglect the effect of mass diffusion in the following discussion.

The response of interface to the increase of p_w is similar to the previously reported confocal microscopy based measurements (Lv et al. 2014), and conceptual description provided in (Bartolo et al. 2006). At relatively low pressure, $1.0<p_w<1.3$ atm, θ_{CL} gradually increases to a maximum of θ_{adv}=150°, while the contact line is pinned at the tip of groove, i.e., $h_{CL}=H$. Consistent with (Verho et al. 2012, Xue et al. 2012), the magnitude of θ_{adv} for the present hierarchical SHS is larger than the typical values of 110°-120° observed for single-level topographies (Checco et al. 2014, Extrand 2011, Kwon et al. 2011, Papadopoulos et al. 2013, Zheng et al. 2005). With increasing pressure to the $1.3<p_w<1.9$ atm range, the contact line de-pins from the tip of the groove while the interface shape remains nearly unchanged, with $\theta_{CL}\approx\theta_{adv}$.

When p_w is subsequently reduced, the plastron recovers. However, the process is not symmetric, i.e., the interface does not recover to the same shape when p_w returns to the original level. Once p_w starts decreasing, θ_{CL} decreases immediately, unlike to the compression phase, and h_{CL} increases gradually. Once p_w reaches 1.30 atm, the interface is nearly flat, i.e., θ_{CL}~90°. Further reduction in p_w to the original pressure creates a convex interface, i.e., $\theta_{CL}<90°$. From the image at t=51 min, it appears that the contact point of the interface is located slightly below the tip of groove, presumably due to variations in the shape of the tip. These findings are quantitatively consistent with the confocal microscopy results reported by Xue *et. al.* (2015) for a dimpled surface, including the asymmetry in contact angle for downward and upward migrations of interface.

4.2.2 Hydrostatic pressure effect on SHSs with random roughness

Here, the effects of hydrostatic pressure on SHSs with randomly distributed roughness are studied by using total internal reflection (Figure 4.2). Figure 4.8(a) provides a series sample characteristic images of the plastron on SP_{Al} during increasing and then decreasing of p_w. The value of k_{rms} is 3 μm for 4.8(a). As expected, at relatively low pressure (p_w<1.60 atm), the surface is bright indicating the uniform coverage of air layer. However, when p_w=1.78 atm, the surface becomes totally dark, indicating the transition to the Wenzel state. There are two possible reasons that cause such a transition. First, the interface may touch the bottom of the surface topography at high p_w. The second reason may due to diffusion of gas. As reducing pressure to the original value (p_w=1.06 atm), the surface remains dark. The irreversible transition may be caused by a single length scale of roughness or diffusion of gas into the liquid. Indeed, using confocal microscopy, Verho et al. 2012 show that a surface with single-level topography is not able to recover the CB state after fully wetting, while a surface with two-level topography (combining of micro- and nano-scale roughness) is able to restore the CB state due to the existence of nano-scale plastron. Figure 4.8(b) shows the state of the plastron on a second SP_{Al} with k_{rms}=6 μm. The surface fabricated using the same method as the one showed in Figure 4.8(a), and the only difference is the magnitude of k_{rms}. Comparing between Figures 4.8(a) and (b), it indicates that a plastron is able to survive at higher pressure by increasing the magnitude of k_{rms}. At the current highest magnitude of p_w=1.90 atm, the plastron still exists as shown in Figure 4.8(b).

After the surface is fully wetted, it is taken out from the facility. It should be noted that the SP_{Al} is not able to restore its super-hydrophobicity even after drying the surface in air or after exposing it to a vacuum condition. The reason needs to be further studied. We have performed the same test for another SHS which is generated on a PVC base, SP_{PVC}, instead of an aluminum base. The coating material is the same as SP_{Al}. Using the same method, the SP_{PVC} is wetted at high pressure. When it is taken out of the facility and exposed to air, the contact angle of droplet is very low (Figure 4.9a). However, after drying the surface in air, it recovers the super-hydrophobicity (Figure 4.9b). Therefore, the base material makes a difference, but the reason is unclear.

Figures 4.10(a) and (b) show the sample characteristic images of the plastron on SB during increasing and then decreasing of p_w. The only difference between Figure 4.10(a) and (b) is the size of surface topography. For Figure 4.10(a), the micro-pores are generated by sandblasting with sandpaper of grit size of 150. While for Figure 4.10(b), the grit size of the sandpaper is 80, which generates larger and taller roughness elements. Consistent with the results shown in Figures 4.8(a) and (b), the plastron with taller roughness elements (Figure 4.10b) could sustain higher pressure than the one with shorter height.

4.3 Mass diffusions of gas out of and into SHSs

As expected from Equation 1.8, gas diffuses out of SHS into the liquid ($J>0$) when $p_w-(p_v+p_\infty)>0$, resulting in a wetting transition. On the other hand, gas diffuses into SHS

($J>0$) when $p_w-(p_v+p_\infty)<0$, which may cause a de-wetting transition. Here, p_v is the vapor pressure of water in the plastron, and p_∞ corresponds to a reference pressure $p_\infty=k_Hc_\infty$. As has been discussed in the previous section, $p_v+p_\infty=1.13$ atm. By varying the magnitude of p_w above or below 1.13 atm, a wetting or de-wetting transition will be observed. The previous section shows that the diffusion rate in stationary liquid is very slow. To accelerate the diffusion process, all the following measurements are performed with flow ($U_m>0.5$ m/s). The SHS involved in this section is the GROOVE. The magnitude of J will be measured as a function of p_w and Reynolds number.

Firstly, the variation of plastron shape due to mass diffusion out of the plastron is summarized in Figures 4.11(a)-(c). Prior to each measurement series, p_w is set to a level above p_v+p_∞, and then the water tunnel speed is increased and then held at constant. For the samples shown, $p_w-(p_v+p_\infty)=0.23$ atm and $Re_{\Theta 0}=518$. At the initial state ($t=0$), the plastron is still pinned to the tip of the groove. Since $J>0$, the plastron slowly loses gas resulting in a decrease in h_{CL} and the interface height at middle of the groove, h_m, defined in the sample image of Figure 4.11(a), as well as an increase in θ_{CL}. The quantitative results are presented in Figures 4.11(b) and 4.11(c), and the evolution of interface shape is shown in the insert of Figure 4.11(c). The entire process could be separated into three stages. The first stage, which is denoted as 'I', occurs at $t<60$ s. It is characterized by a pinned plastron, hence unchanged h_{CL}, as well as a gradually increasing θ_{CL} to $\theta_{adv}=150°$, and a corresponding slight decrease in h_m. During the second stage II, which takes place at $60<t<320$ s, the plastron is de-pinned, h_{CL} and h_m decrease at similar rates, and θ_{CL} remains nearly constant. At stage III, the interface touches the bottom of the groove, i.e. $h_m=0$, and the two gas pockets remaining in the corners continue to shrink with h_{CL} decreasing at a slower rate. At $340<t<350$ s, the plastron is hard to quantify, and the shrinkage of h_{CL} appears to accelerate to nearly zero. The values of θ_{CL} during 'III' are similar to stage 'II'. At the present magnification, the pockets become invisible at t=350 s. We cannot measure whether residual pockets remain with the nano-textures, but nano plastrons are likely to persist given that the corresponding values of surface tension-induced pressure differences have magnitudes of several atmospheres.

Next, the flow in the tunnel is stopped, and the pressure is reduced to a level below p_v+p_∞, and kept at constant for about 10 min. Although the water is supersaturated, there is no evidence of plastron growth at the present imaging resolution, presumably due to the slow diffusion rate in a stationary liquid. Then, the velocity is increased back and maintained at $Re_{\Theta 0}$=518, resulting in a slight decrease in test section pressure to $p_w-(p_v+p_\infty)=-0.07$ atm. The plastron recovery can also be divided to several stages. During stage I, the nucleation stage, small bubbles appear in a few seconds near the corner of the groove, as shown in Figure 4.12(a). Figure 4.12(b) presents the evolution of the bubble radius for three sample cases, including the one corresponding to Figure 4.12(a). Initially, the plastron grows radially from one of the two corners. The duration of this growth phase varies among different locations, falling in the 6s to 65s range for the present samples. Once the bubble reaches the other corner, it flattens in a couple of seconds, and then continues to grow while the interface remains large horizontal. The subsequent evolution of the plastron corresponding to sample 3 of Figure 4.12(b) is summarized in Figures 4.12(c)-(d). Included are plots of h_{CL}, h_m, θ_{CL}, and measured schematics of plastron shape. During stage II, the plastron reaches the so-called metastable stage (Lv et al. 2014), where it grows with θ_{CL}=90° and $h_{CL}\sim h_m$. The growth rate is faster initially (t<200 s), and then becomes nearly constant at 200<t<600 s. Subsequently, during stage III, the top of the plastron reaches at least one of the corners, and becomes pinned to the tip of the grooves. Hence, a CB state is reached, where the magnitudes of h_{CL} and h_m diverge, and θ_{CL} decreases as the interface becomes convex. The present trends during stage III, i.e. starting from a pinned contact line in a CB state, are qualitatively consistent with those observed before for dimpled surfaces in a laminar flow by Dilip *et. al.* (2014).

The above measurements of plastron change due to gas diffusion have been repeated for $p_w-(p_v+p_\infty)$ ranging from −0.07 to 0.23 atm, as well as four different $Re_{\Theta 0}$, as listed in Table 4.2. The effect of p_w on the diffusion rate at the same $Re_{\Theta 0}$=518 is summarized in Figures 4.13(a)-(e). Figure 4.13(a) shows the evolution of h_m. As expected, h_m decreases for $p_w>(p_v+p_\infty)$ and increases for $p_w<(p_v+p_\infty)$. The growth or decay rate increases with the magnitude of $p_w-(p_v+p_\infty)$. Figure 4.13(b) shows characteristic time scales for wetting and de-wetting transitions during stage II, i.e., when h_m is changing while θ_{CL} remains nearly constant. To insure that the measurements are repeatable and the interface can be clearly detected, the time scale for wetting corresponds to h_m/H varying from 0.7 to 0.4, and the dewetting duration is based on h_m/H increasing from 0.6 to 0.9. These choices avoid the initial periods when the plastron changes its shape or the initial bubble growth period, and reflect the same change in volume. The results, denoted as τ_{tr}, are plotted in Figure 4.13(b), with the error bars reflecting the uncertainty in plastron height measurements. As expected, τ_{tr} decreases with increasing magnitude of $p_w-(p_v+p_\infty)$, consistent with previous observations for stationary liquids (Bobji et al. 2009, Lv et al. 2014, Poetes et al. 2010, Samaha et al. 2012b). Figure 4.13(c) shows the evolution of the same h_m/H, but now as a function of non-dimensionalized time, $(t-t_0)/\tau_{tr}$, where t_0 is selected as the time when h_m/H=0.7 and 0.6 for the wetting and de-wetting processes, respectively. As is evident, the four wetting profiles collapse onto each other, and so do the two de-wetting results.

Then, the magnitude of gas flux (J), can be estimated as $J=\rho_{air}\Delta h_m/\tau_{tr}$, where ρ_{air} is the density of air calculated from the pressure and temperature assuming ideal gas, and Δh_m is the change in interface height. The effects of evaporation and condensation of water on the plastron volume are neglected since the gas to vapor molar ratio is not expected to change as long as the temperature remains constant. Figure 4.13(d) shows the calculated values of J for varying $p_w-(p_v+p_\infty)$, all for the same Reynolds number. As expected from Equation 1.8, the present measurements confirm the linear relationship between J and $p_w-(p_v+p_\infty)$ for both wetting and dewetting transitions. The slope of this line, estimated by a least-square-fit, can be used for calculating the diffusion length scale, $\delta_c=D(p_w-p_v-p_\infty)/(Jk_H)$. To normalize δ_c, we opt to use the momentum thickness of the smooth wall at the same freestream velocity (Θ_0) since the actual boundary layer thickness might change with interface height. As Table 4.2 indicates, there is a 5% difference between the momentum thicknesses corresponding to smooth and Wenzel state boundary layers for the same freestream velocity. This choice is discussed further later. The resulting Sherwood number is then:

$$Sh_{\Theta 0}=\Theta_0/\delta_c=Jk_H\Theta_0/[D(p_w-p_v-p_\infty)] \tag{2}$$

As is evident from Figure 4.13(e), the magnitude of $Sh_{\Theta 0}$ does not change with pressure at $Re_{\Theta 0}=518$ within the present uncertainty level.

The effect of $Re_{\Theta 0}$ on the rate of gas diffusion during wetting at a constant $p_w-(p_v+p_\infty)=0.08$ atm is summarized in Figures 4.14(a)-(d). As is evident from Figure 4.14(a), the wetting rate increases with increasing $Re_{\Theta 0}$. Yet, Figure 4.14(b) demonstrates that all the height profiles collapse when plotted as a function of $(t-t_0)/\tau_{tr}$. By calculating J and δ_c, following the procedures described above, Figure 4.14(c) shows that the magnitude of $Sh_{\Theta 0}$ increases with increasing $Re_{\Theta 0}$. For $Re_{\Theta 0}>800$, i.e., when the boundary layer is turbulent, the data suggest a power-law relationship, $Sh_{\Theta 0}=0.47Re_{\Theta 0}^{0.77}$. This relationship is consistent with the typically observed trend for mass diffusion in a turbulent boundary layer over flat plate, namely $Sh_x \propto Re_x^{0.8}$ (Sharma & Rahman 2002), which corresponds to $Sh_{\Theta 0} \propto Re_{\Theta 0}^{0.77}$, assuming that $\Theta_0/x \propto Re_x^{-0.1341}$ (Nagib et al. 2007). Here, $Sh_x=x/\delta_c$, and $Re_x=U_0x/\nu$. According to (Sharma & Rahman 2002), this power-law is valid for a wide range of Schmidt numbers ($Sc=\nu/D$), namely $0.5 \leq Sc \leq 1000$, including the current value of 500. For $Re_{\Theta 0}=518$, i.e., when the flat plate boundary layer is transitional, the magnitude of $Sh_{\Theta 0}$ is lower than that predicted by turbulent power law. This lower mass diffusion rate appears to correspond to a lower wall friction, as shown in Figure 4.5. When the results are replotted as a function of $Re_{\tau 0}$, Figure 4.14(d) shows that both transitional and turbulent flow regimes give the same power law $Sh_{\Theta 0}=0.34Re_{\tau 0}^{0.913}$. This relationship can be predicted for the turbulent regime using $Sh_{\Theta 0} \propto Re_{\Theta 0}^{0.77}$ (Figure 4.14c) and $Re_{\tau 0} \propto Re_{\Theta 0}^{0.843}$ (Schlatter & Örlü 2010). The collapse of the transitional and turbulent flow data suggests that the Sherwood number is predominantly a function of the wall friction.

However, we should recall that the CB, Wenzel and smooth friction Reynolds numbers are different (Table 4.2). The present flux measurements have been performed at the transition between CB to Wenzel states, when the groove is partially filled. For the present case where the wall friction has been measured directly in the CB state, corresponding to $Re_{\tau 0}=820$ (Table 4.2), the CB and smooth wall values of Re_Θ and Re_τ are close to each other. Hence, the same functional relationship is relevant when the groove is filled with air. Presenting the results using the Wenzel state momentum thicknesses, Figure 4.14(c) confirms that the $Sh_\Theta=0.47Re_\Theta^{0.77}$ relation is not affected since the Θ is included in both parameters. Conversely, relying on the log layer curve fit to estimate the Wenzel state $Re_{\tau\mathrm{W}}$, notwithstanding the uncertainty involved, Figure 4.14(d) shows that the power relation changes to $Sh_{\Theta\mathrm{W}} \propto Re_{\tau\mathrm{W}}^{0.70}$ for the turbulent cases.

4.4 Interface vibration in turbulent boundary layers

In this section, the flow-induced vibrations of the interface in turbulent boundary layers are studied. The SHS involved in this study is GROOVE. The interface is visualized by total internal reflection, as shown in Figure 4.2. The Cassie-Baxter state is maintained by controlling $p_w - p_v - p_\infty < 0.01$ atm such that the effect of mass diffusion could be neglected. Figure 4.15 shows a time sequence of the intensities, $Q(x, z, \mathrm{t})$, reflected from the air-water interface. In this case, U_m=2.1m/s, and p_w=1.10 atm. A downstream transport of deformation is clearly observed.

In order to calculate the convection speed of the deformation, denoted as U_c, the values of $Q(x,z,\mathrm{t})$ are spanwise averaged to obtain $<Q>_z(x,\mathrm{t})$. Figures 4.16(a) and (b) show two samples of $<Q>_z(x,\mathrm{t})$ at two different times. Each shows a deformation pattern that transports downstream at a nearly constant speed. By fitting the peaks of $<Q>_z(x,\mathrm{t})$ for each groove (the time when the deformation is the strongest), one could estimate the magnitude of U_c. For sample, as shown in Figure 4.16(a), $U_c=0.74U_0$. The time scale for each groove to recover is $\tau \sim 0.8$ ms. Combining the velocity and time scales, one could estimate the size of the corresponding turbulent structure which causes this vibration, $L_c=\tau U_c=120\delta_v$. For sample showing in Figure 4.16(b), $U_c=0.52U_0$, $\tau\sim 0.3$ ms and $L_c=30\delta_v$. Clearly, the size and convection speed of these turbulent structures are very similar to those of log-layer turbulent eddies. Using Mach-Zehnder interferometry, Zhang et al. (2017) have measured a very similar convection speed of the deformation of a compliant wall in a turbulent channel flow.

To calculate the deformation spectrum, the values of $Q(x,z,\mathrm{t})$ of a single groove are spanwise and streamwise averaged to obtain $<Q>_{x,z}(\mathrm{t})$. Then a fast Fourier transform is used to calculate the energy spectrum, $E_{QQ}(f)$, where f is the frequency of the deformation. Figure

4.17(a) shows two energy spectra at two different mean tunnel speeds, U_m=1.06 and 2.11 m/s (other boundary layer quantities is referred to Table 4.2). Corresponding to higher pressure fluctuations at higher U_m, the spectrum at U_m=2.11 m/s has higher amplitudes in all frequencies than that at U_m=1.06 m/s. It should to be noted that the deformation spectra should be similar to the wall pressure spectra, except those at the high frequency regions due to the finite size of the groove. Yet, the slopes of E_{QQ} increase with wavenumber, similar to the wall pressure spectra, and they transition from the turbulence production range (slope −1) to the inertial subrange (slope −7/3). When normalizing the frequency by inner scales, $f^*=f\upsilon/u_\tau^2$, the two spectra fall on top of each other as shown in Figure 4.17(b), similar to the collapse of wall pressure spectra when normalized by inner scales. Moreover, there are distinctive peaks at f~3000 Hz for U_m=2.11 m/s and f~4000 Hz for U_m=1.06 m/s, which might due to the resonance of the plastron. Detailed analysis of the interface vibration is further needed to understand the reasons for these peaks.

4.5 Air bubble entrainment in turbulent boundary layers

In this section, the entrainment of the air bubble due to high shear and high pressure fluctuation in turbulent boundary layers will be quantified by utilizing the inline digital holography (Figure 4.4). The SHS involved in this study is the $\mathrm{SP_{Por}}$, which has k_{rms}~10 μm. Details of the porous base and coating material could be found in Section 3.1. Figure 4.18(a) shows the topography of the $\mathrm{SP_{Por}}$. Three sample snapshots of the original holograms of the air layer on the $\mathrm{SP_{Por}}$ for U_m varying between 2 to 6 m/s, and p_w varying between 0.96 to 1.12 atm, are shown in Figures 4.18(b)-(d). The pressure beneath the porous base is maintained at p_{por}=1.0 atm. Therefore, for p_w<1.0 atm, the plastron on the $\mathrm{SP_{Por}}$ is slowly replenished. Figures 4.18(b)-(d) provide a direct confirmation that an air layer is indeed attached to the surface, and this interface fluctuates at increasing surface speeds with increasing U_m. As expected, $U^{*}_{a\mathrm{ir}}$ (the normalized entrainment rate of air) increases with increasing U_m and decreasing p_w, as shown in Figure 4.19(a). For U_m=2.0 m/s (τ_{w}~10 Pa), $U^{*}_{a\mathrm{ir}}$ is essentially zero, i.e., the wall shear stresses fall below the threshold required for entraining the air. It increases to 1.5×10^{-10} at U_m=6.0 m/s (τ_{w}~50 Pa), and p_w=0.96 atm. Furthermore, using a separate axis, Figure 4.19(a) also shows the ratio of the gas to liquid flow rates in the boundary layer, Q_g/Q_w. As shown, the maximum value of this ratio is about 7×10^{-7}. According to Ceccio (2010) and Ferrante & Elghobashi (2004), to achieve drag reduction by injecting air bubbles, this ratio has to be in the order of 10^{-3} or higher. Therefore, the present bubble concentration is at least three orders of magnitude lower than that required for affecting the drag force.

Sample ensemble-averaged size distributions of entrained bubbles are shown in Figure 4.19(b). The results for U_m=2.0 m/s are not included since it is zero, but the rest demonstrate that the number of 'large' bubbles (>50 μm) increases with entrainment rate. However, the high-speed movies confirm that both the air layer and the steady entrainment of bubbles are maintained on the $\mathrm{SHS_{Por}}$ for more than four hours for the entire current range of U_m and p_w, presumably because of the continuous replenishment of the plastron by air under the porous surface. The persistence of the entrainment indicates that the capillary forces are sufficient for overcoming the air layer suppression by the higher pressure in the test section. To remove the air layer in some experiments, the entire space under the porous base has to be filled with water. We have not tried pressures exceeding p_w=1.20 atm, fearing that it might damage the substrate.

4.6 De-wetting transitions by moving air bubbles on SHSs

Various approaches have been applied to restore the plastron of a wetted SHS (Hu et al. 2017, Krupenkin et al. 2007, Lee & Kim 2011, Manukyan et al. 2011, Vrancken et al. 2010). Most methods are based on the generation of new layers of vapor or gas adjacent to the substrate through thermal, electrochemical, gas injection, and other methods. Here, we present a new method by moving an air bubble on the SHSs.

Figure 4.20(a) shows a series of images of the plastron states on the SP_{Por} before and after an air bubble moves across the surface. The images are obtained by total internal reflection (Figure 4.2). At t<0, the surface is forced to be wetted by applying high p_w and running the tunnel at U_m=0.6m/s until all air is diffused into the liquid. At t=0, p_w is decreased back to the original value (p_w=1.06 atm), and the tunnel is stopped. As shown in Figure 4.20(a), most parts of the surface remain wetted and appear to be dark, except a ~3 mm air bubble attached to the surface. The bubble may come from air located within the porous base. At t>0, the flow speed is again increased to U_m=0.6m/s which forces the air bubble to move on the surface. Interestingly, immediately after the air bubble moves across, the SP_{Por} becomes very shinny again (t>20s) indicating the restoration of plastron.

Figure 4.20(b) shows a similar process, but on another SHS, i.e., on POST. Taking advantage of the transparence of POST, the front between wetted and de-wetted regions is clearly visualized by imaging perpendicularly to the surface. It is clearly shown in Figure 4.20(b) that the de-wetted region propagates beneath the air bubble when the bubble moves across the surface. It should to be noted that the Cassie-Baxter state of the POST is not thermodynamically stable. Yet, the wetted POST is able to be de-wetted by locally exposing it to air. By calculating the free-surface energy between the two states shown in Figure

4.20(c), one could find that the dried state has lower surface energy compared to that of the wetted state, for any geometry, as long as the solid surface is hydrophobic. Therefore, the de-wetting transition by moving air bubbles on the surface is a very promising method to maintain the drag reduction property of SHS in real-world applications.

#	**Base**	**Roughness type**	**Hydrophobic chemistry**
GROOVE	Aluminum	Micro-grooves + nano-structures	Masurf FS100
SP_{Al}	Aluminum	Sprayed	Fluorinated urethane
SP_{PVC}	PVC	Sprayed	Fluorinated urethane
SP_{Por}	Porous base	Sprayed	F-POSS
SB	Aluminum	Sandblasted + etched	PTFE
POST	PDMS	Micro-post (12 μm)	PDMS

Table 4.1. Specifications of several types of SHSs involved in this chapter, including base type, roughness manufacture method and surface chemistry. PDMS denotes Polydimethylsiloxane.

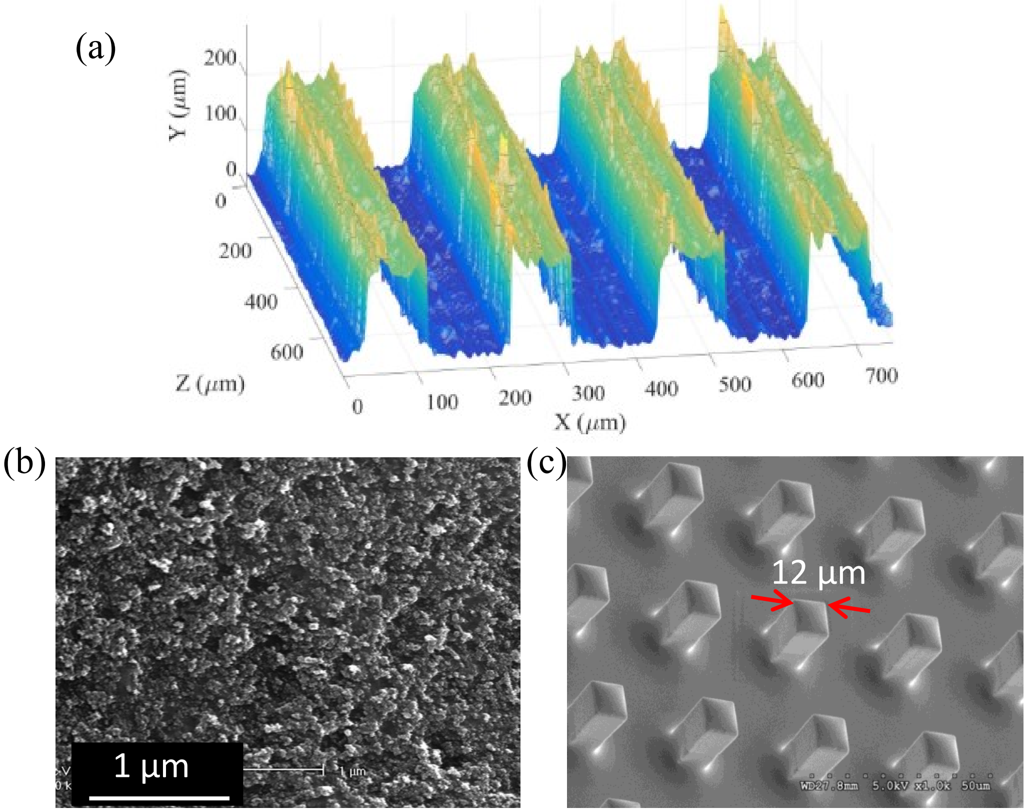

Figure 4.1. Surface topographies for (a) GROOVE, (b) SP_{Al}, and (c) POST.

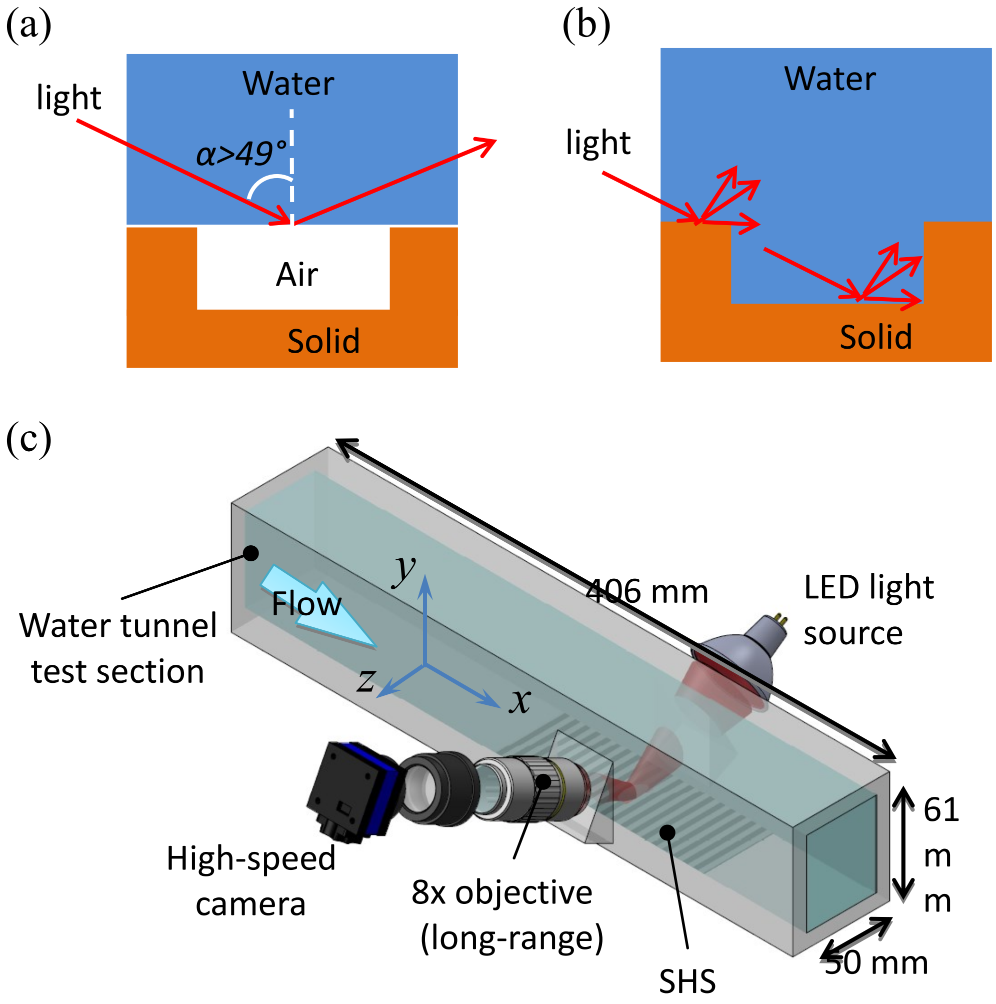

Figure 4.2. Characterization of air layer on SHS by total internal reflection: schematics of light path in Cassie-Baxter (a) and Wenzel (b) states; and (c) the corresponding optical setup.

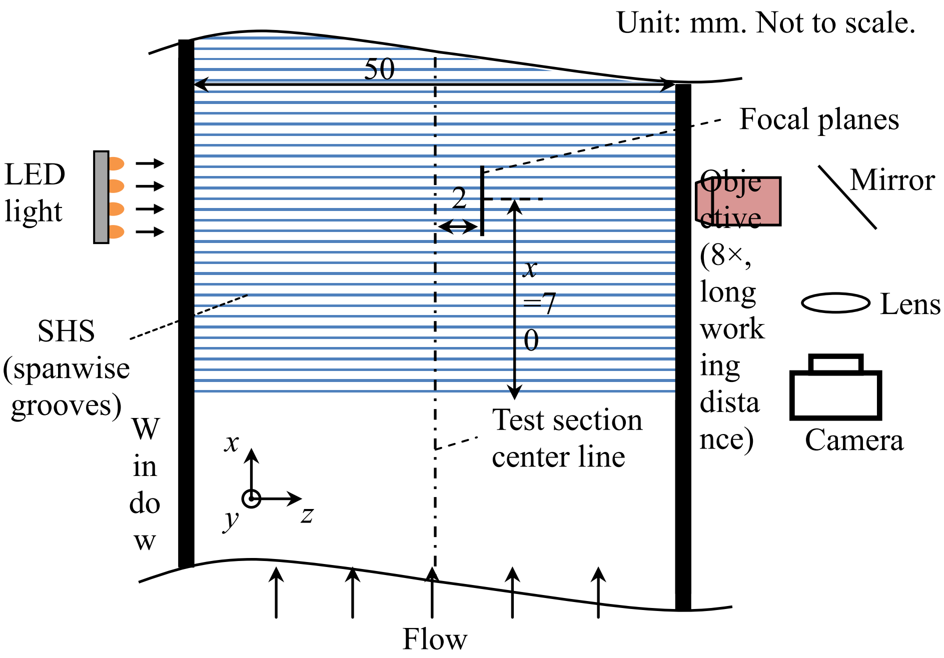

Figure 4.3. Optical setup for direct measurement of the plastron shape on the SHS with spanwise grooves (top view of the test section of the water tunnel).

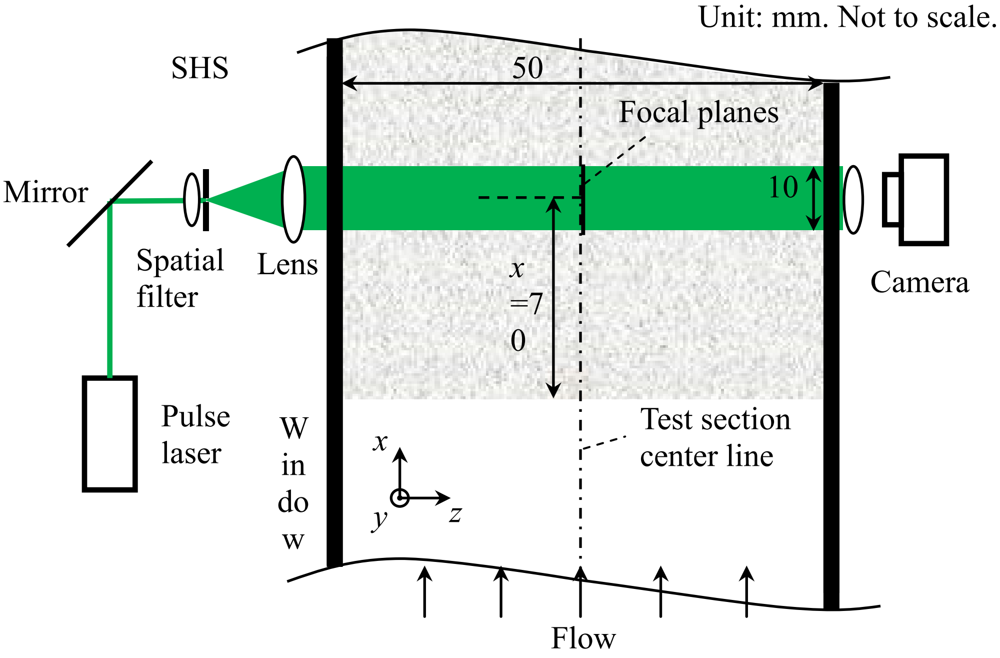

Figure 4.4. Optical setup of the digital holography for monitoring the air-water interface and measuring the entrainment rate of air (top view of the test section of the water tunnel).

Surfaces	***U_m*, m/s**	***U_0*, m/s**	***δ_{99}*, mm**	***Θ*, mm**	***τ_w*, Pa**	***δ_ν*, μm**	***Re_Θ***	***Re_τ***
Smooth wall (2D PIV)	0.65	0.68	7.15	0.76	0.78	35.7	518	200
	1.05	1.10	7.84	0.82	2.70	19.2	900	408
	1.58	1.65	8.44	0.87	5.48	13.5	1429	625
	2.11	2.21	8.70	0.94	8.84	10.6	2088	820
GROOVE$_{CB}$ (DHM)	2.13	-	-	-	8.46	11.8	-	-
GROOVE$_{CB}$ (2D PIV)	2.13	2.23	9.57	0.93	8.93	-	2080	-
GROOVE$_W$ (2D PIV)	0.66	0.69	6.13	0.63	-	-	433	-
	1.07	1.11	7.17	0.78	2.90	18.5	862	387
	1.61	1.67	7.60	0.84	7.92	11.2	1406	678
	2.11	2.20	7.77	0.89	14.4	8.3	1968	936

Table 4.2. Boundary layer parameters for a smooth wall as well as for the GROOVE in Cassie-Baxter and Wenzel states for the same location in the water tunnel.

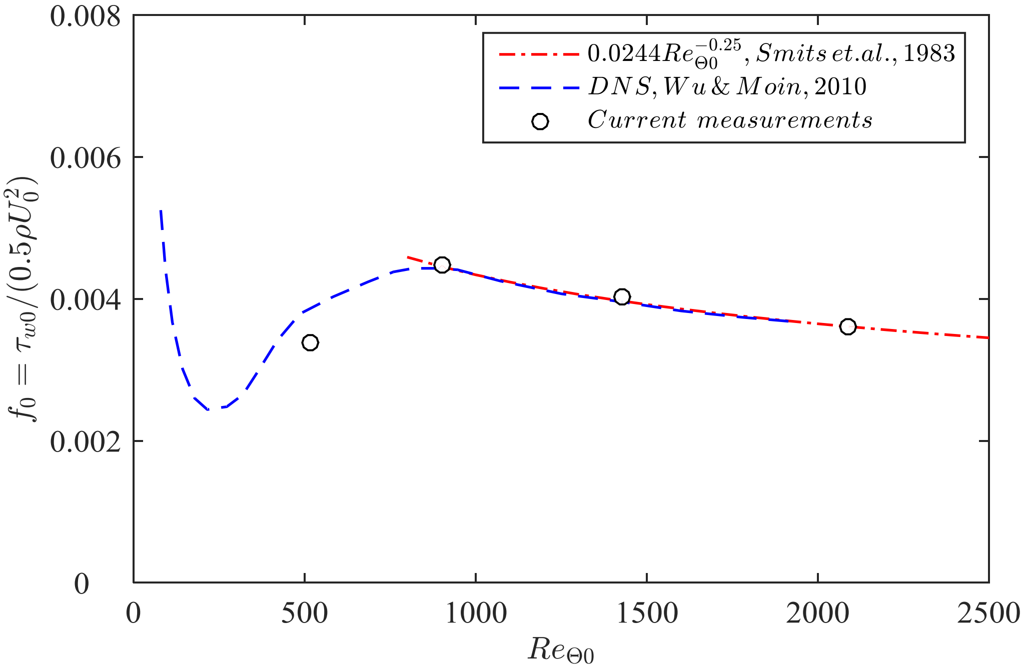

Figure 4.5. Baseline wall friction coefficient for the smooth wall as a function of $Re_{\Theta 0}$ compared to the DNS results of Wu and Moin 2010 and the experimental results by Smits et al. 1983.

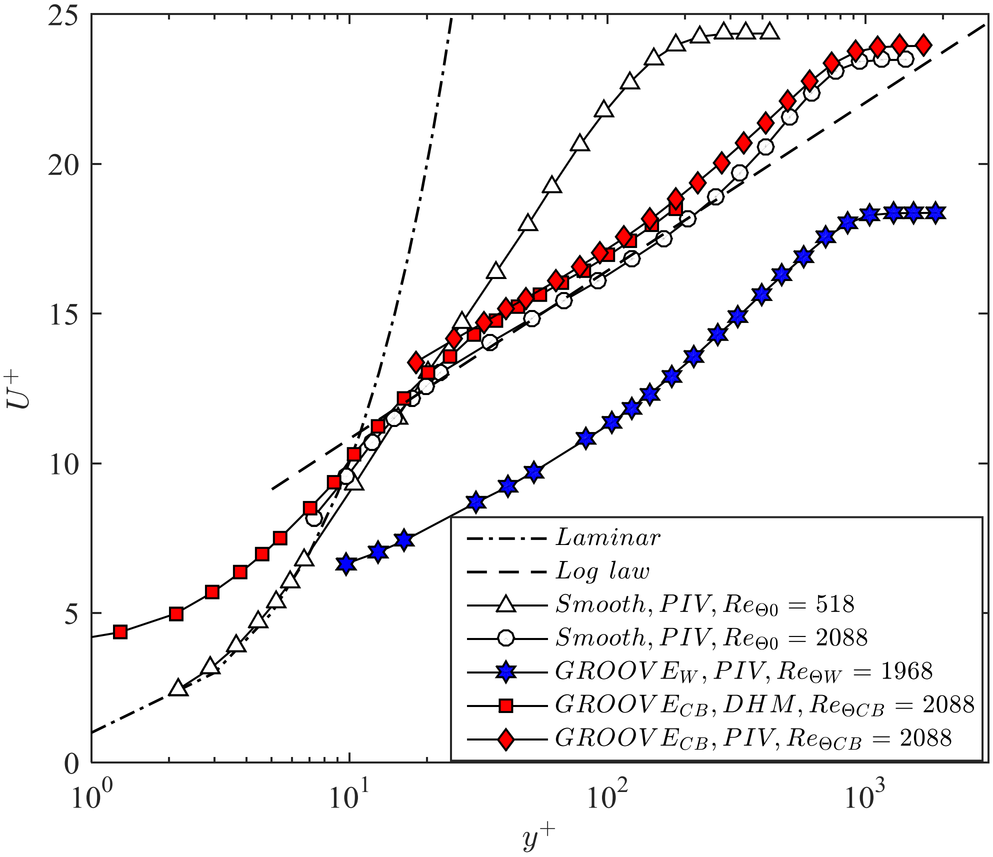

Figure 4.6. Mean velocity profiles for the smooth wall transitional ($Re_{\Theta 0}$=518) and turbulent (U_m=2.11 m/s, $Re_{\Theta 0}$=2088) boundary layers, as well as at U_m=2.13 m/s for the GROOVE in Cassie-Baxter ($Re_{\Theta \mathrm{CB}}$=2080) and Wenzel ($Re_{\Theta W}$=1968) states.

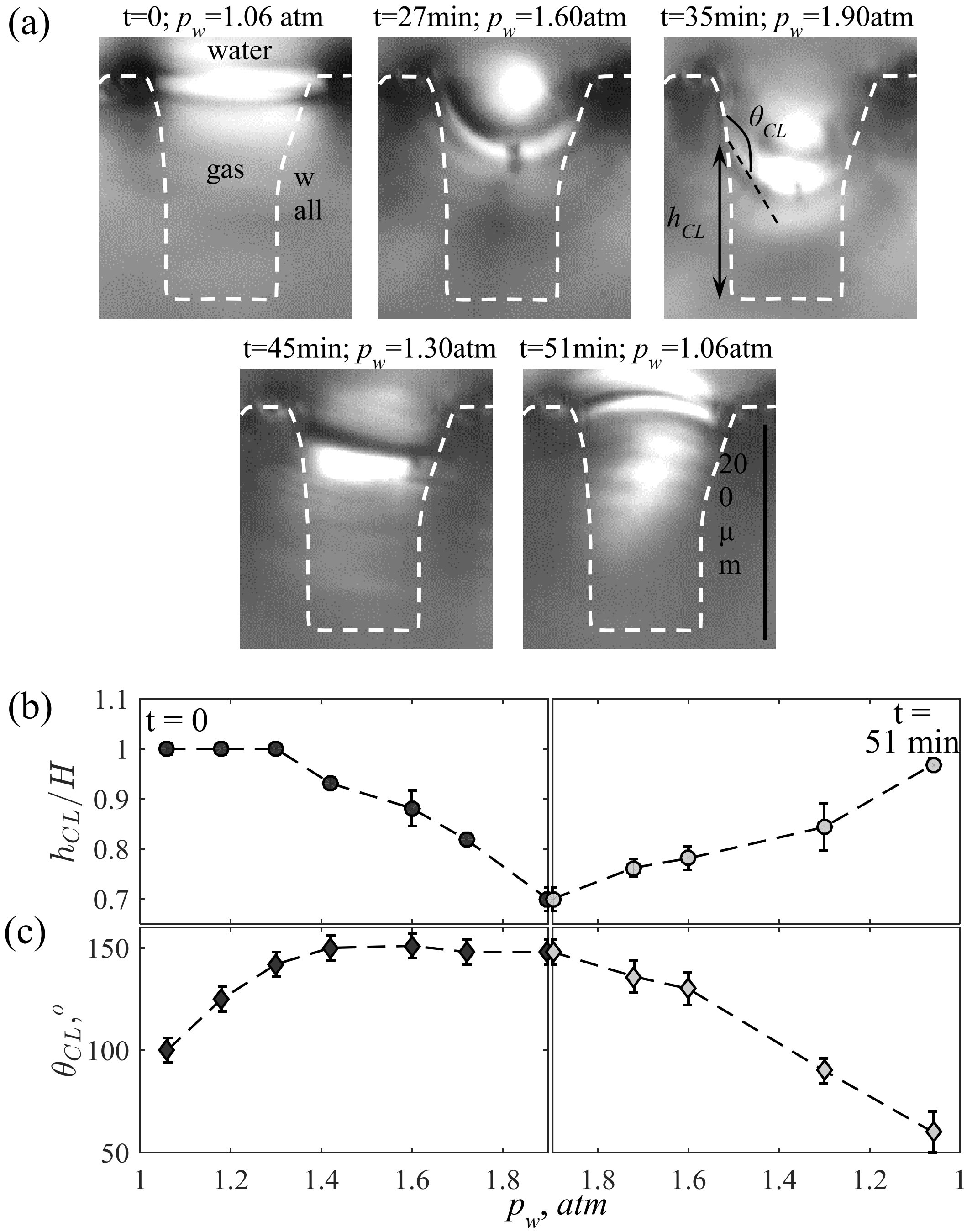

Figure 4.7. The response of a submerged plastron on GROOVE to an increase and subsequent decrease in ambient pressure with no flow: (a) selected images for the specified timing and p_w; (b) corresponding interface height at the contact line averaged of the two sides; and (c) the local contact angle (averaged).

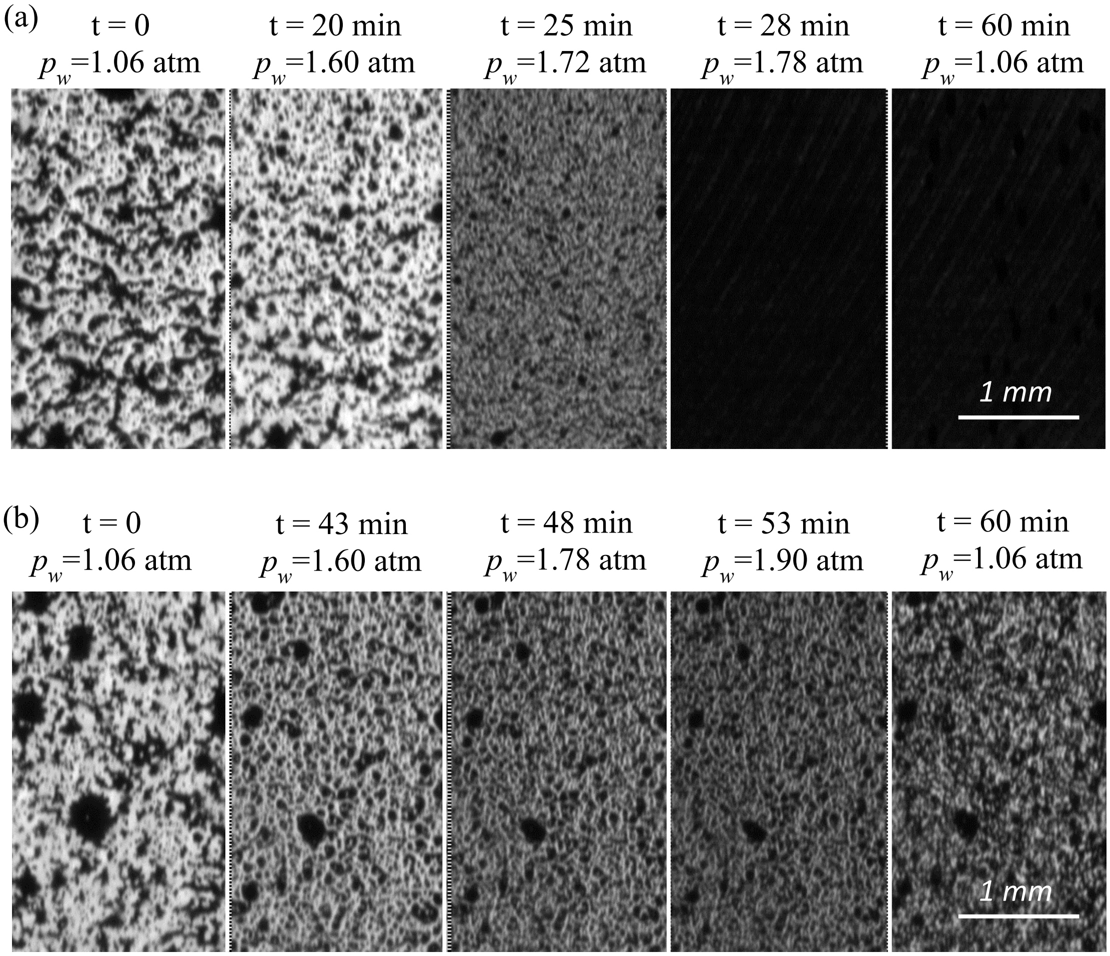

Figure 4.8. The state of interface for the specified timing and p_w during an increase and subsequent decrease of p_w on two SP_{Al} with two different roughness heights: (a) k_{rms}=3 µm, and (b) k_{rms}=6 µm.

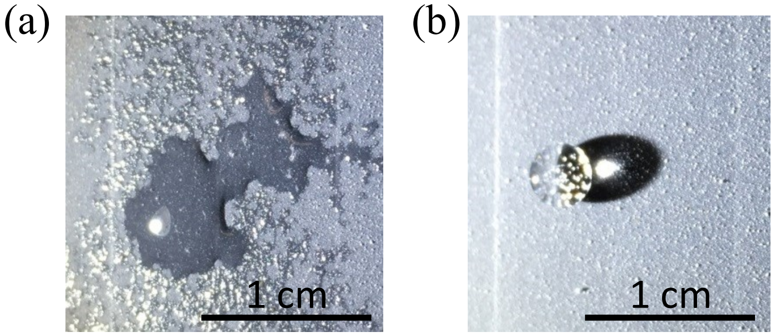

Figure 4.9. States of water droplet seating on SP_{PVC}: (a) immediately after the surface is wetted under high pressure and took out of the facility, and (b) after the surface is dried in air.

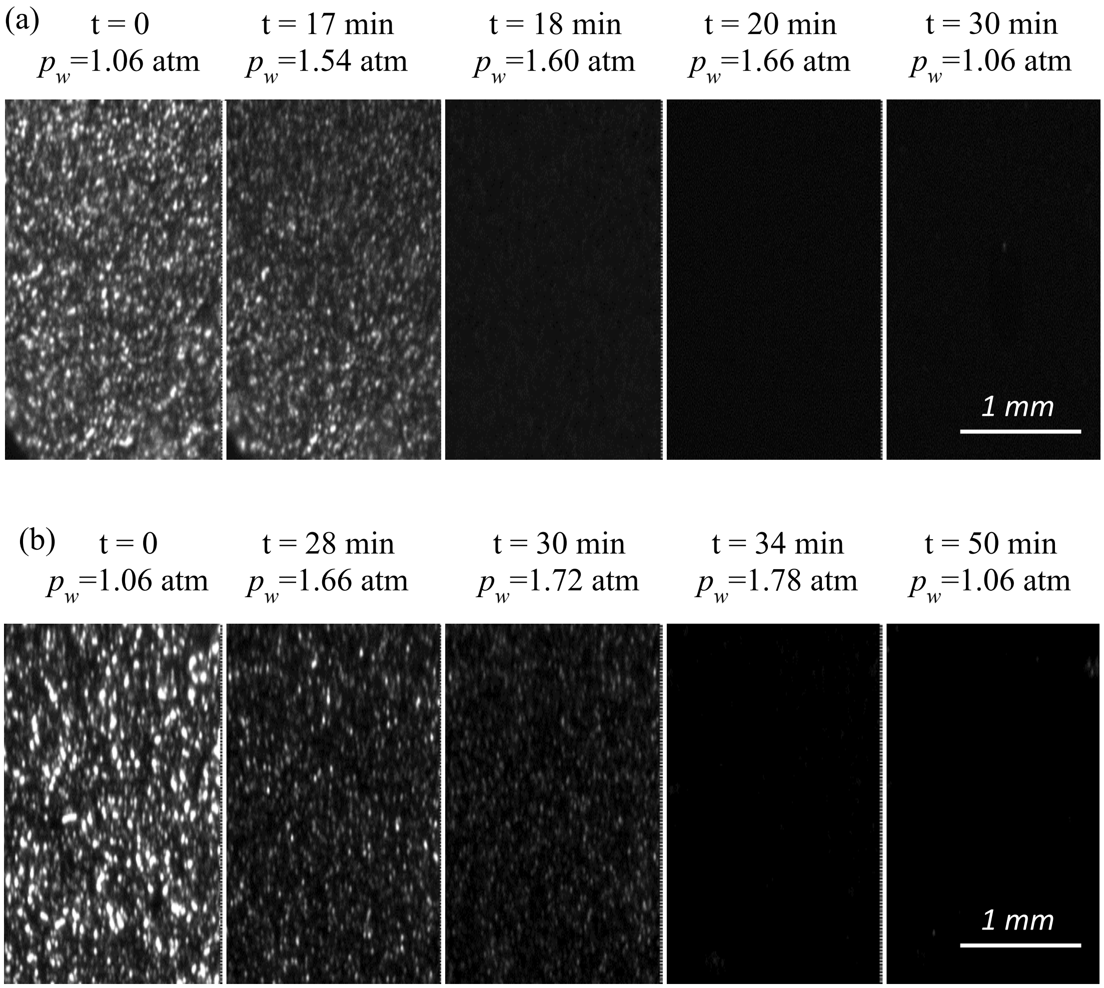

Figure 4.10. The state of interface for the specified timing and p_w during an increase and subsequent decrease of p_w on two SBs of two different sandpaper grit sizes: (a) 150, and (b) 80.

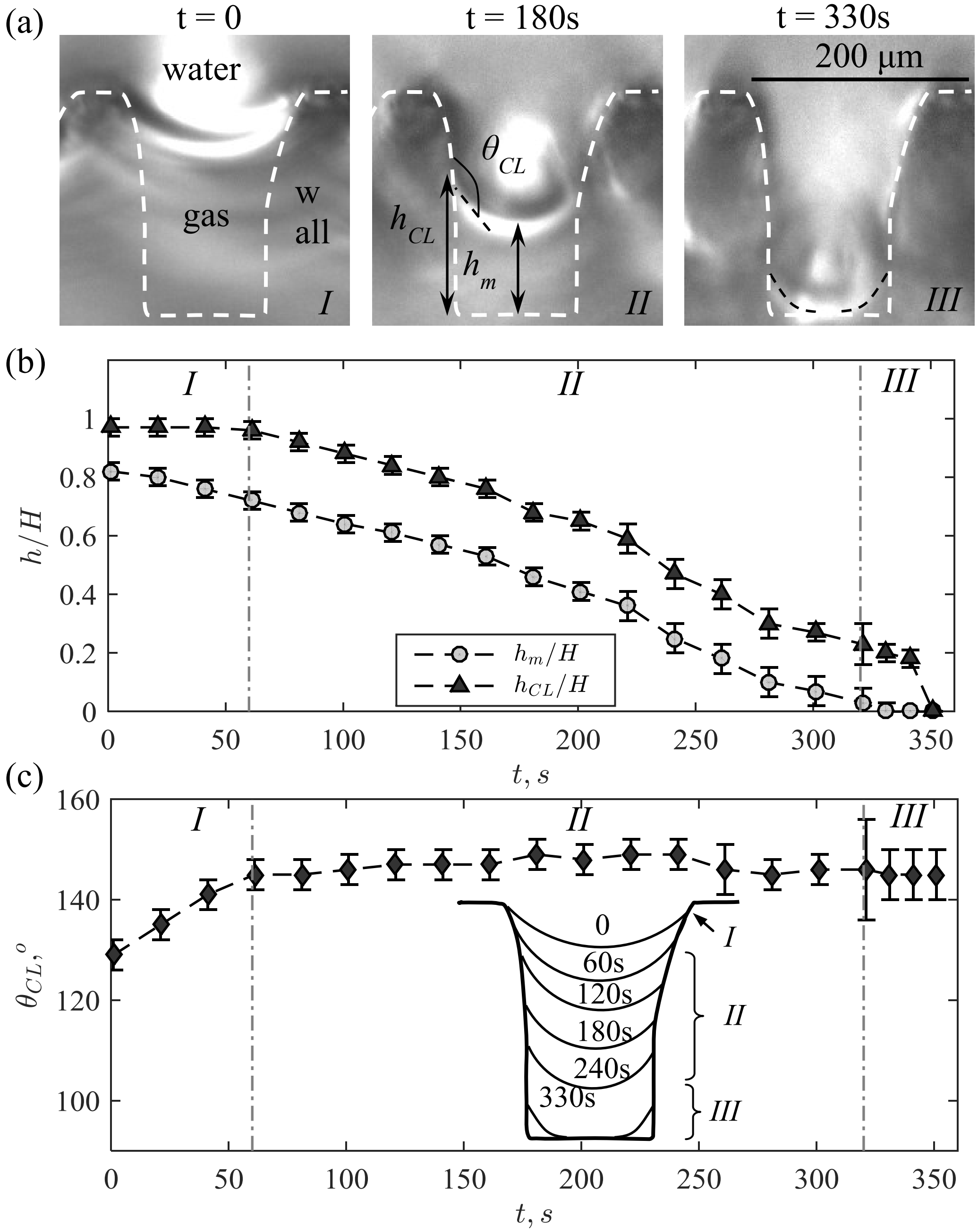

Figure 4.11. A typical wetting transition due to gas diffusion from the plastron to liquid at a constant p_w–p_v–p_∞=0.23 atm and $Re_{\Theta 0}$=518: (a) selected images at the specified times; (b) the average interface heights at the contact line and in the middle of the meniscus, as defined in image for t=180 s; and (c) the average local contact angle with an insert of the measured schematics of the interface shape.

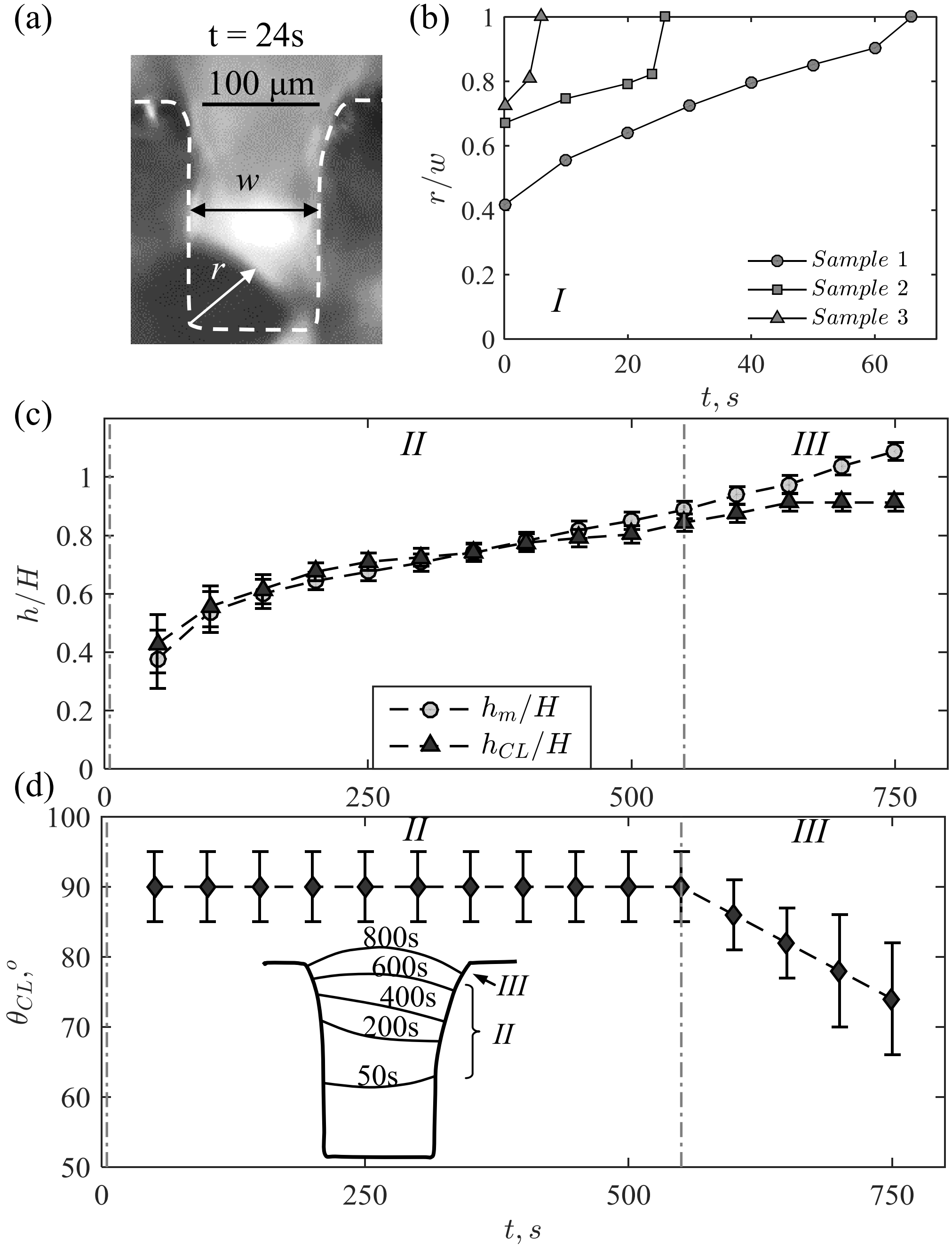

Figure 4.12. Dewetting transition due to gas diffusion from liquid to plastron at $p_w - p_v - p_\infty = -0.07$ atm and $Re_{\Theta 0} = 518$: (a) a sample image showing the bubble during stage I; (b) evolution of the bubble radius for three sample cases, with sample 2 corresponding to the image; (c) the average interface heights at the contact line and in the middle of the meniscus during stage II and III; and (d) the average local contact angle, with the insert showing the interface shape, during stage II and III.

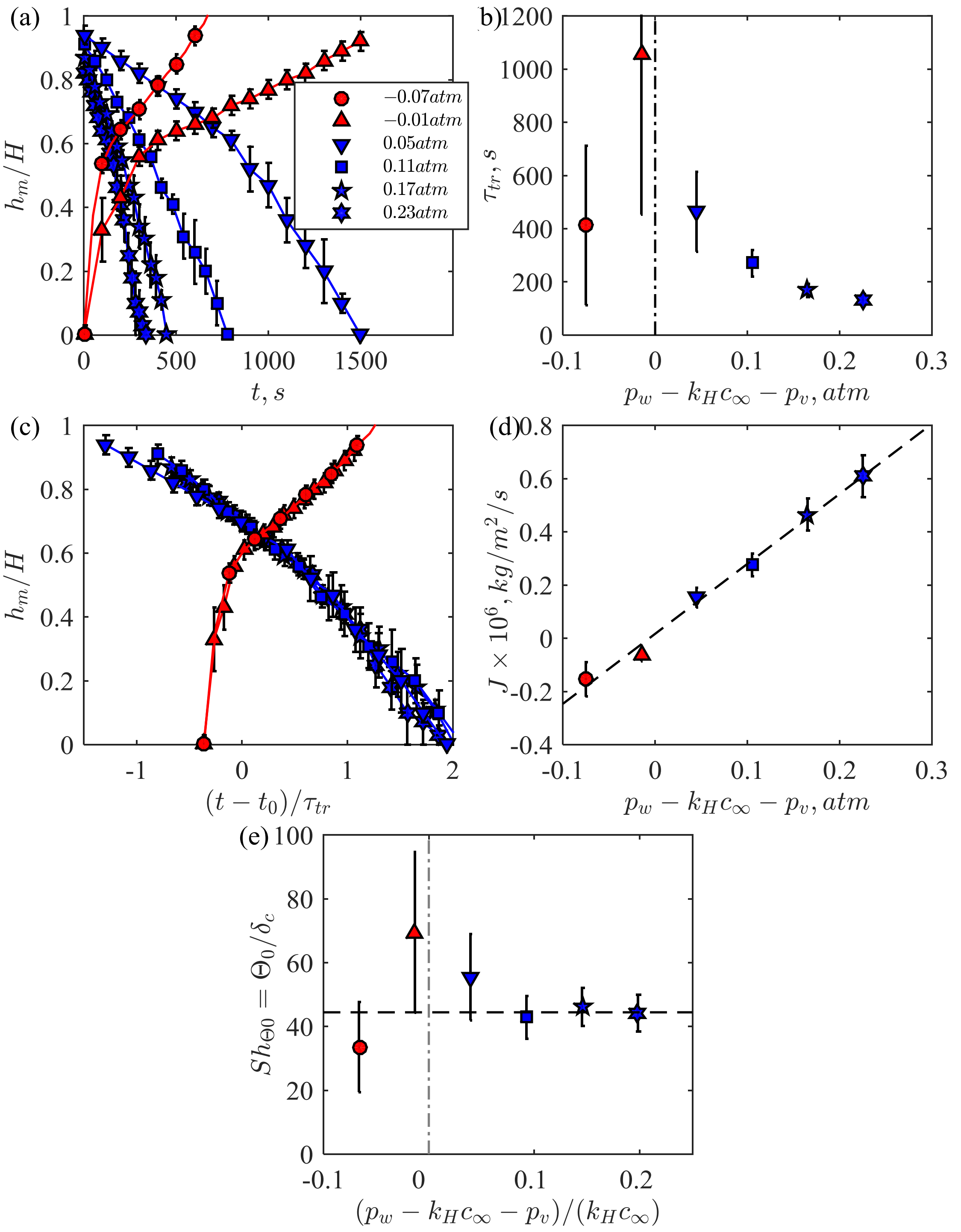

Figure 4.13. Effect of pressure on the wetting and dewetting transitions at $Re_{\Theta 0}$=518: (a) interface height for the specified pressures; (b) time scale for wetting corresponding to h_m/H decreasing from 0.7 to 0.4, and dewetting based on h_m/H increasing from 0.6 to 0.9; (c) interface height replotted as a function of $(t-t_0)/\tau_{tr}$; (d) average rate of mass diffusion during τ_{tr}; and (e) Sherwood number as a function of the dimensionless saturation pressure.

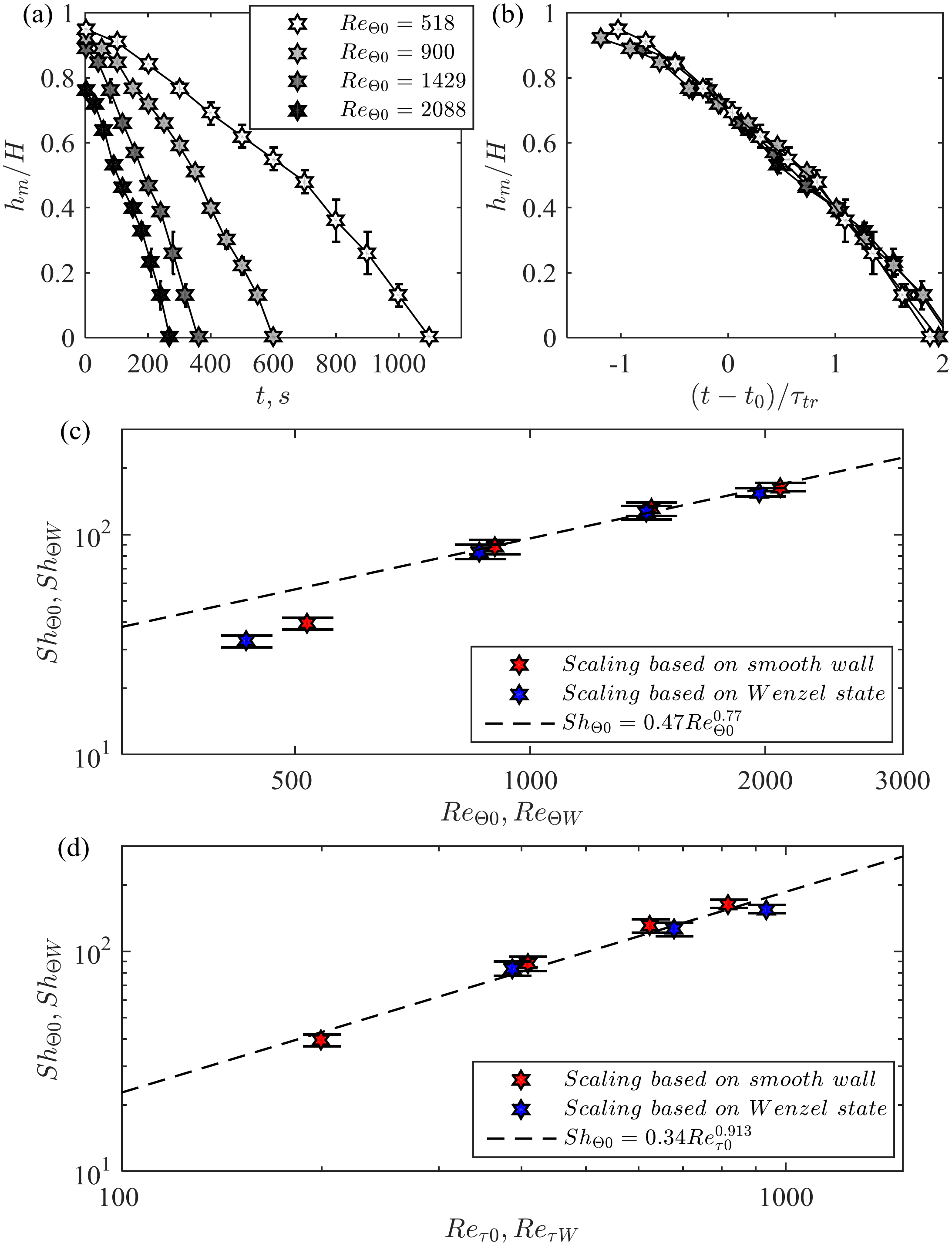

Figure 4.14. Effect of Reynolds number on the wetting transition for $p_w - p_v - p_\infty$=0.08 atm: (a) and (b) interface height; (c) and (d) relationships between Sherwood numbers and momentum thickness Reynolds numbers (c), and friction Reynolds numbers (d).

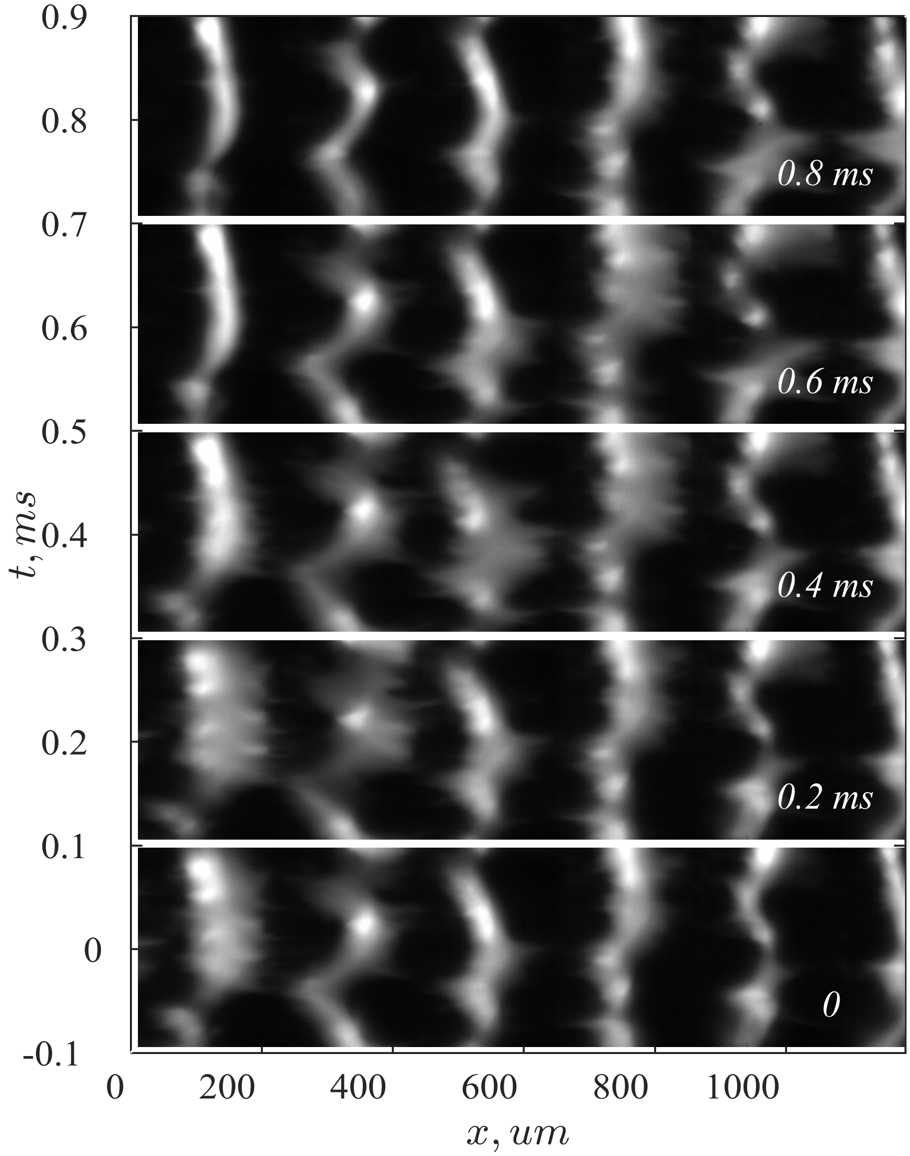

Figure 4.15. A time sequence of the reflected intensity from the GROOVE in a turbulent boundary layer with U_m=2.1 m/s.

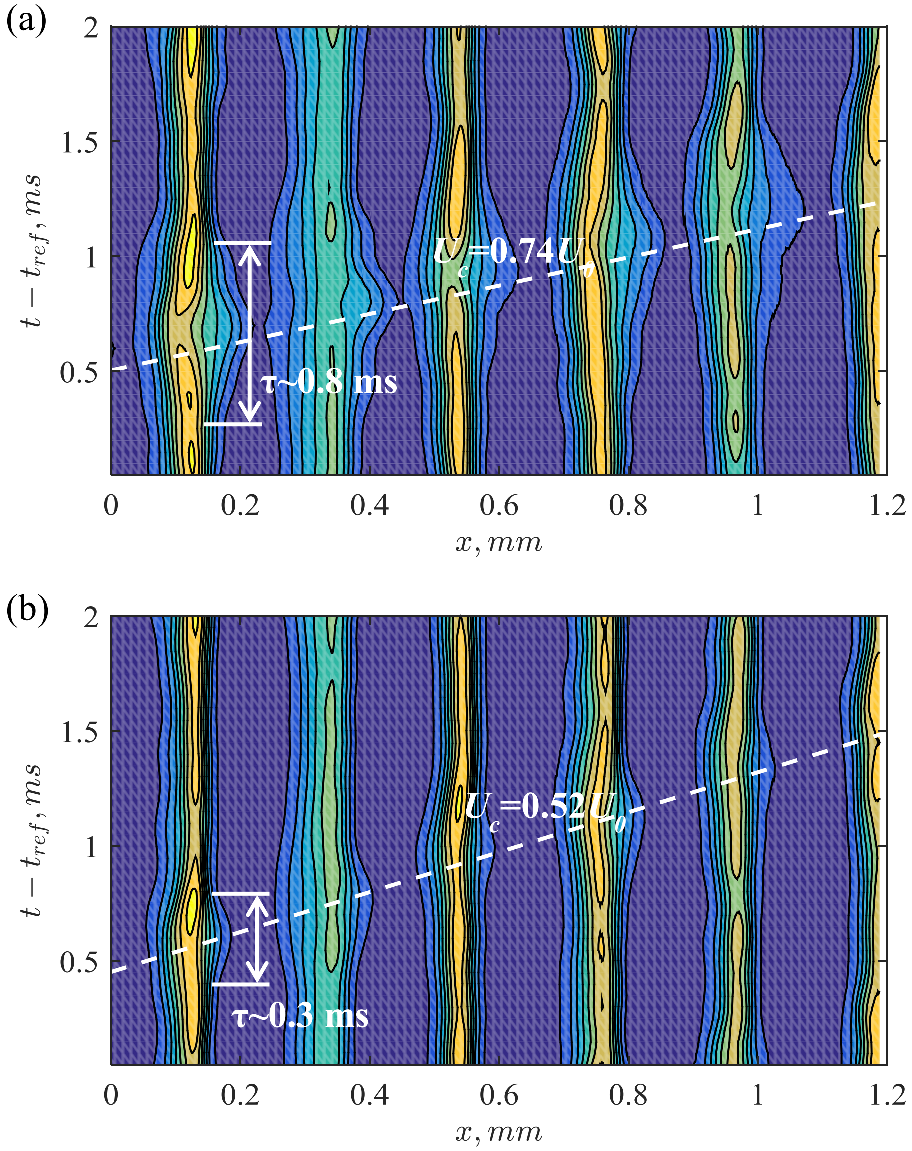

Figure 4.16. Two sample cases of $<Q>_z(x, t)$ showing the downstream convection of interface deformations: (a) $U_c=0.74U_0$ and (b) $U_c=0.52U_0$.

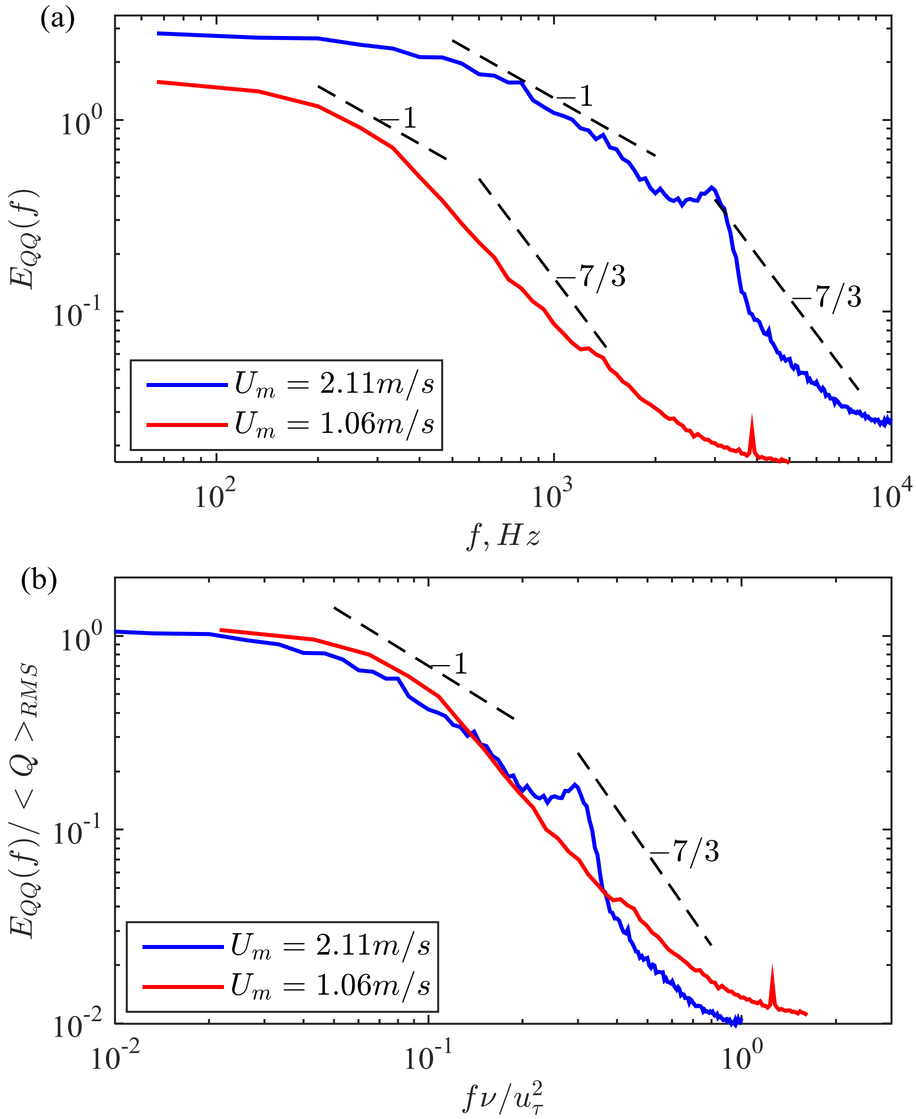

Figure 4.17. Interface deformation spectra for GROOVE in turbulent boundary layers at U_m=1.06 m/s and U_m=2.11 m/s: (a) the frequency is with dimension, and (b) the frequency is normalized by inner scales of turbulent boundary layers.

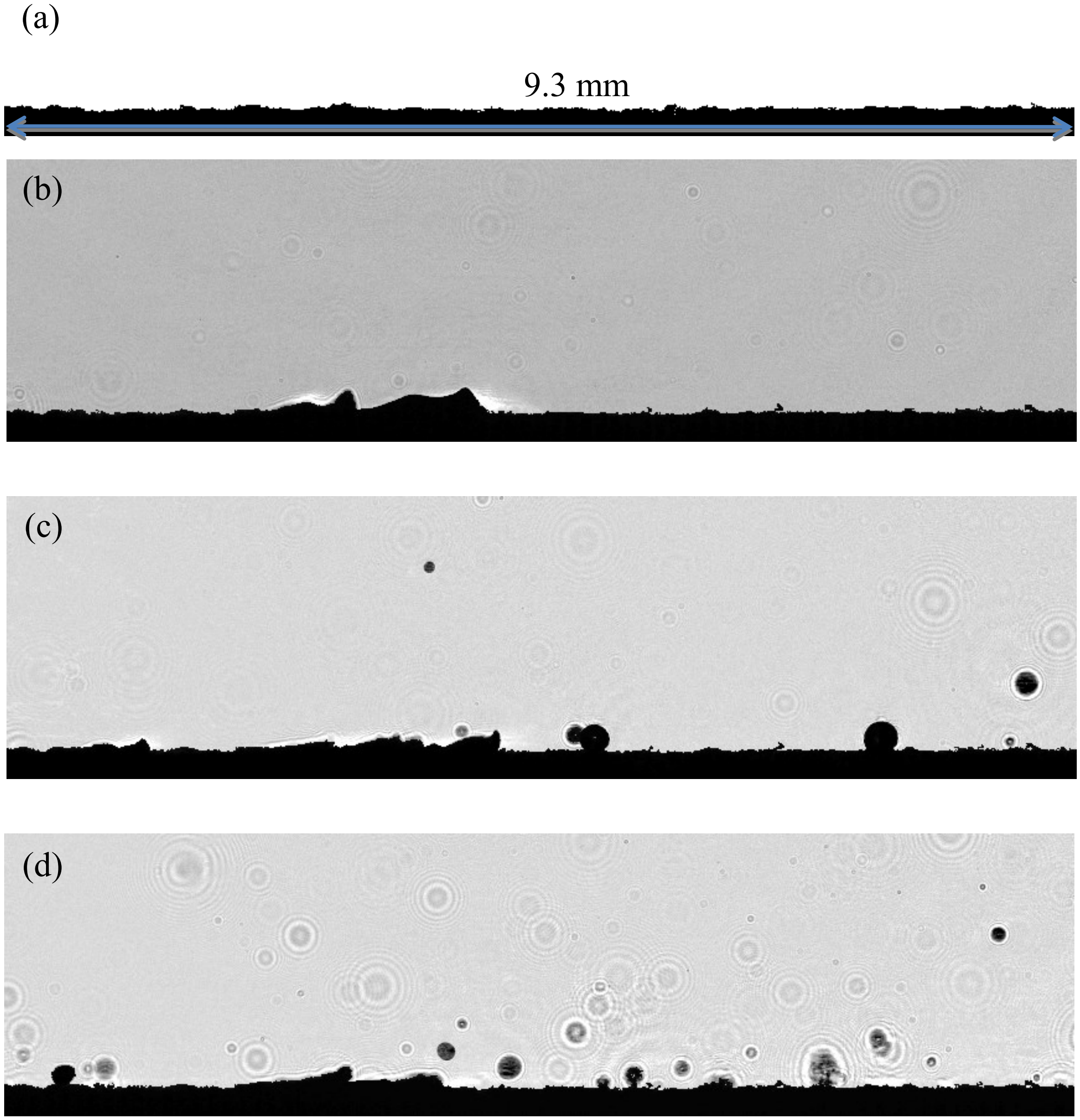

Figure 4.18. Snapshots of the original holograms of the air layer on the SP$_{Por}$ and the entrained bubble distributions: (a) surface topography in stationary liquid; (b) U_m=2.0 m/s, p_w=1.12 atm; (c) U_m=4.0 m/s, p_w=1.06 atm; and (d) U_m=6.0 m/s, p_w=0.96 atm.

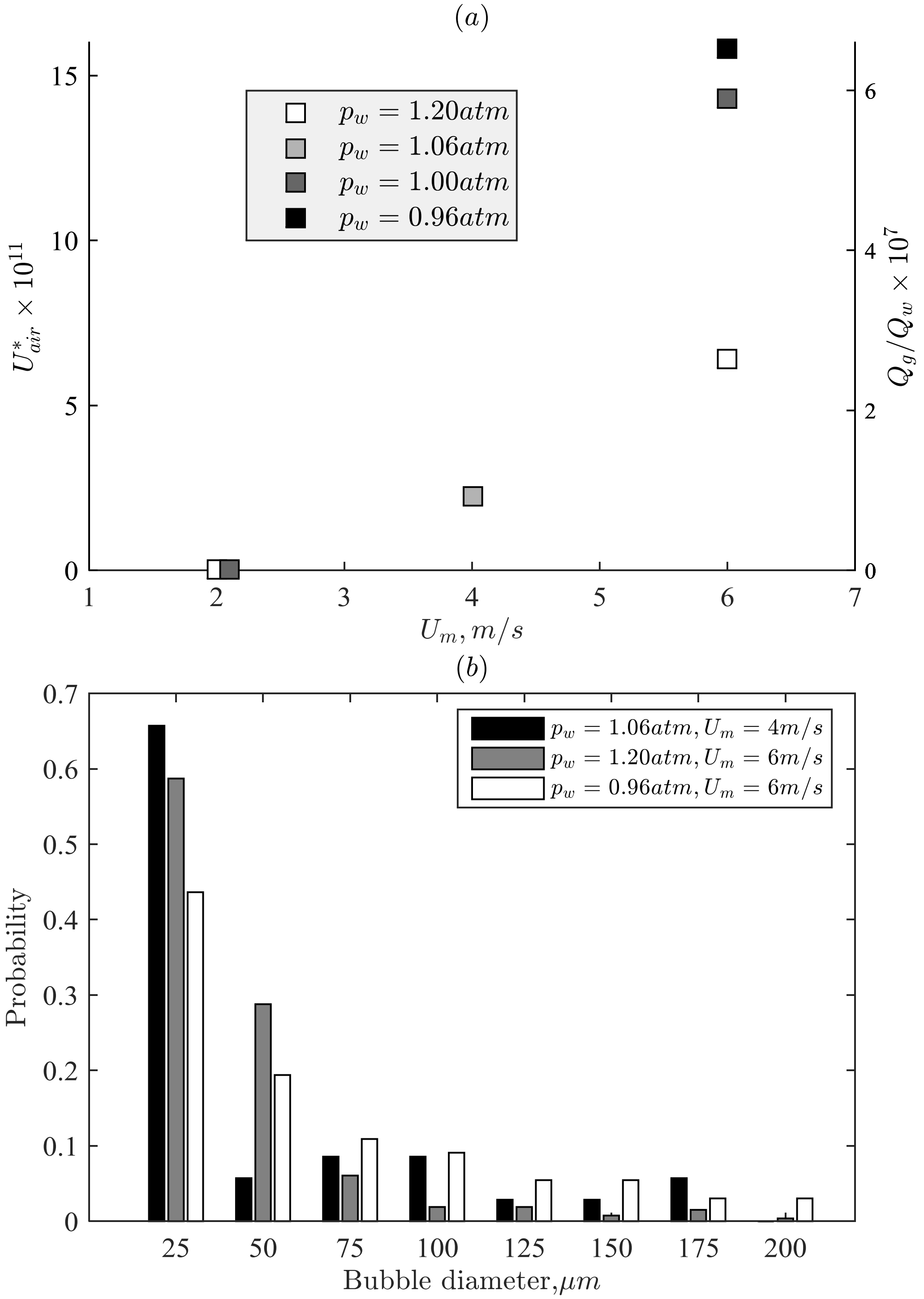

Figure 4.19. Characterization of air entrainment from the SP$_{Por}$ upstream of the sample area by turbulent flows: (a) normalized entrainment rate of air (U^*_{air} and Q_g/Q_w) for several pressure in the facility, and (b) the measured size distribution of the entrained bubbles.

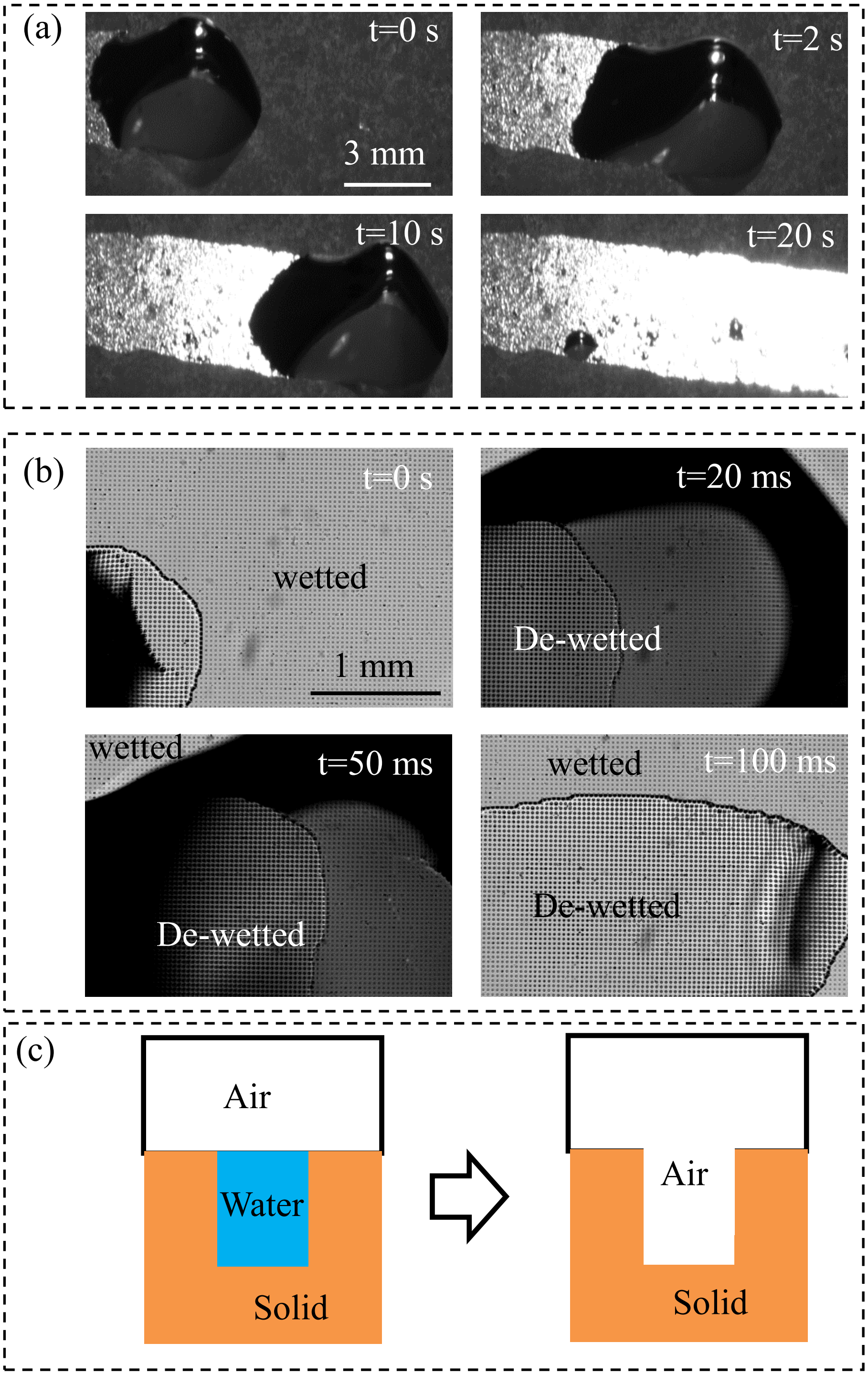

Figure 4.20. De-wetting transitions caused by moving an air bubble on (a) SP_{Por} and (b) POST, and (c) a schematic of the de-wetting transition by exposing a wetted SHS locally to air.

Chapter 5. Summary and Conclusions

The possibilities of using Super-Hydrophobic Surface (SHS) for the skin-friction drag reduction in high-Reynolds number turbulent flows have been experimentally investigated. Section 5.1 summarizes the high-resolution velocity measurement techniques. Section 5.2 summarizes the effects of various types of SHSs on turbulent boundary layers, including wall friction and mean flow quantities. Section 5.3 discusses the plastron stability and lifetime on SHSs subjected to disturbances, including hydrostatic pressure, mass diffusion, as well as turbulence. Section 5.4 discusses several future investigations on this topic.

5.1 Dual-view digital holographic microscopy

A novel optical technique, dual-view digital holographic microscopy (DHM), is developed to solve the long-standing virtual image problem inherent to the inline holography. It is based on simultaneously recording two holograms whose planes are separated by a short distance *D*. During reconstruction, the real images overlap, whereas the virtual images are separated by 2*D*. Two different types of data analysis procedures have been developed. The first one involves reconstruction of the two holograms and correlating their spatial intensity distributions. First, correlations are used to measure the lateral displacements between the two reconstructed fields resulting from slight misalignment between two cameras. When the two fields are matched, axial correlations measure the axial distance between traces. When the sample volume contains a large number of particles, the average axial distance between traces provides a the spatial distribution of $D(x,y)$. Procedures to address particles located very close to the hologram plane are introduced as well. The second data analysis procedure is based on phase-retrieval method, where the complex amplitude of the wave field is obtained by iteratively propagating the wave field back and forth between two planes. By reconstructing this complex amplitude, only the real image is obtained, and the virtual image is total eliminated. The later method improves the quality of reconstructed real images by suppressing the signature of virtual ones, especially when the two hologram planes are aligned carefully.

Lastly, spatial correlations within the same reconstructed field are also used to improve the detection of the axial location of a particle, z_p. For each location z within a particle trace, we sum the correlations among intensity distributions in all planes located symmetrically on both sides of z. As both numerically and experimentally obtained 3D traces confirm, this cumulative correlation peaks at the z_p. Since the correlation distribution is much sharper than that of the intensity, z_p is detected more accurately. Using the two parallel holograms, we show that the uncertainty in localization of z_p of 2 μm particles can be reduced to about one particle diameter.

5.2 Friction reduction in turbulent boundary layers by SHSs

This above developed optical technique is used for characterizing the velocity and turbulence in the inner part of turbulent boundary layers over various types of SHSs. These SHSs are generated using various methods, including spraying, etching and sandblasting. The measurements have been performed at friction Reynolds numbers (Re_τ) varying from 700 to 4400, and normalized rms values of roughness heights (k_{rms}^+) in the 0.2 to 3.3 range. The slip velocity and local wall friction are calculated directly from the mean velocity and total stress (sum of the viscous and Reynolds shear stress) at the top of the SHS roughness. In addition to calculating profiles of mean velocity, Reynolds and total stresses, data analysis examines the distributions of eddy viscosity, Prandtl mixing length, shear production and turbulence spectra.

For flow over SHSs with $k_{rms}^{+}<1$ and relatively low $Re_{\tau}\sim 800$, the viscous stress is lower than that of the smooth wall and the Reynolds shear stress is nearly zero at the top of the SHS roughness, resulting in 10 to 30% reduction of wall friction. The slip velocity varies from 15 to 30% of the freestream mean flow speed, and the slip length λ falls between 30 to 150 μm ($3<\lambda^{+}<15$). The measurements confirm previous theoretical predictions of the relationships between drag reduction and slip velocity allowing for both spanwise and streamwise slip contributions. Aligning the roughness elements in the streamwise direction increases the drag reduction. An upward shift of the mean velocity profile occurs. In the log region, this upward shift is lower than that in the inner layer, a phenomenon observed before in both numerical simulations (e.g., Min & Kim 2004) and experimental measurements (e.g., Woolford *et al.* 2009), and is due to the effect of spanwise slip. These changes are accompanied with increases in $\overline{<u'u'>}^{+}$ and $\overline{<v'v'>}^{+}$, in the inner part of the boundary layer, and shifts of their peaks closer to the wall. Roughness effects, motion of the air-water interface, spatial non-uniformity, and even the non-equilibrium conditions might play a role in the increase of the turbulence level. Streamwise spatial energy spectra of both streamwise and wall-normal velocity fluctuations show that drag-reducing SHSs alter the structure of near-wall turbulence. They reduce the inertial range streamwise fluctuations, and increase the wall normal large scale fluctuations. The latter effect diminishes with increasing distance from the wall, but the former trend persists.

As the magnitude of k_{rms}^{+} increases above 1 by either increasing Reynolds number or roughness height, the flow over the SHSs transitions from drag reduction, where the viscous stress dominates, to drag increase where the Reynolds shear stress becomes the primary contributor. When k_{rms}^{+}=1.71, it appears that there is a balance between drag reduction by the SHS and an increase by the roughness. For the present maximum value of k_{rms}^{+}=3.28, the inner region exhibits the characteristics of a rough wall boundary layer, including elevated wall friction and turbulence, as well as a downward shift in the mean velocity profile. Consistent with prior experimental studies involving measurements of wall friction (Bidkar *et al.* 2014), it appears that the transition between drag reduction to increase occurs when k_{rms} falls in the $1 \leq k_{rms}^{+} \leq 2$ range. Increasing the pressure in the test facility to a level that compresses the air layer on the SHSs and exposes the protruding roughness elements reduces the extent of drag reduction. This effect is similar to that caused by increasing k_{rms}^{+}.

For the drag reducing SHSs, the peaks values of Reynolds shear stress are lower than that of the smooth wall, resulting in a lower turbulence kinetic energy (TKE) shear productions in the log region. In contrast, for the drag increase SHSs, the log region has higher Reynolds shear stresses and TKE production. Very close to the wall (y^{+}<5), all the SHSs have higher velocity fluctuations, TKE production, eddy viscosity, and Prandtl's mixing length compared to those of the smooth wall. However, in the log region, the eddy viscosity and Prandtl's mixing length profiles of the SHSs coincide to those of the smooth wall.

Due to limited total length of the SHSs, 8~20δ_{99}, all the present boundary layers do not reach equilibrium conditions. Hence, for the drag reduction cases, the directly measured local wall stress is lower than that calculated from a fit to the mean velocity profile in the log layer. The latter decreases gradually from the smooth wall value to that of the SHS as the boundary layer develops with streamwise distance. The evolving conditions also introduce wall-normal gradients in the total stress profiles, with the near wall values being lower than the maximum values at the edge of the roughness/viscous sublayers. This maximum also decreases with streamwise distance. Collapse of the normal and shear Reynolds stress components onto those of the smooth wall in the outer part of the log layer is also consistent with the boundary being under non-equilibrium conditions. There is also a mismatch between the local wall stress and that estimated from a log layer fit to the velocity profile for cases where roughness effects dominate. However, in these cases, the log fitted values are higher than both the local values and those of the smooth wall. Furthermore, all the Reynolds stress components and the total stress in the log region are much higher than those of the smooth wall. These observations are consistent to recent results of numerical simulations, which also observe an overshoot of the velocity fluctuation in the log region shortly after a transition from a smooth to a rough wall (Lee & Sung 2007; Saito & Pullin 2014). Clearly, the changing boundary conditions propagate in the wall-normal direction much faster above the rough wall than the SHS which reduces drag.

5.3 Behavior of plastron on SHSs

The effects of hydrostatic pressure, mass diffusion and turbulent flow on the air pocket of SHSs are characterized. The interface is measured using total internal reflection, directly imaging under microscopy, and digital holography. For stationary water, the mass diffusion is slow. With increasing pressure, the wetting process involves initial pinning to the tip of the groove as the contact angle increases, followed by interface migration into the groove with an advancing contact angle of 150°. Upon subsequent decrease in pressure, the plastron growth involves brief pinning at the bottom edge of the groove, followed by upward interface migration, pinning at the tip corner, and formation of a convex interface.

With flow, the diffusion-induced wetting process observed during exposure to under-saturated liquid involves three phases, namely an initial pinned state, followed by downward migration at high contact angle, and shrinkage of bubbles at the bottom corners of the groove. At the end, the size of air pockets decreases below the present resolution limit. During this process, the boundary layer profile changes from slight drag reduction under the CB state to a rough wall boundary layer. Transition to super-saturated water by reducing the pressure initiates growth of a bubble from one of the bottom corners until it reaches the other side of the groove. Subsequently, the interface migrates upward at a low contact angle until it reaches the tips of the groove, and then becomes convex. The diffusion rate increases with the magnitude of under- or super-saturation level and with increasing Reynolds number. A power law relation, $Sh_{\Theta 0}=0.47Re_{\Theta 0}^{0.77}$, is obtained for the turbulent flow regime using the smooth wall momentum thickness for calculating the Sherwood ($Sh_{\Theta 0}$) and Reynolds ($Re_{\Theta 0}$) numbers. Conversely, mass diffusion in the transitional boundary layer is lower than this prediction. This power-law agrees with diffusion rates observed previously for smooth wall turbulent boundary layers. However, when plotted against the friction Reynolds number ($Re_{\tau 0}$) instead, both the transitional and turbulent boundary layer results collapse onto a single power law, $Sh_{\Theta 0}=0.34Re_{\tau 0}^{0.913}$. This trend suggests that turbulent diffusion and wall friction are correlated. The relation between Sherwood number and momentum thickness Reynolds number persists if the Wenzel state length scales are used instead of those of the smooth wall. However, trends with the friction Reynolds number change slightly. These power-laws provide quantitative guidance about the rate of plastron depletion with pressure, and could be used e.g. for estimating the rate of replenishment required for maintaining a CB state.

When the CB state is maintained, a downstream convection of interface deformation is observed in a turbulent boundary layer. The convection speeds are in the range of 0.5 to 0.7

of free-stream velocity, similar to those of the log-layer turbulent structures. The deformation spectrum is measured and found to be similar to the wall pressure spectrum. The entrianment rate of air bubbles from SHS by turbulent flow is measured using digital holography. As expected, both the magnitude of interface deformation and the rate of air entrainment increase as increasing Reynolds number and reducing the hydrostaic pressure. Finally, a passive method to restore the plastron by moving air bubbles on the SHSs is disscussed. This method is found to be suitable for any types of roughness geometries, as long as the surface remains its hydrophobic chemistry.

5.4 Future studies

The present study has shown a great promise of using super-hydrophobic surfaces to achieve significant friction drag reduction in high-Reynolds number turbulent boundary layers. However, a few challenges and problems still remain for applying SHSs in real world, large-scale systems.

Firstly, which surface geometry is optimal to achieve a maximal drag reduction at certain flow condition is not well understood. Indeed, higher drag reduction could be achieved by increasing the slip length of the SHSs. Theoretical relations between slip length and drag reduction have been well established and experimentally confirmed. However, the relationship between surface properties (e.g., geometry and chemistry) and slip length has not been well studied, especially in the turbulent flow region. Which surface parameters, e.g. roughness wavelength and air-friction, govern the slip length? Is the slip length independent of Reynolds number or not? How does the shape of air-water interface affect the magnitude of slip length? What's the ratio between streamwise and spanswise slip for randomly roughed geometries?

Secondly, the nature of turbulence over SHS is not well investigated. It is well accepted that the slip length greatly modifies the near-wall mean velocity profile. However, how the slip length modifies the generation and transportation of turbulent structures is not well understood. Numerical simulations are inconsistent with each other. Some studies show that the SHSs modify the turbulent structures, e.g., attenuate the streamwise vortices and increase the spanwise spacing of streaks, while others report that there is only a shift of turbulent structure closer to the wall. Therefore, either experimental measurements or more intensive numerical simulations are required to understand how the SHSs modify the nature of turbulence.

Other interesting topics include: (i) the development of the turbulent boundary layer from smooth wall to SHS; (ii) the vibration of air-water interface and its correlation to the flow structures; (iii) the relation between surface geometry and stability of the air-water interface; (iv) exploring and implementation of different air replenishment methods; and (v) the effects of surfactant on the slip velocity and mass diffusion at the interface of SHSs.

Bibliography

Aljallis E, Sarshar MA, Datla R, Sikka V, Jones A, Choi C-H. 2013. Experimental study of skin friction drag reduction on superhydrophobic flat plates in high Reynolds number boundary layer flow. *Phys. Fluids*. 25(2):25103

Amrei MM, Tafreshi HV. 2015. Effects of hydrostatic pressure on wetted area of submerged superhydrophobic granular coatings. Part 1: mono-dispersed coatings. *Colloids Surfaces A Physicochem. Eng. Asp.* 465:87–98

Antonia RA, Luxton RE. 1971. The response of a turbulent boundary layer to a step change in surface roughness Part 1. Smooth to rough. *J. Fluid Mech.* 48(4):721–761

Araiza-Esquivel M a, Martínez-León L, Javidi B, Andrés P, Lancis J, Tajahuerce E. 2011. Single-shot color digital holography based on the fractional Talbot effect. *Appl. Opt.* 50(7):B96–101

Awatsuji Y, Tahara T, Kaneko A, Koyama T, Nishio K, et al. 2008. Parallel two-step phase-shifting digital holography. 47(19):183–89

Baehr HD, Stephan K. 2006. *Heat and Mass Transfer*. Springer

Barth C, Samaha M, Tafreshi H, Gad-el-Hak M. 2013a. Convective Mass Transfer From Submerged Superhydrophobic Surfaces. *Int. J. Flow Control*. 5(2):79–88

Barth C, Samaha M, Tafreshi H, Gad-el-Hak M. 2013b. Convective Mass Transfer From Submerged Superhydrophobic Surfaces: Turbulent Flow. *Int. J. Flow Control*. 5(3–4):143–52

Bartolo D, Bouamrirene F, Verneuil E, Buguin A, Silberzan P, Moulinet S. 2006. Bouncing or sticky droplets: impalement transitions on superhydrophobic micropatterned surfaces. *Europhys. Lett.* 74(2):299–305

Bhushan B, Jung YC. 2011. Natural and biomimetic artificial surfaces for superhydrophobicity, self-cleaning, low adhesion, and drag reduction. *Prog. Mater. Sci.* 56(1):1–108

Bico J, Thiele U, Quéré D. 2002. Wetting of textured surfaces. *Colloids Surfaces A Physicochem. Eng. Asp.* 206(1–3):41–46

Bidkar RA, Leblanc L, Kulkarni AJ, Bahadur V, Ceccio SL, Perlin M. 2014. Skin-friction drag reduction in the turbulent regime using random-textured hydrophobic surfaces. *Phys. Fluids*. 26(8):85108

Bobji MS, Kumar SV, Asthana A, Govardhan RN. 2009. Underwater sustainability of the "Cassie" state of wetting. *Langmuir*. 25(20):12120–26

Bormashenko E. 2014. Progress in understanding wetting transitions on rough surfaces. *Adv. Colloid Interface Sci.* 222:92–103

Brzek BG, Cal RB, Johansson G, Castillo L. 2008. Transitionally rough zero pressure gradient turbulent boundary layers. *Exp. Fluids*. 44(1):115–24

Buchmann N a, Atkinson C, Soria J. 2013. Ultra-high-speed tomographic digital holographic velocimetry in supersonic particle-laden jet flows. *Meas. Sci. Technol.* 24:24005

Busse A, Sandham ND. 2012. Influence of an anisotropic slip-length boundary condition on turbulent channel flow. *Phys. Fluids*. 24(5):55111

Busse A, Sandham ND. 2013. Turbulent flow over superhydrophobic surfaces - roughness versus slip. *14th Eur. Turbul. Conf.*

Chan L, Macdonald M, Chung D, Hutchins N, Ooi A. 2015. A systematic investigation of roughness height and wavelength in turbulent pipe flow in the transitionally rough regime. *J. Fluid Mech.* 771:743–77

Checco A, Ocko BM, Rahman A, Black CT, Tasinkevych M, et al. 2014. Collapse and reversibility of the superhydrophobic state on nanotextured surfaces. *Phys. Rev. Lett.* 112(21):1–5

Cheong FC, Krishnatreya BJ, Grier DG. 2010. Strategies for three-dimensional particle tracking with holographic video microscopy. *Opt. Express*. 18(13):13563–73

Choo Y-J, Kang B-S. 2006. The characteristics of the particle position along an optical axis in particle holography. *Trans. Korean Soc. Mech. Eng. B*. 30(4):287–97

Cottin-Bizonne C, Barrat J-L, Bocquet L, Charlaix E. 2003. Low-friction flows of liquid at nanopatterned interfaces. *Nat. Mater.* 2(4):238–40

Cussler EL. 1997. *Diffusion: Mass Transfer in Fluid Systems*. Cambridge university press

Daniello RJ, Waterhouse NE, Rothstein JP. 2009. Drag reduction in turbulent flows over superhydrophobic surfaces. *Phys. Fluids*. 21(8):85103

Das B, Yelleswarapu CS. 2010. Dual plane in-line digital holographic microscopy. *Opt. Lett.* 35(20):3426–28

Das B, Yelleswarapu CS, Rao D. 2012. Parallel-quadrature phase-shifting digital holographic microscopy using polarization beam splitter. *Opt. Commun.* 285(24):4954–5960

De Graaff DB, Eaton JK. 2000. Reynolds-number scaling of the flat-plate turbulent boundary layer. *J. Fluid Mech.* 422:319–46

Dean RB. 1978. Reynolds number dependence of skin friction and other bulk flow variables in two-dimensional rectangular duct flow. *J. Fluids Eng.* 100(2):215–23

Denis L, Fournier C, Fournel T, Ducottet C. 2005. Twin-image noise reduction by phase retrieval in in-line digital holography. *Proc. SPIE*. 5914:59140J–59140J–14

Dilip D, Bobji MS, Govardhan RN. 2015. Effect of absolute pressure on flow through a textured hydrophobic microchannel. *Microfluid. Nanofluidics*. 19(6):1409–27

Dilip D, Jha NK, Govardhan RN, Bobji MS. 2014. Controlling air solubility to maintain "Cassie" state for sustained drag reduction. *Colloids Surfaces A Physicochem. Eng. Asp.* 459:217–24

Dorrer C, Rühe J. 2009. Some thoughts on superhydrophobic wetting. *Soft Matter*. 5(1):51

Emami B, Hemeda AA, Amrei MM, Luzar A, Gad-el-Hak M, Vahedi Tafreshi H. 2013. Predicting longevity of submerged superhydrophobic surfaces with parallel grooves. *Phys. Fluids*. 25(6):62108

Extrand CW. 2011. Repellency of the lotus leaf: Resistance to water intrusion under hydrostatic pressure. *Langmuir*. 27(11):6920–25

Fukagata K, Kasagi N, Koumoutsakos P. 2006. A theoretical prediction of friction drag reduction in turbulent flow by superhydrophobic surfaces. *Phys. Fluids*. 18(5):51703

García-Mayoral R, Jiménez J. 2011. Hydrodynamic stability and breakdown of the viscous regime over riblets. *J. Fluid Mech.* 678:317–47

Giacomello A, Chinappi M, Meloni S, Casciola CM. 2012. Metastable wetting on superhydrophobic surfaces: Continuum and atomistic views of the cassie-baxter-wenzel transition. *Phys. Rev. Lett.* 109(22):1–4

Gopalan S, Katz J. 2000. Flow structure and modeling issues in the closure region of attached cavitation. *Phys. Fluids*. 12(4):895

Greidanus AJ, Delfos R, Westerweel J. 2011. Drag reduction by surface treatment in turbulent Taylor-Couette flow. *J. Phys. Conf. Ser.* 318(8):82016

Guo P, Devaney AJ. 2004. Digital microscopy using phase-shifting digital holography with two reference waves. *Opt. Lett.* 29(8):857–59

Guo Z, Liu W, Su BL. 2011. Superhydrophobic surfaces: From natural to biomimetic to functional. *J. Colloid Interface Sci.* 353(2):335–55

Hasegawa Y, Frohnapfel B, Kasagi N. 2011. Effects of spatially varying slip length on friction drag reduction in wall turbulence. *J. Phys. Conf. Ser.* 318(2):22028

Henoch C, Krupenkin T, Kolodner P, Taylor J, Hodes M, et al. 2006. Turbulent Drag Reduction Using Superhydrophobic Surfaces. *3rd AIAA Flow Control Conf.*, pp. 1–5. Reston, Virigina: American Institute of Aeronautics and Astronautics

Hokmabad BV, Ghaemi S. 2017. Effect of Flow and Particle-Plastron Collision on the Longevity of Superhydrophobicity. *Sci. Rep.* 7(41448):

Hong J, Katz J, Schultz MP. 2011. Near-wall turbulence statistics and flow structures over three-dimensional roughness in a turbulent channel flow. *J. Fluid Mech.* 667:1–37

Hu H, Du P, Wen J, Luo Z, Zhang Z, Song D. 2017. Maintenance of air layer and drag reduction on superhydrophobic surface with random micro-structures. *Ocean Eng.* 130(June 2016):1–18

Jeffs K, Maynes D, Webb BW. 2010. Prediction of turbulent channel flow with superhydrophobic walls consisting of micro-ribs and cavities oriented parallel to the flow direction. *Int. J. Heat Mass Transf.* 53(4):786–96

Jelly TO, Jung SY, Zaki TA. 2014. Turbulence and skin friction modification in channel flow with streamwise-aligned superhydrophobic surface texture. *Phys. Fluids*. 26(9):95102

Jimenez J. 2004. TURBULENT FLOWS OVER ROUGH WALLS. *Annu. Rev. Fluid Mech.*

36(1):173–96

Jung YC, Bhushan B. 2010. Biomimetic structures for fluid drag reduction in laminar and turbulent flows. *J. Phys. Condens. Matter*. 22(3):35104

Kakue T, Yonesaka R, Tahara T, Awatsuji Y, Nishio K, et al. 2011. High-speed phase imaging by parallel phase-shifting digital holography. *Opt. Lett.* 36(21):4131–33

Kapfenberger D, Sonn-Segev a, Roichman Y. 2013. Accurate holographic imaging of colloidal particle pairs by Rayleigh-Sommerfeld reconstruction. *Opt. Express*. 21(10):12228–37

Katz J, Sheng J. 2010. Applications of Holography in Fluid Mechanics and Particle Dynamics. *Annu. Rev. Fluid Mech.* 42:531–55

Kim MK. 2010. Principles and techniques of digital holographic microscopy. *SPIE Rev.* 1(1):18005

Kim P, Kreder MJ, Alvarenga J, Aizenberg J. 2013. Hierarchical or Not? Effect of the Length Scale and Hierarchy of the Surface Roughness on Omniphobicity of Lubricant-Infused Substrates. *Nano Lett.* 13(4):1793–99

Krupenkin TN, Taylor JA, Wang EN, Kolodner P, Hodes M, Salamon TR. 2007. Reversible wetting-dewetting transitions on electrically tunable superhydrophobic nanostructured surfaces. *Langmuir*. 23(18):9128–33

Kusumaatmaja H, Blow ML, Dupuis A, Yeomans JM. 2008. The collapse transition on superhydrophobic surfaces. *Europhys. Lett.* 81(3):36003

Kwon HM, Paxson AT, Varanasi KK, Patankar NA. 2011. Rapid deceleration-driven wetting transition during pendant drop deposition on superhydrophobic surfaces. *Phys. Rev. Lett.* 106(3):1–4

Kwon Y, Patankar N, Choi J, Lee J. 2009. Design of surface hierarchy for extreme hydrophobicity. *Langmuir*. 25(11):6129–36

Lai S, King B, Neifeld MA. 2000. Wave front reconstruction by means of phase-shifting digital in-line holography. *Opt. Commun.* 173(1–6):155–60

Langehanenberg P, Bally G, Kemper B. 2011. Autofocusing in digital holographic microscopy. *3D Res.* 2(1):1–11

Lauga E, Stone H a. 2003. Effective slip in pressure-driven Stokes flow. *J. Fluid Mech.* 489:55–77

Lee C, Choi CH, Kim CJ. 2008. Structured surfaces for a giant liquid slip. *Phys. Rev. Lett.* 101(6):1–4

Lee C, Kim CJ. 2011. Underwater restoration and retention of gases on superhydrophobic surfaces for drag reduction. *Phys. Rev. Lett.* 106(1):1–4

Lee J, Jelly TO, Zaki TA. 2015. Effect of reynolds number on turbulent drag reduction by superhydrophobic surface textures. *Flow, Turbul. Combust.* 95(2–3):277–300

Lee JH. 2015. Turbulent boundary layer flow with a step change from smooth to rough surface. *Int. J. Heat Fluid Flow*. 54:39–54

Lee S-H, Grier DG. 2007. Holographic microscopy of holographically trapped three-dimensional structures. *Opt. Express*. 15(4):1505–12

Lee S-H, Sung HJ. 2007. Direct numerical simulation of the turbulent boundary layer over a rod-roughened wall. *J. Fluid Mech.* 584:125–46

Lee SJ, Seo KW, Choi YS, Sohn MH. 2011. Three-dimensional motion measurements of free-swimming microorganisms using digital holographic microscopy. *Meas. Sci. Technol.* 22(6):64004

Lin M, Nitta K, Matoba O, Awatsuji Y. 2012. Parallel phase-shifting digital holography with adaptive function using phase-mode spatial light modulator. *Appl. Opt.* 51(14):2633

Ling H, Katz J. 2014. Separating twin images and locating the center of a microparticle in dense suspensions using correlations among reconstructed fields of two parallel holograms. *Appl. Opt.* 53(27):G1–11

Ling H, Srinivasan S, Golovin K, Mckinley GH, Tuteja A, Katz J. 2016. High-resolution velocity measurement in the inner part of turbulent boundary layers over super-hydrophobic surfaces. *J. Fluid Mech*. 801:670–703

Liu J-P, Poon T-C. 2009. Two-step-only quadrature phase-shifting digital holography. *Opt. Lett.* 34(3):250–52

Liu K, Tian Y, Jiang L. 2013. Bio-inspired superoleophobic and smart materials: Design, fabrication, and application. *Prog. Mater. Sci.* 58(4):503–64

Liu X, Katz J. 2006. Instantaneous pressure and material acceleration measurements using a four-exposure PIV system. *Exp. Fluids*. 41(2):227–40

Liu X, Katz J. 2013. Vortex-corner interactions in a cavity shear layer elucidated by time-resolved measurements of the pressure field. *J. Fluid Mech.* 728:417–57

Lu Rong LR, Feng Pan FP, Wen Xiao WX, Yan Li YL, Fanjing Wang FW. 2012. Twin image elimination from two in-line holograms via phase retrieval. *Chinese Opt. Lett.* 10(6):060902–4

Lv P, Xue Y, Shi Y, Lin H, Duan H. 2014. Metastable states and wetting transition of submerged superhydrophobic structures. *Phys. Rev. Lett.* 112(19):1–5

Manukyan G, Oh JM, Van Den Ende D, Lammertink RGH, Mugele F. 2011. Electrical switching of wetting states on superhydrophobic surfaces: A route towards reversible Cassie-to-Wenzel transitions. *Phys. Rev. Lett.* 106(1):1–4

Martell MB, Perot JB, Rothstein JP. 2009. Direct numerical simulations of turbulent flows over superhydrophobic surfaces. *J. Fluid Mech.* 620:31–41

Martell MB, Rothstein JP, Perot JB. 2010. An analysis of superhydrophobic turbulent drag reduction mechanisms using direct numerical simulation. *Phys. Fluids*. 22(6):1–13

Marusic I, Mathis R, Hutchins N. 2010. High Reynolds number effects in wall turbulence. *Int. J. Heat Fluid Flow*. 31(3):418–28

Meng XF, Cai LZ, Xu XF, Yang XL, Shen XX, et al. 2006. Two-step phase-shifting interferometry and its application in image encryption. *Opt. Lett.* 31(10):1414–16

Micó V, García J, Zalevsky Z, Javidi B. 2009. Phase-shifting Gabor holography. *Opt. Lett.* 34(10):1492

Min T, Kim J. 2004. Effects of hydrophobic surface on skin-friction drag. *Phys. Fluids*. 16(7):L55–58

Murata S, Harada D, Tanaka Y. 2009. Spatial phase-shifting digital holography for three-dimensional particle tracking velocimetry. *Jpn. J. Appl. Phys.* 48(9 Part 3):1–6

Nagib HM, Chauhan KA, Monkewitz P a. 2007. Approach to an asymptotic state for zero pressure gradient turbulent boundary layers. *Philos. Trans. A. Math. Phys. Eng. Sci.* 365(January):755–70

Nomura T, Murata S, Nitanai E, Numata T. 2006. Phase-shifting digital holography with a phase difference between orthogonal polarizations. *Appl. Opt.* 45(20):4873–77

Nosonovsky M. 2007. Multiscale roughness and stability of superhydrophobic biomimetic interfaces. *Langmuir*. 23(6):3157–61

Ou J, Perot B, Rothstein JP. 2004. Laminar drag reduction in microchannels using ultrahydrophobic surfaces. *Phys. Fluids*. 16(12):4635–43

Ou J, Rothstein JP. 2005. Direct velocity measurements of the flow past drag-reducing ultrahydrophobic surfaces. *Phys. Fluids*. 17(10):103606

Papadopoulos P, Mammen L, Deng X, Vollmer D, Butt H. 2013. How superhydrophobicity breaks down. *Proc. Natl. Acad. Sci. U. S. A.* 110(9):3254–58

Park H. 2015. *A Numerical Study of the Effects of Superhydrophobic Surfaces on Skin-Friction Drag Reduction in Wall-Bounded Shear Flows*. PhD thesis, University of California, Los Angeles

Park H, Park H, Kim J. 2013a. A numerical study of the effects of superhydrophobic surface on skin-friction drag in turbulent channel flow. *Phys. Fluids*. 25(11):110815

Park H, Sun G, Kim CJCJ. 2013b. Turbulent drag reduction on superhydrophobic surfaces confirmed by built-in shear sensing. *Proc. IEEE Int. Conf. Micro Electro Mech. Syst.* 1183–86

Park H, Sun GY, Kim CJ. 2014. Superhydrophobic turbulent drag reduction as a function of surface grating parameters. *J. Fluid Mech.* 747:722–34

Patankar NA. 2004. Transition between superhydrophobic states on rough surfaces. *Langmuir*. 20(17):7097–7102

Patankar N a. 2003. On the modeling of hydrophobic contact angles on rough surfaces. *Langmuir*. 19(4):1249–53

Peguero C, Breuer K. 2009. On Drag Reduction in Turbulent Channel Flow over

Superhydrophobic Surfaces. *12th EUROMECH Eur. Turbul. Conf.*, pp. 233–36

Piao L, Park H. 2015. Two-dimensional analysis of air–water interface on superhydrophobic grooves under fluctuating water pressure. *Langmuir*. 31(29):8022–32

Pillutla V, Abhijeet, Ling H, Rodriguez L, Rodrigues D, et al. 2016. Robust drag reducing superhydrophobic surfaces with large slip lengths. *31st Symp. Nav. Hydrodyn.*

Poetes R, Holtzmann K, Franze K, Steiner U. 2010. Metastable underwater superhydrophobicity. *Phys. Rev. Lett.* 105(16):1–4

Quéré D. 2008. Wetting and roughness. *Annu. Rev. Mater. Res.* 38(1):71–99

Roth GI, Katz J. 2001. Five techniques for increasing the speed and accuracy of PIV interrogation. *Meas. Sci. Technol.* 12(3):238–45

Rothstein JP. 2010. Slip on superhydrophobic surfaces. *Annu. Rev. Fluid Mech*. 42:89–109

Saito N, Pullin DI. 2014. Large eddy simulation of smooth–rough–smooth transitions in turbulent channel flows. *Int. J. Heat Mass Transf.* 78:707–20

Samaha MA, Tafreshi HV, Gad-el-Hak M. 2012a. Influence of Flow on Longevity of Superhydrophobic Coatings. *Langmuir*. 28(25):9759–66

Samaha MA, Vahedi Tafreshi H, Gad-el-Hak M. 2012b. Sustainability of superhydrophobicity under pressure. *Phys. Fluids*. 24(11):112103

Sarkar A, Kietzig A-M. 2015. Design of a robust superhydrophobic surface: thermodynamic and kinetic analysis. *Soft Matter*. 11(18):3733–3733

Schlatter P, Örlü R. 2010. Assessment of direct numerical simulation data of turbulent boundary layers. *J. Fluid Mech.* 659:116–26

Schultz MP, Flack KA. 2007. The rough-wall turbulent boundary layer from the hydraulically smooth to the fully rough regime. *J. Fluid Mech.* 580:381–405

Seo J, García-Mayoral R, Mani A. 2015. Pressure fluctuations and interfacial robustness in turbulent flows over superhydrophobic surfaces. *J. Fluid Mech.* 783:448–73

Seo J, Mani A. 2016. On the scaling of the slip velocity in turbulent flows over superhydrophobic surfaces. *Phys. Fluids*. 28(2):25110

Shaked NT, Newpher TM, Ehlers MD, Wax A. 2010. Parallel on-axis holographic phase microscopy of biological cells and unicellular microorganism dynamics. *Appl. Opt.* 49(15):2872–78

Sharma RN, Rahman SU. 2002. A simple model for turbulent boundary layer mass transfer on flat plate in parallel flow. *Chem. Eng. J.* 85(1):35–39

Sheng J, Malkiel E, Katz J. 2003. Single beam two-views holographic particle image velocimetry. *Appl. Opt.* 42(2):235–50

Sheng J, Malkiel E, Katz J. 2006. Digital holographic microscope for measuring three-dimensional particle distributions and motions. *Appl. Opt.* 45(16):3893

Sheng J, Malkiel E, Katz J. 2008. Using digital holographic microscopy for simultaneous measurements of 3D near wall velocity and wall shear stress in a turbulent boundary layer. *Exp. Fluids*. 45(6):1023–35

Sheng J, Malkiel E, Katz J. 2009. Buffer layer structures associated with extreme wall stress events in a smooth wall turbulent boundary layer. *J. Fluid Mech.* 633:17–60

Sheng J, Malkiel E, Katz J, Adolf J, Belas R, Place AR. 2007. Digital holographic microscopy reveals prey-induced changes in swimming behavior of predatory dinoflagellates. *Proc. Natl. Acad. Sci. U. S. A.* 104(44):17512–17

Situ G, Ryle JP, Gopinathan U, Sheridan JT. 2008. Intensity Measurements At Two Different Planes. *Appl. Opt.* 47(5):711–17

Slimani F, Grehan G, Gouesbet G, Allano D. 1984. Near-field Lorenz-Mie theory and its application to microholography. *Appl. Opt.* 23(3):4140

Smits AJ, Matheson N, Joubert PN. 1983. Low-Reynolds-number turbulent boundary layers in zero and favorable pressure gradients. *J. Sh. Res.* 27(3):147–57

Smits AJ, McKeon BJ, Marusic I. 2011. High–Reynolds number wall turbulence. *Annu. Rev. Fluid Mech.* 43:353–75

Song D, Daniello RJ, Rothstein JP. 2014. Drag reduction using superhydrophobic sanded Teflon surfaces. *Exp. Fluids*. 55(8):1783

Spalart PR. 1988. Direct simulation of a turbulent boundary layer up to $R \theta = 1410$. *J. Fluid Mech.*

187:61–98

Srinivasan S, Chhatre SS, Mabry JM, Cohen RE, McKinley GH. 2011. Solution spraying of poly(methyl methacrylate) blends to fabricate microtextured, superoleophobic surfaces. *Polymer (Guildf)*. 52(14):3209–18

Srinivasan S, Choi W, Park K-C, Chhatre SS, Cohen RE, McKinley GH. 2013. Drag reduction for viscous laminar flow on spray-coated non-wetting surfaces. *Soft Matter*. 9(24):5691–5702

Srinivasan S, Kleingartner JA, Gilbert JB, Cohen RE, Milne AJB, McKinley GH. 2015. Sustainable drag reduction in turbulent Taylor-Couette flows by depositing sprayable superhydrophobic surfaces. *Phys. Rev. Lett.* 114(1):1–5

Subhash Latthe S. 2012. Recent progress in preparation of superhydrophobic surfaces: A review. *J. Surf. Eng. Mater. Adv. Technol.* 2(2):76–94

Suzuki H, Nomura T, Nitanai E, Numata T. 2010. Dynamic recording of a digital hologram with single exposure by a wave-splitting phase-shifting method. *Opt. Rev.* 17(3):176–80

Tahara T, Ito K, Fujii M, Kakue T, Shimozato Y. 2010. Experimental demonstration of parallel two-step phase-shifting digital holography. *Opt. Express*. 18(18):18975–80

Talapatra S, Katz J. 2012. Coherent structures in the inner part of a rough-wall channel flow resolved using holographic PIV. *J. Fluid Mech.* 1–10

Talapatra S, Katz J. 2013. Three-dimensional velocity measurements in a roughness sublayer using microscopic digital in-line holography and optical index matching. *Meas. Sci. Technol.* 24(2):24004

Tao B, Katz J, Meneveau C. 2002. Statistical geometry of subgrid-scale stresses determined from holographic particle image velocimetry measurements. *J. Fluid Mech.* 457:35–78

Tian H, Zhang J, Wang E, Yao Z, Jiang N. 2015. Experimental investigation on drag reduction in turbulent boundary layer over superhydrophobic surface by TRPIV. *Theor. Appl. Mech. Lett.* 5(1):45–49

Tian X, Verho T, Ras RHA. 2016. Moving superhydrophobic surfaces toward real-world applications. *Science*. 352(6282):142–43

Toge H, Fujiwara H, Sato K. 2008. One-shot digital holography for recording color 3-D images. *Pract. Hologr. Xxii Mater. Appl.* 6912:U9120-

Tsai P, Lammertink RGH, Wessling M, Lohse D. 2010. Evaporation-triggered wetting transition for water droplets upon hydrophobic microstructures. *Phys. Rev. Lett.* 104(11):2–3

Vajdi Hokmabad B, Ghaemi S. 2016. Turbulent flow over wetted and non-wetted superhydrophobic counterparts with random structure. *Phys. Fluids*. 28(1):15112

Verho T, Korhonen JT, Sainiemi L, Jokinen V, Bower C, et al. 2012. Reversible switching between superhydrophobic states on a hierarchically structured surface. *Proc. Natl. Acad. Sci.* 109(26):10210–13

Vrancken RJ, Kusumaatmaja H, Hermans K, Prenen AM, Pierre-Louis O, et al. 2010. Fully reversible transition from wenzel to cassie-baxter states on corrugated superhydrophobic surfaces. *Langmuir*. 26(5):3335–41

Watanabe K, Udagawa Y, Udagawa H. 1999. Drag reduction of Newtonian fluid in a circular pipe with a highly water-repellent wall. *J. Fluid Mech.* 381:225–38

Weiss RF. 1970. The solubility of nitrogen,oxygen and argon in water and seawater. *Deep. Res.* 17:721–35

Whyman G, Bormashenko E. 2011. How to make the cassie wetting state stable? *Langmuir*. 27(13):8171–76

Wilson L, Zhang R. 2012. 3D Localization of weak scatterers in digital holographic microscopy using Rayleigh-Sommerfeld back-propagation. *Opt. Express*. 20(15):16735

Woolford B, Prince J, Maynes D, Webb BW. 2009. Particle image velocimetry characterization of turbulent channel flow with rib patterned superhydrophobic walls. *Phys. Fluids*. 21(8):85106

Wu X, Meunier-Guttin-Cluzel S, Wu Y, Saengkaew S, Lebrun D, et al. 2012. Holography and micro-holography of particle fields: A numerical standard. *Opt. Commun.* 285(13–14):3013–20

Wu X, Moin P. 2010. Transitional and turbulent boundary layer with heat transfer. *Phys. Fluids*. 22(8):85105

Xiang Y, Xue Y, Lv P, Li D, Duan H. 2016. Influence of fluid flow on the stability and wetting transition of submerged superhydrophobic surfaces. *Soft Matter*. 12(18):4241–46

Xu M, Sun G, Kim CJ. 2014. Infinite lifetime of underwater superhydrophobic states. *Phys. Rev. Lett.* 113(3):1–5

Xue Y, Chu S, Lv P, Duan H. 2012. Importance of hierarchical structures in wetting stability on submersed superhydrophobic surfaces. *Langmuir*. 28(25):9440–50

Xue Y, Lv P, Lin H, Duan H. 2016. Underwater superhydrophobicity: stability, design and regulation, and applications. *Appl. Mech. Rev.* 68(3):30803

Xue Y, Lv P, Liu Y, Shi Y, Lin H, Duan H. 2015. Morphology of gas cavities on patterned hydrophobic surfaces under reduced pressure. *Phys. Fluids*. 27(9):92003

Yamaguchi I, Zhang T. 1997. Phase-shifting digital holography. *Opt. Lett.* 22(16):1268–70

Yan YY, Gao N, Barthlott W. 2011. Mimicking natural superhydrophobic surfaces and grasping the wetting process: A review on recent progress in preparing superhydrophobic surfaces. *Adv. Colloid Interface Sci.* 169(2):80–105

Yang J, Zhang Z, Xu X, Men X, Zhu X, Zhou X. 2011. Superoleophobic textured aluminum surfaces. *New J. Chem.* 35:2422–26

Yang Y, Kang B. 2008. Experimental validation for the determination of particle positions by the correlation coefficient method in digital particle holography. *Appl. Opt.* 47(32):5953–60

Ybert C, Barentin C, Cottin-Bizonne C, Joseph P, Bocquet L. 2007. Achieving large slip with superhydrophobic surfaces: Scaling laws for generic geometries. *Phys. Fluids*. 19(12):123601

You D, Moin P. 2007. Effects of hydrophobic surfaces on the drag and lift of a circular cylinder. *Phys. Fluids*. 19(8):81701

Zhang C, Wang J, Katz J. 2017. Deformation of compliant wall in a turbulent channel flow. *J. Fluid Mech.* accepted:

Zhang Y, Pedrini G, Osten W, Tiziani H. 2003. Whole optical wave field reconstruction from double or multi in-line holograms by phase retrieval algorithm. *Opt. Express*. 11(24):3234–41

Zhang Y, Pedrini G, Osten W, Tiziani HJ. 2004. Reconstruction of in-line digital holograms from two intensity measurements. *Opt. Lett.* 29(15):1787–89

Zhao J, Du X, Shi X. 2007. Experimental research on friction-reduction with super-hydrophobic surfaces. *J. Mar. Sci. Appl.* 6(3):58–61

Zheng QS, Yu Y, Zhao ZH. 2005. Effects of hydraulic pressure on the stability and transition of wetting modes of superhydrophobic surfaces. *Langmuir*. 21(26):12207–12

Vita

Place of Birth: Hangzhou, Zhejiang, China

Year of Birth: 1989

Education

Ph.D., Johns Hopkins University, Baltimore, MD, July 2017

M.S., Johns Hopkins University, Baltimore, MD, May 2014

B.S., University of Science and Technique of China, Hefei, China, July 2011

Journal & Conference Publications

1. **Ling, H.**, Fu, M., Hultmark, M., Katz, J., (2017). "Effect of Reynolds Number and Saturation Level on Gas Diffusion in and out of A Hierarchical Super-Hydrophobic Surface". *Physical Review Fluids*. *Submitted.*
2. Pillutla, V., Abhijeet, **Ling, H.,** Rodriguez, L., Rodrigues, D. B. C., Katz, J., Choi, W., (2017). "Drag-reducing superhydrophobic surfaces with large drag reduction and high robustness against pressure perturbations". *Advanced Materials. In preparation.*
3. **Ling, H.,** Srinivasan, S., Golovin, K., Pillutla, V., Abhijeet, McKinley, G. H., Tuteja, A., Choi, W., Katz, J., (2016). "Flow Structure and Turbulence in the Inner Part of Turbulent Boundary Layers over Super-Hydrophobic Surfaces". *The 31st Symposium on Naval Hydrodynamics*, September 11-16, Monterey, California, USA.
4. Pillutla, V., Abhijeet, **Ling, H.,** Rodriguez, L., Rodrigues, D. B. C., Katz, J., Choi, W., (2016). "Robust Drag Reduction Superhydrophobic Surfaces with Large Slip Lengths". *The 31st Symposium on Naval Hydrodynamics*, September 11-16, Monterey, California, USA.
5. **Ling, H.**, Srinivasan, S., Golovin, K., McKinley, G. H., Tuteja, A., Kata, J., (2016). "High-resolution velocity measurement in the inner part of turbulent boundary layers over super-hydrophobic surfaces". *Journal of Fluid Mechanics*. Volume 801, 670-703.
6. **Ling, H.**, Katz, J., (2014). "Separating twin images and locating the center of a microparticle in dense suspensions using correlations among reconstructed fields of two parallel holograms". *Applied Optics*. Volume 53(27), G1-G11.

Academic & Conference Presentations

1. **Ling, H.**, Katz, J., (2017). "Experimental study of plastron stability on super-hydrophobic surfaces". *ONR-MURI program review*, June 1, Annapolis, Maryland, USA.
2. **Ling, H.** (2017). "Friction drag reduction in turbulent flow by super-hydrophobic surface". *Invited talk*, April 21, George Mason University, Virginia, USA.
3. **Ling, H.** (2017). "Experimental study of turbulent boundary layers over super-hydrophobic surfaces". *Invited talk*, April 17, Stanford University, CA, USA.
4. **Ling, H.,** Srinivasan, S., Golovin, K., Pillutla, V., Abhijeet, McKinley, G. H., Tuteja, A., Choi, W., Katz, J., (2016). "Effects of roughness height, pressure and streamwise distance on stress profiles in the inner part of turbulent boundary layer over super-hydrophobic surfaces". *The 69th Annual Meeting of the APS Division of Fluid Dynamics*, November 20-22, Portland, Oregon, USA.
5. **Ling, H.**, Katz, J., (2016). "Experimental study of plastron stability on super-hydrophobic surfaces". *ONR-MURI program review*, November 10-11, University of Michigan, Michigan, USA.
6. **Ling, H.**, Katz, J., (2016). "High resolution measurements of flow and turbulence in the inner part of turbulent boundary layers over super-hydrophobic surfaces". *ONR-MURI program review*, April 7-8, Johns Hopkins University, Maryland, USA.
7. **Ling, H.,** Srinivasan, S., Golovin, K., McKinley, G. H., Tuteja, A., Katz, J., (2015). "Velocity and Reynolds stress profiles in the inner part of a turbulent boundary layer over super-hydrophobic surfaces". *The 68th Annual Meeting of the APS Division of Fluid Dynamics*, November 22-24, Boston, Massachusetts, USA.
8. **Ling, H.,** Srinivasan, S., McKinley, G. H., Katz, J., (2015). "High resolution velocity measurements within a turbulent boundary layer over super-hydrophobic surface". *2015 Research Symposium on Environmental and Applied Fluid Dynamics*, May 26, Washington, District of Columbia, USA.
9. **Ling, H.**, Katz, J., (2015). "High resolution velocity measurements within a turbulent boundary layer over super-hydrophobic surface". *ONR-MURI program review*, September 29-30, Princeton University, New Jersey, USA.
10. **Ling, H.**, Katz, J., (2015). "High resolution velocity measurements within a turbulent boundary layer over super-hydrophobic surface". *ONR-MURI program review*, January 23, Stanford University, California, USA.

11. **Ling, H.,** Srinivasan, S., Katz, J., McKinley, G. H., (2014). “High resolution velocity measurements within a turbulent boundary layer over super-hydrophobic surface”. *The 67th Annual Meeting of the APS Division of Fluid Dynamics*, November 23-25, San Francisco, California, USA.
12. **Ling, H.**, Katz, J. (2014). “High resolution velocity measurements within a turbulent boundary layer over super-hydrophobic surface”. *ONR-MURI program review*, June 26, Stanford University, California, USA.
13. **Ling, H.**, Katz, J. (2013). “Real and virtual image separation in digital in-line holography microscopy by recording two parallel holograms”. *The 66th Annual Meeting of the APS Division of Fluid Dynamics*, November 24-26, Pittsburgh, Pennsylvania, USA.
14. **Ling, H.**, Katz, J. (2013). “Preparations for high-resolution measurements in the inner part of a boundary layer over superhydrophobic surfaces”. *ONR-MURI program review*, September 17, Arlington, Virginia, USA.